Universitá degli Studi di Milano-Bicocca

Dipartimento di Fisica 'G. Occhialini'

Corso Di Dottorato in Fisica e Astronomia
Ciclo XXVIII
A. A. 2012-2015

Image Correlation Methods to Follow Dynamic Processes in Biological Systems

Settore Scientifico Disciplinare FIS/07

Supervisor:
Prof.ssa Maddalena Collini

Coordinatore:
Prof. Giuseppe Chirico

Tesi di Dottorato di:
Margaux Bouzin

Contents

Introduction

Transport processes are ubiquitous in biological systems, spanning several orders of magnitude in their characteristic temporal and spatial scales. The transport of organelles, proteins and cargoes within the micron-sized heterogeneous and crowded cellular environment mainly occurs by Brownian diffusion, which plays a crucial role in the cellular signaling, transduction and proper functioning. By imposing order and directionality onto the naturally stochastic behavior of thermal diffusion, directional flow or drift phenomena contribute to enhance the diffusion-mediated intracellular trafficking. They are also responsible for the delivery of blood or nutrients and the clearance of toxins on the larger scale of whole tissues and organs, over which diffusion is less efficient. As technological advancements shrink the spatial and temporal scales of observation of living systems, the theoretical modeling and experimental investigation of biological - diffusive and directional - transport processes has therefore the potential of fueling research breakthroughs in diverse fields ranging from cell or molecular biology to physiology and immunology.

In this work I adopt and extend the quantitative approach of fluorescence Image Correlation Spectroscopy (ICS) for the investigation of diffusive and directional transport processes from the single-cell level up to whole microcirculatory systems. As I extensively review in Part I with the basic principles of both Fluorescence Correlation Spectroscopy (FCS) and ICS, the measurement of transport parameters is performed on raster-scanned images acquired *in-vivo* by fluorescence or reflectance confocal microscopy. By the computation of the temporal, spatial and spatio-temporal correlation function of the detected signal fluctuations, the specific mode of motion of the imaged particles as well as their characteristic dynamic parameters (for example, diffusion coefficients and drift velocities) can be identified. The timescale of the investigated process usually dictates whether the correlation function should be computed as a temporal correlation function on individual

raster-scanned xy-images, or as a spatio-temporal correlation function on a xyt-sequence of images acquired in time lapse mode.

I focus at first on the measurement of flow velocities in geometrically complex microcirculatory networks: Part II is entirely devoted to the development of a novel image-processing method, and flow-measurement technique, which I have called FLICS or FLow Image Correlation Spectroscopy.
FLICS has the peculiarity of exploiting a single raster-scanned xy-image, acquired by detecting the signal of bright, sparse flowing objects (e.g., red blood cells) in confocal or multi-photon fluorescence microscopy. By the computation of the Cross Correlation Function (CCF) of the fluorescence intensity fluctuations detected in pairs of columns of the image, both the modulus and the direction of the flow velocity vector can be mapped, with single-capillary sensitivity and sub-second temporal resolution, in the whole vessel pattern within the imaged field of view.
The explicit analytical expression of the CCF is derived (in Chapter 2) by applying the principles of scanning fluorescence correlation spectroscopy to drifting optically resolved objects. While beginning with the general case of three-dimensional diffusion and uniform flow, I focus then on the simpler case of two-dimensional flow in the focal plane and, by the approximation of negligible Brownian diffusion, I refine the data-analysis protocol to optimize the measurement of the flow speed in extended planar circulatory networks.
The newly developed theoretical framework is subsequently validated (in Chapter 3) in systems of increasing complexity, both *in-vitro* with fluorescent microspheres undergoing laminar flow in a simple microfluidic device, and *in-vivo* in the circulatory system of zebrafish embryos. At first, the correctness of the CCF analytical expression is assessed, by verifying that experimental cross-correlation functions exhibit the theoretically expected functional dependence on the flow velocity (modulus and direction) and on the image acquisition parameters. Then, the comparison with the results of line-scan based flow measurements on the same specimens is employed to validate the speed values measured by FLICS.
Once accomplished the validation of the theoretical framework, I conclude Part II (in Chapter 4) with the employment of the FLICS method for the characterization of the sinusoidal blood flow in the intricate murine hepatic microcirculatory system. I evidence the potential applications and relevance of the FLICS method in immunology, and I outline the main advantages FLICS offers with respect to state-of-the-art techniques and correlation analyses.

On the smaller single-cell spatial scale, I successively employ, in Part III, time-lapse confocal reflectance microscopy and image correlation in both the direct and the reciprocal space to characterize the intracellular transport of branched, star-shaped nanoparticles (GNSs, or Gold NanoStars). This investigation is motivated by the peculiar properties of noble-metal anisotropic nanostructures. As described in Chapter 5, their plasmon-enhanced absorption and scattering cross-sections, the ease in synthesis or functionalization, and the controlled cytotoxicity have already highlighted a number of interesting applications for (gold) nanoparticles, ranging from photo-luminescence or reflectance imaging, to drug delivery and targeted photo-thermal therapies. For all these applications, it is crucial to identify the GNSs complex intracellular trafficking pathways, and to quantitatively address how they behave once inside the cell cytoplasm.
At first (in Chapter 6) different transport mechanisms, spanning from pure Brownian diffusion to (sub-)ballistic super-diffusion, are revealed by Temporal and Spatio-Temporal Image Correlation Spectroscopy on the tens-of-seconds timescale. By combining these findings with numerical simulations and with a Bayesian (Hidden Markov Model based) analysis of single particle tracking data (Chapter 7), I ascribe the super-diffusive, sub-ballistic behavior underlying the GNSs dynamics to a two-state switch between Brownian diffusion in the cytoplasm and molecular motor-mediated active transport along the semi-flexible oriented filaments of the cytoskeleton. I propose therefore (in Chapter 8) a novel analytical theoretical framework for the investigation of intermittent-type transport phenomena by Fourier-space Image Correlation Spectroscopy (kICS).
The effect of all the dynamic and kinetic parameters (the diffusion coefficient, the drift velocity and the transition rates between the diffusive and the active transport regimes) is evaluated on simulated kICS correlation functions. Then I outline the optimal procedure for the analysis of experimental data and I derive whole-cell maps for each parameter underlying the GNSs intracellular dynamics.
Capable of identifying even simpler transport phenomena, whether purely diffusive or ballistic, the proposed intermittent kICS approach recovers the simplest stochastic transport model that accurately describes the experimental data: by not requiring any prior assumption on its Brownian or super-diffusive nature, this kICS analysis allows the exhaustive investigation of the dynamics of GNSs as well as of other biological macromolecules.

Part I

Theoretical background

Chapter 1

Fluorescence Correlation Spectroscopy

First developed in 1972 by Magde et al. for the investigation of the binding reaction of ethidium bromide to double-stranded DNA [1], Fluorescence Correlation Spectroscopy (FCS) is nowadays a well-established technique employed to measure a multitude of kinetic and thermodynamic parameters, including particle concentrations [2], translational [3] and rotational [4,5] diffusion coefficients, flow velocities [6,7], kinetic rate constants [1,8], triplet state lifetimes [9] and photochemical or photobleaching properties of dyes [10]. In contrast to much more invasive conventional relaxation methods - which recover kinetic and thermodynamic parameters from the way a system relaxes back to equilibrium after an initial external perturbation (for example, an induced concentration gradient or a temperature jump) - FCS takes advantage of the spontaneous fluctuations of the fluorescence signal emitted by a highly dilute fluorescent sample in a $\sim \mu m^3$ excitation volume [11,12]. These fluctuations, whether due to photophysical and photochemical reactions or to the molecular diffusion in and out of the excitation volume, exhibit average characteristic dissipation rates that are assigned by the underlying macroscopic transport coefficients and chemical rate constants [13]: these parameters can therefore be quantified by statistically analyzing fluorescence intensity fluctuations by the computation of the so-called auto- and cross- correlation functions.

1.1 Auto-correlation analysis

The raw data in FCS experiments consist in a temporal intensity trace $F(t)$ of the fluorescence signal emitted in a $\sim \mu m^3$ volume - typically defined by a diffraction-limited focused excitation laser beam and confocal detection optics - by a solution of fluorescent molecules with average concentration in the $\sim 1 - 100$ nM range [12,14]. Spontaneous fluorescence fluctuations resulting from whatever process is occurring in this volume are defined as $\delta F(t) = F(t) - < F(t) >_t$ and analyzed through the computation of the normalized temporal autocorrelation function $G(\tau)$ [12,14,15]:

$$G(\tau) = \frac{< \delta F^*(t)\delta F(t+\tau) >_t}{< F(t) >_t^2} = \frac{< F^*(t)F(t+\tau) >_t}{< F(t) >_t^2} - 1 \tag{1.1}$$

τ is the correlation lag time, while the star symbol $*$ denotes the operation of complex conjugation. Angular brackets $< ... >_t$ define a temporal average over a given, in principle infinite, time period:

$$< F^*(t)F(t+\tau) >_t = \lim_{T\to+\infty} \frac{1}{T}\int_0^T F^*(t)F(t+\tau)\, dt \tag{1.2}$$

The auto-correlation function experimentally recovered over a finite data integration time T approximates therefore the ideal correlation function defined in the limit $T \to +\infty$ [16].

Since by definition the auto-correlation function is the time-averaged product of the fluorescence intensity fluctuations $\delta F^*(t)$ at a given time t and $\delta F(t+\tau)$ at a delayed time $t+\tau$, $G(\tau)$ measures the self-similarity of the signal in time: it is expected to be a decreasing function of the lag time τ, exhibiting the maximum value (i.e., the maximum signal correlation) for $\tau = 0$. I begin by deriving the explicit analytical expression for this decaying function for the general case of a multiple-population system, with each chemical component undergoing both diffusive / directed transport and chemical reactions; in the following subsections, I focus on a few simplified cases (namely, Brownian diffusion of a single fluorescent species in the absence of chemical reactions and the coupling of free diffusion and uniform drift) of general interest.

1.1.1 General formalism

I derive the explicit expression for the auto-correlation function of eq. (1.1) by mostly adopting the notation and formalism originally developed by Magde, Elson

and Webb [3] and recently reviewed by Krichevsky and Bonnet [17]. I consider a solution of m species participating in chemical reactions while undergoing Brownian diffusion and uniform drift. The fluorescence intensity emitted by the molecules of the i^{th} species at time t can be written [12,17] as

$$F_i(t) = \phi_i \int_{-\infty}^{+\infty} I_{exc}(\underline{r}) S(\underline{r}) C_i(\underline{r}, t)\, d^3\underline{r} \tag{1.3}$$

where ϕ_i is the product of the fluorescence detection efficiency and of the molecules quantum yield and absorption cross-section; $I_{exc}(\underline{r})$ is the spatial distribution of the excitation intensity, $S(\underline{r})$ is the dimensionless optical transfer function of the objective-pinhole combination (specifying the effectively collected fraction of the emitted signal) and $C_i(\underline{r}, t)$ defines the local concentration of the molecules of species i. For the sake of compactness, $I_{exc}(\underline{r})$ and $S(\underline{r})$ can be combined into a single function $W(\underline{r})$, leading to

$$F_i(t) = \phi_i \int_{-\infty}^{+\infty} W(\underline{r}) C_i(\underline{r}, t)\, d^3\underline{r} \tag{1.4}$$

This fluorescence signal may fluctuate in time due to both fluctuations $\delta\phi_i$ of the molecular quantum yield or absorption cross-section, and number fluctuations $\delta C_i(\underline{r}, t)$ related to the molecular transit through the excitation volume: explicitly,

$$\delta F_i(t) = \int_{-\infty}^{+\infty} W(\underline{r}) \delta(\phi_i C_i(\underline{r}, t))\, d^3\underline{r} \tag{1.5}$$

For negligible fluctuations affecting the particles absorption and emission rates, $\delta(\phi_i C_i(\underline{r}, t)) = \delta\phi_i C_i(\underline{r}, t) + \phi_i \delta C_i(\underline{r}, t) \approx \phi_i \delta C_i(\underline{r}, t)$. By further performing a summation over all m molecular species,

$$\delta F(t) = \int_{-\infty}^{+\infty} W(\underline{r}) \sum_{i=1}^{m} \phi_i \delta C_i(\underline{r}, t)\, d^3\underline{r} \tag{1.6}$$

The substitution of eq. (1.6) into the auto-correlation function definition (eq. 1.1) leads to

$$\begin{aligned} G(\tau) &= \frac{\iint_{-\infty}^{+\infty} W^*(\underline{r}) W(\underline{r}') \sum_{i,j=1}^{m} \phi_i \phi_j < \delta C_i^*(\underline{r}, t) \delta C_j(\underline{r}', t+\tau) >_t d^3\underline{r} d^3\underline{r}'}{\left(< \int W(\underline{r}) \sum_{i=1}^{m} \phi_i C_i(\underline{r}, t)\, d^3\underline{r} >_t \right)^2} \\ &= \frac{\iint_{-\infty}^{+\infty} W^*(\underline{r}) W(\underline{r}') \sum_{i,j=1}^{m} \phi_i \phi_j < \delta C_i^*(\underline{r}, t) \delta C_j(\underline{r}', t+\tau) >_t d^3\underline{r} d^3\underline{r}'}{\left(\sum_{i=1}^{m} \phi_i < C_i > \int_{-\infty}^{+\infty} W(\underline{r})\, d^3\underline{r} \right)^2} \end{aligned} \tag{1.7}$$

For a stationary system, the concentration correlation term in the numerator of eq. (1.7) can be evaluated as

$$< \delta C_i^*(\underline{r}, t)\delta C_j(\underline{r}', t+\tau) >_t = < \delta C_i^*(\underline{r}, 0)\delta C_j(\underline{r}', \tau) > \tag{1.8}$$

Eq. (1.8) requires the concentration fluctuations $\delta C_i(\underline{r}, t)$ for $i = 1...m$. Near equilibrium, these satisfy [11,17]:

$$\frac{\partial}{\partial t}\delta C_i(\underline{r}, t) = D_i\nabla^2\delta C_i(\underline{r}, t) - \underline{v}_i \cdot \underline{\nabla}\delta C_i(\underline{r}, t) + \sum_{j=1}^{m} K_{ij}\delta C_j(\underline{r}, t) \tag{1.9}$$

The first two terms on the right-hand side of eq. (1.9) describe Brownian diffusion with diffusion coefficient D_i and directed transport with constant velocity $\underline{v}_i$ for the molecules of the i^{th} species; the last term contains kinetic constants K_{ij}, which are combinations of the equilibrium concentrations of the various species and of the chemical reaction rate constants. These differential equations are conveniently solved in Fourier space: their Fourier transform leads to

$$\frac{\partial}{\partial t}\delta\widehat{C}_i(\underline{q}, t) = \sum_{j=1}^{m}(-D_i\delta_{ij}|\underline{q}^2| + i\underline{q} \cdot \underline{v}_i\delta_{ij} + K_{ij})\delta\widehat{C}_j(\underline{q}, t) \equiv \sum_{j=1}^{m} M_{ij}\delta\widehat{C}_j(\underline{q}, t) \tag{1.10}$$

where I have adopted the convention

$$\delta\widehat{C}_i(\underline{q}, t) = \frac{1}{(2\pi)^{3/2}}\int_{-\infty}^{+\infty}\delta C_i(\underline{r}, t)e^{i\underline{q}\cdot\underline{r}}\, d^3\underline{r} \tag{1.11}$$

for the Fourier transform definition in 3D and with $M_{ij} \equiv -D_i\delta_{ij}|\underline{q}^2| + i\underline{q} \cdot \underline{v}_i\delta_{ij} + K_{ij}$. The solutions of eq. (1.10) are found by the computation of the eigenvalues $\lambda^{(s)}$ and of the eigenvectors $\chi^{(s)}$ of the matrix M [17]:

$$\delta\widehat{C}_i(\underline{q}, t) = \sum_{s=1}^{m}\chi_i^{(s)}h_{(s)}exp(\lambda^{(s)}t) \tag{1.12}$$

The coefficients $h_{(s)}$ are assigned by the initial conditions:

$$\delta\widehat{C}_i(\underline{q}, 0) = \sum_{s=1}^{m}\chi_i^{(s)}h_{(s)} \longrightarrow h_{(s)} = \sum_{k=1}^{m}\chi_k^{-1(s)}\delta\widehat{C}_k(\underline{q}, 0) \tag{1.13}$$

where χ^{-1} is the inverse eigenvectors matrix. Globally,

$$\delta\widehat{C}_i(\underline{q},t) = \sum_{s=1}^{m} \chi_i^{(s)} exp(\lambda^{(s)} t) \sum_{k=1}^{m} \chi_k^{-1(s)} \delta\widehat{C}_k(\underline{q},0) \tag{1.14}$$

Eq. (1.14) allows computing explicitly the concentration correlation term of eq. (1.8):

$$< \delta C_i^*(\underline{r},t)\delta C_j(\underline{r}',t+\tau) >_t = < \delta C_i^*(\underline{r},0)\delta C_j(\underline{r}',\tau) > = \tag{1.15}$$

$$= \frac{1}{(2\pi)^{3/2}} \int_{-\infty}^{+\infty} < \delta C_i^*(\underline{r},0)\delta\widehat{C}_j(\underline{q},\tau) > e^{-i\underline{q}\cdot\underline{r}'}\, d^3\underline{q}$$

$$= \frac{1}{(2\pi)^{3/2}} \int_{-\infty}^{+\infty} \sum_{s=1}^{m} \chi_j^{(s)} exp(\lambda^{(s)}\tau) \sum_{k=1}^{m} \chi_k^{-1(s)} < \delta C_i^*(\underline{r},0)\delta\widehat{C}_k(\underline{q},0) > e^{-i\underline{q}\cdot\underline{r}'}\, d^3\underline{q}$$

$$= \frac{1}{(2\pi)^3} \iint_{-\infty}^{+\infty} \sum_{s=1}^{m} \chi_j^{(s)} exp(\lambda^{(s)}\tau) \sum_{k=1}^{m} \chi_k^{-1(s)} < \delta C_i^*(\underline{r},0)\delta C_k(\underline{r}'',0) > e^{-i\underline{q}\cdot(\underline{r}'-\underline{r}'')}\, d^3\underline{q} d^3\underline{r}''$$

For an ideal solution, the zero - lag time concentration correlation can be evaluated [11,17] as

$$< \delta C_i^*(\underline{r},0)\delta C_k(\underline{r}'',0) > = < C_i > \delta_{ik}\delta(\underline{r}-\underline{r}'') \tag{1.16}$$

Therefore eq. (1.15) turns into

$$< \delta C_i^*(\underline{r},0)\delta C_j(\underline{r}',\tau) > = \frac{< C_i >}{(2\pi)^3} \int_{-\infty}^{+\infty} \sum_{s=1}^{m} \chi_j^{(s)} exp(\lambda^{(s)}\tau)\chi_i^{-1(s)} e^{i\underline{q}\cdot(\underline{r}-\underline{r}')}\, d^3\underline{q} \tag{1.17}$$

The substitution of eq. (1.17) into the auto-correlation function of eq. (1.7) allows writing

$$G(\tau) = \frac{\int_{-\infty}^{+\infty} |\widehat{W}(\underline{q})|^2 \sum_{i,j=1}^{m} \phi_i\phi_j < C_i > \sum_{s=1}^{m} \chi_j^{(s)} exp(\lambda^{(s)}\tau)\chi_i^{-1(s)}\, d^3\underline{q}}{\left(\sum_{i=1}^{m} \phi_i < C_i > (2\pi)^{3/2}\widehat{W}(0)\right)^2} \tag{1.18}$$

For the point spread function, a 3D Gaussian is assumed for $\flat$-photon excitation ($\flat = 1,2$) with $1/e^2$ distances ω_0 and ω_{0z} along the radial and axial directions, respectively [18,19]:

$$\begin{cases} W(\underline{r}) = W(x,y,z) = W_0 exp\{ -\frac{2\flat(x^2+y^2)}{\omega_0^2} - \frac{2\flat z^2}{\omega_{0z}^2} \} \\ \\ \widehat{W}(\underline{q}) = \widehat{W}(q_x,q_y,q_z) = [W_0\omega_0^2\omega_{0z}/(8\flat^{3/2})] exp\{ -\frac{\omega_0^2(q_x^2+q_y^2)}{8\flat} - \frac{\omega_{0z}^2 q_z^2}{8\flat} \} \end{cases} \tag{1.19}$$

With respect to the Gaussian-Lorentzian profile alternatively assumed for two-photon excitation, the 3D Gaussian approximation has the advantage of allowing the analytical solution of the integrals involved in the correlation function derivation [20]. The $\flat = 2$ term for two-photon excitation accounts for the non-linearity of the two-photon absorption process and for the proportionality of the excited fluorescence signal on the squared excitation intensity [21].
The substitution of eq. (1.19) into eq. (1.18) concludes the derivation of the auto-correlation function:

$$G(\tau) = \frac{\int_{-\infty}^{+\infty} e^{-\frac{\omega_o^2(q_x^2+q_y^2)}{4\flat} - \frac{\omega_{oz}^2 q_z^2}{4\flat}} \sum_{i,j=1}^{m} \phi_i \phi_j < C_i > \sum_{s=1}^{m} \chi_j^{(s)} exp(\lambda^{(s)}\tau)\chi_i^{-1(s)} \, d^3\underline{q}}{(2\pi)^3 \left(\sum_{i=1}^{m} \phi_i < C_i >\right)^2} \tag{1.20}$$

All the diffusion coefficients, drift velocities and chemical rate constants defining the dynamics of the investigated m-species system contribute to the decay of the auto-correlation function, so that in principle all of them can be recovered from the fit of the experimental $G(\tau)$ once the exact $\underline{q}$-dependence of the eigenvalues and eigenvectors of the matrix M has been derived. Experimentally, this is often hampered by difficulties in both the analytical derivation of λ and χ terms and in the separation, within the $G(\tau)$ decay, of the individual contributions arising from transport phenomena and chemical reactions. As anticipated previously, the next Subsections are therefore devoted to the description of two simpler cases that, being frequently encountered in the analysis of experimental data, will be of particular interest for the results presented in Parts II and III.

1.1.2 Brownian diffusion

I begin by considering an ideal solution of identical, point-like fluorescent particles experiencing three dimensional Brownian diffusion with isotropic diffusion coefficient D. The matrix notation and the concentration subscripts for this single population system ($m = 1$) are redundant, since the systems of differential equations (1.9) and (1.10) reduce to

$$\begin{cases} \frac{\partial}{\partial t}\delta C(\underline{r}, t) = D\nabla^2 \delta C(\underline{r}, t) \\ \\ \frac{\partial}{\partial t}\delta \widehat{C}(\underline{q}, t) = -D|\underline{q}|^2 \delta \widehat{C}(\underline{q}, t) \end{cases} \tag{1.21}$$

The substitution of the solution $\delta\widehat{C}(\underline{q},t) = \delta\widehat{C}(\underline{q},0)exp(-D|\underline{q}|^2t)$ into eq. (1.7) yields

$$G(\tau) = \frac{1}{< C >} \frac{1}{\pi^{3/2}\flat^{-3/2}\omega_0^2\omega_{0z}} \frac{1}{\left(1+\frac{\tau}{\tau_D}\right)} \frac{1}{\sqrt{1+\zeta^2\frac{\tau}{\tau_D}}} \tag{1.22}$$

where the excitation volume form factor ζ and the characteristic diffusion time τ_D have been introduced according to $\zeta = \omega_0/\omega_{0z}$ and $\tau_D = \omega_0^2/(4\flat D)$ ($\flat = 1, 2$ for one and two photon excitation, respectively). As shown in Fig. 1.1, the higher τ_D, the longer is the auto-correlation decay time ($G(\tau_D) \sim 1/2G(0)$). The denominator of eq. (1.22) contains the effective excitation volume

$$V = \frac{\left(\int_{-\infty}^{+\infty} W(\underline{r})\,d^3\underline{r}\right)^2}{\int_{-\infty}^{+\infty} W^2(\underline{r})\,d^3\underline{r}} = \pi^{3/2}\flat^{-3/2}\omega_0^2\omega_{0z} \tag{1.23}$$

Hence recalling the average number of fluorescing particles in the excitation volume, defined as $< N >= V < C >$, $G(\tau)$ can be written as:

$$G(\tau) = \frac{1}{< N >} \frac{1}{\left(1+\frac{\tau}{\tau_D}\right)} \frac{1}{\sqrt{1+\zeta^2\frac{\tau}{\tau_D}}} \tag{1.24}$$

On the one hand, this highlights that the fluctuations in the particle number and in the fluorescence signal are more and more discernible (and the $G(0)$ amplitude increases) as the number of detected particles decreases;[1] this justifies the previously mentioned employment of highly diluted solutions and requires the optical sectioning properties of two-photon excitation or confocal optics. On the other hand, eq. (1.24) also suggests exploiting the correlation zero-lag amplitude $G(0)$ to measure, for a calibrated setup with known V, the average concentration of the investigated fluorescent sample. Analogously, the fluorophores brightness can be recovered as the product of the temporally-averaged fluorescence intensity times the zero lag time correlation amplitude.

[1] The inverse proportionality of $G(\tau)$ to $< N >$ can also be obtained by computing $G(0) = \frac{<(\delta F(0))^2>}{<F(t)>^2} = \frac{\phi^2<\delta N(0)^2>}{(\phi<N(t)>)^2}$, where ϕ is the fluorescence quantum yield and $F(t) = \phi N(t)$ is the fluorescence emitted at time t by $N(t)$ particles in the excitation volume: for an ideal dilute solution with particles interacting negligibly with each other, the number of molecules in the volume V obeys a Poisson distribution so that $< \delta N(0)^2 >=< N(t) >$ and $G(0) = 1/ < N(t) >$ [11].

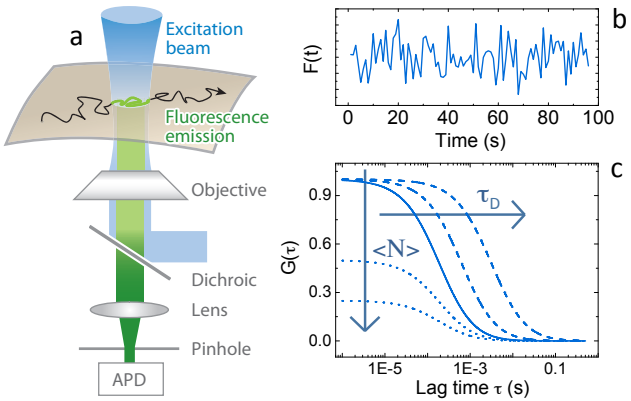

Figure 1.1: *FCS setup and auto-correlation analysis for the investigation of Brownian diffusion.* (a, b) Main components of a confocal FCS setup [22] and fluctuating temporal fluorescence intensity trace $F(t)$ produced by molecules diffusing through the excitation volume. Fluorescence fluctuations are accurately sampled if the emitted signal is detected (by a photo-multiplier tube or an avalanche photo-diode) with a total measurement time $T >> \tau_D$ and a temporal resolution $\Delta t << \tau_D$. (c) Auto-correlation function $G(\tau)$ for isotropic 3D Brownian diffusion (eq. 1.24), simulated with D=50 $\mu m^2/s$, ω_0=0.2 μm, ω_{0z}=0.5 μm and $< N >= 1$ (continuous line). The correlation half-decay time provides a good estimate of the mean diffusion time τ_D (from which D and the hydrodynamic radius of the observed fluorescent molecules can be recovered) and it increases as the diffusion coefficient decreases; the $G(0)$ amplitude decreases for higher concentrations as discussed in the text.

Multi-component Brownian diffusion

When point-like and non-interacting molecules of two different species ($m = 2$) are simultaneously sampled in the excitation volume while undergoing free thermal diffusion, the dynamics of the system is governed by two independent differential diffusion equations of the form

$$\begin{cases} \frac{\partial}{\partial t}\delta C_1(\underline{r}, t) = D_1 \nabla^2 \delta C_1(\underline{r}, t) \\ \\ \frac{\partial}{\partial t}\delta C_2(\underline{r}, t) = D_2 \nabla^2 \delta C_2(\underline{r}, t) \end{cases} \tag{1.25}$$

D_1 and D_2 are the diffusion coefficients of species 1 and 2, respectively; they are related to the molecular hydrodynamic radii R_1 and R_2 by the Stokes-Einstein's

equation ($D_i = KT/(6\pi\eta R_i)$, where K is Boltzmann's constant, T is the temperature and η is the medium viscosity). The matrix M I have introduced in eq. (1.10), as well as its eigenvalues and eigenvectors, can be readily obtained by taking a Fourier transform of eqs. (1.25):

$$M = \begin{bmatrix} -D_1|\underline{q}|^2 & 0 \\ 0 & -D_2|\underline{q}|^2 \end{bmatrix} \longrightarrow \begin{cases} \lambda^{(1)} = -D_1|\underline{q}|^2 \\ \lambda^{(2)} = -D_2|\underline{q}|^2 \end{cases}, \begin{cases} \chi^{(1)} = (1,0) \\ \chi^{(2)} = (0,1) \end{cases} \tag{1.26}$$

Their substitution into eq. (1.20) yields an auto-correlation function which is a linear combination of two independent terms of the type I have previously derived for the simpler one-population system:

$$G(\tau) = \sum_{i=1}^{2} \frac{\phi_i^2 < N_i >}{(\sum_{k=1}^{2} \phi_k < N_k >)^2} \frac{1}{(1 + \frac{\tau}{\tau_{Di}})} \frac{1}{\sqrt{1 + \zeta^2 \frac{\tau}{\tau_{Di}}}} \tag{1.27}$$

Each species contributes to the correlation decay, and its contribution is weighted by its concentration and quantum yield. However, the recovery of exact characteristic diffusion times τ_{D1} and τ_{D2} by a nonlinear least-squares fit of an experimental $G(\tau)$ requires a minimum separation between the two timescales of diffusion: care has to be taken in the interpretation of the multi-component fit unless the investigated diffusion coefficients differ by a factor $D_1/D_2 > 1.6$ (for two identical quantum yields and a high signal to noise ratio). An extensive investigation of the reliability of FCS measurements of translational diffusion in both one- and two-component systems is reported in [23].

1.1.3 Brownian diffusion and drift

The theoretical framework of eqs. (1.3)-(1.20) can be readily adapted to the description of a single population of ideal fluorescent molecules exhibiting a combination of Brownian diffusion and uniform drift. Several applications of FCS auto-correlation analyses to the measurement of flows have been reported, with examples including the investigation of DNA-mediated nuclear trafficking, the *in-vivo* measurement of blood flow speeds [24] and the recovery of flow velocities in microfluidic structures [7,25].

Let D and $\underline{v}$ be the diffusion coefficient and three-dimensional (flow or drift) velocity vector of the investigated objects. Eq. (1.9) reduces to the well-known

diffusion+drift Fick's equation

$$\frac{\partial}{\partial t}\delta C(\underline{r},t) = D\nabla^2\delta C(\underline{r},t) - \underline{v}\cdot\underline{\nabla}\delta C(\underline{r},t) \tag{1.28}$$

The solution in Fourier space, $\delta\widehat{C}(\underline{q},t) = \delta\widehat{C}(\underline{q},0)exp(-D|\underline{q}|^2t + i\underline{q}\cdot\underline{v}t)$, leads to

$$G(\tau) = \frac{1}{(2\pi)^3 < C >}\int_{-\infty}^{+\infty} exp\big(-\frac{\omega_o^2(q_x^2+q_y^2)}{4b} - \frac{\omega_{0z}^2 q_z^2}{4b}\big)exp(-D|\underline{q}|^2\tau + i\underline{q}\cdot\underline{v}\tau)\, d^3\underline{q} \tag{1.29}$$

Recalling that

$$\int_{-\infty}^{+\infty} exp(-ax^2+bx+c)\, dx = \sqrt{\frac{\pi}{a}}exp\left(\frac{b^2}{4a}+c\right) \tag{1.30}$$

I perform the three-dimensional integration and obtain [25,26]

$$\begin{aligned} G(\tau) = {} & \frac{1}{V < C >}\frac{1}{\big(1+\frac{\tau}{\tau_D}\big)}\frac{1}{\sqrt{1+\zeta^2\frac{\tau}{\tau_D}}}\cdot \\ & \cdot exp\left\{-\big(\frac{\tau}{\tau_{vx}}\big)^2\frac{1}{\big(1+\frac{\tau}{\tau_D}\big)} - \big(\frac{\tau}{\tau_{vy}}\big)^2\frac{1}{\big(1+\frac{\tau}{\tau_D}\big)} - \big(\frac{\tau}{\tau_{vz}}\big)^2\frac{1}{\big(1+\zeta^2\frac{\tau}{\tau_D}\big)}\right\} \end{aligned} \tag{1.31}$$

As before, $V = \pi^{3/2}b^{-3/2}\omega_0^2\omega_{0z}$. Characteristic drift times along the three Cartesian axes are defined as $\tau_{vx} = \omega_0/(b^{1/2}v_x)$, $\tau_{vy} = \omega_0/(b^{1/2}v_y)$ and $\tau_{vz} = \omega_{0z}/(b^{1/2}v_z)$: they determine the relaxation time of the exponential term that, in the presence of a non-zero drift speed, modulates the nearly-hyperbolic decay produced in the FCS auto-correlation function by isotropic Brownian diffusion.
For a velocity vector lying in the focal xy-plane ($v_z = 0$), I combine τ_{vx} and τ_{vy} into a single drift time $\tau_v = \omega_0/(b^{1/2}|\underline{v}|)$ and write eq. (1.31) in the simpler form

$$G(\tau) = \frac{1}{< N >}\frac{1}{\big(1+\frac{\tau}{\tau_D}\big)}\frac{1}{\sqrt{1+\zeta^2\frac{\tau}{\tau_D}}}exp\left\{-\big(\frac{\tau}{\tau_v}\big)^2\frac{1}{\big(1+\frac{\tau}{\tau_D}\big)}\right\} \tag{1.32}$$

No information can be gained on the direction of the drift velocity vector. The τ_D and τ_v characteristic times obtained by the non linear least-squares fit of the experimental correlation function can be exploited to recover the diffusion coefficient D and the modulus $|\underline{v}|$ if the necessary conditions on the timescales of drift and diffusion exemplified in Fig. 1.2 are satisfied.

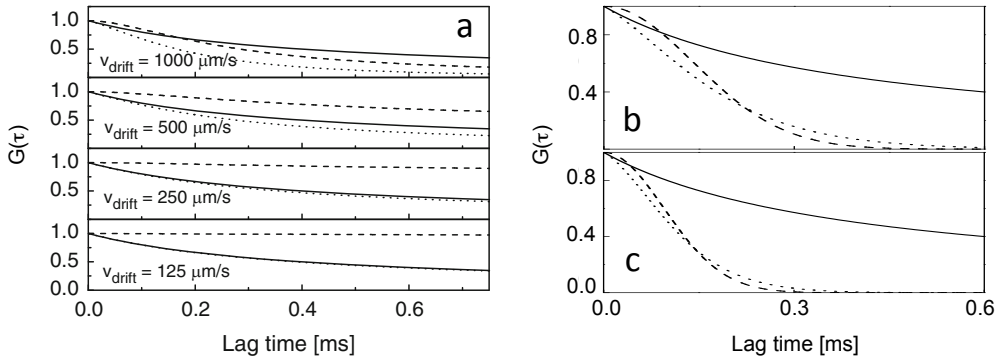

Figure 1.2: *FCS auto-correlation analysis of uniform drift and Brownian diffusion [26].* (a) Dotted lines: auto-correlation functions $G(\tau)$ simulated according to eq. (1.32) with ω_0=0.4 μm, D=100 $\mu m^2/s$ (τ_D=0.4 ms) and $|\underline{v}|$=1000, 500, 250, 125 $\mu m/s$ (τ_v=0.4, 0.8, 1.6, 3.2 ms). In each panel, auto-correlation functions for pure diffusion (simulated according to eq. 1.24 with the same τ_D=0.4 ms) and pure drift (simulated according to eq. 1.32 with D=0 and τ_v values of 0.4, 0.8, 1.6, 3.2 ms increasing from top to bottom) are reported for comparison (continuous and dashed line, respectively). For $\tau_v >> \tau_D$ (lowest panel) diffusion dominates the decay of the whole correlation function; the contribution of the drift exponential factor becomes increasingly discernible as the drift speed increases (upper panels). (b) Auto-correlation functions simulated according to eq. (1.24) with τ_D=0.4 ms (pure diffusion, continuous line), according to eq. (1.32) with τ_D=0.4 ms and τ_v=0.2 ms (diffusion+drift, dotted line) and according to eq. (1.32) with D=0 and τ_v=0.2 ms (pure drift, dashed line): the combination of D=100 $\mu m^2/s$ and $|\underline{v}|$=2000 $\mu m/s$ (corresponding to $\tau_v < \tau_D$) leads to a correlation function that can not be satisfactorily fit by neither a pure diffusion nor a pure drift model. Hence if $\tau_v < \tau_D$ the presence of both diffusion and drift can be inferred from the $G(\tau)$ decay. (c) Same as (b) with τ_v=0.13 ms ($|\underline{v}|$=3000 $\mu m/s$): if $\tau_v << \tau_D$ Brownian diffusion almost does not contribute to the correlation decay.

1.2 Cross-correlation analysis

In the previous section, I already pointed out that a multi-component non-linear fit of experimental FCS auto-correlation functions - whether devoted to the discrimination of two fluorescent populations with different diffusional properties, or to the separation of the contributions of diffusion and active transport within the dynamics of a single population - not always leads to a reliable estimate of the underlying transport parameters. This hampers, for example, the exploitation of the changes in the diffusion coefficients accompanying molecular aggregation and

binding processes for the determination of the concentration and size of reaction products; since the diffusion time scales only with the third root of the molecular mass, and a minimum ratio τ_{D2}/τ_{D1} of ~ 1.6 is required in the $G(\tau)$ fit, successful applications have been limited to those cases characterized by a considerable change in molecular mass upon binding [27,28]. A second limitation affecting FCS auto-correlation analyses concerns their lack of sensitivity toward the direction of drift velocities, due to the symmetric circular shape of the excitation volume.
Both these problems have been overcome by the development and adoption of two cross-correlation schemes: (i) dual-color fluorescence cross-correlation spectroscopy, mainly developed for multi-component diffusional analyses in solution, and (ii) dual-beam fluorescence cross-correlation spectroscopy, devoted to the investigation of directed transport phenomena.

1.2.1 Dual-color fluorescence cross-correlation spectroscopy

In dual-color Fluorescence Cross-Correlation Spectroscopy (dcFCCS) [29–31], two differently labeled reaction partners are simultaneously excited by two superimposed laser beams (in one-photon excitation configuration) and the spectrally distinct fluorescence emissions of the two dyes are collected by separate detection devices. For each detection channel (say, for instance, the green and red channels G and R), an auto-correlation function is computed according to eq. (1.1):

$$G_G(\tau) = \frac{< \delta F^*_G(t)\delta F_G(t+\tau) >_t}{< F_G(t) >^2_t} \quad , \quad G_R(\tau) = \frac{< \delta F^*_R(t)\delta F_R(t+\tau) >_t}{< F_R(t) >^2_t} \tag{1.33}$$

Both the G and R channels obviously detect the fluorescence signal emitted by both single-label and double-label molecules: recalling eq. (1.6),

$$\begin{cases} \delta F_G(t) = \phi_g \int W_g(\underline{r})\delta C_g(\underline{r},t)\, d^3\underline{r} + \phi_{gr} \int W_g(\underline{r})\delta C_{gr}(\underline{r},t)\, d^3\underline{r} \\ \\ \delta F_R(t) = \phi_r \int W_r(\underline{r})\delta C_r(\underline{r},t)\, d^3\underline{r} + \phi_{rg} \int W_r(\underline{r})\delta C_{gr}(\underline{r},t)\, d^3\underline{r} \end{cases} \tag{1.34}$$

ϕ_g and ϕ_r contain, in addition to the detection efficiency, the fluorescence quantum yield and the absorption cross-section of the green and red dyes, respectively; ϕ_{gr} and ϕ_{rg} follow the same definition for the green and red dyes in the bound form. By assuming, for simplicity, equal ϕ terms for the dyes and identical distributions $W_g(\underline{r})$ and $W_r(\underline{r})$ at the two excitation wavelengths, the derivation I have previously

reported for two non-interacting diffusing populations leads to

$$\begin{cases} G_G(\tau) = \frac{<C_g>d_g+<C_{gr}>d_{gr}}{V(<C_g>+<C_{gr}>)^2} \\ G_R(\tau) = \frac{<C_r>d_r+<C_{gr}>d_{gr}}{V(<C_r>+<C_{gr}>)^2} \\ d_m = \frac{1}{\left(1+\frac{\tau}{\tau_{Dm}}\right)} \frac{1}{\sqrt{1+\zeta^2\frac{\tau}{\tau_{Dm}}}} \quad (m = g, r, gr) \end{cases} \tag{1.35}$$

In addition to auto-correlations, a cross-correlation function $G_{GR}(\tau)$ is computed to selectively observe coordinated fluorescence fluctuations in the green and red channels:

$$G_{GR}(\tau) = \frac{< \delta F_G^*(t)\delta F_R(t+\tau) >_t}{< F_G(t) >_t < F_R(t) >_t} \tag{1.36}$$

Under the same assumptions adopted for fluorescence quantum yields and optical transfer functions,

$$G_{GR}(\tau) = \frac{< C_{gr} >}{V(< C_g > + < C_{gr} >)(< C_r > + < C_{gr} >)} \frac{1}{\left(1+\frac{\tau}{\tau_{Dgr}}\right)} \frac{1}{\sqrt{1+\zeta^2\frac{\tau}{\tau_{Dgr}}}} \tag{1.37}$$

Eq. (1.37) evidences that, in contrast to single-channel auto-correlation functions, the $G_{GR}(\tau)$ decay is only governed by the transport properties of the double-label species: its diffusion coefficient can therefore be determined without the problems intrinsically affecting multi-component fitting procedures. Furthermore, the amplitude of the cross-correlation curve is a very sensitive parameter to follow the temporal evolution of the reaction product concentration: $G_{GR}(0) = 0$ if the solution only contains single-label molecules, whereas the amplitude increases with the bound fraction during the temporal evolution of the binding process.
Clearly, the direct proportionality of the cross-correlation amplitude to the concentration of bound molecules imposes a lower limit to the detectable green+red fraction, since too low amplitudes are usually too noisy to be practically analyzed. Some artifact risks should also be considered when planning a dcFCCS experiment on a non-ideal system: examples include the modification of the cross-correlation function due to spectral cross-talk (i.e., the detection of the green dye in the red detection channel), a decrease in the cross-correlation amplitude due to a partial overlap of the two excitation volumes and a decrease in the amplitude of the red auto-correlation function due to the bigger red excitation volume predicted

by Abbe's diffraction limit. Since dcFCCS will not be of particular practical relevance for Parts II and III, I refer to [29,30] for a detailed treatment of dual-color cross-correlation artifacts and troubleshoots.

1.2.2 Dual-beam fluorescence cross-correlation spectroscopy

A cross-correlation based technique able to overcome the major limitation of FCS in flow measurements -the lack of sensitivity toward the flow direction- is dual-beam Fluorescence Cross-Correlation Spectroscopy (dbFCCS) [32–34], that, to date, has been applied to both flow mapping in microfluidic devices and *in-vivo* blood velocimetry [35].
dbFCCS relies on the cross-correlation of the fluorescence signals gathered from two spatially separated excitation volumes. In the typical experimental realization, these are obtained, starting from a single laser beam, by two polarizing beam-splitters and the emitted signals are collected by two optical fibers, each leading to a separate detector, at a typical $\sim 20-150\mu m$ fixed distance [33,34]. The temporal fluorescence intensity traces $F_1(t)$ and $F_2(t)$ arising from volumes V_1 and V_2 fluctuate in time due to molecular diffusion and flow (Fig. 1.3): it is assumed here that fluorescent particles diffuse in a three-dimensional space with diffusion coefficient D, while flowing with uniform planar velocity $\underline{v} = (v_x, v_y, v_z = 0)$ between V_1 and V_2.
A normalized cross-correlation function is computed as

$$G_{12}(\tau) = \frac{< \delta F_1^*(t)\delta F_2(t+\tau) >_t}{< F_1(t) >_t < F_2(t) >_t} \tag{1.38}$$

The analytical derivation of the explicit expression of $G_{12}(\tau)$ is similar to the one reported above for auto-correlation functions. For negligible fluctuations affecting the fluorophores quantum yield, the substitution of eq. (1.6) into eq. (1.38) leads to

$$G_{12}(\tau) = \frac{\iint_{-\infty}^{+\infty} W_1^*(\underline{r}) W_2(\underline{r}') < \delta C^*(\underline{r}, t)\delta C(\underline{r}', t+\tau) >_t \, d^3\underline{r} d^3\underline{r}'}{< C >^2 \int_{-\infty}^{+\infty} W_1(\underline{r}) \, d^3\underline{r} \int W_2(\underline{r}') \, d^3\underline{r}'} \tag{1.39}$$

Spatial coordinates $\underline{r} = (x, y, z)$ and $\underline{r}' = (x', y', z')$ are employed for V_1 and V_2, respectively. As in the general derivation of eqs. (1.3)-(1.20), for both one- and two-photon excitation ($\flat = 1, 2$) $W_1(\underline{r})$ and $W_2(\underline{r}')$ can be approximated by a 3D Gaussian distribution with $1/e^2$ distances ω_0 and ω_{0z} along the radial and axial directions. If two excitation volumes of equal size are assumed ($\omega_{01} = \omega_{02} \equiv \omega_0$

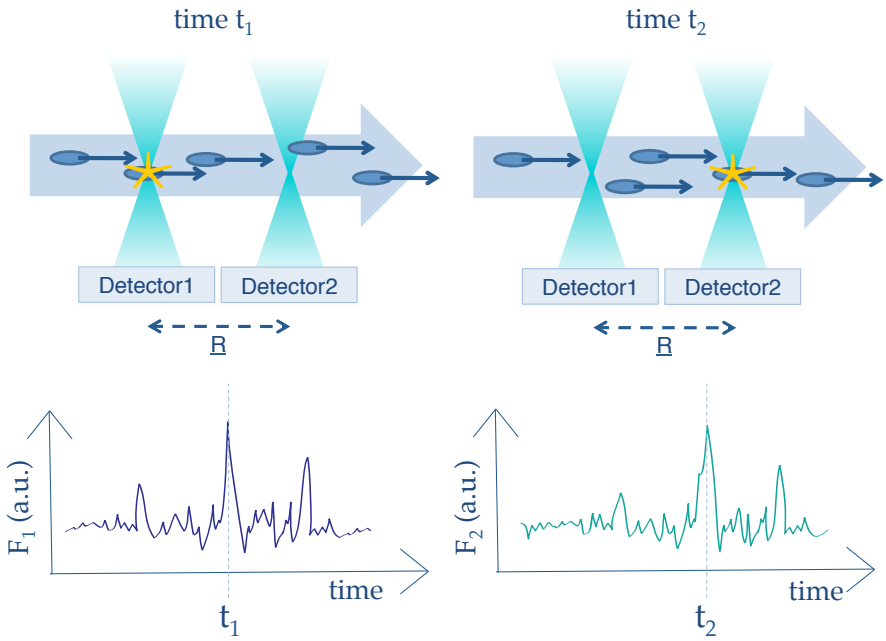

Figure 1.3: *Dual-beam Fluorescence Cross-Correlation Spectroscopy.* In dbFCCS, temporal fluorescence intensity traces $F_1(t)$ and $F_2(t)$ are gathered from two separate excitation volumes V_1 and V_2 by two detectors. The principles underlying the measurement of flow speeds by means of dbFCCS can be intuitively explained by considering - for simplicity, and without loss of generality - a single flowing fluorescent particle. If the particle is detected at time t_1 in the first excitation volume (left column) , the same particle will be detected - due to the flow - at a delayed time t_2 in the second excitation volume positioned downstream (right column). Hence the maximum cross-correlation (eq. 1.38) between the temporal traces $F_1(t)$ and $F_2(t)$ is expected at a delayed time $(t_2 - t_1)$, equal to the time it takes for the particle to travel the distance between the volumes. Since the distance between V_1 and V_2 is known, the particle speed can be determined from the cross-correlation peak lag time (i.e., from the particle 'time of flight') under the hypothesis of uniform flow.

and $\omega_{0z1} = \omega_{0z2} \equiv \omega_{0z}$),

$$\begin{cases} W_1(\underline{r}) = W_{01} exp\{ - \frac{2b(x^2+y^2)}{\omega_0^2} - \frac{2bz^2}{\omega_{0z}^2} \} \\ \\ W_2(\underline{r}') = W_{02} exp\{ - \frac{2b(x'^2-R_x^2)}{\omega_0^2} - \frac{2b(y'^2-R_y^2)}{\omega_0^2} - \frac{2bz'^2}{\omega_{0z}^2} \} \end{cases} \tag{1.40}$$

The vector $\underline{R} = (R_x, R_y, R_z)$ has been introduced to account for the inter-spot distance; since the focal spots are assumed to lie in the same xy-plane, $R_z = 0$.
By recalling the formalism of eqs. (1.14)-(1.17) and the solution of the Fick's equation (eq. 1.28) governing the dynamics of diffusing and flowing fluorescent molecules, I get for the concentration correlation term

$$\begin{aligned} < \delta C^*(\underline{r}, t)\delta C(\underline{r}', t+\tau) >_t &= < \delta C^*(\underline{r}, 0)\delta C(\underline{r}', \tau) > \\ &= \frac{< C >}{(2\pi)^3} \int_{-\infty}^{+\infty} exp(-D|\underline{q}|^2\tau + i\underline{q}\cdot\underline{v}\tau) e^{i\underline{q}\cdot(\underline{r}-\underline{r}')}\, d^3\underline{q} \end{aligned} \tag{1.41}$$

Once inserted into eq. (1.39), this yields

$$G_{12}(\tau) = \frac{\int_{-\infty}^{+\infty} \widehat{W}_1(\underline{q})\widehat{W}_2^*(\underline{q}) exp(-D|\underline{q}|^2\tau + i\underline{q}\cdot\underline{v}\tau) d^3\underline{q}}{< C > (2\pi)^3 \widehat{W}_1(0)\widehat{W}_2(0)} \tag{1.42}$$

By the substitution of the Fourier transforms $\widehat{W}_1(\underline{q})$ and $\widehat{W}_2^*(\underline{q})$ and by the computation of the resulting Gaussian integral (see eq. 1.30), eq. (1.42) leads in turn to the expression of the cross-correlation function [33–35]:

$$\begin{aligned} G_{12}(\tau) &= \frac{1}{< N >} \frac{1}{1+\tau/\tau_D} \frac{1}{\sqrt{1+\zeta^2\tau/\tau_D}} exp\left\{ - \frac{|\underline{R} - \underline{v}\tau|^2}{\omega_o^2/b(1+\tau/\tau_D)} \right\} \\ &= \frac{1}{< N >} \frac{1}{1+\tau/\tau_D} \frac{1}{\sqrt{1+\zeta^2\tau/\tau_D}} exp\left\{ - \frac{|\underline{v}|^2}{\omega_o^2/b} \frac{(\tau^2 + \tau_v^2 - 2\tau\tau_v \cos\gamma)}{1+\tau/\tau_D} \right\} \end{aligned} \tag{1.43}$$

$< N > = < C > \pi^{3/2} b^{-3/2} \omega_0^2 \omega_{0z}$ and $\tau_D = \omega_o^2/(4bD)$ as previously defined for auto-correlations. The drift time $\tau_V = |\underline{R}|/|\underline{v}|$ is the time needed by fluorescent particles to cover the distance between the excitation volumes and γ is the angle subtended by the velocity vector $\underline{v}$ and the inter-spot distance $\underline{R}$ (see Figure 1.4). If

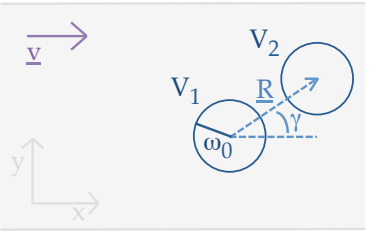

Figure 1.4: *Dual-beam fluorescence cross-correlation spectroscopy.* Two excitation volumes V_1 and V_2 with radial waist ω_0 are positioned at fixed distance $|\underline{R}|$. $\underline{R}$ subtends an angle γ with the flow velocity vector $\underline{v}$. For the derivation of eq. (1.43), $\underline{v}$ has been assumed to lie in the same *xy*-plane as the two volumes V_1 and V_2.

the velocity vector $\underline{v}$ also has a non-vanishing $z-$component, the same derivation leads to the cross-correlation function of eq. (1.43) with a modified Gaussian factor $exp\{-[(R_x - v_x\tau)^2 + (R_y - v_y\tau)^2]/[\omega_0^2/\flat(1 + \tau/\tau_D)] - v_z^2\tau^2/[\omega_{0z}^2/\flat(1 + \zeta^2\tau/\tau_D)]\}$.

The cross-correlation function $G_{12}(\tau)$ of eq. (1.43) is a peaked function, due to the Gaussian factor that modulates the hyperbolic decay describing the contribution of Brownian diffusion. The peak position along the lag-time axis (τ_{max}) and the peak amplitude ($G(\tau_{max})$) are regulated by the inter-spot distance, by the flow speed, by the angle subtended by the vectors $\underline{v}$ and $\underline{R}$ and by the diffusion coefficient of the investigated objects.

- The effect of the angle γ on $G_{12}(\tau)$ is shown in Fig. 1.5. The maximum cross-correlation amplitude is found for $\gamma = 0$ (i.e., for volume elements aligned to the flow velocity $\underline{v}$); for increasing γ, the probability that a flowing molecule traverses the second excitation volume having already traversed the first rapidly decreases, leading to a remarkable decrease of the correlation amplitude. When $\gamma \to 180°$, the vectors $\underline{v}$ and $\underline{R}$ point in opposite directions (molecules flow from volume V_2 to volume V_1) and no cross-correlation is detected when computing

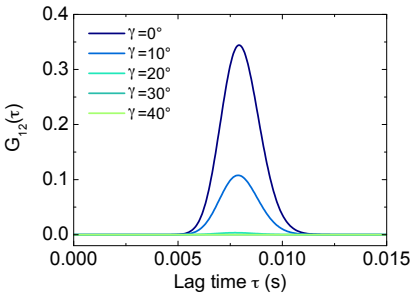

Figure 1.5: *dbFCCS: effect of the angle γ on the cross-correlation function.* Cross-correlation functions simulated according to eq. (1.43) with τ_D=5 ms, $|\underline{R}|$=2 µm, $|\underline{v}|$=250 µm/s and increasing angle γ between $\underline{v}$ and $\underline{R}$; ω_0=0.2 µm, ω_{0z}=0.5µm, $\flat = 1$. The decrease in the amplitude $G(\tau_{max})$ with increasing γ is more and more pronounced as the distance $|\underline{R}|$ is increased.

$< \delta F_1^*(t)\delta F_2(t+\tau) >_t$: instead of evaluating the fluorescence fluctuations in volume V_1 at time t and in volume V_2 at time $t+\tau$, I evaluate signal fluctuations in volume V_1 at time $t+\tau$ and in volume V_2 at time t. This corresponds to the computation of the reverse cross-correlation $G_{21}(\tau)$ defined as

$$G_{21}(\tau) = \frac{< \delta F_2^*(t)\delta F_1(t+\tau) >_t}{< F_1(t) >_t < F_2(t) >_t} \tag{1.44}$$

The explicit expression for $G_{21}(\tau)$ is given again by eq. (1.43) provided that the same definition for the angle between $\underline{v}$ and $\underline{R}$ is adopted ($\gamma = 0$ for $\underline{v}//\underline{R}$).
Experimentally, when no prior information is given concerning the flow direction, both $G_{12}(\tau)$ and $G_{21}(\tau)$ are computed: one contains the contribution of flow, diffusion and pseudo-autocorrelation (i.e., the auto-correlation contribution arising from the detection in channel 1 of photons emitted in volume V_2 and viceversa), while the other only contains pseudo-autocorrelation. The peaked cross-correlation function immediately assigns the flow direction ($V_1 \rightarrow V_2$ or $V_2 \rightarrow V_1$), and its fit to eq. (1.43) allows determining, more precisely, the angle γ.
I remark that, for small inter-spot distances (overlapping excitation volumes), pseudo-autocorrelation can not be neglected, so that the back cross-correlation should be subtracted from the forth cross-correlation function prior to the fitting procedure; by contrast, when excitation volumes do not overlap significantly (as in usual experimental geometries) pseudo-autocorrelation is negligible.

- The effect of the diffusion coefficient D on the cross-correlation peak time τ_{max} is investigated in Fig. 1.6a, where cross-correlation functions are simulated with $\gamma = 0$ (the most favorable and usually adopted experimental configuration) for increasing D in the range $10^{-3} - 10^2 \mu m^2/s$. τ_{max} increases for decreasing D and asymptotically approaches τ_{max}^0 - the peak time for an identically zero diffusion coefficient - as $D \rightarrow 0$. Both τ_{max} and τ_{max}^0 can be easily derived by computing the derivative $\partial G_{12}(\tau)/\partial\tau$; for one-photon excitation and $\gamma = 0$,

$$\left.\frac{\partial G_{12}(\tau)}{\partial\tau}\right|_{\tau_{max}} = 0 \rightarrow \begin{cases} \tau_{max} = -\frac{\omega_0^2}{4D} - \frac{2D}{|\underline{v}|^2} + \sqrt{\frac{4D^2}{|\underline{v}|^4} + \frac{|\underline{R}|}{|\underline{v}|}\frac{\omega_0^2}{2D} + \left(\frac{|\underline{R}|}{|\underline{v}|}\right)^2 + \left(\frac{\omega_0^2}{4D}\right)^2} \\ \tau_{max}^0 = \frac{|\underline{R}|}{|\underline{v}|} = \tau_v \end{cases} \tag{1.45}$$

When $\tau_D \rightarrow +\infty$, the characteristic flow time τ_v is a good approximation to the exact peak time τ_{max}. This suggests exploiting the experimentally measured peak

time τ_{max}^{exp} to easily recover the flow speed according to $\tau_{max}^{exp} \cong \tau_v = |\underline{R}|/|\underline{v}|$. This fast and easy data processing, that allows avoiding the non-linear least-squares fit of experimental cross-correlation functions, proofs to be particularly valuable when investigating flows over extended samples.
The error produced by the approximation $\tau_{max}^{exp} \cong \tau_v$ for $D \neq 0$ can be quantified by evaluating the ratio τ_{max}/τ_{max}^0, that I report as a function of the diffusion coefficient D in Fig. 1.6b-c: for a fixed inter-spot distance the discrepancy τ_{max}/τ_{max}^0 monotonically decreases for higher values of the flow speed, whereas it decreases for higher values of the inter-spot distance for a fixed value of the flow speed.

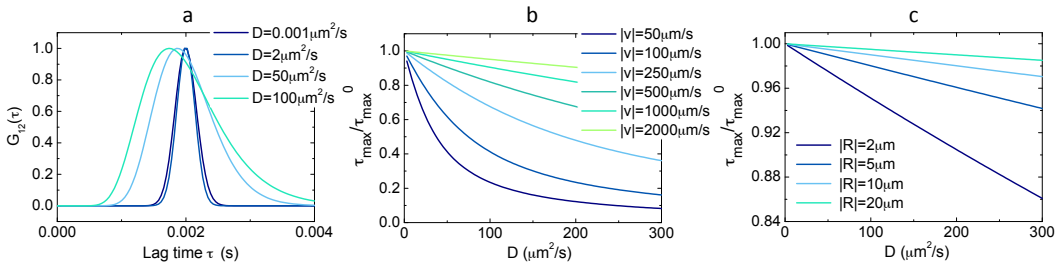

Figure 1.6: *dbFCCS: effect of the diffusion coefficient on the cross-correlation peak time.* (a): simulated $G_{12}(\tau)$ (eq. 1.43) for increasing diffusion coefficient, with $|\underline{v}|$=1000 μm/s and $|\underline{R}|$=2 μm. (b), (c): simulated trend of the discrepancy between the exact peak time τ_{max} and the peak time τ_{max}^0 computed in the approximation D=0 according to eq. (1.45); $|\underline{R}|$=2 μm in (b) and $|\underline{v}|$=2000 μm/s in (c). The following parameters have been kept fixed for all the simulations: γ=0, ω_0=0.2 μm, ω_{0z}=0.5 μm. With the typical $|\underline{R}|$ and $|\underline{v}|$ values of the experimental data presented in Part II (2 μm and 1000 μm/s, respectively), the discrepancy between the peak times is below 10% for diffusion coefficients up to 100 $\mu m^2/s$.

Figure 1.7: *dbFCCS: effect of the flow speed and of the inter-spot distance on the cross-correlation peak time.* Continuous lines: simulated peak time τ_{max} (left axis) as a function of the flow speed, for $|\underline{R}|$=2 μm and γ=0; for D=0 the hyperbolic increase of τ_{max} for decreasing speed is retrieved (eq. 1.45). Dotted lines: simulated τ_{max} (right axis) as a function of the distance $|\underline{R}|$, for $|\underline{v}|$=1000 μm/s and γ=0. The same color code is adopted to identify diffusion coefficients in continuous and dotted lines.

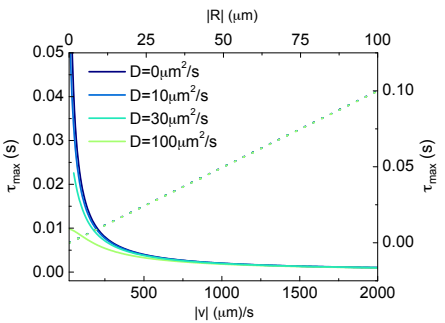

1.3 Beyond FCS: image correlation spectroscopy

With a total measurement time typically ranging from a few seconds to a few minutes and with a very high - even less than a microsecond - temporal resolution, FCS allows the investigation of dynamic processes on the broad microsecond to second timescale, covering about six decades in time. These very high temporal resolution and broad dynamic range are combined to a diffraction-limited, sub-micron, spatial resolution and make FCS ideally suited for fast diffusion and chemical reaction measurements in solution. By contrast, the exploitation of a single stationary laser beam hampers the application of FCS to the investigation of slow transport phenomena at the sub-cellular level: in the presence of slowly moving molecules, the measurement at one location would require long time for the diffusive process to be sampled with sufficiently accurate statistics, so that typical FCS measurements suffer from noisy correlation functions and photo-bleaching phenomena [36]. Furthermore, the sampling of fluorescence fluctuations in a single point in the sample does not provide any information on how the physical, chemical or biological dynamic process under investigation varies across the whole cell.

A way to overcome the limitations of single-point FCS and extend its range of applicability in biological systems consists in repeatedly scanning the excitation laser beam (i.e., scanning the measurement volume) along a pre-defined pattern on the specimen. sFCS (scanning FCS) [37–40] profits from a confocal laser scanning microscope to collect fluorescence intensity fluctuations along a linear or circular path within the focal plane; when the scan path length l is much larger than the radial size ω_0 of the excitation volume, the measurement is effectively performed at multiple spatial locations, their number being approximately defined by the ratio l/ω_0. Thanks to the beam scanning, the molecules dwell time in the illuminated volume and, consequently, their photo-bleaching can be reduced [41] and the signal-to-noise ratio of the recovered auto-correlation function can be improved, when necessary and for homogeneous samples, by averaging over all the sampled points (spatial and temporal averaging are equivalent for ergodic systems). Alternatively, temporal auto-correlation curves can be computed separately for all the points in the scan path, multiplexing FCS results and deriving dynamic parameters (for example, transport properties) over a broad spatial scale with diffraction-limited spatial resolution. The technical requirements for sFCS are those of single-point FCS, apart from the possibility of scanning the excitation laser beam with a speed such that molecules do not move appreciably during a single scan period (the scan period identifies the temporal resolution in sFCS: for commercial confocal

microscopes equipped with a conventional or a resonant scanning head it is of the order of 1000 or 100 μs, respectively).
The concept of sFCS can be extended to scan paths of arbitrary shape and complexity. Various FCS-derived image-processing methods have been developed to exploit the spatial and temporal information encoded in confocal images scanned along a raster pattern: among them, Temporal, Raster, Spatio-Temporal and Fourier-space Image Correlation Spectroscopy (referred to as TICS, RICS, STICS and kICS, respectively) [42–44] differ in how fluorescence fluctuations are analyzed (in space, time, or both) and in the timescale they effectively access. The following sections describe the conceptual basis of TICS, RICS, STICS and Scanning Laser Image Correlation (SLIC), and discuss their temporal resolution and potential applications. kICS will be extensively treated in Part III.

1.3.1 Temporal Image Correlation Spectroscopy

Temporal Image Correlation Spectroscopy is the simplest, and closest to FCS, image correlation technique. The raw data for the TICS analysis consist in an *xyt*-stack of images acquired, either in confocal or two-photon microscopy, by detecting the fluorescence intensity primed by a diffraction-limited excitation laser beam that is repeatedly raster-scanned on the sample. Each image can be regarded as a 2D matrix of fluorescence intensity values $F(x, y, t)$, stored as a function of the pixel location (x, y) and of the sampling time t, with $x \in [0, N_x - 1]$, $y \in [0, N_y - 1]$ and $t \in [0, (T - 1)\Delta t]$; N_x, N_y, T and Δt are the total number of pixels along the *x*- and *y*- axis of the image (or of the region of interest on which the TICS analysis is performed), the total number of sampled time-points and the single-frame acquisition time, respectively.
From the temporal intensity trace $F(x, y, t)$ recorded at image pixel position (x, y), a correlation function is computed for each lag time τ as

$$G(\tau|x, y) = \frac{< \delta F^*(x, y, t)\delta F(x, y, t + \tau) >_t}{< F(x, y, t) >_t^2} \tag{1.46a}$$

$$G(\tau \equiv n\Delta t|x, y) \approx \frac{\frac{1}{(T-n)} \sum_{t=0}^{(T-n-1)\Delta t} \delta F^*(x, y, t)\delta F(x, y, t + \tau)}{\left(\frac{1}{T} \sum_{t=0}^{(T-1)\Delta t} F(x, y, t)\right)^2} \tag{1.46b}$$

Intensity fluctuations are defined as $\delta F(x, y, t) = F(x, y, t) - < F(x, y, t) >_t$ as

is point-FCS experiments (eq. 1.1). The angular brackets denote a temporal average over the entire time series; x and y are fixed parameters identifying the pixel position where $G(\tau|x,y)$ is computed, not appearing explicitly in the auto-correlation function. In eq. (1.46b) the approximation to the exact TICS correlation function computed over a finite discrete data-set is reported.
Since the collection of temporal intensity traces $F(x,y,t)$ is equivalent to performing several separate single-point FCS experiments (one for each pixel), the explicit expression of $G(\tau|x,y)$ can be derived following the same formalism of Section 1.1. In the case, for example, of a single population of fluorescent molecules undergoing Brownian diffusion and/or active transport,

$$G(\tau|x,y) = \begin{cases} \frac{1}{<N>}\frac{1}{\left(1+\frac{\tau}{\tau_D}\right)}\frac{1}{\sqrt{1+\zeta^2\frac{\tau}{\tau_D}}} \text{ (3D diffusion)} \\ \frac{1}{<N>}\frac{1}{\left(1+\frac{\tau}{\tau_D}\right)}\frac{1}{\sqrt{1+\zeta^2\frac{\tau}{\tau_D}}} exp\left\{-\left(\frac{\tau}{\tau_v}\right)^2\frac{1}{\left(1+\frac{\tau}{\tau_D}\right)}\right\} \text{ (3D diffusion and 2D flow)} \end{cases} \tag{1.47}$$

The characteristic diffusion and drift times follow the definitions previously reported: $\tau_D = \omega_0^2/(4bD)$ and $\tau_v = \omega_0/(b^{1/2}|\underline{v}|)$. Once instrumental parameters ω_0 and ζ have been independently calibrated (for example, by resolution measurements on sub-resolved immobile fluorescent spheres), D and $|\underline{v}|$ can be recovered from the fit to eq. (1.47) of experimental correlation functions: diffusion coefficients and speed values, determined in each pixel, can therefore be mapped with diffraction-limited resolution across the imaged area. This obviously applies not only to transport phenomena, but also to kinetic processes and chemical reactions leading to fluorescence intensity fluctuations on the timescale that can be investigated provided the total measurement time T and the temporal resolution Δt. Δt is equal to the temporal separation between consecutive frames in the *xyt*-stack: with the typical $\sim 0.3-3$ s frame rate of commercial confocal microscopes on 512x512 images, TICS is ideally suited to map dynamic processes on the second-to-minute timescale. It has already been applied to the investigation of the heterogeneities in the dynamics of α5-integrin and α-actinin in the context of the formation and disassembly of adhesions during cell migration [45], with typical diffusion coefficients ranging from $10^{-3}\mu m^2/s$ to the detection limit of $\sim 10^{-5}\mu m^2/s$ determined with control experiments on immobilized fluorescent spheres [46].

In an alternative definition of the TICS correlation function [46–48], fluorescence

intensity fluctuations are computed as the difference between the fluorescence intensity at pixel location (x, y) at time t and the spatially-averaged image intensity:

$$\delta F(x, y, t) = F(x, y, t) - < F(x, y, t) >_{xy} \tag{1.48}$$

The auto-correlation function, computed on a discrete data-set as

$$G(\tau \equiv n\Delta t) = \frac{1}{N_x N_y} \sum_{x=0}^{N_x-1} \sum_{y=0}^{N_y-1} \left\{ \frac{1}{T-n} \cdot \right.$$
$$\left. \cdot \sum_{t=0}^{(T-n-1)\Delta t} \frac{\delta F^*(x, y, t)\delta F(x, y, t+\tau)}{\frac{\sum_{x'=0}^{N_x-1} \sum_{y'=0}^{N_y-1} F(x', y', t)}{N_x N_y} \frac{\sum_{x'=0}^{N_x-1} \sum_{y'=0}^{N_y-1} F(x', y', t+\tau)}{N_x N_y}} \right\} \tag{1.49}$$

is the result of a spatial average over the imaged area or the selected region of interest. The averaging operation improves the statistics and the signal-to-noise ratio of the temporal auto-correlation, at the expence of spatial resolution: recovered transport and kinetic parameters represent average values over the entire analyzed region. Eq. (1.49) should therefore be applied to highly homogeneous cellular compartments or regions of interest.

Irrespectively of the adopted definition for the auto-correlation function, the exploitation of raster-scanned *xy*-images, and of the morphological information they are intrinsically endowed with, allows the *a posteriori* selection of regions of interest and a more precise and controlled positioning of the excitation volume with respect to single-point FCS cellular experiments. This advantage is common to all image correlation techniques.

1.3.2 Raster Image Correlation Spectroscopy

The theory and principles underlying Raster Image Correlation Spectroscopy (RICS) extend the approach of Image Correlation Spectroscopy (ICS) developed by Petersen *et al.* [49]. ICS, mainly devoted to the study of aggregation phenomena and to the quantification of the density of receptor clusters on cellular membranes, relies on the spatial correlation of the fluorescence intensity values recorded in a single raster-scanned xy-image. The two-dimensional spatial auto-correlation

function, defined for spatial lag variables ξ and η as

$$G(\xi,\eta) = \frac{< \delta F^*(x,y,t)\delta F(x+\xi,y+\eta,t) >_{xy}}{< F(x,y,t) >^2_{xy}} \tag{1.50}$$

is approximated on a discrete data-set by

$$G(\xi,\eta) \approx \frac{\frac{1}{(N_x-\xi)(N_y-\eta)} \sum_x \sum_y \delta F^*(x,y,t)\delta F(x+\xi,y+\eta,t)}{\left(\frac{1}{N_x N_y} \sum_{x=0}^{N_x-1} \sum_{y=0}^{N_y-1} F(x,y,t)\right)^2} \tag{1.51}$$

The computation is generally performed for $\xi \in [-N_x/2, N_x/2]$, $\eta \in [-N_y/2, N_y/2]$. Summations over x and y extend from $x = 0$, $y = 0$ to $x = (N_x - 1 - \xi)$, $y = (N_y - 1 - \eta)$ for positive ξ and η; for negative ξ and η, summations extend from $x = |\xi|$, $y = |\eta|$ to $x = (N_x - 1)$, $y = (N_y - 1)$. As for single-point FCS, the variance of the fluorescence intensity fluctuations is equal to the value of the auto-correlation in the limit of vanishing ξ and η; since the variance, in turn, is inversely proportional to the average number of molecules in the excitation volume, the density of fluorescent particles can be inferred from the experimental, extrapolated $G(0,0)$ amplitude [49]:

$$G(0,0) = \lim_{\xi,\eta \to 0} G(\xi,\eta) = \frac{1}{< N >} \tag{1.52}$$

Under the assumption that molecules do not move substantially on the timescale of a single image acquisition, $G(0,0)$ is recovered by fitting the ICS spatial correlation function to a 2D Gaussian with $1/e^2$ radius σ:

$$G(\xi,\eta) = G(0,0) exp\left\{-\frac{2(\xi^2+\eta^2)}{\sigma^2}\right\} \tag{1.53}$$

For sub-resolved sized fluorescent objects, σ equals the excitation laser beam waist ω_0. The measured value for $< N >$ can be employed to obtain the number of imaged fluorescent entities (each cluster contributing to the detected signal as a single entity): the size of the clusters, if present, and the number of receptors per cluster should be inferred by combining ICS results to calibration concentration-dependent studies [49].

In RICS [50–53], the theoretical framework of ICS is extended to account for the displacement of the investigated fluorescent objects during image acquisition: in this case, the 2D spatial correlation function of eq. (1.50) decays on a spatial scale defined not only by the size of the excitation volume, but also by the transport properties of the imaged particles. To illustrate the point, I consider signal fluctuations due to the diffusion of particles in a highly dilute homogenous medium, neglecting other possible sources of fluorescence fluctuations such as rotational diffusion or conformational transitions. For nearly immobile particles, as in ICS, as different spatial locations are sampled in the raster-scanned image the intensity detected in different pixels is correlated only if the pixels are within the size of the PSF: sub-resolved fluorescent objects appear in the xy-image as Gaussian spots with width assigned by the excitation beam waist, and the spatial correlation function approaches the shape of the laser beam PSF. By contrast, for diffusing particles, fluorescence correlation can be detected in pixels separated by a distance greater than the spatial extent of the PSF due to the particle motion between them; diffusion makes fluorescent objects appear in the xy-image as irregular, asymmetric streaks, depending on the magnitude of the diffusion coefficient and on the adopted scan speed. Ideally, the excitation beam should be raster-scanned on the sample at a rate such that the very same molecule is excited, and detected, in a few adjacent pixels along the horizontal x-direction (the fast-scan axis) and in a few consecutive lines along the vertical y-direction (the slow-scan axis). The correlation function appears in this case elongated along the horizontal axis, with increasing width along the vertical axis for decreasing D (Fig. 1.8).

The tight interplay of transport parameters and image acquisition settings has to be accounted for in the derivation of the explicit expression of the spatial correlation function of eqs. (1.50-1.51). Since RICS is effectively the limiting case of STICS (Spatio-Temporal Correlation Spectroscopy) for vanishing lag time, I refer to Section 1.3.3 for the complete derivation, and just report here the analytical solution for the case of 2D isotropic Brownian diffusion with diffusion coefficient D [50, 51] investigated in one-photon excitation configuration:

$$G(\xi,\eta) = \frac{1}{< N >}\frac{1}{\left(1+\frac{4D(\xi\tau_p+\eta\tau_l)}{\omega_o^2}\right)}\exp\left\{-\frac{|\frac{\xi\delta x}{\omega_0}|^2+|\frac{\eta\delta x}{\omega_0}|^2}{\left(1+\frac{4D(\xi\tau_p+\eta\tau_l)}{\omega_o^2}\right)}\right\} \tag{1.54}$$

$< N >=< C > \pi\omega_0^2$, δx is the pixel size; τ_p and τ_l are the pixel dwell time and the line scan time, respectively. With a typical τ_p of the order of a few microseconds and with τ_l of the order of a millisecond, RICS bridges the gap between

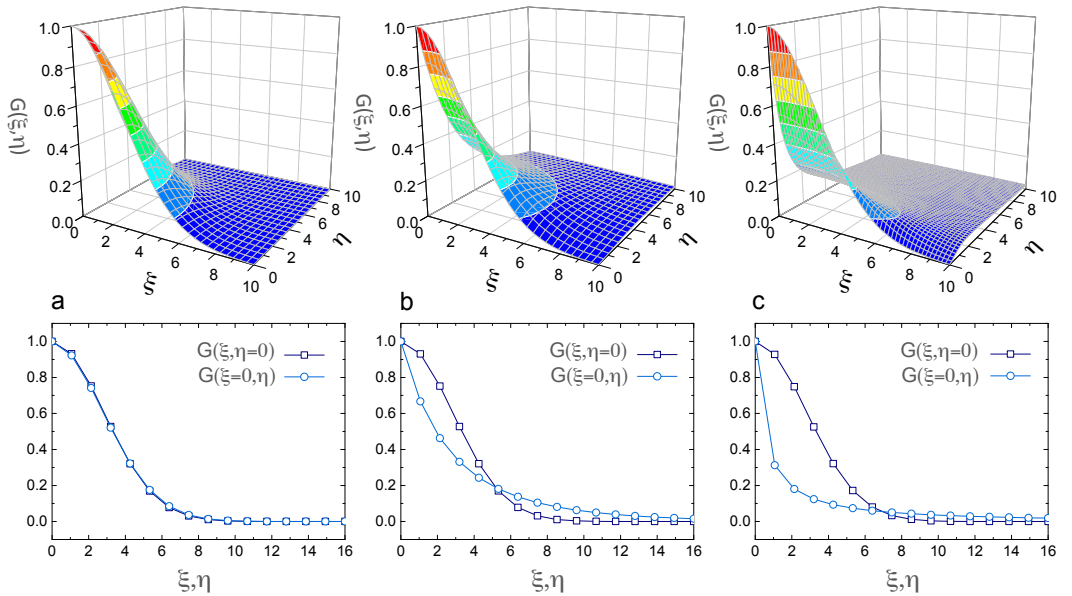

Figure 1.8: *Raster Image Correlation Spectroscopy.* Exemplifying RICS correlation functions $G(\xi,\eta)$ (upper panels) and $G(\xi,\eta=0)$, $G(\xi=0,\eta)$ profiles (lower panels) simulated according to eq. (1.54) for D=0.1 $\mu m^2/s$ (column a), D=4 $\mu m^2/s$ (column b) and D=20 $\mu m^2/s$ (column c). $<N>$=1, ω_0=0.2 μm, δx=0.05 μm, τ_l=1 ms and τ_p=1.9 μs; ξ and η are in pixel units. In the literature, experimental spatial correlation functions are usually reported in the whole range $\xi \in [-N_x/2, N_x/2]$, $\eta \in [-N_y/2, N_y/2]$.

the timescales of single-point FCS ($\sim \mu s$) and ICS ($\sim s$). Diffusion coefficients that can be measured range from $\sim 0.1 \mu m^2/s$ (typical of transmembrane proteins and receptors) up to $\sim 80 \mu m^2/s$ (for free protein diffusion in solution). The spatial resolution, as previously discussed for TICS, is regulated by the size of the region of interest over which $G(\xi,\eta)$ is averaged and computed.

Operatively, $G(\xi,\eta)$ is computed separately on each frame of the acquired xyt-stack; the RICS correlation functions are subsequently averaged to ensure an adequate sampling of the dynamic process under investigation. General guidelines regarding the minimum number of frames, as well as the optimal image acquisition parameters and scan settings, are provided in [52] together with a characterization of the effect of analogue detectors on the RICS correlation function.

Process	Characteristic time	Technique
Rotational diffusion	1–10 µs	Polarized FCS
Blinking	1–10 µs	FCS
Diffusion of a small molecule in solution	0.2 ms	FCS, S-FCS, RICS
Diffusion of GFP in the cytoplasm	1 ms	FCS, S-FCS, RICS
Lipid or lipid anchored protein diffusion	10 ms	FCS, S-FCS, RICS, FRAP
Diffusion of a protein in a membrane	100 ms	t-ICS, FRAP
Vesicle transport	0.1–1 s	t-ICS
Weak binding–unbinding	0.1–10 s	FCS, S-FCS, t-ICS, TIRF t-ICS

Figure 1.9: *Characteristic times for various cellular processes and suitable techniques for their investigation [52].* FRAP stands for Fluorescence Recovery After Photo-bleaching.

Immobile fraction subtraction

Large, immobile fluorescent structures are often detected in live-cell (confocal or two-photon excitation) imaging. To isolate the contribution of fast diffusing molecules in the RICS correlation function, a high-pass filter must be applied to the confocal xyt-stack prior to the computation of the correlation function. Basically, for each pixel location (x, y) at a given time point t, the raw detected fluorescence intensity $F(x, y, t)$ is replaced by a corrected pixel intensity $f(x, y, t)$:

$$f(x, y, t) = F(x, y, t) - < F(x, y, t) >_t + < F(x, y, t) >_{xyt} \tag{1.55}$$

The average intensity of the pixel time trace $< F(x, y, t) >_t$ is subtracted to eliminate the contribution of bright, immobile structures; the scalar average intensity of the entire stack $< F(x, y, t) >_{xyt}$ is then added to avoid oscillatory, noisy correlation functions, that would be obtained otherwise due to spatially-averaged image intensities close to zero [50, 52]. The same definition for corrected pixel intensities can also be adopted for TICS and STICS analyses. The only drawback is that after the immobile population removal the correlation amplitude $G(0, 0)$ is no longer directly related to the average number of molecules in the excitation volume.
A similar correction, differing in the computation of $< F(x, y, t) >_t$ on a reduced number of frames (moving window averaging), can be applied to correct for slow cellular movements [54].

1.3.3 Spatio-Temporal Image Correlation Spectroscopy

The STICS [48,55,56] analysis of an xyt-stack of images combines the temporal information of single pixel intensity traces with the spatial information embedded in the whole imaged field of view. A generalized spatio-temporal correlation function is computed, for each lag time τ and for spatial lag variables ξ and η, as

$$G(\xi,\eta,\tau) = \left\langle \frac{< \delta F^*(x,y,t)\delta F(x+\xi,y+\eta,t+\tau) >_{xy}}{< F(x,y,t) >_{xy} < F(x,y,t+\tau) >_{xy}} \right\rangle_t \tag{1.56a}$$

$$\approx \frac{< \delta F^*(x,y,t)\delta F(x+\xi,y+\eta,t+\tau) >_{xyt}}{(< F(x,y,t) >_{xy})^2} \tag{1.56b}$$

By definition, $G(\xi,\eta,\tau)$ is computed as a temporal average over all pairs of images a time τ apart and as a spatial average over all pairs of pixels (a lag time τ apart) separated by distances ξ and η along the horizontal and vertical directions, respectively. Spatially-averaged intensities of the entire xy-images (or of the selected region of interest on which the STICS analysis is performed) at time t and time $t+\tau$ in the temporal series, appearing in the denominator of eq. (1.56a), are exploited for the computation of fluorescence intensity fluctuations as $\delta F(x,y,t) = F(x,y,t) - < F(x,y,t) >_{xy}$. When $< F(x,y,t) >_{xy} \approx < F(x,y,t+\tau) >_{xy}$ $\forall t,\tau$ (i.e., when the spatially averaged intensity is nearly the same for all the images of the stack), the approximation of eq. (1.56b) applies. Globally, $G(\xi,\eta,\tau)$ can be regarded as a time series in the temporal variable τ, each frame being the average spatial correlation (function of ξ and η delays) of pairs of images a fixed lag time τ apart.
As for ICS, the computation is generally performed for $\xi \in [-N_x/2, N_x/2]$ and $\eta \in [-N_y/2, N_y/2]$, with summations over x and y extending from $x=0$, $y=0$ to $x=(N_x-1-\xi)$, $y=(N_y-1-\eta)$ for positive ξ and η, and from $x=|\xi|$, $y=|\eta|$ to $x=(N_x-1)$, $y=(N_y-1)$ for negative ξ and η.

Exactly as for single-point FCS, the explicit expression of the correlation function $G(\xi,\eta,\tau)$ is determined by both the geometry of the excitation volume and the dynamic processes underlying fluorescence intensity fluctuations. I focus here on a single species of fluorescent objects exhibiting a combination of isotropic 2D Brownian diffusion and uniform drift in the focal xy-plane; the more complex case of transport phenomena coupled to binding reactions will be the object of Part III. The formalism I adopt is similar to the one of eqs. (1.3)-(1.20). Provided the

convolution integral

$$\delta F(\underline{x}, t) = \phi \int_{-\infty}^{+\infty} d^2\underline{r}\, W(\underline{r} - \underline{x})\delta C(\underline{r}, t) \tag{1.57}$$

for the fluorescence intensity fluctuations detected at spatial coordinates $\underline{x} = (x, y)$ at time t, its substitution into the numerator of eq. (1.56b) yields

$$g(\underline{\Delta}, \tau) \equiv g(\xi, \eta, \tau) \equiv < \delta F^*(x, y, t)\delta F(x + \xi, y + \eta, t + \tau) >_{xyt} =$$

$$= \phi^2 \lim_{R\to+\infty} \frac{1}{R^2} \int_{-R/2}^{R/2} d^2\underline{x} \iint_{-\infty}^{+\infty} d^2\underline{r} d^2\underline{r}'\, W^*(\underline{r}-\underline{x})W(\underline{r}'-\underline{x}-\underline{\Delta}) < \delta C^*(\underline{r}, t)\delta C(\underline{r}', t+\tau) >_t$$

$$= \phi^2 \lim_{R\to+\infty} \frac{1}{R^2} \int_{-R/2}^{R/2} d^2\underline{x} \iint_{-\infty}^{+\infty} d^2\underline{r} d^2\underline{r}'\, W^*(\underline{r}-\underline{x})W(\underline{r}'-\underline{x}-\underline{\Delta}) < \delta C^*(\underline{r}, 0)\delta C(\underline{r}', \tau) >_t \tag{1.58}$$

The vector $\underline{\Delta}$ has been introduced according to $\underline{\Delta} = (\xi, \eta)\delta x$ (δx being the pixel size) and the spatial average has been replaced by the integral over an area R^2, following the notation of eq. (1.2).
By recalling eqs. (1.15)-(1.17) and the Fick's equation for drift and diffusion (eq. 1.28), I express the concentration correlation term as

$$< \delta C^*(\underline{r}, 0)\delta C(\underline{r}', \tau) >= \frac{< C >}{(2\pi)^2} \int_{-\infty}^{+\infty} e^{(-D|\underline{q}|^2\tau + i\underline{q}\cdot\underline{v}\tau)} e^{i\underline{q}\cdot(\underline{r}-\underline{r}')}\, d^2\underline{q} \tag{1.59}$$

When substituted into eq. (1.58) together with the Fourier transforms of the excitation distributions W, it yields

$$g(\underline{\Delta}, \tau) = \frac{\phi^2 < C >}{(2\pi)^4} \lim_{R\to+\infty} \frac{1}{R^2} \int_{-R/2}^{R/2} d^2\underline{x} \int_{-\infty}^{+\infty} d^2\underline{r} \int_{-\infty}^{+\infty} d^2\underline{r}' \int_{-\infty}^{+\infty} d^2\underline{q}'\widehat{W}^*(\underline{q}')e^{i\underline{q}'\cdot(\underline{r}-\underline{x})}\cdot$$

$$\cdot \int_{-\infty}^{+\infty} d^2\underline{q}''\widehat{W}(\underline{q}'')e^{-i\underline{q}''\cdot(\underline{r}'-\underline{x}-\underline{\Delta})} \int_{-\infty}^{+\infty} d^2\underline{q}\, e^{(-D|\underline{q}|^2\tau + i\underline{q}\cdot\underline{v}\tau)} e^{i\underline{q}\cdot(\underline{r}-\underline{r}')} \tag{1.60}$$

Recalling that in two dimensions

$$\begin{cases} \delta(\underline{s}) = \frac{1}{2\pi}\int_{-\infty}^{+\infty} e^{i\underline{k}\cdot\underline{s}}\, d^2\underline{k} = \lim_{R\to\infty} \frac{1}{2\pi}\int_{-R/2}^{R/2} e^{i\underline{k}\cdot\underline{s}}\, d^2\underline{k} \\ \\ \delta(0) = \lim_{R\to\infty} \frac{1}{2\pi}\int_{-R/2}^{R/2} d^2\underline{k} = \lim_{R\to\infty} \frac{1}{2\pi} R^2 \end{cases} \tag{1.61}$$

$g(\underline{\Delta},\tau)$ can be rewritten as

$$g(\underline{\Delta},\tau) = \frac{\phi^2 < C >}{(2\pi)} \frac{1}{R^2} \int_{-\infty}^{+\infty} d^2\underline{q} \int_{-\infty}^{+\infty} d^2\underline{q}\,' \int_{-\infty}^{+\infty} d^2\underline{q}\,'' \widehat{W^*}(\underline{q}\,')\widehat{W}(\underline{q}\,'')\cdot$$

$$\cdot exp\left\{ i\underline{q}\,'' \cdot \underline{\Delta} \right\} exp\left\{ -D|\underline{q}|^2\tau + i\underline{q} \cdot \underline{v}\tau \right\} \delta(\underline{q} + \underline{q}\,')\delta(\underline{q}\,'' + \underline{q})\delta(\underline{q}\,'' - \underline{q}\,') \qquad (1.62)$$

Successive integrations over $\underline{q}$ and $\underline{q}\,''$ lead to

$$g(\underline{\Delta},\tau) = \frac{\phi^2 < C >}{(2\pi)} \frac{1}{R^2} \int_{-\infty}^{+\infty} d^2\underline{q}\,' \int_{-\infty}^{+\infty} d^2\underline{q}\,'' \widehat{W^*}(\underline{q}\,')\widehat{W}(\underline{q}\,'')\cdot$$

$$\cdot exp\left\{ i\underline{q}\,'' \cdot \underline{\Delta} \right\} exp\left\{ -D|\underline{q}\,''|^2\tau - i\underline{q}\,'' \cdot \underline{v}\tau \right\} \delta(\underline{q}\,'' - \underline{q}\,')\delta(\underline{q}\,' - \underline{q}\,'') \quad \rightarrow \qquad (1.63)$$

$$g(\underline{\Delta},\tau) = \frac{\phi^2 < C >}{(2\pi)} \frac{1}{R^2} \int_{-\infty}^{+\infty} d^2\underline{q}\,' |\widehat{W}(\underline{q}\,')|^2 exp\left\{ i\underline{q}\,' \cdot \underline{\Delta} - D|\underline{q}\,'|^2\tau - i\underline{q}\,' \cdot \underline{v}\tau \right\} \delta(0)$$

$$= \lim_{R\to\infty} \frac{\phi^2 < C >}{(2\pi)} \frac{1}{R^2} \int_{-\infty}^{+\infty} d^2\underline{q}\,' |\widehat{W}(\underline{q}\,')|^2 exp\left\{ i\underline{q}\,' \cdot \underline{\Delta} - D|\underline{q}\,'|^2\tau - i\underline{q}\,' \cdot \underline{v}\tau \right\} \frac{R^2}{2\pi}$$

$$= \frac{\phi^2 < C >}{(2\pi)^2} \int_{-\infty}^{+\infty} d^2\underline{q}\,' |\widehat{W}(\underline{q}\,')|^2 exp\left\{ i\underline{q}\,' \cdot \underline{\Delta} - D|\underline{q}\,'|^2\tau - i\underline{q}\,' \cdot \underline{v}\tau \right\} \qquad (1.64)$$

If the excitation distribution $W(\underline{r})$ is approximated with a 2D Gaussian with radial $1/e^2$ distance ω_0 and amplitude W_0,

$$\widehat{W}(\underline{q}\,') = \frac{W_0\omega_o^2}{4} exp\left\{ -\frac{\omega_0^2|\underline{q}\,'|^2}{8} \right\} \qquad (1.65)$$

Once substituted into eq. (1.64) it leads to a Gaussian integral (analogous to eq. 1.30) that can easily be solved into

$$g(\underline{\Delta},\tau) = \frac{W_0^2\phi^2 < C > \omega_0^2}{16\pi} \frac{1}{(1 + 4D\tau/\omega_0^2)} exp\left\{ -\frac{1}{\omega_0^2} \frac{|\underline{\Delta} - \underline{v}\tau|^2}{1 + 4D\tau/\omega_0^2} \right\} \qquad (1.66)$$

The lag time τ is given explicitly by $\tau = \xi\tau_p + \eta\tau_l + \psi\tau_f$, where τ_p is the pixel dwell time, τ_l is the line scan time, τ_f is the inverse of the frame rate and ψ is the

delay, in frame units, between the pairs of images a time $\psi\tau_f$ apart exploited for the computation of $g(\xi,\eta,\tau)$.

$$g(\xi,\eta,\tau) = \frac{W_0^2\phi^2 < C > \omega_0^2}{16\pi}\left[1+\frac{4D(\xi\tau_p+\eta\tau_l+\psi\tau_f)}{\omega_0^2}\right]^{-1}\cdot$$

$$\cdot exp\left\{-\frac{1}{\omega_0^2}\frac{[\xi\delta x-\nu_x(\xi\tau_p+\eta\tau_l+\psi\tau_f)]^2}{\left(1+\frac{4D(\xi\tau_p+\eta\tau_l+\psi\tau_f)}{\omega_0^2}\right)}\right\}\cdot exp\left\{-\frac{1}{\omega_0^2}\frac{[\eta\delta x-\nu_y(\xi\tau_p+\eta\tau_l+\psi\tau_f)]^2}{\left(1+\frac{4D(\xi\tau_p+\eta\tau_l+\psi\tau_f)}{\omega_0^2}\right)}\right\} \tag{1.67}$$

For a typical 1024x1024 image, scanned with a 400 Hz line frequency, $\tau_l = 2.5ms$ and $\tau_p = 2.4\mu s$; if the STICS analysis is performed on a 64x64 ROI, $\xi\tau_p+\eta\tau_l \sim 2.5-80ms << \tau_f \sim 1-5s$. Under this condition ($\tau = \xi\tau_p+\eta\tau_l+\psi\tau_f \approx \psi\tau_f$), τ can be simply regarded as an integer multiple of the image scan time τ_f and, for a fixed lag time, eq. (1.67) can be approximated by a 2D Gaussian in the spatial delays ξ and η. By further dividing by the squared spatially averaged intensity $< F(x,y,t) >_{xy}^2 = \phi^2\widehat{W}(0)^2 < C >^2$, the normalized STICS correlation function $G(\xi,\eta,\tau)$ is obtained:

$$G(\xi,\eta,\tau) \approx \frac{1}{< C > \pi\omega_0^2}\frac{1}{\left(1+\frac{4D\tau}{\omega_0^2}\right)}exp\left\{-\frac{1}{\omega_0^2}\frac{[\xi\delta x-\nu_x\tau]^2}{\left(1+\frac{4D\tau}{\omega_0^2}\right)}\right\}exp\left\{-\frac{1}{\omega_0^2}\frac{[\eta\delta x-\nu_y\tau]^2}{\left(1+\frac{4D\tau}{\omega_0^2}\right)}\right\} \tag{1.68}$$

For vanishing lag time $\psi\tau_f$, $G(\xi,\eta,\tau=\xi\tau_p+\eta\tau_l)$ reduces to the RICS spatial correlation function. If fluorescent objects move appreciably during the time required for a single image acquisition, it can be exploited to recover transport parameters as previously pointed out with eq. (1.54). In this case the computation of $G(\xi,\eta,\tau)$ for higher τ values (for non-zero $\psi\tau_f$ values) is not useful, since the temporal resolution is too low for intensity fluctuations to be correlated between successive images. By contrast, when particles move on the second-to-minute timescale, $G(\xi,\eta,\tau=\xi\tau_p+\eta\tau_l)$ coincides with the PSF-sized 2D Gaussian of Image Correlation Spectroscopy and $G(\xi,\eta,\tau)$ with $\psi\tau_f \neq 0$ can be exploited to recover information on the particles motion. Precisely, the variance of $G(\xi,\eta,\tau)$ increases with the lag time and with the diffusion coefficient of the investigated objects, equally along the ξ- and η- directions as a consequence of the tendency of the diffusing particles to exit the correlation area in a symmetric way. D can therefore

be recovered by surface fitting the experimental 2D correlation functions to eq. (1.68) for each lag time τ and by the linear regression of the variance-versus-τ plot. Information on drift velocities (both modulus and direction) can instead be recovered from the coordinates $(\xi,\eta)_{max}$ of the peak of the correlation function. The peak value is located at $(\xi,\eta)_{max}\delta x = (0,0)$ if $v_x, v_y = 0$, whereas it shifts at $(\xi,\eta)_{max}\delta x = (v_x\tau, v_y\tau)$ when $|\underline{v}| \neq 0$. This allows measuring the x- and y-components of the drift velocity by simply tracking the Gaussian peak coordinates as a function of τ. I finally remark that all the transport parameters, apart from the drift velocity direction, can also be recovered by the STICS amplitude at vanishing spatial delays, $G(\xi = 0, \eta = 0, \tau)$, coinciding with the TICS correlation function of eq. (1.49).

1.3.4 Scanning Laser Image Correlation

This Subsection concludes the general treatment of Image Correlation Spectroscopy with Scanning Laser Image Correlation (SLIC) [57]: conceived as the imaging analogue of dual-beam fluorescence cross-correlation spectroscopy, it will be exploited for hemodynamics measurements in Part II.
SLIC exploits images acquired by means of a line-scanning procedure in fluorescence confocal or two-photon excitation microscopy. A linear path within the sample is repeatedly scanned in time and the consecutive scans are juxtaposed along the vertical direction in the form of a so-called xt-image: adjacent pixels along the horizontal axis represent adjacent positions along the scan path, while consecutive pixels along the vertical axis provide successive fluorescence intensity measurements gathered from the same spatial location of the sample. In the presence of directed motion, the scan path is conveniently aligned to the flow direction and a scan speed much higher than the speed of the investigated objects is selected: in this case flowing particles appear as diagonal lines with a slope inversely proportional to their speed (Fig. 1.10). In the limiting case of immobile particles vertical lines are obtained, whereas objects much faster than the scan speed create horizontal lines in the xt-image.
Quantitative information concerning the drift speed can be obtained by cross-correlating the fluorescence intensity fluctuations detected in pairs of columns of the image: exactly as for dbFCCS (eq. 1.38), molecular flow and diffusion from column 1 to column 2 are detected by computing

$$G_{12}(\tau) = \frac{< \delta F_1(t)\delta F_2(t+\tau) >_t}{< F_1(t) >_t < F_2(t) >_t} \tag{1.69}$$

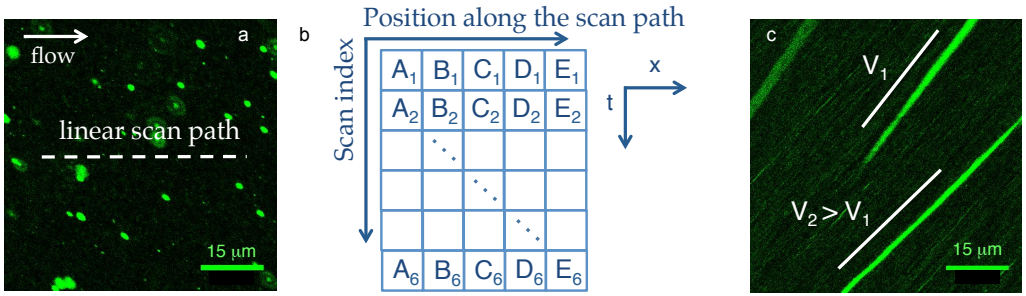

Figure 1.10: *Scanning Laser Image Correlation.* (a): xy-image acquired along a conventional raster-pattern by detecting the fluorescence signal of 0.1 μm fluorescent microbeads undergoing laminar flow in a square borosilicate capillary (800 μm nominal square section); the scan speed is adjusted to be much higher than the speed of the flowing objects, which appear in the image as diffraction-limited fluorescent quasi-Gaussian spots. Suppose now a linear scan path is selected (an exemplifying possible choice is depicted as a dashed line in panel a): the excitation laser beam does not follow a raster pattern any more, but repeats in time the scan of the same line. The consecutive scans can be aligned along the vertical direction as shown in panel (b); the horizontal x-axis of the resulting image defines adjacent positions along the scan path (denoted as pixels A, B, C, etc.), while the vertical axis now encodes the temporal information: the first column contains the fluorescence intensity registered in A during successive scans (A_1, A_2, A_3, etc.), the second column contains the fluorescence intensity registered in B during successive scans (B_1, B_2, B_3, etc.), and so on. An exemplary resulting xt-image acquired along the linear path depicted in (a) is reported in panel (c). As described in the text, particles flowing with different speeds v_1 and v_2 produced in the image diagonal lines with different slopes.

Explicitly, the only difference to be accounted for in the derivation of $G_{12}(\tau)$ with respect to the dual-beam case is that fluorescence is not sampled simultaneously in both excitation volumes: they are separated in time by an interval $R\tau_p$, where τ_p is the pixel dwell time and R is the distance, in pixel units, between the two columns. $R\tau_p$ sums to an integer multiple of the line scan time τ_l (~ ms) in defining the lag time τ=$(R\tau_p + \psi\tau_l)$. As long as $R\tau_p << \tau_l$ (a condition that is typically satisfied, especially for small column distances), no formal difference exists between the SLIC configuration and the dual-beam setup. The cross-correlation $G_{12}(\tau)$ is explicitly given by:

$$G_{12}(\tau) = \frac{1}{< N >} \frac{1}{1 + \tau/\tau_D} \frac{1}{\sqrt{1 + \zeta^2\tau/\tau_D}} \exp\left\{ - \frac{|\underline{R} - \underline{v}\tau|^2}{\omega_o^2/\flat(1 + \tau/\tau_D)} \right\} \qquad (1.70)$$

$$\rightarrow G_{12}(\tau) = \frac{1}{< N >} \frac{1}{1+\tau/\tau_D} \frac{1}{\sqrt{1+\zeta^2\tau/\tau_D}} \exp\left\{ -\frac{|\underline{v}|^2}{\omega_o^2/\flat} \frac{(\tau^2+\tau_v^2-2\tau\tau_v\cos\gamma)}{1+\tau/\tau_D} \right\} \tag{1.71}$$

It resembles eq. (1.43), with the inter-spot distance $|\underline{R}|$ replaced by the separation $R\delta x$ between the two columns; the pixel size δx is typically a fraction of the excitation beam waist, so that spatial locations along the scan orbit are oversampled with respect to ω_0. What has been previously pointed out for dbFCCS regarding the effect of the diffusion coefficient D, of the scan speed $|\underline{v}|$ and of the angle γ between the drift velocity and the inter-column vector on the cross-correlation peak time and amplitude equally applies in the SLIC case.

In summary, while sharing its theoretical framework, SLIC offers two main advantages with respect to dbFCCS: (i) the exploitation of commercially available confocal microscopes instead of an *ad-hoc* experimental setup and (ii) the possibility of investigating, on a single xt-image, multiple column distances. This has already been exploited within the Pair Correlation approach [37, 58] to evidence the presence of barriers and obstacles to diffusion and flow in intracellular compartments.

Part II

FLICS: FLow Image Correlation Spectroscopy

Chapter 2

FLICS: A Novel Method for Flow Measurements

The measurement of flow fields and velocities in micron-scaled structures is required in a wide range of disciplines ranging from physics, engineering and chemistry to biology and medicine. Microfluidics, referring to both the theoretical modeling and the development of devices for controlling and manipulating fluids in vessels less than a millimeter in width [59], is developing into a hot research topic. It provides new methodologies to tackle biological issues down to the single cell level and allows investigating the physics of fluid dynamics at the micron-scale (characterized by low Reynolds number, laminar flow and fast diffusion, opposing to the higher Reynolds number, turbulence and slow diffusion exhibited by bulk fluids at the macroscale [60]); fueled by high performance, low cost, design flexibility, miniaturization, portability and reduced reagent consumption [61], the development of micro-fabrication techniques for lab-on-chip devices has enabled applications including drug testing [62], cell sorting [63] and clinical diagnostics [64].
Equally relevant are flow measurements in the microcirculation of living organisms. Microcirculation, a complex network of small vessels with a typical diameter ranging from 5 to 100 μm, plays a crucial role in the maintenance and hemodynamics of tissues and organs, delivering blood, nutrients and signaling molecules, interacting extensively with the immune system and leading to severe pathologies in case of impairments and dysfunctions [65,66]. Non-invasive tools for studying *in-vivo* the blood flow in extended microcirculatory vessel networks are therefore continuously

developed. Ideally, these methods should be endowed with single-capillary sensitivity to characterize the heterogeneity in the structure, function and treatment response of different vessels within the network [67] and should combine the blood flow measurement with the simultaneous diffraction-limited resolution imaging of vascular cells [68]. In this Chapter, a novel method fulfilling these requirements, that I have called FLICS or FLow Image Correlation Spectroscopy [69,70], is described: it employs a single raster-scanned xy-image acquired by confocal or multi-photon excitation fluorescence microscopy to quantitatively measure the (blood) flow velocity in the whole vessel pattern within the imaged field of view, while simultaneously maintaining the morphological information concerning the immobile structures of the explored circulatory system. Although equally applicable to the flow characterization in microfluidic devices, in the following Chapters FLICS will be mostly employed for hemodynamics studies in small animal model organisms. Prior to the description of the FLICS principles and to the derivation of its theoretical framework, I provide therefore a brief overview of various existing methods for blood flow speed measurements.

2.1 Blood flow measurement techniques

Common state-of-the-art (clinical) optical techniques employed for the measurement of the blood flow include laser Doppler flowmetry, optical Doppler tomography, ultrasound imaging and laser-speckle contrast imaging.

Laser Doppler Flowmetry (LDF) exploits a monochromatic laser beam (with a typical wavelength λ in the range 600-780 nm, above the absorption maximum of hemoglobin and below the maximal absorption of water [71]) impinging on the investigated specimen and scattered by both static and moving objects within a $\sim$ mm depth; while light reflected from stationary components remains unchanged in frequency, light reflected by flowing particles (erythrocytes, for example) undergoes a frequency shift according to the Doppler principle. Denoting with $\Delta\nu$ the Doppler frequency shift $\nu' - \nu$ (ν and ν' being the original and the shifted beam frequencies, respectively), the component $|\underline{v}|$ along the line of sight of the velocity of the scattering moving objects can be recovered as $|\underline{v}| = c\Delta\nu/(2\nu)$, where c is the speed of light [73]. Therefore, only the Doppler frequency shift $\Delta\nu$ is required, in addition to the original frequency and the speed of light, to measure the axial $|\underline{v}|$ component. The typical practical implementation exploits the beat phenomenon resulting from the superposition of the Doppler-shifted beam with a reference beam at the original

wavelength λ: the frequency of the signal to be detected is conveniently reduced to the difference in frequency between the two waves, which being much lower than ν and ν' is much easier to measure. In more sophisticated realizations, variable frequencies of the reference beam are exploited or multiple-angle measurements are implemented to also gain information on the flow direction and on the lateral radial component of the flow velocity [73].

Laser Doppler velocimetry has been used to measure the blood flow speed, both in basic research on model organisms and in clinical diagnostics, for nearly 40 years [73–75]. The effects of the laser beam radius, of the radius of the blood vessel and of the depth of the vessel in the tissue have been extensively investigated [76] and scanning modalities have been implemented to overcome the limitation of LDF in measuring the blood flow velocity at a single point [77]. Particularly relevant has been the development of Optical Doppler Tomography (ODT) [78], a non-invasive Doppler-based optical technique to simultaneously image the tissue structure and the blood flow dynamics at specific ($\sim$ 1-2 mm) depths inside the tissue: by using a Michelson interferometer with a broadband low-coherence light source -i.e., by exploiting the principles of Optical Coherence Tomography (OCT) [79]-, Optical Doppler Tomography provides high resolution tomographic images of static and moving components and measures the blood flow speed from the amplitude and frequency of the interference fringes produced by the reference and target arms of the interferometer. Although a time-domain processing of interference fringes is possible, the Frequency-Domain Optical Doppler Tomography (FD-ODT) has largely enhanced the imaging and acquisition speed. Motivated by the quest for methods to measure flow velocities in micron-scaled channels, attempts have been made to increase the sensitivity and resolution of Doppler-based techniques, which have already been applied both *in-vivo* and in microfluidics with a spatial resolution of a few μm and a velocity sensitivity $\sim$10 μm/s [80,81].

The Doppler effect is also exploited by ultrasound-based flow measurement techniques, which recover both the blood volume and the axial flow speed by exposing the investigated circulatory system to pulsed ultrasound waves and by measuring in time the Doppler-shifted frequency of the ultrasonic waves backscattered by tissues and fluids [82]. To date, the application of conventional ultrasound methods has been limited to the main arteries: the necessity of high-pass filtering the frequencies associated to the motion of tissues (due, for example, to cardiac pulsatility and respiration) imposes a lower limit to the blood flow speed that can be measured ($\sim$ 4 mm/s for a 15-MHz ultrasound probe).

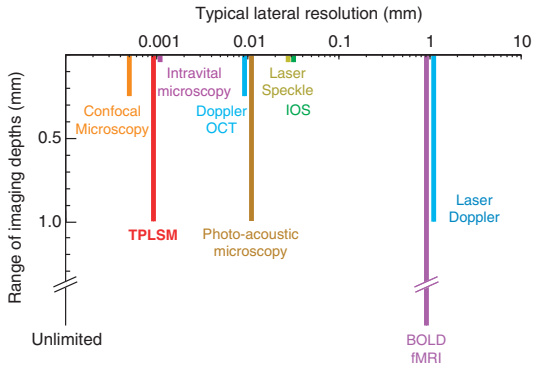

Figure 2.1: *Lateral resolution and tissue penetration for state-of-the-art blood flow measurement techniques [72].* Two-photon laser scanning microscopy is identified in [72] as the optimal technique for the *in-vivo* imaging and measurement of the blood flow in model organisms. (BOLD fMRI: Blood-Oxygenation Level-Dependent functional Magnetic Resonance Imaging; TPLSM: Two-Photon Laser Scanning Microscope.)

An alternative approach in the context of ultrasound-based techniques is exploited by the so-called transit-time method [83, 84]. An ultrasound wave emitted by a transducer traverses the investigated vessel, rebounds off an acoustic reflector and traverses the vessel again, in the opposite direction, back to the transducer where it is captured and converted into an electrical signal; the variation in the expected transit time, along and opposite to the flow direction, due to the flow is employed to recover the flow volume. Commercially available setups allow the blood flow measurement in vessels ~ 200 μm in diameter [83], thereby hampering the application of the transit-time method to the investigation of smaller microcirculatory vessels.

In summary, despite a few reported applications in microfluidic devices and in the microcirculation of small animal model organisms, Doppler and ultrasound-based techniques are mainly suited for flow measurements on large-scale vessels, and the greatest efforts have been devoted to improve their performance in clinical diagnostics and applications.

An alternative, optical, full-field blood flow measurement technique is Laser Speckle Contrast Imaging (LSCI) [73, 85, 86], which exploits the spatio-temporal variations of the speckle pattern produced by flowing objects. When coherent and

nearly monochromatic (typically infrared) laser light impinges on erythrocytes, the scattered radiation traverses slightly different path lengths, adds constructively or destructively and produces an interference speckle pattern on a detector (typically, a Charged Coupled Device CCD camera). Since the movement of red blood cells produces spatial and temporal fluctuations in the interference pattern, information on the flow speed is naturally encoded in the statistics of the speckle pattern itself. Specifically, LSCI takes advantage of the spatial statistics (basically, the contrast) of time-averaged speckle patterns.

While a very short camera-exposure time would 'freeze' the speckles and result in a high-contrast speckle pattern, a long exposure time would allow the speckles to average out, leading to a low contrast; similarly, the higher the flow speed, the more averaging occurs within a given exposure time, so that the speed distribution in the field of view can be mapped by mapping the variations in the speckle contrast [73]. The contrast, K, is defined as the ratio of the spatial standard deviation σ_S of the time-averaged speckle intensity I to the mean intensity $< I >$: $K = \sigma_S / < I >$ [87,88], and it varies between 0 and 1. By relating the contrast to the temporal average of the autocorrelation of the intensity fluctuations, and by assuming a specific (Lorentzian, or Gaussian-Lorentzian) velocity distribution, K can be explicitly related to the correlation time τ_c of the intensity fluctuations; then the relative blood velocity variations are estimated by computing the changes in τ_c from a baseline state and by the assumption of inverse proportionality between the speed and τ_c. A dedicated software finally produces a false-color contrast map indicating velocity variations.
The processing time can be less than a second, making LSCI a real-time technique [73]. The illuminated area of interest can vary from a few mm to several cm, and a spatial resolution of 10-20 μm can be achieved. Moreover, the user-selected exposure time (typically of the order of 1-20 ms) can be tuned to select the velocity range being mapped. The main drawbacks of single-exposure LSCI rely in the limited penetration depth of the laser wavelength (less than 1 mm) and in the impossibility of quantifying the absolute value of the flow speed. Additionally, the theoretical relation between the contrast and the speed can only be outlined if the velocity distribution is known, which is usually not the case; even though a Lorentzian approximation can be adopted, more accurate statistical theories are often required [89].

Laser Speckle Contrast Imaging has been employed for a number of blood flow measurements in tissues where the microcirculatory system of interest is superficial,

retina and skin being significant examples. LSCI has also been applied for the *in-vivo* imaging of deep tissues (brain, liver or kidney) in small animal models upon proper surgical preparation.

Flow measurements in the microcirculation of animal organisms can also be successfully performed by those techniques combining the high spatial resolution of confocal and two-photon excitation fluorescence microscopes with the principles of fluorescence correlation. Among these techniques, μ-Particle Image Velocimetry (μ-PIV) [90–92], Scanning Laser Image Correlation (SLIC) [57] and dual-beam Fluorescence Cross-Correlation Spectroscopy (dbFCCS) [32,33,35] have already been employed for both *in-vivo* and *in-vitro* flow measurements, and offer the remarkable advantage of providing absolute values for the measured flow speed.

SLIC and dbFCCS have been extensively described in Chapter 1; they are endowed with high temporal (~ ms) and spatial (< 1μm) resolution, but lack the ability to simultaneously correlate the flow speed values with the morphological details in an intricate network of capillaries. This obviously also applies to the Radon transform-based analyses of the same line-scan experimental data [93,94].

μ-PIV - the small-scale counterpart of Particle Image Velocimetry [95,96] - is an optical, non-invasive, whole-field velocity measurement technique which has turned in the last ten years into the standard tool for fluid velocity measurements in micro-vessels. Fluorescent tracer particles, typically made of polystyrene and with suitable diameters in the range ~ 10-200 nm, are injected into the investigated fluid to provide contrast, and the signal they emit upon one- or two-photon excitation (or their scattered radiation) is collected by a high-sensitivity CCD camera in the form of a temporal xyt-stack of two-dimensional images. Provided that the positions of the tracer particles are registered at a sufficiently high temporal resolution, the spatial cross-correlation of consecutive frames allows deriving the displacement of the tracer particles and, consequently, their flow velocity under the assumption of uniform drift. The cross-correlation analysis is usually performed on regions of interest (small enough so that the particle displacement in the region is uniform, but large enough to get sufficient statistics) and the results are output as a uniform grid of the two in-plane components of the velocity vector in the 2D measurement plane. For the extraction of the third component of the velocity vector, 3D extensions of the μ-PIV technique, relying on dual-plane acquisitions or on holographic recordings, have also been developed. Though PIV provides global velocity data within a 2D/3D domain, other important differentiable quantities, such as vorticity and strain rates, or integral quantities, such as circulation, streamlines or potential

lines, can also be post-calculated starting from the velocity fields.
Flexibility is the main advantage of μ-PIV, which allows the measurement of flow velocities in the wide range ∼ nm/s - m/s on regions from a few μm up to several mm in width [91], depending on the microscope objective magnification and on the temporal and spatial resolution of the CCD detection device. By contrast, care has to be taken in the exploitation of injected tracer particles, which should be non-corrosive, non-toxic and chemically inert. Moreover, as microfluidic devices (or the investigated micron-sized vessels) shrink, particles must also become smaller to avoid a significant flow distortion or even the channel obstruction; this affects the detected signal intensity, and could prevent the applicability of PIV (and particle tracking methods analyzing the same kind of experimental data) requiring sufficiently large and bright fluorescent particles.

Summarizing, a number of techniques exist for the measurement of blood flow velocities: they differ in the temporal and spatial resolution, in the spatial scale of the circulatory systems they can effectively address, and in the possibility of combining the speed measurement with the morphological imaging of the explored circulatory network. They also differ in the requirement of tracer particles or exogenous fluorescent markers, in the capability of recovering absolute speed values and in the sensitivity toward the planar and axial components of the velocity vector. Instead of anticipating here the advantages and disadvantages of the FLICS method proposed in the next Sections, I outline its basic principles and derive its theoretical framework. I will summarize the pros and cons of FLow Image Correlation Spectroscopy at the end of Chapter 4, once demonstrated its applicability to blood flow speed measurements in micron-sized vessels both *in-vitro* and *in-vivo*.

2.2 Principles of FLow Image Correlation Spectroscopy

FLow Image Correlation Spectroscopy (FLICS) [69] allows the measurement of flow velocities by exploiting a single xy-image acquired by detecting along a raster pattern, by a confocal or a two-photon excitation laser scanning microscope, the fluorescence signal emitted by bright, sparse flowing objects (for example, genetically modified red blood cells or injected fluorescent beads). Depending on the parameters selected for the image acquisition (the pixel size, the field of view and, most importantly, the scan frequency) and on the properties of the

flowing particles (their size, their diffusion coefficient and their flow velocity), these produce in the xy-image diagonal lines. The size and the diffusion coefficient of the imaged particles mainly assign the width of the diagonal lines; the field of view (the zoom factor), the relative speed of flow and scan and the angle subtended by the flow velocity vector with respect to the scan path regulate their slope.

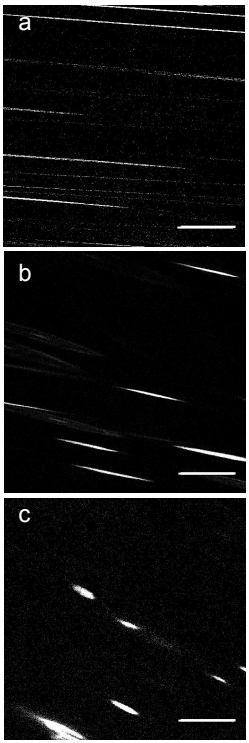

I begin by investigating the effect of the scan speed. I first consider particles flowing with uniform speed $|\underline{v}|$ along the scan direction; in the following, I assume the usual x-oriented raster scan path (as depicted in Fig. 2.6), and I refer to the line scan speed as $|\underline{v}|_{scan} = N\delta x/\tau_{line}$, where N, δx and τ_{line} are the number of pixels along the x-side of the image, the pixel size and the line scan time, respectively. If the adopted line scan speed is higher than the speed $|\underline{v}|$ of the flowing objects, by the time they take to travel the whole field of view the excitation laser beam scans them several times: the displacement of each particle along the flow x-direction during the scanning procedure results in the excitation and detection of the particle at slightly shifted positions, along the x-axis, between consecutive lines. As exemplified in Fig. 2.2, the particle is imaged therefore as a diagonal line, with the slope increasing and the length decreasing for an increasing scan speed. In the limiting case of a scan speed much higher than the flow speed $|\underline{v}|$ of the flowing objects ($|\underline{v}|_{scan} \gg |\underline{v}|$), each particle does not move appreciably during the time required by the excitation laser beam to scan it in its entirety: flowing objects approach (diffraction-limited or more extended, depending on their size) two-dimensional spots in the xy-image. While images acquired under the

Figure 2.2: *FLICS:* raster-scanned confocal xy-images acquired by detecting the signal of 1 μm fluorescent beads undergoing laminar flow in a square borosilicate capillary (inner section, 720 μm) along the x- scan direction. $|\underline{v}|$=160 $\mu m/s$ and $|\underline{v}|_{scan}$=6460 $\mu m/s$ in (a), 12920 $\mu m/s$ in (b) and 25830 $\mu m/s$ in (c) (τ_{line}=10, 5 and 2.5 ms in (a), (b) and (c), respectively); λ_{exc}=514 nm, detection bandwidth: 530-600 nm, δx=0.13 μm, scale bar=15 μm. Provided that the concentration of the flowing objects is sufficiently low to make individual particles discernible, if $|\underline{v}|_{scan} > |\underline{v}|$ each of them is imaged as a diagonal line.

condition $|\underline{v}|_{scan} \gg |\underline{v}|$, at high frame rate and in the form of a temporal stack, are conveniently analyzed by Spatio-Temporal Image Correlation Spectroscopy (STICS) [48] or Single Particle Tracking methods [98], a single xy-image raster-scanned with $|\underline{v}|_{scan} > |\underline{v}|$ provides the raw data for the FLICS analysis. I remark that the condition $|\underline{v}|_{scan} > |\underline{v}|$ required for the image acquisition is easily satisfied by live scanning the sample at decreasing τ_{line} until diagonal lines appear: hence the choice of a suitable scan speed is easily accomplished without any prior knowledge of the flow speed to be measured.

By now assuming that the condition $|\underline{v}|_{scan} > |\underline{v}|$ is satisfied, a significant role in regulating the slope of the diagonal lines produced in the xy-image by flowing particles is also played by the direction of the flow velocity vector relative to the scan path. I do not consider this effect in detail here, since it will be the object of an extensive investigation and of calibration measurements in the next Chapter. I just remark (Fig. 2.3) that the angle γ subtended by the velocity vector $|\underline{v}|$ with respect to the x-oriented scan path regulates the orientation of the diagonal lines produced by flowing objects in the reference Cartesian xy-frame.
Finally, Fig. 2.4 shows the effects of the size of the imaged field of view: for a given flow speed and a fixed scan frequency per line, a reduction of the field of view acts as a decrease of the scan speed, thereby reducing the slope of the diagonal lines.

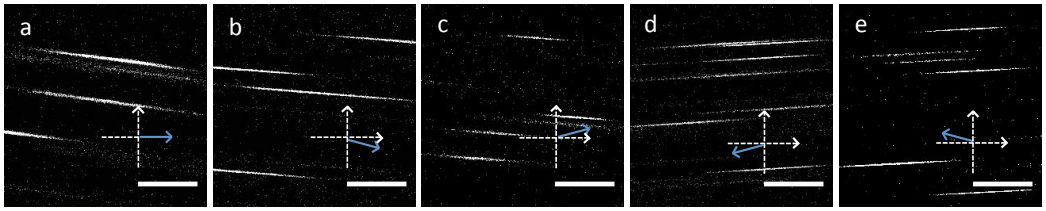

Figure 2.3: *FLICS:* raster-scanned confocal xy-images acquired by detecting the signal of 1 μm fluorescent beads undergoing laminar flow in a square borosilicate capillary (inner section, 720 μm). The angle γ between the flow velocity vector $|\underline{v}|$ and the scan path (pointing as the positive x-axis) was varied in the four quadrants of the Cartesian xy-plane. In (a), (b) and (c) $|\underline{v}|$ (in light blue) points in the positive x-direction: the diagonal lines due to the beads motion keep the same orientation irrespectively of the angle γ, which affects their length and slope. In (d) and (e) $|\underline{v}|$ points in the negative x-direction (i.e., opposite to the scan path) and the orientation of the diagonal lines is reversed. λ_{exc}=514 nm, detection bandwidth: 530-600 nm, $|\underline{v}|$=690 $\mu m/s$, τ_{line}=1 ms, δx=0.04 μm, scale bar=3 μm.

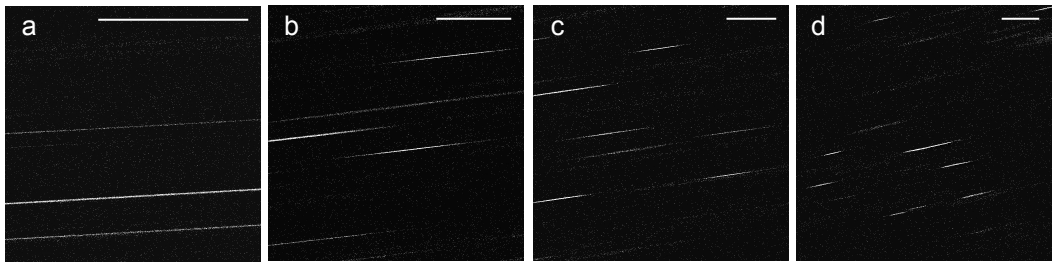

Figure 2.4: *FLICS:* raster-scanned confocal xy-images acquired by detecting the signal of 1 μm fluorescent beads undergoing laminar flow in a square borosilicate capillary (inner section, 720 μm). The imaged field of view has been varied from 25x25 μm^2 in (a) to 100x100 μm^2 in (d) (scale bar=15 μm in all the panels). λ_{exc}=514 nm, detection bandwidth: 530-600 nm, image format: 1024x1024, $|\underline{v}|$=410 $\mu m/s$ and τ_{line}=1 ms.

In summary, the slope of the streaks produced by optically resolved flowing objects in an xy-image raster-scanned with $|\underline{v}|_{scan} > |\underline{v}|$ is the result of a tight interplay between known instrumental acquisition parameters and the properties (namely, modulus $|\underline{v}|$ and direction γ) of the flow velocity vector. This suggests the possibility of exploiting the spatial and temporal information encoded in the image to recover the two unknowns, $|\underline{v}|$ and γ. To this aim, sharing the approach of other image correlation based methods like RICS and STICS, FLow Image Correlation Spectroscopy exploits the computation of the Cross-Correlation Function (CCF) between pairs of columns of the image (or of a selected region of interest where diagonal lines appear) (see Fig. 2.5). The CCF is defined as the normalized time-averaged product of the fluorescence intensity fluctuations detected in the pixels sampled at time t in a first column and at a delayed time $t + \tau$ in a second column: it allows to quantify the tame it takes, on average, for flowing objects to travel the distance between the selected columns and the consequent measurement of the (blood) flow speed under the assumption of uniform drift.

2.2.1 Derivation of the FLICS cross-correlation function

The definition and derivation of the FLICS cross-correlation function rely on the description of a raster-scanned xy-image as a matrix of $N_x x N_y$ pixels, each identified by a couple of integer indexes (x, y), with $x \in [0, N_x-1]$ and $y \in [0, N_y-1]$. Given a pixel residence time τ_{pixel} and a scan frequency per line $f_{line} = 1/\tau_{line}$, if

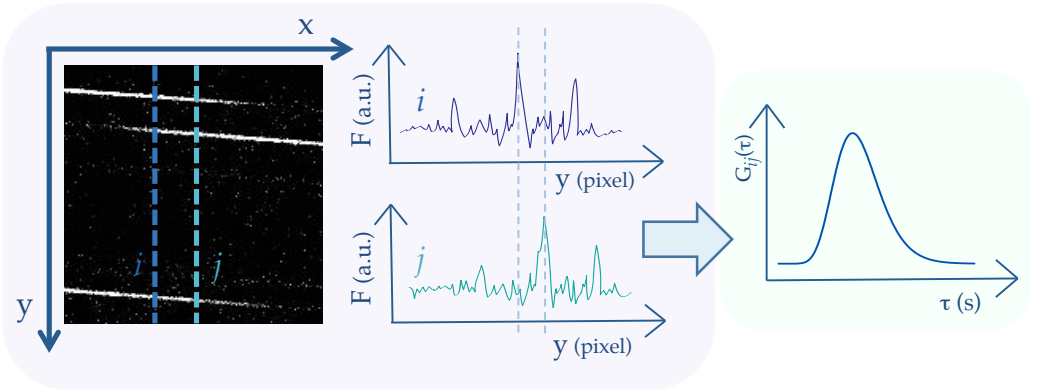

Figure 2.5: *FLICS principles.* The fluorescence intensity profile along each column of an xy-image raster scanned, in the presence of bright and sparse flowing objects, with $|\underline{v}|_{scan} > |\underline{v}|$ shows bright peaks superimposed on a low background, each peak corresponding to the detection of a particle in a specific spatial location (and a specific sampling time) of the image. If a particle is detected at time t in a given pixel of the i^{th} column, it will be detected, due to the flow, at a delayed time in a vertically-shifted pixel of the j^{th} column: the separation of the peaks produced by the same particle in the fluorescence intensity profiles extracted (as a function of the y-coordinate, or as a function of the sampling time) from two columns a distance $(j - i)$ apart is related therefore to the time required by the particle to travel the same distance. Quantitative information about this time-of-flight is recovered by FLow Image Correlation Spectroscopy by the computation of the cross-correlation function between columns i and j. The CCF computation can be visualized as the sliding of the plot of the fluorescence intensity of the first column (upper graph) over the plot of the fluorescence intensity of the second column (lower graph) and the multiplication of the two signals for increasing values of the time shift (or lag) τ: a peak is found in the CCF when τ approximately matches the time-of-flight (i.e., when overlapping peaks are multiplied), whereas the width of the CCF reflects the width of the diagonal lines (the width of the peaks in the fluorescence plots) produced by flowing particles. We expect therefore the peak and the width of the CCF to be related, respectively, to the flow speed and direction and to the size and diffusion coefficient of the imaged objects.

position $(0, 0)$ is sampled at time $t = 0$, then the pixel of coordinates (x, y) will be sampled at a delayed time $t = x\tau_{pixel} + y\tau_{line}$. Therefore, since each pixel can be univocally assigned to the time at which it is sampled and vice versa, for all the pixels of the same column (i.e., fixed x) I can express the fluorescence intensity as $F_x(y(t), t)$, using the variable time to discriminate the different pixels. Similarly,

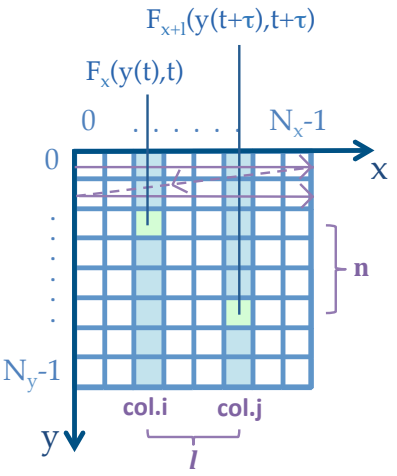

Figure 2.6: *FLICS: cross-correlation on a raster-scanned xy-image.* A raster-scanned 2D image is a matrix of $N_x x N_y$ pixels, representing a series of parallel intensity measurements from many adjacent confocal excitation volumes. The sketch highlights (in green) two arbitrary pixels a distance $n \approx \tau/\tau_{line}$ apart along the vertical direction, involved in the computation of the cross-correlation function $G_{ij}(\tau)$ between two columns (filled) $l \equiv (j - i)$ pixels apart. The raster scan path is partly sketched in violet: the excitation laser beam scans the specimen (and primes fluorescence emission) along the positively oriented fast-scan x-axis (continuous line); τ_{line} is the time required for a single line scan plus the retracing (dashed line).

I denote as $\delta F_x(y(t), t)$ the fluctuation of the detected intensity $F_x(y(t), t)$ relative to the signal averaged over the entire column. In this notation, the CCF of the fluorescence intensity fluctuations collected in two columns a fixed distance l apart is given by

$$G_{x,x+l}(\tau) = \frac{< \delta F^*_x(y(t), t)\delta F_{x+l}(y(t+\tau), t+\tau) >_t}{< F_x(y(t), t) >_t < F_{x+l}(y(t), t) >_t} \tag{2.1}$$

The subscripts x and $x + l$ identify the chosen columns and τ is the correlation lag time. If I call n the spatial lag along the vertical y-direction between the pixel sampled at time t in the first column and the pixel sampled at time $t + \tau$ in the second column, the lag time τ can be expressed as $\tau = l\tau_{pixel} + n\tau_{line}$. Since pixels are typically a few microseconds apart along the horizontal direction and a few millisecond apart along the vertical direction, especially for small column distances the relation $l\tau_{pixel} \ll n\tau_{line}$ generally holds, so that, by construction and definition of the CCF, the lag time is approximately an integer multiple of the inverse of the scan frequency per line ($n \approx \tau/\tau_{line}$). The brackets indicate the temporal (and, implicitly, spatial) averaging performed, for each lag time τ, by taking all the pairs of pixels belonging to the selected columns and at a distance $\sim \tau/\tau_{line}$ apart along the vertical y-direction.

In the following I employ a simplified, more compact notation for eq. (2.1), which

defines the cross-correlation function as

$$G_{ij}(\tau) = \frac{< \delta F_i^*(t)\delta F_j(t+\tau) >_t}{< F_i(t) >_t < F_j(t) >_t} \tag{2.2}$$

Integer subscripts i and j identify the chosen columns, a fixed distance $l \equiv (j-i)$ apart (I assume $j > i$ and $i \neq j$, since for $i = j$ an auto-correlation function is obtained; $i \in [0, N_x - 2]$ and $j \in [i+1, N_x - 1]$). $< F_i(t) >_t$ is the average fluorescence intensity computed over all the pixels in column i and $\delta F_i(t) = F_i(t) - < F_i(t) >_t$. Similar definitions apply to column j. This notation has the advantage of implying the spatial coordinates: i and j identify the position of the involved pixels along the horizontal direction, while, as previously noticed, time specifies the position of the pixels along the vertical y-direction of the image.

In order to derive the explicit expression of the FLICS cross-correlation function $G_{ij}(\tau)$, I consider a suspension of non-pointlike, identical fluorescent particles flowing (for example in a blood vessel, or inside a microfluidic device) with uniform velocity $|\underline{v}|$ while undergoing Brownian diffusion with diffusion coefficient D. I define the density of fluorophores on each particle as $\rho(\underline{u})$, with the vector $\underline{u}$ measured with respect to the center of the particle; $\int \rho(\underline{u}) d\underline{u}$ is therefore the total number of fluorophores the particle contains. If the center of the k^{th} particle is located at position $\underline{r}_k$ at time t, the emitted fluorescence intensity in $\underline{r}_k$ can be computed [99] as

$$F_k(\underline{r}_k, t) = \phi \iint d\underline{r} d\underline{u}\, \rho(\underline{u}) W(\underline{r} - \underline{u}) \delta(\underline{r} - \underline{r}_k) \tag{2.3}$$

The integrals extend over the whole space; for the sake of compactness, integration limits $-\infty$ and $+\infty$ will be omitted throughout the derivation. As in Chapter 1, ϕ is the product of the detection efficiency, of the fluorescence quantum yield and of the absorption cross-section of the molecules, $W(\underline{r} - \underline{u})$ is the spatial distribution of the excitation intensity and the Dirac delta expresses the fact that there can only be absorption at the location of the particle.
By rewriting $\rho(\underline{u})$ and $W(\underline{r} - \underline{u})$ in terms of their Fourier transforms[1] $\widehat{\rho}(\underline{q}')$ and

[1] As in chapter 1, I adopt the convention $\widehat{f}(\underline{q}) = (2\pi)^{-d/2} \int_{-\infty}^{+\infty} f(\underline{x}) e^{i\underline{q}\cdot\underline{x}}\, d\underline{x}$ for the Fourier transform definition in d-dimensions; $d = 3$ in the present derivation.

$\widehat{W}(\underline{q})$,

$$\begin{aligned} F_k(\underline{r}_k, t) &= \frac{\phi}{(2\pi)^3} \iint d\underline{r} d\underline{u} \int d\underline{q}' \widehat{\rho}(\underline{q}') e^{-i\underline{q}'\cdot\underline{u}} \int d\underline{q} \widehat{W}(\underline{q}) e^{-i\underline{q}\cdot(\underline{r}-\underline{u})} \delta(\underline{r}-\underline{r}_k) \\ &= \frac{\phi}{(2\pi)^3} \iint d\underline{q}' d\underline{q}\, \widehat{\rho}(\underline{q}') \widehat{W}(\underline{q}) e^{-i\underline{q}\cdot\underline{r}_k} \int d\underline{u}\, e^{i(\underline{q}-\underline{q}')\cdot\underline{u}} \\ &= \frac{\phi}{(2\pi)^3} \int d\underline{q}\, \widehat{\rho}(\underline{q}) \widehat{W}(\underline{q}) e^{-i\underline{q}\cdot\underline{r}_k} \end{aligned} \tag{2.4}$$

The total fluorescence for $\mathbb{N}$ particles in the excitation volume is $F(t) = \sum_{k=1}^{\mathbb{N}} F_k(\underline{r}_k, t)$. By now introducing the local number concentration at time t as $C(\underline{r}-\underline{u}, t) = \sum_{k=1}^{\mathbb{N}} \delta((\underline{r}-\underline{u}) - \underline{r}_k)$ [99] and its Fourier transform $\widehat{C}(\underline{q}, t) = (2\pi)^{-3/2} \sum_{k=1}^{\mathbb{N}} e^{i\underline{q}\cdot\underline{r}_k}$, I can rewrite the fluorescence intensity as

$$F(t) = \frac{\phi}{(2\pi)^{3/2}} \int d\underline{q}\, \widehat{\rho}(\underline{q}) \widehat{W}(\underline{q}) \widehat{C}^*(\underline{q}, t) \tag{2.5}$$

Correspondingly, in terms of the concentration fluctuations $\delta\widehat{C}(\underline{q}, t) = \widehat{C}(\underline{q}, t) - <\widehat{C}(\underline{q}, t)>_t$ and in the absence of fluctuations affecting the ϕ term, $\delta F(t)$ is given by

$$\delta F(t) = \frac{\phi}{(2\pi)^{3/2}} \int d\underline{q}\, \widehat{\rho}(\underline{q}) \widehat{W}(\underline{q}) \delta\widehat{C}^*(\underline{q}, t) \tag{2.6}$$

I can now compute the cross-correlation function $G_{ij}(\tau)$ by substituting into eq. (2.2) the complex conjugate of the fluctuations $\delta F_i(t)$ in column i at time t and the fluctuations $\delta F_j(t+\tau)$ evaluated in the pixels of column j at a delayed time $t+\tau$, and then performing a temporal average. This leads to

$$G_{ij}(\tau) \propto \iint d\underline{q}_i d\underline{q}_j\, \widehat{\rho}^*(\underline{q}_i) \widehat{W}^*(\underline{q}_i) \Big|_t \widehat{\rho}(\underline{q}_j) \widehat{W}(\underline{q}_j) \Big|_{t+\tau} < \delta\widehat{C}(\underline{q}_i, t) \delta\widehat{C}^*(\underline{q}_j, t+\tau) >_t \tag{2.7}$$

The proportionality symbol includes the constant $\phi/(2\pi)^3$ and the normalization factor $< F_i(t) >_t < F_j(t) >_t$, which can be neglected unless particle concentrations must be recovered from the cross-correlation amplitude.
The concentration correlation term can be computed through the Fick's equation: as reported in Chapter 1, if fluorescent particles undergo both flow and diffusive motion, with a translational isotropic diffusion coefficient D and a flow velocity $|\underline{v}|$,

the temporal derivative of the concentration fluctuations satisfies

$$\begin{cases} \frac{\partial}{\partial t}\delta C(\underline{r}-\underline{u},t) = D\nabla^2\delta C(\underline{r}-\underline{u},t) - \underline{v}\cdot\underline{\nabla}\delta C(\underline{r}-\underline{u},t) \\ \frac{\partial}{\partial t}\delta\widehat{C}(\underline{q},t) = -D|\underline{q}|^2\delta\widehat{C}(\underline{q},t) + i\underline{q}\cdot\underline{v}\delta\widehat{C}(\underline{q},t) \end{cases} \tag{2.8}$$

This leads to

$$\delta\widehat{C}(\underline{q},t) = \delta\widehat{C}(\underline{q},0)e^{-D|\underline{q}|^2t+i\underline{q}\cdot\underline{v}t} \tag{2.9}$$

yielding in turn

$$\begin{aligned} <\delta\widehat{C}(\underline{q}_i,t)\delta\widehat{C}^*(\underline{q}_j,t+\tau)>_t &= <\delta\widehat{C}(\underline{q}_i,0)\delta\widehat{C}^*(\underline{q}_j,\tau)> \\ &= <\delta\widehat{C}(\underline{q}_i,0)\delta\widehat{C}^*(\underline{q}_j,0)> e^{-D|\underline{q}_j|^2\tau-i\underline{q}_j\cdot\underline{v}\tau} \\ &= <C>\delta(\underline{q}_i-\underline{q}_j)e^{-D|\underline{q}_j|^2\tau-i\underline{q}_j\cdot\underline{v}\tau} \end{aligned} \tag{2.10}$$

$<C>$ stands here for the mean square fluctuations of $\widehat{C}(\underline{q}_i,0)$, being equal to its average for Poisson statistics. By substituting eq. (2.10) into eq. (2.7) I get

$$G_{ij}(\tau) \propto \iint d\underline{q}_i d\underline{q}_j\, \widehat{\rho}^*(\underline{q}_i)\widehat{W}^*(\underline{q}_i)\Big|_t \widehat{\rho}(\underline{q}_j)\widehat{W}(\underline{q}_j)\Big|_{t+\tau} \delta(\underline{q}_i-\underline{q}_j)e^{-D|\underline{q}_j|^2\tau-i\underline{q}_j\cdot\underline{v}\tau} \tag{2.11}$$

Eq. (2.11) requires the explicit functional form of the Fourier transforms of both the fluorophore density and the beam profile. I model the fluorophore density on a each particle with a Gaussian function

$$\rho(\underline{u}) = exp\left(-\frac{4|\underline{u}|^2}{a^2}\right) \tag{2.12}$$

so that the coefficient a, related to the width of the Gaussian factor (for $|\underline{u}| = a$, ρ drops to $1/e^4 \sim 2\%$ of the peak value), provides an estimate of the radius of the particles. It is mandatory to account for the size of the investigated particles when they are comparable to or larger than the excitation Point-Spread-Function (PSF), since the point-like approximation generally adopted by the FCS theory (see Chapter 1) is in this case no longer valid; with respect to the more complex expressions proposed in the literature [99] for the form factor, the Gaussian approximation of eq. (2.12) has the advantage of allowing an analytical derivation of the CCF while accounting for the finite extent of the investigated particles.

For the PSF, a 3D Gaussian is assumed for $\flat$ ($\flat$=1,2)-photon excitation, with $1/e^2$ radii ω_0 and ω_{0z} assigned by the waists of the laser beam along the radial and axial directions, respectively. Recalling that, by definition, $G_{ij}(\tau)$ is computed at each lag time τ by multiplying the fluorescence intensity fluctuations detected in separate spatial locations of the image, I introduce a time-dependent vector $\underline{R}$ - which will be considered explicitly in the following for the specific case of a raster pattern - accounting for the separation between the excitation volumes sampled at each pair of time points t and $t+\tau$; hence I adopt a formalism similar to the one exploited for the derivation of the cross-correlation function in dual-beam FCCS.

$$W(\underline{u},t) = exp\left\{ -\frac{2\flat}{\omega_o^2}\left[(u_x - R_x(t))^2 + (u_y - R_y(t))^2\right] - \frac{2\flat}{\omega_{oz}^2}\left[(u_z - R_z(t))^2\right] \right\} \quad (2.13)$$

Provided the expressions for the fluorophore density and for the beam profile (eqs. 2.12 and 2.13), the substitution of their Fourier transforms into eq. (2.11) leads to

$$\begin{aligned} G_{ij}(\tau) \propto & \int dq_{jx} exp\left\{ -q_{jx}^2\left(D\tau + \frac{a^2}{8} + \frac{\omega_0^2}{4\flat}\right)\right\} exp\left\{ -iq_{jx}(R_x(t) - R_x(t+\tau) + v_x\tau)\right\} \cdot \\ & \cdot \int dq_{jy} exp\left\{ -q_{jy}^2\left(D\tau + \frac{a^2}{8} + \frac{\omega_0^2}{4\flat}\right)\right\} exp\left\{ -iq_{jy}(R_y(t) - R_y(t+\tau) + v_y\tau)\right\} \cdot \\ & \cdot \int dq_{jz} exp\left\{ -q_{jz}^2\left(D\tau + \frac{a^2}{8} + \frac{\omega_{0z}^2}{4\flat}\right)\right\} exp\left\{ -iq_{jz}(R_z(t) - R_z(t+\tau) + v_z\tau)\right\} \end{aligned} \quad (2.14)$$

The Gaussian integrals in the x-, y- and z-dimensions can be solved into

$$G_{ij}(\tau) \propto \frac{1}{\left(4\flat D\tau + \frac{a^2\flat}{2} + \omega_0^2\right)} \frac{1}{\sqrt{4\flat D\tau + \frac{a^2\flat}{2} + \omega_{0z}^2}} exp\left\{ -\frac{|\underline{R}(t+\tau) - \underline{R}(t) - \underline{v}\tau|^2}{4\flat D\tau + \frac{a^2\flat}{2} + \widetilde{\omega}^2} \right\} \quad (2.15)$$

where $\widetilde{\omega}^2$ has been introduced in the last term for the sake of compactness, denoting ω_0^2 in the x- and y-directions and ω_{0z}^2 when considering the axial z-direction.
In the specific case of a raster scan, the vector $\underline{R}$ lies in the image plane (the xy-plane, in my notation) $\forall t$: hence $R_z(t) = 0$ and $R_z(t+\tau) = 0$. This simplifies the z-component of the last term in eq. (2.15) to $exp\{-v_z^2\tau^2/(4\flat D\tau + a^2\flat/2 + \omega_{0z}^2)\}$. Moreover, since the vector $\underline{R}$ lies in column i at time t and in column j at time $t+\tau$, I express as (i,m) and $(j,(m+n))$ the x- and y- coordinates of the pixels

the vector identifies at times t and $t+\tau$ ($n \in [N_y - 1]$ and $m \in [0, N_y - 1 - n]$); therefore, $\underline{R}(t) = (i\delta x, m\delta x, 0)$ and $\underline{R}(t+\tau) = (j\delta x, (m+n)\delta x, 0)$, where δx is the pixel size, assumed equal along the horizontal and vertical direction of the image. Since the CCF only depends on the difference $\underline{R}(t+\tau)$-$\underline{R}(t)$ (i.e., it only depends on the distance between the excitation volumes, not on their individual coordinates in the xy-plane), no explicit dependence remains on the m coordinate; by contrast n, acting as the spatial lag between the y-components of $\underline{R}(t)$ and $\underline{R}(t+\tau)$, appears explicitly in $G_{ij}(\tau)$ in the form of the ratio $n \approx \tau/\tau_{line}$ previously discussed.
By substituting $\underline{R}(t+\tau)$-$\underline{R}(t)$ into the CCF (eq. 2.15), I finally obtain

$$G_{ij}(\tau) \propto \frac{1}{\left(4\flat D\tau + \frac{a^2\flat}{2} + \omega_0^2\right)} \frac{1}{\sqrt{4\flat D\tau + \frac{a^2\flat}{2} + \omega_{0z}^2}} \cdot \\ \cdot \exp\left\{-\frac{[(j-i)\delta x - v_x\tau]^2}{4\flat D\tau + \frac{a^2\flat}{2} + \omega_0^2}\right\} \exp\left\{-\frac{\left[\frac{\delta x}{\tau_{line}} - v_y\right]^2\tau^2}{4\flat D\tau + \frac{a^2\flat}{2} + \omega_0^2}\right\} \exp\left\{-\frac{v_z^2\tau^2}{4\flat D\tau + \frac{a^2\flat}{2} + \omega_{0z}^2}\right\} \tag{2.16}$$

The expression of the cross-correlation function can be simplified when focusing on applications of the FLICS method to circulatory systems with an approximately planar structure, where the velocity vector $\underline{v}$ practically lies in the same xy-plane sampled by the excitation laser beam. Both in the calibration measurements I have performed in Zebrafish embryos (Chapter 3) and in the investigation of the murine hepatic microcirculation (Chapter 4), the geometry of the imaged system allowed to discard the z-component $v_z \approx 0$ of the velocity vector. Therefore, if I further call α the angle that the planar flow velocity vector subtends with the horizontal x-axis (as depicted in Fig. 2.7a,b), the CCF simplifies to

$$G_{ij}(\tau) \propto \frac{1}{\left(4\flat D\tau + \frac{a^2\flat}{2} + \omega_0^2\right)} \frac{1}{\sqrt{4\flat D\tau + \frac{a^2\flat}{2} + \omega_{0z}^2}} \cdot \\ \cdot \exp\left\{-\frac{[(j-i)\delta x - |v|\cos(\alpha)\tau]^2}{4\flat D\tau + \frac{a^2\flat}{2} + \omega_0^2}\right\} \exp\left\{-\frac{\left[\frac{\delta x}{\tau_{line}} - |v|\sin(\alpha)\right]^2\tau^2}{4\flat D\tau + \frac{a^2\flat}{2} + \omega_0^2}\right\} \tag{2.17}$$

The angle α is positive and comprised in the range $[0°; 90°]$ when the velocity vector $\underline{v}$ points in the direction of positive x- and y-axes (the downward direction as depicted in Fig. 2.7, panel a), while it is negative in the range $[-90°; 0°]$ when $\underline{v}$

points upward with positive x-component and negative y-component (Fig. 2.7, panel b).

2.2.2 Back cross-correlation

In the derivation of eqs. (2.1) - (2.17) a vector $\underline{v}$ pointing along the positive x-direction has been assumed. For a flow velocity directed along the negative x-axis, the cross-correlation function should be computed as

$$G_{ji}(\tau) = \frac{< \delta F_j^*(t)\delta F_i(t+\tau) >_t}{< F_i(t) >_t < F_j(t) >_t} \tag{2.18}$$

The fluorescence fluctuations are evaluated in column i at time $t+\tau$ and in column j at time t: hence the derivation of the CCF remains unchanged except for the components of the vector $\underline{R}$, that I define as $\underline{R}(t) = (j\delta x, m\delta x, 0)$ and $\underline{R}(t+\tau) = (i\delta x, (m+n)\delta x, 0)$. This leads to

$$|\underline{R}(t+\tau) - \underline{R}(t) - \underline{v}\tau|^2 = (-(j-i)\delta x - |\underline{v}|\cos(\alpha)\tau)^2 + (n\delta x - |\underline{v}|\sin(\alpha)\tau)^2 \tag{2.19}$$

$\alpha \in [90°; 180°]$ in the Cartesian quadrant with $(x < 0, y > 0)$, while $\alpha \in [-180°; -90°]$ in the Cartesian quadrant with $(x < 0, y < 0)$ (Fig. 2.7, panels c,d). By the substitution $\beta \equiv (180° - \alpha)$ I can rewrite the squared modulus as

$$|\underline{R}(t+\tau) - \underline{R}(t) - \underline{v}\tau|^2 = ((j-i)\delta x - |\underline{v}|\cos(\beta)\tau)^2 + (n\delta x - |\underline{v}|\sin(\beta)\tau)^2 \tag{2.20}$$

exactly as it appears in eq. (2.16). Therefore, this notation has the advantage of making the analytical expressions of the back ($G_{ji}(\tau)$) and forth ($G_{ij}(\tau)$) cross-correlation functions equal. Globally, provided the experimental forth cross-correlation for a positive v_x and the back cross-correlation for a negative v_x, I employ for data fitting

$$\begin{aligned} G(\tau) \propto & \frac{1}{\left(4b D\tau + \frac{a^2 b}{2} + \omega_0^2\right)} \frac{1}{\sqrt{4b D\tau + \frac{a^2 b}{2} + \omega_{0z}^2}} \cdot \\ & \cdot \exp\left\{-\frac{[(j-i)\delta x - |v|\cos(\gamma)\tau]^2}{4b D\tau + \frac{a^2 b}{2} + \omega_0^2}\right\} \exp\left\{-\frac{\left[\frac{\delta x}{\tau_{line}} - |v|\sin(\gamma)\right]^2 \tau^2}{4b D\tau + \frac{a^2 b}{2} + \omega_0^2}\right\} \end{aligned} \tag{2.21}$$

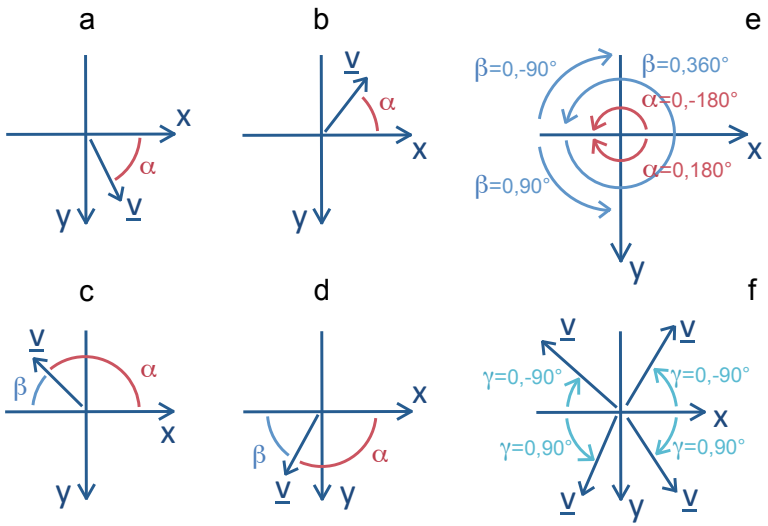

Figure 2.7: *FLICS: definition of the angles employed for the derivation of the cross-correlation function.* (a),(b): representation of the angle α that the positively x-oriented planar vector $\underline{v}$ subtends with the horizontal x-axis. (c),(d): representation of the angles α and β that the negatively x-oriented vector $\underline{v}$ subtends with the x-axis; β is introduced for the derivation of the back cross-correlation as described in the text. (e): definition of the possible range of values for the angles α and β in the four quadrants of the Cartesian xy-plane; each interval is spanned in the direction of the arrow. (f): definition of the angle γ employed to describe all the possible orientations of the vector $\underline{v}$ relative to the x-axis. The range of its possible values and four arbitrarily-directed vectors for the flow velocity are shown.

where

$$\gamma \in \begin{cases} [0°; 90°], & \text{if } x \gtrless 0,\ y > 0 \\ [-90°; 0°], & \text{if } x \gtrless 0,\ y < 0 \end{cases} \tag{2.22}$$

Eq. (2.21) concludes the derivation of the FLICS correlation function. It evidences that the CCF is a peaked function that explicitly accounts for all the parameters, described previously, affecting the width, length and slope of the diagonal lines produced by flowing and diffusing objects in the raster-scanned xy-image. The size a of the imaged particles and their diffusion coefficient D, regulating the width of the diagonal lines, contribute to the width of the CCF: they appear in the nearly hyperbolic term ($\sim (4bD\tau + a^2b/2 + \omega_0^2)^{3/2}$) and in the variance

of the quasi-Gaussian factors. By contrast, both the modulus and the direction of the flow velocity vector, the scan speed (the line scan time τ_{line}) and the column distance $(j - i)$, appearing in the numerator of the quasi-Gaussian terms, mainly affect the position, along the lag time axis, of the cross-correlation peak: this is coherent with the fact that the same parameters are those strongly impacting the slope of the diagonal streaks in the image.
Before analytically deriving the functional dependence of both the peak time and the peak amplitude on the flow velocity and on the diffusion coefficient, as well as on the image acquisition parameters, I exploit simulated cross-correlation functions to inspect the effect of $|\underline{v}|$, γ, τ_{line}, $(j - i)$ and D on the CCF overall shape.

2.3 Simulated FLICS cross-correlation functions

Cross-correlation functions simulated according to eq. (2.21) are reported in Fig. 2.8. When all the parameters apart from the flow speed $|\underline{v}|$ are fixed, the effect of an increasing flow speed is to shift the CCF peak toward shorter lag times. In fact as I previously mentioned, the peak time - hereafter referred to as τ_{max}- is directly related to the time it takes on average for flowing objects to travel the distance between the columns selected for the CCF derivation. For the same reason, an opposite shift of the peak time τ_{max} toward longer lag times is found when the column distance is increased.
As $|\underline{v}|$ increases and τ_{max} decreases, a higher scan frequency is required for an accurate sampling of the CCF peak: beside affecting the peak position along the τ-axis, the scan frequency determines the temporal resolution with which the experimental CCF can be recovered (the lag time τ being approximately an integer multiple of the inverse of the scan frequency per line). Furthermore, the adopted f_{line} assigns the range of accessible flow speeds, as will be investigated once derived the τ_{max} functional form (Section 2.7).
τ_{max} is also significantly affected by the angle γ between the flow velocity vector and the scan path. The diagonal lines produced in the xy-image by particles flowing along the scan direction (γ=0°) turn into horizontal lines when the flow direction is orthogonal to the scan path (γ=90°): correspondingly, the CCF peak time decreases as γ increases, and tends to zero as $\gamma \to 90°$.
Finally, the diffusion coefficient D regulates the width of the CCF but barely affects the peak time. This suggests the specific, fast data analysis procedure described in the next Section.

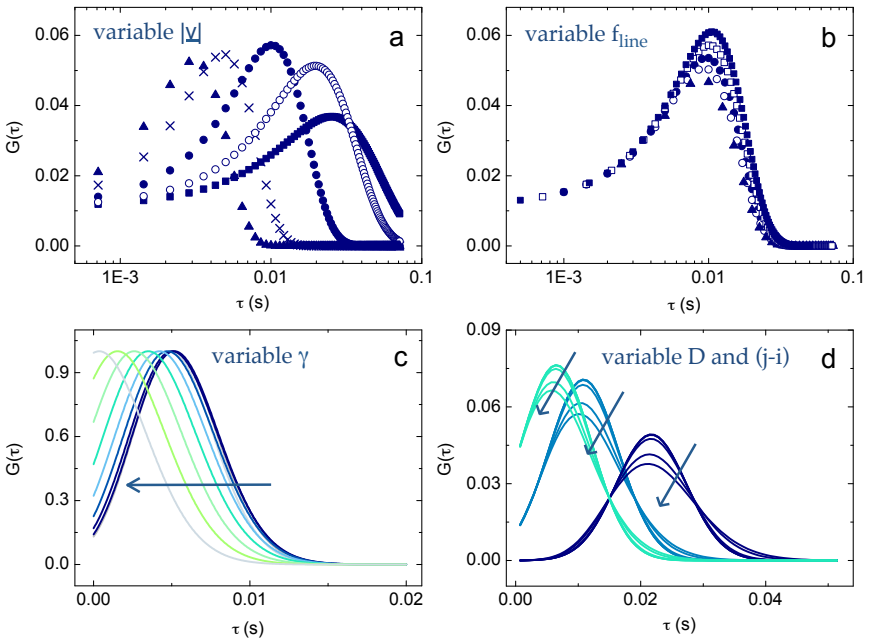

Figure 2.8: *Simulated FLICS cross-correlation functions.* (a): CCFs simulated according to eq. (2.21) for flow speed values $|\underline{v}|$=1500, 1000, 500, 250 and 150 $\mu m/s$ (filled triangles, crosses, filled circles, open circles, filled squares, respectively), with γ=30°, f_{line}=1400 Hz and $(j-i)\delta x$=5 μm. (b): CCFs simulated according to eq. (2.21) for a scan frequency f_{line}=2000, 1400, 1000, 700, 400 Hz (filled squares, open squares, filled circles, open circles, filled triangles, respectively); $|\underline{v}|$=500 $\mu m/s$, γ=30°, $(j-i)\delta x$=5 μm. (c): CCFs simulated according to eq. (2.21) for γ in the range $[0°, 90°]$ (increasing in the direction of the arrow) with $|\underline{v}|$=1000 $\mu m/s$, f_{line}=1400 Hz and $(j-i)\delta x$=5 μm; CCFs have been normalized to the range $[0, 1]$ to highlight the effect of the angle γ on the correlation peak time. (d): CCFs simulated according to eq. (2.21) for $(j-i)\delta x$=3 μm (turquoise), 5 μm (light blue) and 10 μm (blue); $|\underline{v}|$=500 $\mu m/s$, f_{line}=1400 Hz, γ=30° and D=0.01, 0.1, 1, 10, 50, 80 $\mu m^2/s$ (D increases in the direction of the arrows). The following parameters have been kept at fixed values through all the simulations: ω_0=0.2 μm, ω_{0z}=0.5 μm, δx=0.1 μm, a=5 μm, s=1 and, except for panel (d), D=80 $\mu m^2/s$; speed values, scan frequencies and column distances have been selected close to the ones adopted for, or recovered in, the experimental data of Chapters 3 and 4.

2.4 FLICS procedures for data analysis

Operatively, provided that the image acquisition parameters are set so that flowing objects produce diagonal lines in the raster-scanned image, the non-linear least squares fit to eq. (2.21) of experimental CCFs allows the measurement of the flow velocity. Once a column distance $(j-i)$ has been selected, all the pairs of columns in the image a distance $(j-i)$ apart can be exploited: a total of $(N_x-(j-i))$ CCFs can therefore be computed and averaged, improving the statistics with which the single average function is recovered. As a rule of thumb, the column distance is chosen so that the correlation peak is sampled with a minimum of ~ 10 data points. The statistics is further improved when CCFs are derived for multiple column distances: in this case, a global fit to eq. (2.21) of the set of experimental CCFs is performed. The flow speed $|\underline{v}|$ and the properties of the flowing objects (a and D) are always kept as free parameters in the fitting procedure, whereas the optical and scan parameters (ω_0, ω_{0z}, $(j-i)$, δx, τ_{line}) are treated as known quantities. The angle γ can either be recovered as a best-fit parameter (as will be shown by calibration measurements in Chapter 3), or it can be fixed and treated as known: the orientation of the investigated vessel with respect to the x-axis in the image allows measuring the absolute value of the angle (assuming that fluorophores flow in a direction parallel to the vessel wall, as in our case), whereas its sign is provided by the orientation of the diagonal streaks left by flowing objects in the image (see Fig. 2.3).

A second possible procedure to recover the flow speed is suggested by the simulations reported in Fig. 2.8: panels a and d highlight that, while being practically unaffected by the diffusive properties of the imaged particles, the correlation peak time τ_{max} is strongly regulated by the modulus of the flow velocity. The peak time alone can therefore be exploited to recover $|\underline{v}|$, making the (global) fit of experimental CCFs unnecessary and allowing a straightforward and much faster determination of the flow speed. All that is required is the functional form of τ_{max} in terms of $|\underline{v}|$ and of the image acquisition parameters: then by substituting to τ_{max} the experimentally measured peak lag time and by solving for $|\underline{v}|$, the estimate of the flow speed is obtained. This procedure is repeated for each of the column distances $(j-i)$ used in the CCFs derivation to yield a weighted average of the resulting $|\underline{v}|$ values.

Both the data-analysis procedures, outlined for an xy-image encompassing a single vessel, can in principle be applied to a raster-scanned image acquired on a branched region of the investigated circulatory network. In this case, since FLICS

does not require a scan path parallel to the flow direction (see Fig. 2.8c), the analysis can be performed on separate ROIs centered on in-focus vessels. Anticipated here, the ROI-based FLICS analysis will be exploited in Chapters 3 and 4.

2.5 Cross-correlation peak time

In order to derive the analytical expression for the lag time τ_{max} associated to the maximum of the cross-correlation function, it is convenient to rewrite eq. (2.21) as

$$G(\tau) \propto \frac{1}{A_1(\tau)} \frac{1}{A_2(\tau)} exp\left\{-\frac{[B(\tau)]^2}{A_1(\tau)}\right\} exp\left\{-\frac{C_1\tau^2}{A_1(\tau)}\right\} \tag{2.23}$$

where $A_1(\tau)$, $A_2(\tau)$, $B(\tau)$ and the constant C_1 are defined as follows:

$$\begin{cases} A_1(\tau) \equiv 4\flat D\tau + C_2 \\ A_2(\tau) \equiv \sqrt{4\flat D\tau + C_3} \\ B(\tau) \equiv [(j-i)\delta x - v_x\tau] \end{cases} \qquad \begin{cases} C_1 \equiv \left(\frac{\delta x}{\tau_{line}} - v_y\right)^2 \\ C_2 \equiv \omega_0^2 + \frac{a^2\flat}{2} \\ C_3 \equiv \omega_{0z}^2 + \frac{a^2\flat}{2} \end{cases} \tag{2.24}$$

The computation of the partial derivative of the CCF with respect to the lag time leads to

$$\frac{\partial G(\tau)}{\partial \tau} = \left\{-\frac{4\flat D}{A_1(\tau)} - \frac{2\flat D}{[A_2(\tau)]^2} - \frac{2C_1\tau}{A_1(\tau)} + \frac{2B(\tau)v_x}{A_1(\tau)} + \frac{4\flat DC_1\tau^2}{[A_1(\tau)]^2} + \frac{4\flat D[B(\tau)]^2}{[A_1(\tau)]^2}\right\} \cdot$$

$$\cdot \frac{1}{A_1(\tau)A_2(\tau)} exp\left\{-\frac{[B(\tau)]^2}{A_1(\tau)} - \frac{C_1\tau^2}{A_1(\tau)}\right\} \tag{2.25}$$

By now requiring that $\frac{\partial G}{\partial \tau}\big|_{\tau=\tau_{max}} = 0$, I obtain a third order equation that can be solved for τ_{max}:

$$\mathbb{A}_3\tau_{max}^3 + \mathbb{A}_2\tau_{max}^2 + \mathbb{A}_1\tau_{max} + \mathbb{A}_0 = 0 \tag{2.26}$$

where the $\mathbb{A}_{i=0...3}$ terms are given by

$$\begin{cases} \mathbb{A}_3 = -8b^2D^2(v_x^2 + C_1) \\ \mathbb{A}_2 = -48b^3D^3 - 2bD[v_x^2(2C_2 + C_3) + C_1(C_3 + 2C_2)] \\ \mathbb{A}_1 = -8b^2D^2(C_3 + 2C_2) - C_2C_3(v_x^2 + C_1) + 4bD\delta x(j-i)[v_xC_2 + 2bD\delta x(j-i)] \\ \mathbb{A}_0 = -bDC_2(C_2 + 2C_3) + C_3\delta x(j-i)[v_xC_2 + 2bD\delta x(j-i)] \end{cases} \tag{2.27}$$

Eq. (2.26) can be solved by the substitution $\tau_{max} = t - \frac{\mathbb{A}_2}{3\mathbb{A}_3}$, which leads to the following third order equation for the auxiliary variable t:

$$t^3 + \mathbb{B}t + \mathbb{C} = 0 \text{ , with } \begin{cases} \mathbb{B} = \dfrac{\mathbb{A}_1}{\mathbb{A}_3} - \dfrac{\mathbb{A}_2^2}{3\mathbb{A}_3^2} \\ \mathbb{C} = \dfrac{\mathbb{A}_0}{\mathbb{A}_3} - \dfrac{\mathbb{A}_1\mathbb{A}_2}{3\mathbb{A}_3^2} + \dfrac{2\mathbb{A}_2^3}{27\mathbb{A}_3^3} \end{cases} \tag{2.28}$$

The three solutions $t_{1,2,3}$ for t in the complex field are found by computing

$$t_{i=1...9} = \sqrt[3]{-\frac{\mathbb{C}}{2} + \sqrt{\frac{\mathbb{C}^2}{4} + \frac{\mathbb{B}^3}{27}}} + \sqrt[3]{-\frac{\mathbb{C}}{2} - \sqrt{\frac{\mathbb{C}^2}{4} + \frac{\mathbb{B}^3}{27}}} \tag{2.29}$$

and by selecting, among these nine values (a real number has one real cube root and two complex conjugate cube roots, so that nine combinations are possible in eq. 2.29), the three $t_{1,2,3}$ that satisfy

$$\sqrt[3]{-\frac{\mathbb{C}}{2} + \sqrt{\frac{\mathbb{C}^2}{4} + \frac{\mathbb{B}^3}{27}}} \cdot \sqrt[3]{-\frac{\mathbb{C}}{2} - \sqrt{\frac{\mathbb{C}^2}{4} + \frac{\mathbb{B}^3}{27}}} = -\frac{\mathbb{B}}{3} \tag{2.30}$$

In other words, $t_{1,2,3}$ are identified by selecting, and summing, the only three pairs of cube roots leading to a real number $(-\mathbb{B}/3)$ when multiplied.

Only one of the solutions $t_{1,2,3}$ is real if $\dfrac{\mathbb{C}^2}{4} + \dfrac{\mathbb{B}^3}{27}$ is positive, and it is found by adding in eq. (2.29) the only two real cube roots. I focus on the case $\dfrac{\mathbb{C}^2}{4} + \dfrac{\mathbb{B}^3}{27} < 0$, since this is the condition that $\mathbb{B}$ and $\mathbb{C}$ satisfy when computed from the typical

parameters I employed for the data acquisition and the CCFs derivation. In this case,

$$-\frac{\mathbb{C}}{2} \pm \sqrt{\frac{\mathbb{C}^2}{4} + \frac{\mathbb{B}^3}{27}} = -\frac{\mathbb{C}}{2} \pm i\sqrt{-\left(\frac{\mathbb{C}^2}{4} + \frac{\mathbb{B}^3}{27}\right)} = \rho e^{\pm i\theta} \tag{2.31}$$

with $\rho = \sqrt{-\frac{\mathbb{B}^3}{27}}$ and

$$\theta = \begin{cases} \arctan\left(\frac{\sqrt{-(\frac{\mathbb{C}^2}{4} + \frac{\mathbb{B}^3}{27})}}{-\frac{\mathbb{C}}{2}}\right) & \text{if } -\frac{\mathbb{C}}{2} > 0 \\ \arctan\left(\frac{\sqrt{-(\frac{\mathbb{C}^2}{4} + \frac{\mathbb{B}^3}{27})}}{-\frac{\mathbb{C}}{2}}\right) + \pi & \text{if } -\frac{\mathbb{C}}{2} < 0 \end{cases} \tag{2.32}$$

By substituting eqs. (2.31)-(2.32) into eq. (2.29) and by selecting the three solutions that satisfy eq. (2.30), I obtain

$$t_1 = 2\sqrt{-\frac{\mathbb{B}}{3}}\cos\frac{\theta}{3}, \quad t_2 = 2\sqrt{-\frac{\mathbb{B}}{3}}\cos\frac{\theta + 2\pi}{3}, \quad t_3 = 2\sqrt{-\frac{\mathbb{B}}{3}}\cos\frac{\theta + 4\pi}{3} \tag{2.33}$$

Eq. (2.33) provides three real solutions for the variable t and leads to the solutions $\tau_{max\,1,2,3}$ for the CCF peak time by subtracting $\mathbb{A}_2/(3\mathbb{A}_3)$. For my typical values, $\tau_{max\,2}$ and $\tau_{max\,3}$ are negative, allowing to univocally determine the peak time $\tau_{max} \equiv \tau_{max\,1}$:

$$\tau_{max} = \begin{cases} -\frac{\mathbb{A}_2}{3\mathbb{A}_3} + 2\sqrt{-\frac{\left(\frac{\mathbb{A}_1}{\mathbb{A}_3} - \frac{\mathbb{A}_2^2}{3\mathbb{A}_3^2}\right)}{3}}\cos\frac{\arctan\left(\frac{\sqrt{-(\frac{\mathbb{C}^2}{4} + \frac{\mathbb{B}^3}{27})}}{-\frac{\mathbb{C}}{2}}\right)}{3} & \text{if } -\frac{\mathbb{C}}{2} > 0 \\ -\frac{\mathbb{A}_2}{3\mathbb{A}_3} + 2\sqrt{-\frac{\left(\frac{\mathbb{A}_1}{\mathbb{A}_3} - \frac{\mathbb{A}_2^2}{3\mathbb{A}_3^2}\right)}{3}}\cos\frac{\arctan\left(\frac{\sqrt{-(\frac{\mathbb{C}^2}{4} + \frac{\mathbb{B}^3}{27})}}{-\frac{\mathbb{C}}{2}}\right) + \pi}{3} & \text{if } -\frac{\mathbb{C}}{2} < 0. \end{cases} \tag{2.34}$$

I remark that no constraints are imposed by the square root term $\sqrt{-\mathbb{B}/3}$, since $\mathbb{B}$

is negative for $\frac{\mathbb{C}^2}{4} + \frac{\mathbb{B}^3}{27} < 0$.

Eq. (2.34) allows to express the CCF peak time as a combination of the four quantities $\mathbb{A}_0$, $\mathbb{A}_1$, $\mathbb{A}_2$, $\mathbb{A}_3$ containing the dependence on known instrumental parameters and acquisition settings (the pixel size, the column distance, the scan frequency and the laser beam waist), as well as the dependence on the radius, the diffusion coefficient and the velocity of the flowing objects. The mean radius and, consequently, an estimate of the expected diffusion coefficient are frequently known for the fluorescent particles investigated (red blood cells and micro-spheres, in my case). Similarly, as discussed in the previous Section, I can treat as a known variable the angle γ subtended by the flow velocity vector and the scan path. The flow speed $|\underline{v}|$ acts therefore as the only unknown in the expression for the peak time τ_{max}.
What hampers the exploitation of the experimentally measured τ_{max} to recover the flow speed is the impossibility of solving analytically eq. (2.34) for $|\underline{v}|$, unless simplifying assumptions are introduced. Specifically, I assume that the Brownian diffusion of the investigated objects can be neglected: the assumption $D = 0$ remarkably simplifies the relation between the peak time of the CCF and the flow speed, while being justified by the small effect of D on the peak position which I have shown with simulated curves in Fig. 2.8d.

In the following, I refer to the peak time computed for a vanishing diffusion coefficient as τ^0_{max}. It can be derived directly from eq. (2.25), which, for $D = 0$, reduces to

$$\frac{\partial G(\tau)}{\partial \tau}_{(D=0)} = \frac{1}{C_2}\frac{1}{\sqrt{C_3}}\left\{-\frac{2C_1\tau}{C_2} + \frac{2B(\tau)v_x}{C_2}\right\}\exp\left\{-\frac{[B(\tau)]^2}{C_2} - \frac{C_1\tau^2}{C_2}\right\} \tag{2.35}$$

By solving $\left.\frac{\partial G}{\partial \tau}_{(D=0)}\right|_{\tau=\tau^0_{max}} = 0$, I obtain

$$\tau^0_{max} = \frac{(j-i)\delta x v_x}{\left(\frac{\delta x}{\tau_{line}} - v_y\right)^2 + v_x^2} \tag{2.36}$$

Eq. (2.36) can be employed to approximate the functional form of the peak time experimentally determined and can be solved for the flow speed. The superscript

$'0'$ that I add to the two components v_x^0, v_y^0 and to the modulus $|\underline{v}|^0$ underlines that the flow speed computed directly from the peak time τ_{max}^0 is approximate ($|\underline{v}|^0$ exactly equals $|\underline{v}|$ only for an identically null diffusion coefficient), and the validity of the approximation worsens for increasing values of D. Explicitly, $|\underline{v}|^0$ is given by

$$|\underline{v}|_{\pm}^0 = \frac{(j-i)\delta x \cos(\gamma) + 2\sin(\gamma)\frac{\delta x}{\tau_{line}}\tau_{max}^0 \pm \sqrt{\Delta}}{2\tau_{max}^0} \tag{2.37}$$

with

$$\Delta = \left[(j-i)\delta x \cos(\gamma) + 2\sin(\gamma)\frac{\delta x}{\tau_{line}}\tau_{max}^0\right]^2 - 4[\tau_{max}^0]^2\left(\frac{\delta x}{\tau_{line}}\right)^2 \tag{2.38}$$

The subscript $\pm$ in the $|\underline{v}|_{\pm}^0$ expression identifies the two solutions provided by the second-order equation obtained from eq. (2.36) when solving for the flow speed. The requirement $|\underline{v}|_{\pm}^0 > 0$ and the constraint $\Delta \geq 0$ imposed by the square root of eq. (2.37) determine the set of possible values for the parameters appearing in the CCF (scan frequency, angle γ, etc.) which lead to a real, positive number as estimate for the flow speed $|\underline{v}|^0$. These conditions can be cast as

$$\begin{cases} \tan(\gamma) > -\dfrac{1}{2}(j-i)\dfrac{\tau_{line}}{\tau_{max}^0} \\ \\ \tan(\gamma) \geq \dfrac{1}{(j-i)}\dfrac{\tau_{max}^0}{\tau_{line}} - (j-i)\dfrac{\tau_{line}}{4\tau_{max}^0} \end{cases} \tag{2.39}$$

The applicability of eq. (2.37) for the determination of the flow speed can therefore be rapidly checked, by substituing into eq. (2.39) all the involved quantities: τ_{line}, the column distance, the experimental peak time and the angle γ. If the conditions of eq. (2.39) are satisfied a straightforward determination of the flow speed is possible (with variable accuracy, as discussed in the next Section); otherwise, eq. (2.39) can be used, prior to the data analysis, to determine the optimal parameters for the computation of the CCF.

I also remark that, when both the values $|\underline{v}|_{\pm}^0$ are real and positive, they are often sufficiently different (of ~ 2 orders of magnitude for the experimental data presented in Chapters 3 and 4) to allow to confidently select the one that is physically relevant for the experimental case under investigation.

2.6 Accuracy in the recovery of the flow speed from the cross-correlation peak time

The possibility of determining the flow speed directly from eq. (2.36), by the substitution of the peak time of the experimental CCF to τ^0_{max}, obviously depends on the validity of the assumption $D = 0$. The error affecting the estimate of the flow speed can be quantified by first evaluating the ratio τ_{max}/τ^0_{max}, derived from eqs. (2.34) and (2.36) as a function of the diffusion coefficient. I expect τ_{max}/τ^0_{max} to tend to 1 for $D \to 0$. Moreover, when all the parameters apart from D are fixed, the peak time of the CCF shortens for increasing D (see Fig. 2.8d; exceptions are only found for a very low - $\lesssim 100\mu m/s$ - flow speed): hence I expect an overestimate of the peak time when the approximation $D = 0$ is adopted (i.e., $\tau_{max}/\tau^0_{max} \to 0$ for $D \to +\infty$).
Fig. 2.9 (panels a-d) shows the simulated trend of τ_{max}/τ^0_{max} for diffusion coefficients in the broad range 0-300 $\mu m^2/s$ (covering the typical D values for red blood cells and synthetic micro-spheres up to the diffusion coefficient of free dye molecules in solution). Due to the dependency of the ratio τ_{max}/τ^0_{max} on several parameters, the effect of the flow speed, of the scan frequency per line, of the angle γ and of the column distance has been investigated separately; for all the simulation datasets, I evaluated the discrepancy of the exact and approximate peak times in conditions close to the ones of the experimental data. Similarly, Fig. 2.9 (panels e-h) shows the simulated trend of the ratio $|\underline{v}|/|\underline{v}|^0$ as a function of the diffusion coefficient D in the range 0-300 $\mu m^2/s$. This ratio quantifies the discrepancy between a given flow speed $|\underline{v}|$ and the approximate estimate of the same speed recovered by substituting the *exact* peak time (eq. 2.34) of the simulated CCFs into eq. (2.37). Since the exact peak time is employed, but its approximate expression is exploited to derive the flow speed, an overestimate of the modulus of the flow velocity is obtained (once again, exceptions are found for a very low - $\lesssim 100\mu m/s$ - flow speed). As before, the effects of $|\underline{v}|$, f_{line}, γ and $(j - i)$ on the ratio $|\underline{v}|/|\underline{v}|^0$ have been investigated separately.

I focus on the range 0-100 $\mu m^2/s$ for the diffusion coefficient, which is relevant for the experimental conditions of both the calibration measurements in zebrafish embryos and the investigation of hemodynamics in the hepatic microcirculatory system. For $D \sim 100$ $\mu m^2/s$ and a typical $|\underline{v}|$=500 $\mu m/s$, the overestimate of the flow speed computed directly from the peak of the CCF for a column distance

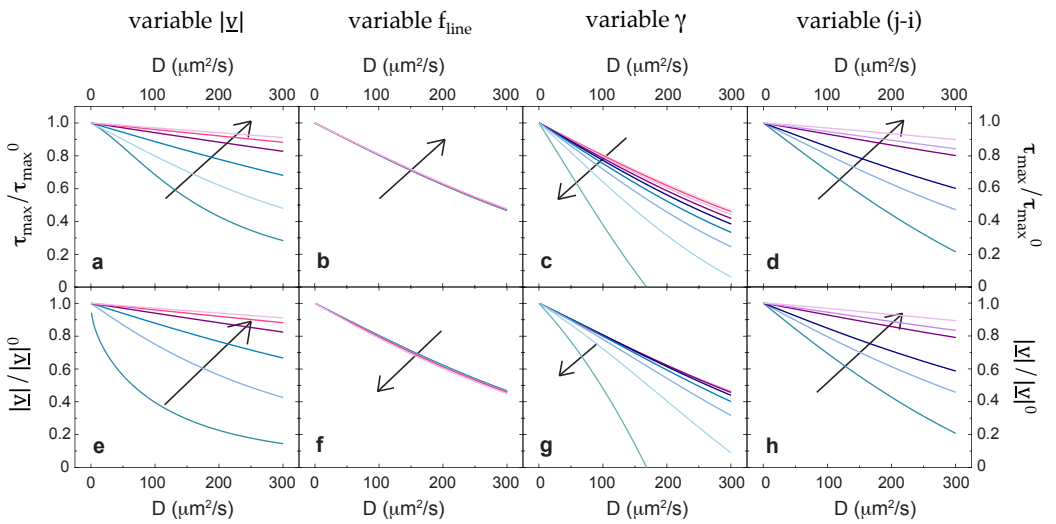

Figure 2.9: *FLICS: estimate of the flow speed in the approximation* $D = 0$. (a)-(d): simulated trend of the ratio of the peak time τ_{max} computed exactly from the analytical expression of the CCF to the approximate peak time τ^0_{max} computed in the approximation $D = 0$. (a): the higher the flow speed, the less relevant is the contribution of Brownian diffusion and the lower is the discrepancy between the peak times, simulated here for $\gamma = 0°$, f_{line}=1000 Hz and $(j-i)\delta x$=5 μm; $|\underline{v}|$=100, 250, 500, 1000, 1500, 2000 μm/s, increasing in the direction of the arrow. (b): effect of the scan frequency on the ratio of the peak times, simulated here for $\gamma = 0°$, $(j-i)\delta x$=3 μm, $|\underline{v}|$=500 μm/s and f_{line}=200, 400, 700, 1000, 1400 Hz; f_{line} increases in the direction of the arrow. The effect of f_{line} is not distinguishable on the simulated curves; nevertheless, the precision with which the peak time is recovered experimentally increases with the scan frequency, since f_{line} defines the temporal resolution in the sampling of the CCF. (c): ratio τ_{max}/τ^0_{max} simulated for f_{line}=1000 Hz, $(j-i)\delta x$=3 μm, $|\underline{v}|$=500 μm/s and increasing angle γ in the range $[0°; 80°]$; γ increases in the direction of the arrow with steps of 10°. The ratio τ_{max}/τ^0_{max} becomes negative when, for a high angle γ, the CCF turns into a decay instead of showing a clear peak for positive lag times. (d): effect of the column distance on the ratio of the peak times, simulated here for $\gamma = 0°$, $|\underline{v}|$=500 μm/s, f_{line}=1000 Hz and $(j-i)\delta x$=2, 3, 4, 8, 10, 15 μm; the distance increases in the direction of the arrow. (e)-(h): simulated ratio $|\underline{v}|/|\underline{v}|^0$ as a function of the diffusion coefficient D. The same parameters adopted in panels (a), (b), (c), and (d) have been exploited for panels (e), (f), (g), and (h), respectively. The following parameters have been kept at fixed values through all the simulations: ω_0=0.2 μm, ω_{0z}=0.5 μm, δx=0.1 μm, $\flat$=1, α=5 μm. All the simulations have been implemented by a custom-written Python code.

$(j-i)\delta x$=3 μm and an angle $\gamma = 60°$ amounts to ~28% ($(|\underline{v}|^0 - |\underline{v}|)/|\underline{v}| \approx 0.28$); however, it is to be noted that this overestimate reduces to ~3% when, for $\gamma = 0°$, the column distance is increased to $(j-i)\delta x$=15 μm. Experimentally, for all the data presented in Chapters 3 and 4 the approximate $|\underline{v}|^0$ has been compared to the value $|\underline{v}|$ obtained from the CCFs fit (taken as unbiased estimate of the flow speed): the retrieved average ratio $|\underline{v}|/|\underline{v}|^0$ ranging from 0.87 to 0.96 confirms that the blood flow speed can be obtained directly from the peak time of the experimental CCFs in most of the examined cases, thereby simplifying the analysis.

2.6.1 Experimental uncertainty on the recovered estimate of the flow speed

When the systematic overestimate of the flow speed due to the approximation $D = 0$ is negligible, the exploitation of the peak time of the CCF for the velocity measurement is particularly advantageous since it allows fastening the data analysis. An estimate for the error $\sigma_{|\underline{v}|^0}$ affecting the approximate estimate $|\underline{v}|^0$ can be derived by error propagation:

$$\sigma_{|\underline{v}|^0} = \sqrt{\left(\frac{\partial |\underline{v}|^0}{\partial \tau^0_{max}}\right)^2 (\sigma_{\tau^0_{max}})^2} \tag{2.40}$$

$\sigma_{\tau^0_{max}}$ is the uncertainty on the peak time of the experimental CCF: recalling that the scan frequency per line defines the temporal resolution with which the CCF is sampled, for cross-correlation functions with high signal-to-noise ratio (as those reported in Chapters 3 and 4) a reasonable estimate for $\sigma_{\tau^0_{max}}$ is one half of the line scan time ($\sigma_{\tau^0_{max}}=\tau_{line}/2$). In eq. (2.40), $\sigma_{\tau^0_{max}}$ is assumed to be the main source of uncertainty on the approximate estimate of the flow speed: in fact, the angle between the scan path and the flow direction can be determined from the orientation of the vessel in the raster-scanned image as previously explained, and the other variables appearing in the explicit expression for $|\underline{v}|^0$ are the pixel size, the column distance and the scan frequency, for which the error is null or negligible. Starting from eqs. (2.37)-(2.38), we obtain

$$\sigma_{|\underline{v}|^0} = \sqrt{\left(-\frac{2(j-i)\delta x \cos(\gamma) \pm \sqrt{\Delta} \mp \tau^0_{max} \Delta \dfrac{\partial \Delta}{\partial \tau^0_{max}}}{4(\tau^0_{max})^2}\right)^2 (\sigma_{\tau^0_{max}})^2} \tag{2.41}$$

where Δ is defined according to eq. (2.38) and

$$\frac{\partial \Delta}{\partial \tau^0_{max}} = 4\frac{\delta x}{\tau_{line}} \sin(\gamma)\left[2\frac{\delta x}{\tau_{line}} \sin(\gamma)\tau^0_{max} + (j-i)\delta x \cos(\gamma)\right] - 8\tau^0_{max}\left(\frac{\delta x}{\tau_{line}}\right)^2 \quad (2.42)$$

Eq. (2.41) underlines the dependence of the uncertainty $\sigma_{|\underline{v}|^0}$ on several parameters; higher errors are generally found for a lower scan frequency, whereas a non-monotonic trend is detected when $\sigma_{|\underline{v}|^0}$ is evaluated as a function of the column distance $(j-i)$. Given a single xy-image, it is therefore convenient to derive the cross-correlation functions for multiple values of the column distance and to compute a weighted average of all the values of the flow speed provided by their peak times.

2.7 Measurable flow speeds

Beside offering a straightforward method for the determination of the flow speed of the imaged particles, the analytical expression of the cross-correlation peak time (eq. 2.34) allows estimating the maximum flow speed that can be measured provided a given scan frequency. In this Section, I combine the theoretical predictions derived from eq. (2.34) with *in-vitro* measurements on 1 μm fluorescent micro-spheres to quantify the minimum and the maximum flow speed values accessible with a given scan frequency per line.

Maximum flow speed. For a fixed f_{line}, the higher the flow speed, the shorter is the CCF peak time τ_{max}. I can therefore define the maximum accessible speed by requiring a minimum number of data points in the peak sampling: in other words, if I require the peak lag time being at least the n^{th} data point in the CCF curve, the maximum measurable speed $|\underline{v}|_{max}$ is the one satisfying the condition $\tau_{max}(|\underline{v}|_{max})=n\tau_{line}$.
Instead of analytically solving for $|\underline{v}|_{max}$ the equation $\tau_{max}(|\underline{v}|_{max})=n\tau_{line}$, I proceed graphically. I simulate the τ_{max} plot as a function of the flow speed, and identify the maximum measurable speed $|\underline{v}|_{max}$ by its intersection with the constant $n\tau_{line}$-vs-$|\underline{v}|$ plot. I perform the simulation with n=10, D=0.4 $\mu m^2/s$ (as expected for micro-beads 1 μm in diameter), γ=0° (non-zero angles between the flow direction and the scan path decrease the modulus of the maximum accessible flow speed) and f_{line}=1400 Hz (τ_{line}=714μs); 1400 Hz is the highest scan frequency allowed by the conventional scanner of our experimental setup (see Materials and Methods

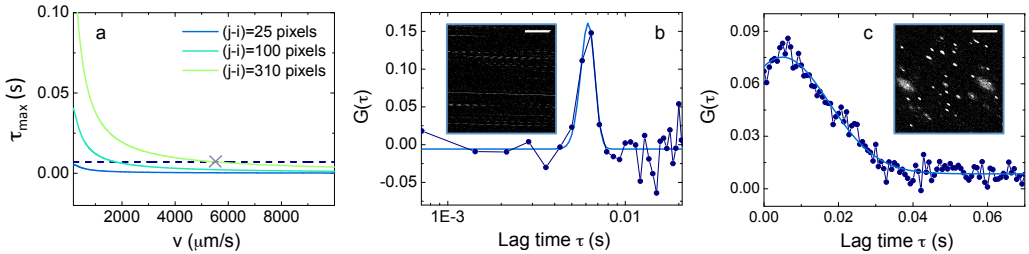

Figure 2.10: *FLICS: estimate of the minimum and maximum measurable flow speeds.* (a): cross-correlation peak lag time τ_{max} as a function of the flow speed, simulated according to eq. (2.34) with f_{line}=1400 Hz, γ=0°, D=0.4 $\mu m^2/s$, a=0.5 μm, δx=0.13 μm, ω_0=0.2 μm, ω_{0z}=0.5 μm and variable column distance $(j-i)$ ($(j-i)\delta x$=1.9, 12.6 and 39 μm). The dashed blue line is the constant plot $\tau_{max} = 10\tau_{line}$. (b): raster-scanned xy-image acquired by detecting the signal of 1 μm fluorescent spheres undergoing laminar flow in a square borosilicate capillary (inner section=720 μm). f_{line}=1400 Hz, δx=0.13 μm, scale bar=15 μm. The CCF reported has been computed on the same xy-image with $(j-i)$=310 pixels; the fit has been performed according to eq. (2.21), with best-fit parameter $|\underline{v}|$=(6631±103) $\mu m/s$. (c): raster-scanned xy-image acquired by detecting the signal of 1 μm fluorescent spheres undergoing laminar flow in the 720 μm square borosilicate capillary. f_{line}=1400 Hz, δx=0.13 μm, scale bar=15 μm. The CCF reported has been computed on the same xy-image with $(j-i)$=25 pixels; the fit has been performed according to eq. (2.21), with best-fit parameter $|\underline{v}|$=(174±10) $\mu m/s$.

in Section 3.2), allowing to provide a general estimate of the maximum speed accessible by the FLICS method on commercial confocal microscopes. I simulate the τ_{max}-vs-$|\underline{v}|$ plot for various column distances: in the most favorable case, diagonal lines produced by flowing objects in the xy-image last for the entire image width (see Fig. 2.10b) and no constraints are found on the choice of $(j-i)$.
The results are shown in Fig. 2.10a: if the flow is parallel to the scan path, imaged at the highest available scan frequency and inspected at high column distances, FLICS can access flow speed values as high as 6 mm/s. This conclusion is reinforced in Fig. 2.10b, where the FLICS measurements performed on 1 μm fluorescent beads flowing with $|\underline{v}|$=(6631±103) $\mu m/s$ are reported.

Minimum flow speed. As I pointed out in Section 2.2, particles flowing with speed $|\underline{v}|$ and imaged along a raster pattern with scan speed $|\underline{v}|_{scan} \gg |\underline{v}|$ do not produce diagonal lines in the xy-image: they are instead reconstructed in their shape, appearing as two-dimensional spots. Therefore the adopted scan frequency

also imposes a lower limit to the measurable flow speed. With a 1400 Hz scan frequency per line, the minimum flow speed that can be measured by FLICS on 1 μm fluorescent micro-spheres is $\sim 170\ \mu m/s$ (Fig. 2.10c).

Summarizing, at the highest scan frequency per line allowed by our commercial confocal microscope, FLICS allows flow measurements in the broad speed range 170-6000 $\mu m/s$. Lower $|\underline{v}|$ values can obviously be measured by lowering at will the scan frequency, whereas higher speed values can in principle be measured at the 8 kHz line scan frequency of resonant scanning heads. By simulating the τ_{max}-vs-$|\underline{v}|$ plot, and adopting a procedure analogous to the one employed here for 1 μm spheres, the maximum accessible flow speed can be quantified for any other adopted value of f_{line} and for particles of different size.

2.8 Cross-correlation peak amplitude

The approximate expression for the cross-correlation peak time derived under the assumption of vanishing diffusion coefficient will be extensively exploited in Chapter 3 for the experimental validation of the FLICS method. Since the same applies to the peak amplitude, we conclude this Chapter by deriving here its functional dependence upon the flow speed and the other instrumental and image acquisition parameters.
Recalling eq. (2.21) and assuming $D = 0$,

$$G(\tau^0_{max}) \propto \frac{1}{\left(\frac{a^2_b}{2} + \omega^2_0\right)} \frac{1}{\sqrt{\frac{a^2_b}{2} + \omega^2_{0z}}} \cdot \\ \cdot \exp\left\{-\frac{[(j-i)\delta x - |v|\cos(\gamma)\tau^0_{max}]^2}{\frac{a^2_b}{2} + \omega^2_0}\right\} \exp\left\{-\frac{\left[\frac{\delta x}{\tau_{line}} - |v|\sin(\gamma)\right]^2 (\tau^0_{max})^2}{\frac{a^2_b}{2} + \omega^2_0}\right\} \tag{2.43}$$

By substituting eq. (2.36) to τ^0_{max} and by rearranging the Gaussian terms, I obtain

$$G(\tau^0_{max}) \propto \frac{1}{\left(\frac{a^2_b}{2} + \omega^2_0\right)} \frac{1}{\sqrt{\frac{a^2_b}{2} + \omega^2_{0z}}} \exp\left\{-\frac{(j-i)^2\delta x^2}{\left(\frac{a^2_b}{2} + \omega^2_0\right)}\left[1 + \Gamma_1[\Gamma_1 + \Gamma_2 - 2]\right]\right\} \tag{2.44}$$

with Γ_1 and Γ_2 defined as

$$\begin{cases} \Gamma_1 \equiv \dfrac{|\underline{v}|^2 \cos^2(\gamma)}{|\underline{v}|^2 \cos^2(\gamma) + \left(\dfrac{\delta x}{\tau_{line}} - |\underline{v}| \sin(\gamma)\right)^2} \\ \Gamma_2 \equiv \dfrac{\left(\dfrac{\delta x}{\tau_{line}} - |\underline{v}| \sin(\gamma)\right)^2}{|\underline{v}|^2 \cos^2(\gamma) + \left(\dfrac{\delta x}{\tau_{line}} - |\underline{v}| \sin(\gamma)\right)^2} \end{cases} \tag{2.45}$$

Chapter 3

FLICS Validation

FLow Image Correlation Spectroscopy exploits a single raster-scanned xy-image acquired by detecting, in confocal or multi-photon excitation microscopy, the signal emitted by fluorescent particles undergoing (Brownian diffusion and) uniform flow: both the modulus and the direction of the flow velocity vector are recovered by computing the cross-correlation of the fluorescence intensity fluctuations detected in pairs of columns of the image. The whole frame is employed when, in the simplest implementation, a single vessel is imaged at high magnification; by contrast, separate regions of interest are selected when a branched, extended portion of the investigated circulatory system is included in the field of view. Suggested by the general theoretical framework and by the simulated CCFs reported in the previous Chapter, the possibility of performing the FLICS analysis separately on each in-focus vessel, for any relative orientation of the scan and flow directions, provides us with a method capable, in principle, of recovering and mapping the (blood) flow velocity at the level of individual capillaries even in the presence of a geometrically complex vessel network.
Prior to the application of the FLICS method to circulatory systems of such a complexity, the experimental validation of the principles and theoretical framework of FLow Image Correlation Spectroscopy is mandatory. First, the correctness of the analytical expression I derived for the cross-correlation function must be assessed, by verifying that experimentally recovered cross-correlation functions exhibit the theoretically expected functional dependence on the scan frequency, on the flow speed, on the flow direction and on the distance between the columns selected for the CCFs derivation. Secondly, the speed values measured by FLICS should

be validated by their comparison with those provided by other well-established (blood) flow measurement techniques. Third, the minimum image or ROI size (or equivalently, the minimum number of detected fluorescence fluctuations) required for an accurate statistical sampling of the correlation function must be determined. In this Chapter, all these FLICS validation measurements are reported. They have been mostly performed *in-vivo* in the main venous vessel of zebrafish embryos, which offer the practical advantage of a geometrically simple circulatory system, while retaining significant biological relevance due to their widespread use as a model system in cardiovascular research. *In-vitro* measurements on fluorescent microspheres undergoing laminar flow in a microfluidic device have been performed if controlled variations of the speed of the imaged flowing particles were required.

3.1 Model organism

Animal models have a pre-eminent role in biomedical research: they are widely employed to investigate the pathogenesis of various human diseases at a cellular and molecular level and allow the development and test of novel therapies. This especially applies to murine - and, more in general, mammalian - models, which beside offering genetic and physiological similarities to humans, also naturally develop diseases affecting the immune, endocrine, nervous, cardiovascular and skeletal systems; certain human diseases normally not affecting mice can be induced by genome manipulation, fueling the development of sophisticated transgenic approaches aimed at the creation of mouse models accurately reproducing the pathology of human diseases [100]. The main disadvantage of forward-genetic screens and random mutagenesis-based reverse genetics, when applied to mice, is that they inevitably require considerable staff and infrastructure support; mice maintenance and breeding are prohibitively expensive as well.
In this context, the zebrafish (*Danio rerio*, a teleost fish of the cyprinid family) has emerged as a useful complement to mammals in modeling human diseases [100–102]. The main focus of zebrafish research has traditionally been on developmental biology, due to the specimen optical clarity, allowing for visual analyses of early embryogenetic processes, and to the fast development: in about two days all common vertebrate specific features, including a compartmentalized brain and all internal organs, can be observed. Nowadays, zebrafish embryos also find increasing applications in the area of new drug discovery and in cancer research, since they spontaneously develop almost any tumor type known from

humans, with similar morphology and comparable signaling pathways [103]. Furthermore, the ongoing sequencing of the zebrafish genome allows the identification of disease-causing mutations, leading to the availability of thousands of clinically relevant zebrafish mutants for the investigation, just to name a few, of immune, neuronal, hematopoietic and cardiovascular disorders [101, 104].

Due to their wide employment in the investigation of the development, function and pathologies of the cardiovascular system and in the observation of vascularization and tumor angiogenesis, zebrafish embryos represent the organism of choice to test and validate FLow Image Correlation Spectroscopy. What is particularly advantageous is the relative geometrical simplicity of the main vessels in the cardiocirculatory system, which I briefly describe prior to reporting the results of the FLICS experiments.

3.1.1 Anatomy of the cardiovascular system

The embryonic zebrafish two-chamber heart is the first organ to develop and shows remarkable similarities to the embryonic human heart: developmental parity has been documented between the twenty-four hours post fertilization (h.p.f.) zebrafish heart and the human heart at three weeks gestation [101]. The cardiac activity is not coupled with metabolic demand, so that fish, unlike rodent models, are not dependent on a cardiovascular system for survival during embryogenesis. Two major trunk axial vessels, the Dorsal Aorta (DA) and the Posterior Cardinal Vein (PCV), are fully formed two days post fertilization (d.p.f.). The formation of these two longitudinally aligned vessels and of the primitive cranial vasculature occurs by vasculogenesis, i.e. by the coalescence of early mesoderm-derived precursor endothelial cells or angioblasts [105]. As these first vessels assemble, they concomitantly acquire the arterial and venous properties crucial for the proper functioning of the circulatory system: the cardiac contractions promote the blood flow through the arterial vessel, which turns 180° at its caudal end to empty into the cardinal vein; through the PCV, erythrocytes head back to the heart.
Following the initial DA an PCV development by vasculogenesis, most subsequent vessel formation occurs via angiogenesis (the formation of new vessels by growth from, or remodeling of, preexisting vessels). The intersegmental angiogenic arterial and venous vessels (ISAs and ISVs) of the trunk, developing between two and three d.p.f., form throughout the specimen length and interconnect to form the Dorsal Longitudinal Anastomotic Vessel (DLAV) [105]. In addition to the trunk vasculature,

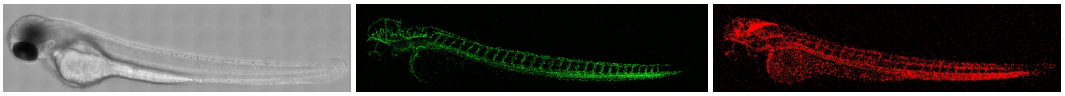

Figure 3.1: *Three d.p.f. zebrafish embryo.* Non-confocal transmitted light image (left) and confocal fluorescence images acquired by detecting the signal of the Green Fluorescent Protein (GFP) expressed by the endothelial cells (center, λ_{exc}=488 nm) and the signal of the DsRed fluorescent protein expressed by the red blood cells (right, λ_{exc}=561 nm) of a genetically modified zebrafish embryo belonging to the mutant transgenic line mitfa$^{w2/w2}$;roy$^{a9/a9}$;Tg(kdrl:EGFP)^{s843};Tg(gata1:dsRed)^{sd2}. The images have been acquired on a confocal Leica TCS SP5 microscope (see section 3.2) in mosaic mode; image length 3 mm.

a rather complex cranial circulatory system begins developing at approximately 26 h.p.f.; I refer to [106] for the complete description of its morphology and developmental stages.

The typical diameter of the zebrafish main vessels (DA and PCV) is around 20-30 μm. When small intersegmental vessels are considered, the diameter reduces to $\sim$ 10 μm, almost equaling the size of red blood cells (the major component of blood, with a radius of $\sim$ 4 μm and a thickness of $\sim$ 1-2 μm [107]).
The DA and PCV blood flow speed depends on both the venous or arterial nature of the vessel and on the developmental stage of the embryo. A characterization of the flow speed in zebrafish embryos ranging from two to four d.p.f. has been carried out in the laboratory (data not shown) by means of Scanning Laser Image Correlation (SLIC) [57]. In the dorsal aorta, the blood flow is promoted by the ventricular contractions and relaxations of the heart: periodic changes are detected in the erythrocytes speed, which oscillates from the maximum value reached during systole (heart contraction) to a minimum value during diastolic phases (ventricular relaxation); in the healthy zebrafish, three pulsations per second are detected. The systolic speed typically ranges from $\sim$ 1500 $\mu m/s$ to $\sim$ 3000 $\mu m/s$ in both two and four d.p.f. embryos, whereas it increases up to $\sim$ 4000 $\mu m/s$ at three d.p.f.; the diastolic speed ranges from $\sim$ 400 $\mu m/s$ to $\sim$ 900 $\mu m/s$, irrespectively of the developmental stage. While a decreasing trend has been observed for the systolic speed from the heart to the tail of the embryos, the diastolic speed exhibits a constant value through the whole vessel length. A more irregular behavior has been detected when measuring the decrease of the blood flow speed along the posterior cardinal vein; in contrast to the flow speed in the DA, the venous speed is

not affected by the heart contractions and ranges from ~ 300 $\mu m/s$ to ~ 1600 $\mu m/s$ in two and four d.p.f. zebrafish, slightly increasing up to ~ 2000 $\mu m/s$ in three d.p.f. embryos. The cardinal vein is the vessel in which all the FLICS measurements reported in this Chapter have been performed.

3.2 Materials and methods

3.2.1 Sample preparation

Animal models: validation measurements have been performed on zebrafish embryos (*Danio rerio*, 3 days post fertilization, ~ 3-4 mm long), belonging to the mutant transgenic line mitfa$^{w2/w2}$; roy$^{a9/a9}$; Tg(gata1:dsRed)^{sd2}, in which the red fluorescent protein DsRed (λ_{exc}^{peak}=560 nm, λ_{em}^{peak}=580 nm) is expressed by erythrocytes. In the Casper variety, the embryos do not present skin pigmentation and are optically weakly scattering. Zebrafish embryos have been anesthetized in 40 mg/l tricaine (Ethyl 3-aminobenzene methansulfonate, Sigma-Aldrich, USA) and then embedded in lateral position in small custom-built chambers filled with 1.5% low-melting agarose (Sigma Aldrich, USA). The low tricaine concentration anesthetizes the sample without impairing cardiac functions and heart rate [108, 109], while the agarose concentration helps in holding it immobilized throughout the measurement. All the experimental protocols have been reviewed and approved by the Institutional Review Board at the Department of Life Sciences of Università degli Studi di Milano and experiments have been conducted in accordance with national and European laws controlling experiments on live animals.

Chemicals: 1 μm amine-modified polystyrene fluorescent microspheres (λ_{exc}^{peak}= 520 nm, λ_{em}^{peak}=540 nm) (Sigma-Aldrich, USA) have been diluted in MilliQ water and used without further purification. For cross-correlation measurements, a borosilicate capillary (CM Scientific Ltd., UK) with 800x800 μm^2 nominal square section and 40 μm wall thickness has been employed; the square section has been chosen to minimize aberrations in the focal volume. The laminar flow in the capillary has been obtained by connecting both its sides to 4-cm^3 glass syringes used as sample reservoirs: the syringes have been placed horizontally and positioned at different heights by a micrometric regulation, so that the flow speed could be changed by varying the relative height of the two reservoirs as described elsewhere [35].

3.2.2 Experimental setup

All the FLICS validation and calibration measurements have been performed on an inverted Leica confocal microscope (TCS SP5 STED-CW, Leica Microsystems, D). It is equipped with three objectives (HCX PL FLUOTAR 20x / N.A. 0.5 air, HCX PL APO CS 40x / N.A. 1.3 oil and HCX PL APO STED 100x / N.A. 1.4 oil). Eight laser lines are available: 458, 476, 488, 496 and 514 nm, provided by an Argon ion laser; 561 nm, provided by a solid-state diode-pumped laser; 592 nm, provided by a continuous-wave fiber laser beam for STED nanoscopy; 633 nm, provided by a Helium-Neon laser. The fluorescence detection is accomplished by two PhotoMultiplier Tubes (PMTs) and two high sensitivity hybrid detectors; a fifth, non spectral dedicated detector is employed for the acquisition of images in transmitted light. In addition to a conventional scanning head, providing scan frequencies per line in the range 10-1400 Hz, the system is endowed with a resonant scanner operating at a fixed 8 kHz scan frequency per line (or 16 kHz, when in bidirectional mode).

For the measurements in zebrafish embryos, the excitation of the DsRed protein has been primed by the 561 nm solid state laser with a typical $\sim 10\ \mu W$ power and the confocal detection has been accomplished by means of a photomultiplier tube in the detection bandwidth 575-650 nm. Fluorescent microspheres have been excited at 514 nm with a $\sim 5\ \mu W$ power and the emitted signal has been detected in the range 525-600 nm. No offset has been applied in the signal detection, a 8-bit dynamic range has been selected and the PMT gain has always been adjusted to avoid saturation in the pixels intensity; details concerning image sizes and formats and the adopted line scan frequencies are reported in each figure caption. For the fit of experimental cross-correlation functions, the PSF $1/e^2$ radius has been fixed to 0.2 μm in the radial direction and to 0.5 μm in the axial direction, as obtained by resolution measurements on immobile sub-resolved fluorescent beads.

3.2.3 Data analysis softwares

All the acquired images have been visualized, linearly contrast-adjusted for display and exported in *tif* format using ImageJ (U.S. National Institutes of Health, USA). Cross correlation functions have been computed by means of a custom-written Python code exploiting Fast Fourier Transform (FFT) routines. All the non-linear least-squares fits have been performed by the OriginPro 8.6 software (OriginLab, USA).

3.3 Validation of the FLICS theoretical framework

In Chapter 2 I derived the analytical expressions of the FLICS cross-correlation function $G(\tau)$ and of its peak lag time τ_{max}, thereby evidencing their functional dependence on both the flow speed and direction, on the diffusion coefficient of the imaged particles, on the scan frequency and on the column distance considered for the CCF derivation. In this Section, I validate the theoretical framework on cross-correlation functions experimentally recovered, either *in-vivo* in zebrafish embryos or *in-vitro* in a simple microfluidic device.

3.3.1 *In-vivo* experiments and comparison with Scanning Laser Image Correlation

An exemplifying confocal raster-scanned xy-image encompassing the two main vessels of a three d.p.f. zebrafish embryo is reported in Fig. 3.2. Cross-correlation functions have been recovered in the cardinal vein for increasing column distances (Fig. 3.3a): they have been satisfactorily fit to the analytical expression derived in Chapter 3 (eq. 2.21) and exhibit the linear scaling of the peak time (Fig. 3.3b) as a function of the column distance $(j-i)\delta x$ expected from eqs. (2.34) and (2.36). The estimates of the blood flow speed ($|\underline{v}|$=323±2 $\mu m/s$) and of the radius of the red blood cells (a=5.3±0.1 μm) obtained by the CCFs fit are compatible with the values in the literature [107] and with the SLIC measurements reported in the following. The only parameter which is not reliably recovered by the curve fitting procedure is the diffusion coefficient, that is typically overestimated with respect to the prediction of the Stokes-Einstein's relation (~0.05 $\mu m^2/s$). As already pointed out in [107], at the low Reynolds number of the microcirculatory blood

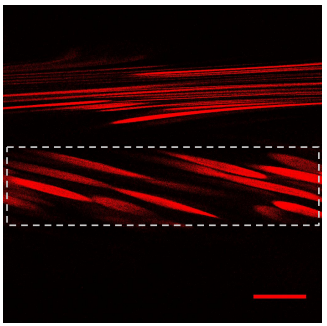

Figure 3.2: *FLICS image acquisition in zebrafish embryos.* Raw raster-scanned confocal xy-image acquired by detecting the fluorescence emission of DsRed-expressing red blood cells in the dorsal aorta (upper vessel) and in the posterior cardinal vein (lower vessel) of a three d.p.f. zebrafish embryo. Scan frequency f_{line} = 1000 Hz, scale bar = 15 μm; the flow direction in the venous vessel subtends an angle γ=0° with the horizontal x-axis. The dashed box defines the vessel in which the CCFs reported in Fig. 3.3 have been computed.

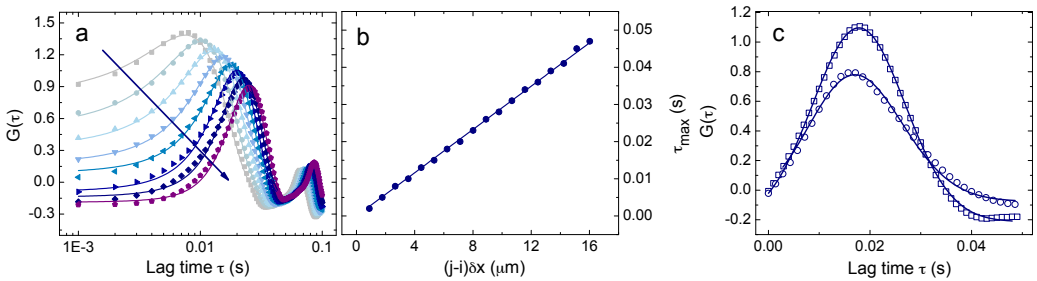

Figure 3.3: *FLICS measurements in the zebrafish posterior cardinal vein: effect of the column distance and of the scan frequency.* (a): exemplifying CCFs derived for increasing column distances in the range 30-100 pixels (2.7 - 15.2 μm) with a 10-pixel step (the distance increases in the direction of the arrow). Each CCF is averaged over all the pairs of columns a fixed distance $(j-i)$ apart, improving the statistics and leading to error bars - reported as s.e.m, standard error of the mean- lying within the size of the data points. The CCFs have been fit to eq. (2.21), yielding $|\underline{v}|$=(323±2) $\mu m/s$ and an estimate a=(5.3±0.1) μm for the RBCs radius; τ_{line}=1 ms, δx=0.09 μm, γ=0°, ω_0=0.2 μm and ω_{0z}=0.5 μm have been treated as fixed parameters. (b): linear dependence of the CCF peak time τ_{max} on the column distance selected for the CCF derivation; $(j-i)$ varies in the range 10-180 pixels with 10-pixel step. Given the high signal-to-noise ratio in the recovered cross-correlation functions, the experimental uncertainty on each τ_{max} value has been assumed equal to one half of the line scan time. (c): comparison between the CCFs derived for a fixed column distance $(j-i)$=70 pixels on two xy-images acquired sequentially on the same specimen with different line scan frequencies: f_{line}=1000 Hz (open squares; the image is the same reported in Fig. 3.2) and f_{line}=700 Hz (open circles). A global fit with shared parameter $|\underline{v}|$ has been performed according to eq. (2.21) yielding a flow speed $|\underline{v}|$=(338±1) $\mu m/s$: provided that the scan speed is adjusted so that flowing objects produce diagonal lines in the raster-scanned image, the same estimate of the blood flow speed is recovered for any value of f_{line}.

flow the diffusion coefficient must be regarded as an effective parameter, scaling as $D \sim \dot{\gamma} l^2$ where $\dot{\gamma}$ is the local shear rate and l is the mean free path travelled by each particle between two consecutive interactions. The size of the RBCs, their mutual separation and their distance from the vessel boundaries all contribute in regulating l, leading to a considerable deviation from the usually adopted value of the diffusion coefficient and justifying the experimental findings.

By a series of consecutive scans of the same field of view with different f_{line} frequencies, the independence on the scan frequency of the blood flow speed recovered by the CCFs best fit has also been assessed. All the employed frequencies

in the range 400-1400 Hz allowed the imaging of flowing RBCs as diagonal lines and allowed the computation of peaked CCFs with a sufficiently high temporal resolution (we recall that the lag time τ is approximately an integer multiple of $f_{line}^{-1} \equiv \tau_{line}$): a global fit to eq. (2.21) with shared parameter $|\underline{v}|$ well describes the experimental curves, as reported for two exemplifying CCFs (those obtained with f_{line} equal to 700 and 1000 Hz) in Fig. 3.3c.

Once investigated the effect of the column distance and of the scan frequency, I addressed the dependence of the cross-correlation functions and peak time on the flow direction. The possibility of accurately measuring the blood flow speed irrespectively of the angle subtended by the flow velocity and the scan path is of particular relevance when aiming at applying the FLICS method to the previously mentioned intricate, geometrically complex vessel networks: without the need for a rotation, neither of the specimen nor of the scan path, a single xy-image can effectively be exploited to recover the flow speed in differently oriented vessels.
Raster-scanned xy-images (Fig. 3.4a-d) have been acquired in the zebrafish PCV by progressively varying the angle γ in the range $[-90°; +90°]$ (10° step); the scan direction has been modified by means of the confocal microscope scan field rotation, instead of rotating the specimen. For each value of γ, a CCF has been computed at a fixed column distance ($(j-i)\delta x$=6.6 μm): as predicted by the FLICS model (Fig. 2.8 and eqs. 2.34, 2.36), the CCF peak shifts toward shorter lag times when γ increases from 0° to 90° (Fig. 3.4e) due to a reduction in the slope of the diagonal lines produced by RBCs in the raster-scanned images. Equivalently, the expected decrease of the CCF peak time has been detected for γ in the range $-10° \rightarrow -90°$ (Fig. 3.4f). In the whole range $[-90°; +90°]$, the dependence of the experimental CCF peak time and amplitude on γ is well described by the analytical expressions derived in Chapter 2 (eqs. 2.36 and 2.40, respectively), confirming the validity of the newly developed theoretical framework (Fig. 3.4g).
To further assess the sensitivity of the FLICS cross-correlation functions towards the flow direction, each CCF has also been fit to eq. (2.21), yielding an estimate of $|\underline{v}|$ and γ. The angle recovered from the fit always agrees with the angle selected prior to the image acquisition, as shown by the linear regression of the γ_{fit}-vs-γ plot reported in Fig. 3.5a. The recovered values of the blood flow speed $|\underline{v}|$ are reported in Fig. 3.5b: apart from small (temporal) fluctuations affecting the blood flow speed of a living biological sample, no regular trend is observed in the $|\underline{v}|$-vs-γ plot. This confirms that the recovered speed values do not depend on the angle γ, and that the decrease of the peak time shown in Fig. 3.4e,f for increasing values of

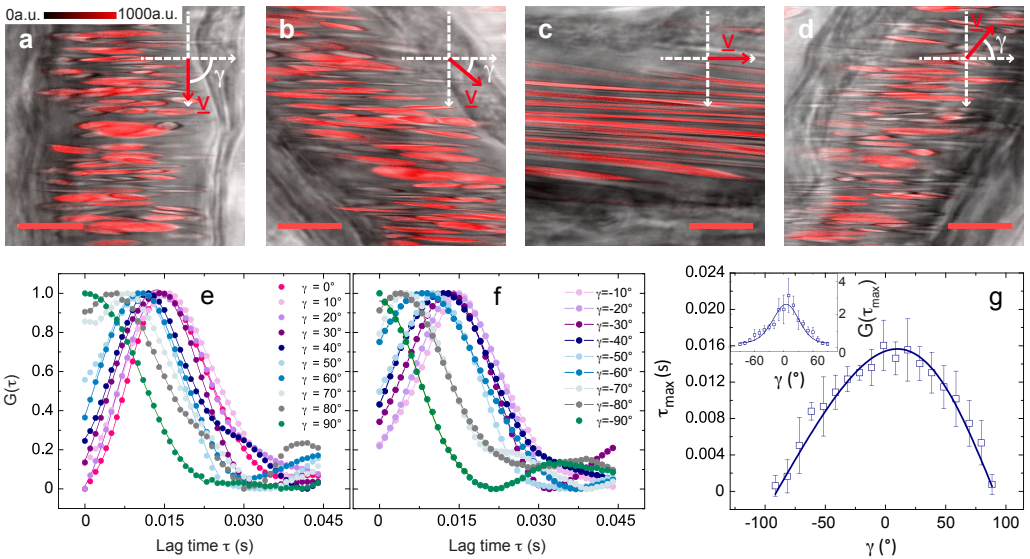

Figure 3.4: *FLICS measurements in the zebrafish posterior cardinal vein: effect of the flow direction (I).* (a)-(d): confocal raster-scanned xy-images acquired in the posterior cardinal vein of a 3 d.p.f. zebrafish embryo by detecting the fluorescence signal (shown in red) of the protein DsRed expressed by erythrocytes. Fluorescence images are overlaid to the (non-confocal) transmitted-light images acquired simultaneously. f_{line}=1000 Hz, δx=0.04 μm, scale bar=10 μm. The angle γ (defined in Fig. 2.7) between the direction of the blood flow and the scan path has been varied in the range $[-90°;+90°]$ (10° step). Four arbitrary, exemplifying orientations of the venous vessel with respect to the horizontal (x-oriented) scan direction are shown: γ=90° in (a), 50° in (b), 0° in (c) and $-50°$ in (d). Both the angle γ and the velocity vector $|\underline{v}|$ are sketched in the insets with respect to the reference Cartesian xy-plane. (e): normalized CCFs (mean±s.e.m.) computed with $(j-i)\delta x$=6.6 μm for $\gamma \in [0°;+90°]$; the column distance has been selected so that the CCF peak is well distinguishable in the whole γ range. All the curves are overlaid to the best-fit performed according to eq. (2.21). (f): normalized CCFs (mean±s.e.m.) computed with $(j-i)\delta x$=6.6 μm for $\gamma \in$ [-10°;-90°]. (g): experimental CCF peak time for $\gamma \in$ [-90°;+90°]. Each data point is reported as mean ± standard deviation over n=7 xy-images. The fit has been performed according to eq. (2.36) with best-fit parameter $|\underline{v}|$=(424±11) $\mu m/s$. Inset: experimental CCF peak amplitude for $\gamma \in$ [-90°;+90°] fitted to eq. (2.40) with fixed $|\underline{v}|$=424 $\mu m/s$ and best-fit parameter a=(6.3±0.2) μm: each data point is reported as mean ± standard deviation over n=7 xy-images.

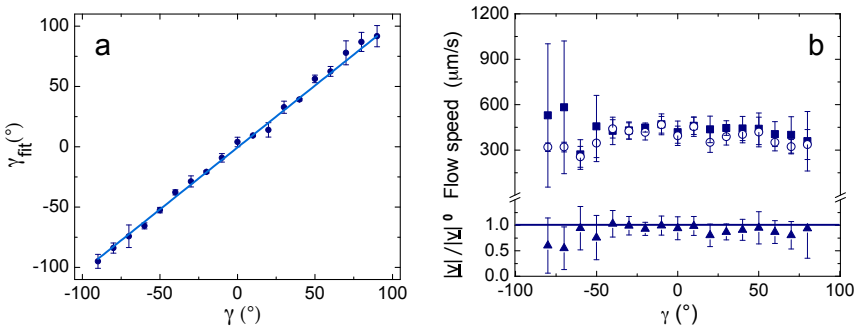

Figure 3.5: *FLICS measurements in the zebrafish posterior cardinal vein: effect of the flow direction (II).* (a): the estimates γ_{fit} of the angle subtended by the flow velocity and the scan path, obtained by the CCFs fit, are plotted versus the corresponding expected values (provided by the manual setting, prior to the image acquisition, of the scan direction); each value is reported as mean± standard deviation over 7 independent measurements. The linear trend (slope=1.03±0.01, intercept=-0.6° ± 0.5°) proves the sensitivity of the cross-correlation function to the blood flow direction. (b): flow speed $|\underline{v}|$ (open circles) recovered from the fit of experimental CCFs, and approximate flow speed $|\underline{v}|^0$ (filled squares) recovered directly from the peak time of the experimental CCFs, for each value of the angle γ. Each data point is reported as mean±standard deviation over n=7 xy-images. In the lower panel, the discrepancy $|\underline{v}|/|\underline{v}|^0$ is shown for each value of the angle γ. I remark that the comparison between the two recovered estimates of the flow speed is limited to the range [-80°;+80°]: for γ=-90° the expression for the peak time derived in the approximation $D \to 0$ does not lead to real solutions for the modulus $|\underline{v}|^0$ (see eq. 2.39), whereas for γ=90° the uncertainty associated to the determination of an almost vanishing peak time reflects in a too large uncertainty in the recovered speed.

the angle can be ascribed to the variation in the relative scan and flow direction rather than to an increase of the flow speed.

Fig. 3.5b also shows the comparison of the exact and approximate estimates, $|\underline{v}|$ and $|\underline{v}|^0$, of the blood flow speed (recovered, respectively, by the CCFs fit or by approximating their peak time τ_{max} to eq. 2.36 and by solving for the speed as in eq. 2.37). Within the large range $[-80°; +80°]$, an average ratio $|\underline{v}|/|\underline{v}|^0$=0.87 has been obtained; in agreement with the theoretical predictions of Fig. 2.9, $|\underline{v}|/|\underline{v}|^0$ is as high as 0.99 for a flow direction parallel to the scan path, proving that the CCF peak time alone can be exploited to gain a straightforward and reliable estimate of the flow speed.

Comparison with the SLIC results

To further strengthen the results of Figs. 3.4 and 3.5 and provide a reference value of the blood flow speed to be compared with the one recovered by FLICS, Scanning Laser Image Correlation (SLIC) [57, 58] has been performed on the same three d.p.f. zebrafish embryo. xt-images have been acquired in the posterior cardinal vein with an 8 kHz line-scan frequency, along a linear scan path subtending an angle γ=0° with the flow direction. 8192 consecutive scans of the same line have been performed and re-assembled, by their juxtaposition along the vertical direction, in each xt-frame. As previously described (Section 1.3.4), fluorescent red blood cells, flowing with constant velocity $|\underline{v}|$, appear in the xt-image as

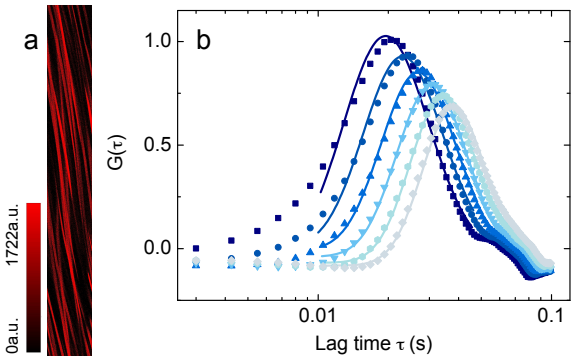

Figure 3.6: *SLIC measurements.* (a): confocal xt-image acquired by detecting the fluorescence signal of the protein DsRed expressed by erythrocytes in the posterior (caudal) cardinal vein of a 3 d.p.f. zebrafish embryo (the same on which the measurements shown in Figs. 3.4 and 3.5 were performed). A line-scanning procedure has been employed for the image acquisition: the same line (512 pixels, 126 μm) has been repeatedly scanned and the consecutive scans have been aligned along the vertical direction (for the sake of display, 4096 lines out of a total of 8192 scans are shown). (b): CCFs (mean$\pm$s.e.m.) computed from the xt-image in (a) at increasing column distances of 7.4, 8.6, 9.9, 11.1, 12.3, 13.6 μm (one tenth of the total data points is plotted for the sake of display). The higher the column distance, the longer is the lag time at which the peak of the CCF is located. The fit has been performed according to eq. (1.70), with best-fit parameter $|\underline{v}|$=(322.9$\pm$0.3) μm/s. The average flow speed provided by five separate measurements is $|\underline{v}|$=(328$\pm$21) μm/s. The diffusion coefficient is largely overestimated by the fitting procedure (D=222$\pm$25 $\mu m^2/s$), mainly for the interactions of red blood cells with the vessel walls and for the finite (non-pointlike) size of erythrocytes, which is not accounted for in eq. (1.70).

parallel diagonal lines (Fig. 3.6a); the blood flow speed, regulating their slope, can be quantified by computing the cross-correlation between pairs of columns of the image. Exemplifying CCFs are reported in Fig. 3.6b with their global fit to eq. (1.70): the recovered flow speed $|\underline{v}|$=(328±21) $\mu m/s$ is compatible with the average $|\underline{v}|$=(365±65) $\mu m/s$ of the values shown in Fig. 3.5b and with the estimate $|\underline{v}|$=(323±2) $\mu m/s$ recovered from Figs. 3.2 and 3.3.

3.3.2 *In-vitro* experiments

The dependence of experimental FLICS cross-correlation functions on the flow speed has been investigated with *in-vitro* experiments, which allow controlling, and regulating at will, the magnitude of the flow velocity. Raster-scanned confocal xy-images have been acquired by detecting the signal of fluorescent micro-beads (nominal diameter, 1 μm) dispersed in water and undergoing laminar flow in a square borosilicate capillary (inner section, 720 μm). As described in Section 3.2, the flow speed is regulated by the height h between two insulin syringes, used as sample reservoirs and connected to the capillary by means of Teflon tubes. According to Poiseuille's law [110], the flow speed $|\underline{v}|$ scales linearly with the height difference h between the two reservoirs:

$$|\underline{v}| = 0.084 h d^2 \frac{\rho g}{L \eta} \tag{3.1}$$

where d is the capillary square section, ρ and η are the density and the viscosity of the fluid (water, in the present case), L is the tubing length and g is the gravity acceleration. I have therefore varied the flow speed $|\underline{v}|$ by micro-regulating the relative height h, and for each h value I have measured $|\underline{v}|$ by means of FLow Image Correlation Spectroscopy. The results are reported in Fig. 3.7, with the comparison of the CCFs computed as a function of h (or equivalently, as a function of $|\underline{v}|$) at fixed column distance. The flow speed measured by fitting experimental cross-correlation functions to eq. (2.21) allows verifying that: (i) the linear dependence predicted by eq. (3.1) for the $|\underline{v}|$-versus-h plot is retrieved, with a slope $|\underline{v}|/h$=(0.127±0.003) s^{-1} that well compares to the theoretically expected value $|\underline{v}|/h$= 0.129 s^{-1}; (ii) the CCF peak time τ_{max} obeys the non-linear dependence on the flow speed derived in Chapter 2 with eqs. (2.34) and (2.36).

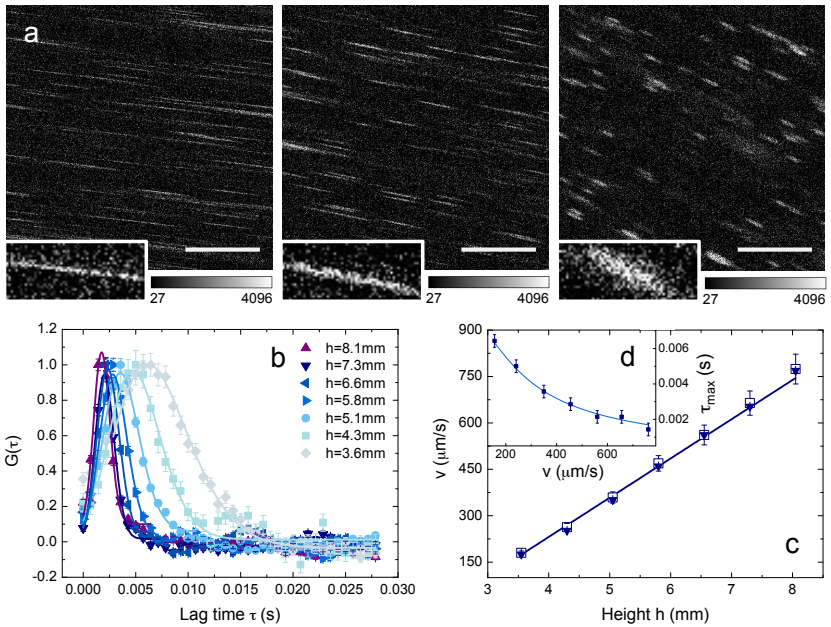

Figure 3.7: *FLICS sensitivity to flow speed changes.* (a): Raw confocal raster-scanned xy-images acquired by detecting the fluorescence signal of 1 μm spheres flowing through an 800 μm square capillary; f_{line}=1400 Hz, δx=0.07 μm, scale bar=10 μm; calibration bar on the bottom in arbitrary units. Images refer to a relative reservoirs height h of 8.1 mm (left panel), 5.8 mm (central panel) and 3.6 mm (right panel). Insets show magnified views of individual flowing beads to highlight the difference, associated to the different flow speed values, in the slope and width of the diagonal lines produced by flowing objects in the xy-images. (b): CCFs computed for a fixed column distance $(j-i)$=20 pixels for various heights h in the range 3.6-8.1 mm; the higher the distance between the two reservoirs, the higher is the flow speed and the smaller is the lag time at which the CCF peak is located. The fit has been performed according to eq. (2.21); error bars on the CCF curves are within the size of data points, reported as mean±s.e.m.. (c): linear dependence of the flow speed on the height h. Open squares are the weighted averages of the flow speed estimates obtained from the peak time of the CCFs derived for $(j-i)$ in the range 10-55 pixels (5-pixel step); filled triangles are the estimates of the flow speed recovered from the global fit of the CCFs computed for $(j-i)$ in the range 5-35 pixels (5-pixel step). The solid line is the best fit to eq. (3.1), with slope $|\underline{v}|/h$=(0.127±0.003) s^{-1}. (d): peak time of the CCFs of panel (b) plotted as a function of the flow speed $|\underline{v}|$ recovered by their fit to eq. (2.21): the experimental τ_{max}-versus-$|\underline{v}|$ plot obeys eq. (2.36), as expected (solid line: fit to eq. 2.36 with $(j-i)$=20 pixels, δx=0.07 μm and γ=0° treated as fixed parameters).

3.4 FLICS on regions of interest of variable size

The exploitation of a single raster-scanned xy-image for the measurement of the flow speed in all the vessels within the (often large) chosen field of view of an extended sample requires an evaluation of the effect produced on experimental cross-correlation functions by a reduction of the size of the Region Of Interest (ROI) on which the CCFs are computed. The minimum ROI size for a reliable recovery of the blood flow speed must be determined, and the absence of a systematic under / overestimate of the speed $|\underline{v}|$ depending on the ROI size should be assessed as well. I investigate the effect of the selected ROI starting from a single xy-image, acquired in the posterior cardinal vein of a 3 d.p.f. zebrafish embryo (Fig. 3.8a); the signal-to-noise ratio in the image and the brightness of the fluorescent objects are sufficiently high to exclude the necessity of introducing a threshold on the intensity counts, so that eventual alterations affecting the CCFs can be univocally assigned to the modification of the ROI size. I start from the largest useful ROI (512x274 pixels^2, which only excludes the regions outside the vessel) and I proceed by further reductions of the portion of the image on which the CCFs are computed; I reduce the x-size while keeping the y-size fixed and vice versa, so that the effects of the reduction of the two ROI sides can be investigated separately. For all the values of the x- and y- sides, the CCFs are compared with the results obtained from the largest possible ROI, used as reference (Fig. 3.8b).

3.4.1 Effect of a reduction of the x-side of the ROI for a fixed y-size

For a selected column distance $(j-i)$, $N_x-(j-i)$ individual CCFs are computed (one for each pair of columns a fixed number of pixels $(j-i)$ apart along the x-direction), where N_x is the total number of pixels along the horizontal axis of the image. These cross-correlation functions are then averaged to obtain a single CCF. Therefore, for a fixed number of pixels N_y along the vertical y-direction, a reduction of the x-side of the ROI acts as a reduction of the number of cross-correlation functions averaged for each column distance $(j-i)$. Fig. 3.9a shows the CCFs for $(j-i)$=60 pixels, recovered for a fixed N_y=274 pixels and a variable x-size in the range 61-512 pixels. For N_x>70 pixels, a reduction of the ROI size only produces a slight decrease in the CCF amplitude, without affecting the peak time of the cross-correlation function and the estimate of the blood flow speed. The recovered values of the speed $|\underline{v}|$ are reported in Fig. 3.9c, for all the investigated values of the ROI x-axis in the range 70-512 pixels: the estimated speed fluctuates

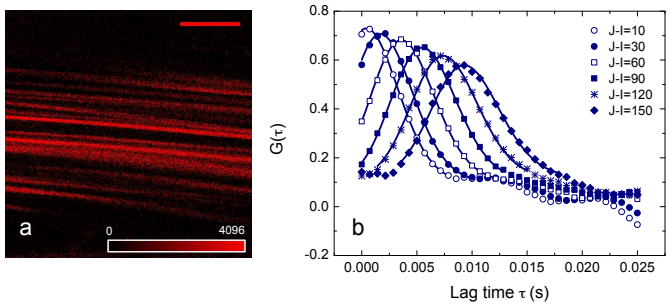

Figure 3.8: *Computation of FLICS CCFs on regions of interest of variable size (I).* (a): raw confocal xy-image acquired by detecting the signal of the fluorescent protein DsRed expressed by RBCs in the posterior cardinal vein of a 3 d.p.f. zebrafish embryo. f_{line}=1400 Hz, δx=0.08 μm, γ=0°, scale bar=10 μm; intensity calibration bar on the bottom in arbitrary units. Starting from this 512x512 image, ROIs of variable size have been selected for the CCFs derivation, keeping the center of the regions of interest coincident with the center of the image. (b): experimental CCFs (mean±s.e.m.) computed on the largest useful ROI (512x274 pixels^2) selected in the image shown in (a), for increasing column distances $(j-i)$=10, 30, 60, 90, 120, 150 pixels. The global fit to eq. (2.21) provides a reference flow speed $|\underline{v}|^{ref}$=(1260±3) $\mu m/s$.

around the reference value $|\underline{v}|^{ref}$=(1260±3) $\mu m/s$ provided by the analysis of the largest (512x274 pixels) ROI, with a maximum discrepancy $(|\underline{v}| - |\underline{v}|^{ref})/|\underline{v}|^{ref}$=0.02. This highlights that an averaging operation over roughly ten pairs of columns is sufficient for the recovery of the CCF and for the measurement of the flow speed. By contrast, when the x-side of the ROI is reduced to 61-62 pixels (and therefore only one or two pairs of columns are exploited for the derivation of the CCF with $(j-i)$=60 pixels), the behavior of the CCF is largely affected by the limited (temporal) average performed on the sampling of the observed red blood cells, and by spurious events registered in the few considered columns. The relative error σ_G/G associated to the peak value of the experimental CCF increases (Fig. 3.9d) and the discrepancy of the recovered speed $|\underline{v}|$ with respect to the reference value can be as high as ~0.2. The minimum required ROI size is therefore regulated by statistical considerations and, ultimately, by the column distance chosen for the computation of the CCFs (or, vice versa, when the maximum ROI size is assigned by the vessels dimensions, it fixes an upper limit to the exploitable column distance). For further confirmation, I reduced the column distance to $(j-i)$=30 pixels and I derived the CCFs (shown in Fig. 3.9b) on ROIs having a fixed N_y=274 pixels and a

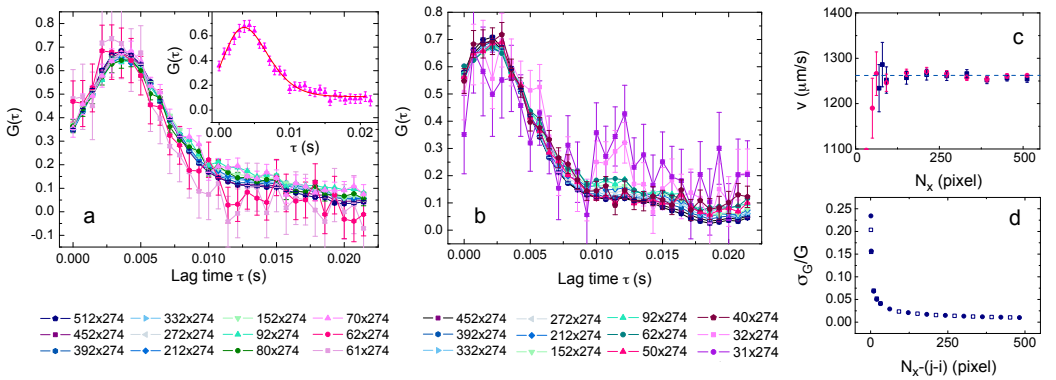

Figure 3.9: *Computation of FLICS CCFs on regions of interest of variable size (II).* (a),(b): CCFs (mean±s.e.m.) derived for $(j-i)$=60 pixels (a) and $(j-i)$=30 pixels (b) on ROIs (selected in the xy-image reported in Fig. 3.8a) having a fixed N_y=274 pixels and a variable x-size in the range 31-512 pixels. Inset of panel (a): the CCF computed for $(j-i)$=60 pixels, N_y=274 pixels and N_x=70 pixels is isolated for the sake of display and overlaid to the fit to eq. (2.21). (c): estimates (filled squares, blue) of the flow speed $|\underline{v}|$ obtained by the fit of the CCFs reported in (a): for an x-side between 70 and 512 pixels, the speed can be measured with a small discrepancy $((|\underline{v}|-|\underline{v}|^{ref})/|\underline{v}|^{ref}$=0.02) with respect to the reference value (dashed blue line) provided by the largest analyzed ROI. The estimates of the flow speed (filled circles, pink) provided by the global fit of the CCFs computed, for each of the ROIs, for increasing column distances in the range [10,(N_x-10)] pixels (10-pixel step) are also shown for comparison (we remark the similarity with the strategy adopted throughout Chapters 2-4 for the speed measurement, based on the exploitation of multiple column distances and on the global fit of all the corresponding CCFs). (d): relative error σ_G/G on the peak value of the CCF as a function of the number of cross-correlation functions averaged for each value of the ROI x-size. Data refer to N_y=274 pixels and $(j-i)$=30 pixels (filled circles) and to N_y=274 pixels and $(j-i)$=60 pixels (open squares).

x-side as small as 31 pixels: in this case too, an average over ten pairs of columns is sufficient for the recovery of the CCF.

3.4.2 Effect of a reduction of the y-side of the ROI for a fixed x-size

Two main effects are associated to a reduction of the vertical y-side of the ROI on which the CCFs are computed. On the one hand, the lag time τ being approximately an integer multiple of the inverse of the scan frequency per line, the

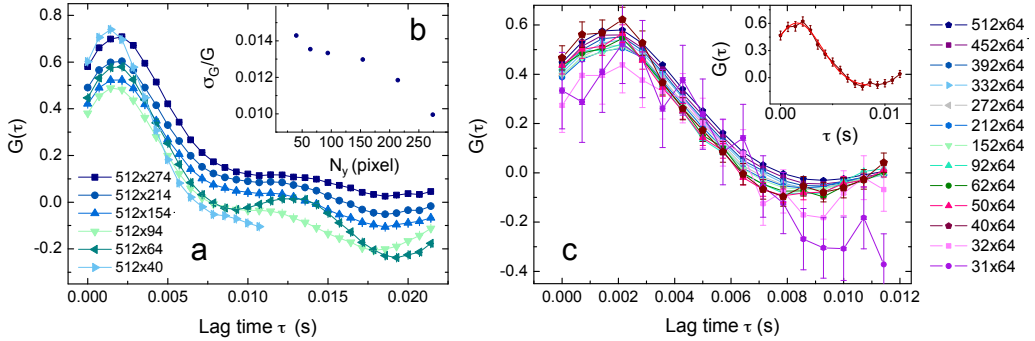

Figure 3.10: *Computation of FLICS CCFs on regions of interest of variable size (III).* (a): CCFs (mean±s.e.m.) computed for a fixed column distance $(j-i)$=30 pixels, on ROIs (selected in the xy-image reported in Fig. 3.8a) having a 512-pixels x-size and a variable y-size in the range 40-274 pixels. (b): relative error σ_G/G on the peak value of the CCF as a function of the number of pixels N_y for a fixed N_x=512 pixels. (c): a size reduction along the y-direction is combined to a reduction along the horizontal axis of the image: CCFs (mean±s.e.m.) are shown for $(j-i)$=30 pixels, a fixed ROI y-size of 64 pixels and a variable x-size in the range 31-512 pixels. The effect produced by a reduction of the horizontal x-side of the ROI does not depend on the number of pixels along the vertical direction (see panel (b) in Fig. 3.9 for comparison): even for a small N_y=64 pixels, an average over ten pairs of columns provides sufficient statistics for the recovery of the CCF. The CCF recovered for $(j-i)$=30 pixels and N_x=40 pixels is isolated in the inset for the sake of display.

number of rows in the region of interest determines the maximum temporal length of the cross-correlation function: $(N_y-1)\tau_{line}$ is the maximum lag time for which the cross-correlation value can be computed, and it reduces to $(N_y-1)\tau_{line}/2$ when the CCF is derived through Fourier transforms-based algorithms. Therefore a reduction of the y-side of the ROI might limit the maximum distance between the columns exploited for the derivation of the CCFs (the higher $(j-i)$, the longer is the peak time of the cross-correlation function). On the other hand, a reduction of the vertical side of the ROI reduces the number of fluorescent objects whose signal is exploited for the cross-correlation derivation (practically, it reduces the number of diagonal stripes produced by flowing objects in the xy-image and included in the ROI). The result is shown in Fig. 3.10a, with the CCFs computed for a fixed column distance $(j-i)$=30 pixels, a fixed N_x=512 pixels and a variable y-size

in the range 40-274 pixels: the average over a smaller number of events due to the reduction of the ROI size does not lead to CCFs with a noisy appearance, but seldom affects the CCF width and peak time. The slight differences in the recovered speed values reflect the distribution of speeds of the different observed red blood cells. Provided that the guidelines outlined in the previous Subsection are followed for the selection of the ROI x-size, even small ROIs can be employed to recover the CCFs and determine the drift speed (in the limiting case, of a single erythrocyte).

In summary, even if statistical considerations are at the basis of the observed results in both cases, the x- and y- sides of the ROI affect the cross-correlation analysis in different ways. When the x-size is reduced, the number of red blood cells detected (i.e., the number of events registered in the ROI) may be unchanged, but all of them are sampled with lower statistics. When the y-size is reduced, the number of observed events diminishes, but each of them can be sampled accurately thanks to the averaging operation performed on a large number of columns.[1]

3.5 Effect of the signal-to-noise ratio on experimental cross-correlation functions

I conclude this Chapter with an investigation of the effect of the image signal-to-noise (S/N) ratio on the experimental FLICS cross-correlation functions.
As previously pointed out in the literature [47,111] for Temporal Image Correlation Spectroscopy (TICS) and for spatial ICS, two main noise sources simultaneously affect the pixel intensities of a raster-scanned xy-image acquired by a one- or two-photon excitation fluorescence microscope. The first source comprises the specimen autofluorescence, the incomplete rejection of scattered light and the effect of the detector dark current: the resulting background noise, which is particularly relevant when the fluorescence signal of interest is low, can be considered constant across the image and independent on the true fluorescence intensity at each pixel

[1] All these considerations apply to xy-images where the diagonal lines produced by flowing objects last for the entire image width (as in Fig. 3.8a). When, either for the slower flow speed or for a non-zero angle γ, shorter diagonal lines are obtained (as in the case of fluorescent micro-spheres in Fig. 3.7a), also the reduction of the ROI x-size would produce a reduction in the number of the detected particles. Provided the considerations of Subsections 3.4.1 and 3.4.2, the minimum ROI size is the one allowing -for each of the few sampled objects- a CCF averaging operation over roughly a ten of columns.

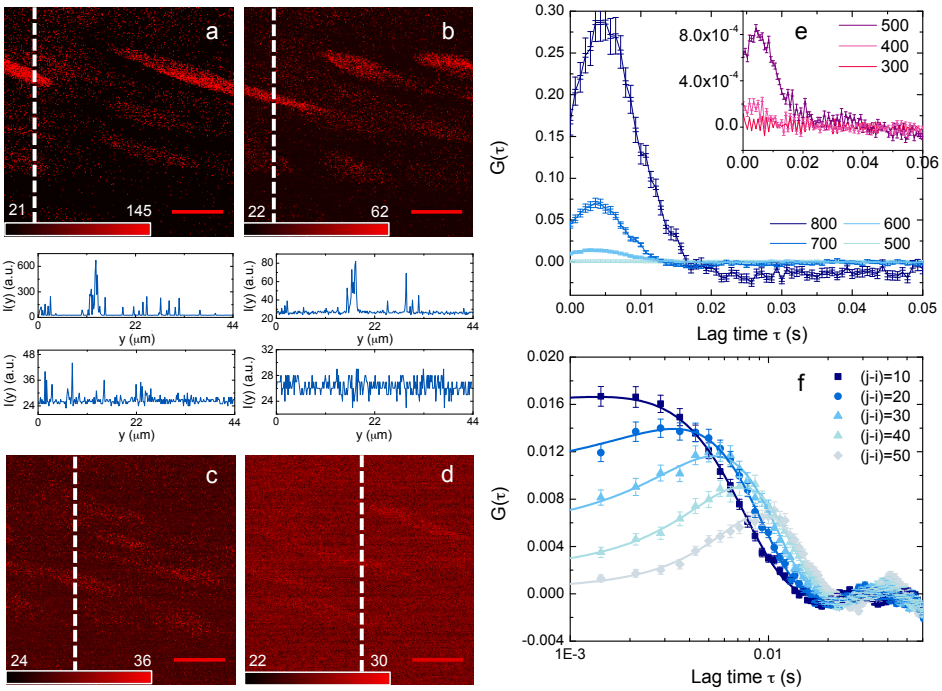

Figure 3.11: *Effect of the image S/N ratio on experimental cross-correlation functions.* (a)-(d): confocal raster-scanned xy-images acquired in the PCV of a 3 d.p.f. zebrafish embryo with fixed excitation laser power ($P_{exc\,561nm}$=5 μW) and variable detector gain; the PMT voltage has been set at 800 V (a, S/N=25±1), 600 V (b, S/N=3.0±0.1), 500 V (c, S/N=1.6±0.1) and 400 V (d, S/N=1.3±0.1). f_{line}=1400 Hz, δx=0.17 μm, scale bar=10 μm; the intensity calibration bar of the look-up table adopted for display is reported on the bottom of each frame in arbitrary units. For each xy-image, the intensity profile extracted along the corresponding dashed white line is reported to highlight the contrast worsening with the reduction of the detection gain. (e): comparison of the CCFs (mean±s.e.m.) computed for a fixed column distance $(j-i)$=20 pixels with variable PMT gain in the range 300-800 V (corresponding to a S/N ratio varying in the range 25±1 - 1.1±0.1). The S/N ratio evidently affects the CCF amplitude, but as long as it is higher than 3.0±0.1 it has no effect on the peak lag time and on the resulting estimate of the flow speed. (f): CCFs derived from the image of panel (b) (PMT voltage=600 V) for $(j-i)$=20...50 pixels. The CCFs have been fit to eq. (2.21) with best-fit parameter $|\underline{v}|$=(821±9) μm/s; the column distance, the pixel size, the scan frequency, the excitation laser beam waist and the angle γ have been treated in the fit as fixed parameters.

position. The second noise source encompasses the stochastic nature of photon emission and the signal amplification electronics. In fact the shot noise, obeying Poisson's statistics and resulting from the statistical variation in the number of emitted and detected photons, is combined with noise contributions arising from the processes of photo-electron generation, signal amplification and digitization inherent in light detection.
In this Section I do not attempt to separately characterizing the contributions of background and counting noise: I determine instead, empirically, the minimum S/N ratio required for the recovery of the cross-correlation functions and, consequently, for the measurement of the flow speed. To this aim, confocal xy-images have been acquired sequentially in the posterior cardinal vein of a three d.p.f. zebrafish embryo with fixed imaging conditions apart from a variable detector (PMT) gain (Fig 3.11a-d). By lowering the PMT voltage from 800 V to 300 V, I have intentionally worsened the image S/N ratio: when estimated as the ratio of the maximum detected intensity in the image to the average signal in dark regions within the vessel (i.e., outside fluorescent erythrocytes), the S/N ratio varies between 25 ± 1 and 1.1 ± 0.1 (see intensity profiles in Fig. 3.11). The comparison of the CCFs derived for fixed column distance at decreasing S/N ratios (Fig. 3.11e) reveals that the cross-correlation amplitude is severely affected by the image noise. Nevertheless, as long as the signal-to-noise ratio is higher than 3.0 ± 0.1, no influence on the CCF peak lag time and on the estimate of the recovered flow speed is detected. Exemplifying cross-correlation functions recovered with what I identify as the minimum S/N ratio=3 are reported in Fig. 3.11f.

Chapter 4

FLICS in the hepatic microcirculation

FLow Image Correlation Spectroscopy finds its best application in the measurement of flow velocities in circulatory systems with complex geometry. Having validated the FLICS theoretical framework with the measurements reported in the previous Chapter, I turn now to the *in-vivo* application of the FLICS method in the murine hepatic microvascular system.
The liver is a unique anatomical and immunological site, which has been considered second only to the brain in its complexity [112]. It is endowed with a structurally intricate microvascular system which, beside guaranteeing the correct oxygen and nutrients supply, is also responsible for the clearance of toxins from the bloodstream and serves as the gate for leukocyte entrance during hepatic inflammation [112–114]. A crucial role in regulating tolerance and immunity in the liver is especially played by sinusoids, that along with portal venules, central venules and hepatic arteries constitute the major components of this microcirculatory network: thanks to their peculiar fenestrated endothelium, and to the lack of a basement membrane, hepatic sinusoids facilitate immune-cell interactions and the transvascular exchange between the blood and the liver cells [113–116]. Intravascular antigen recognition processes have been recently demonstrated [117], suggesting a possible reciprocal impact, at the level of individual sinusoids, of hemodynamics on immune cells trafficking.
Sinusoids are precisely the vessels which I focus on with the FLICS measurements. Prior to reporting in this Chapter the experimental results, I briefly describe the

anatomy of the hepatic microcirculatory vessel network and outline the biological and medical relevance of the characterization of the intra-hepatic sinusoidal blood flow.

4.1 Anatomy of the hepatic microcirculation

The anatomy of the hepatic microvascular bed [112–115, 118, 119] (Fig. 4.1) has been studied in detail, mainly by transmission and scanning electron microscopy and by optical microscopy [120–124]. While histological techniques lack the ability of providing information on dynamic processes, the recent developments in the field of *in-vivo* (fluorescence) microscopy have allowed the analysis of both the morphology and the flow and resistance of hepatic vessels under physiological and pathological conditions. These studies have revealed that the mammalian liver has a dual blood supply, receiving poorly oxygenated but nutrient-rich blood from the portal vein and well oxygenated blood from the hepatic artery [112–114]. The portal flow constitutes about 80% of the total hepatic inflow, so that, due to its high flow rate, the portal vein provides to the liver half of the oxygenation it requires. Both the portal vein and the hepatic artery repeatedly branch within the liver: their terminal branches, namely the portal venules and the hepatic arterioles, supply blood to the sinusoids. They drain in turn into the central venules, connecting to the hepatic veins through which the blood is returned to the inferior vena cava [113, 114]. Although various models of the organization of the liver circulation into structural and functional units have been proposed by anatomists, pathologists and clinicians, the basic structural unit is usually identified in the "classic hepatic lobule" [113, 118, 125, 126] (Fig. 4.2). It has a polygonal structure, developing around a central axis coinciding with a terminal hepatic venule; portal venous tracts are distributed along the peripheral boundary, while sinusoids run between the terminal portal and hepatic venules, creating a nearly hexagonal vascular structure.

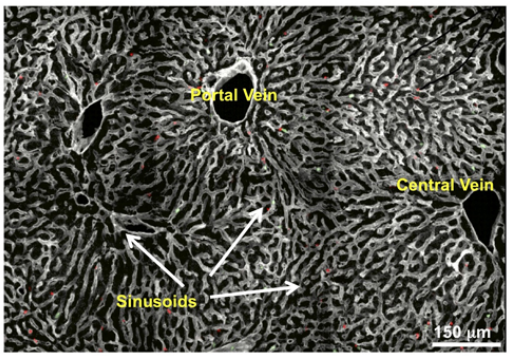

Figure 4.1: *Anatomy of the murine hepatic circulatory system,* imaged by confocal fluorescence microscopy in mosaic mode.

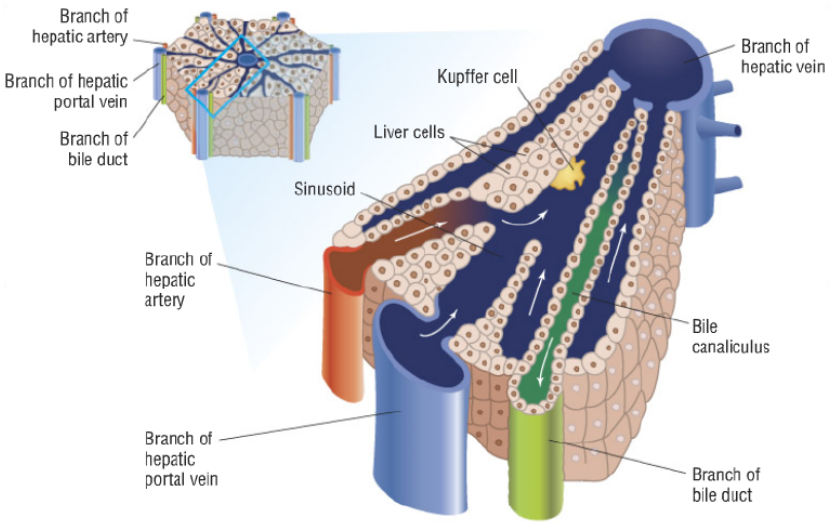

Figure 4.2: *Schematic of the functional unit of the murine hepatic circulatory system.* The classic hepatic lobule (on the left) develops hexagonally around a branch of the hepatic vein as described in the text; sinusoids distribute blood from the peripheral branches of the hepatic portal vein and artery to the central vein, while bile ducts transport the bile from the canaliculus through the extrahepatic biliary system to the gut. The lobule is in turn divided into separate subunits, each known as "hepatic acinus", as magnified on the right.

Within the complex liver vessel network, the term "hepatic microcirculation" specifically refers to the circulatory system that begins with the portal venules (50 to 100 μm in diameter), extends to the terminal portal venules (15 to 50 μm) and to the sinusoids (5 to 15 μm), and ends with the post-capillary terminal hepatic venules (~ 25 μm) and with the collecting and muscular venules (~ 40 and 60 μm, respectively) [118, 127]. All these vascular segments represent potential sites of regulation of the blood flow [128]. Nevertheless, the major blood pressure drop in the liver takes place in the sinusoids [113, 129]; even though the existence of sphincterlike specialized structures at the entrance to and at the exit from the sinusoids has not been completely demonstrated yet, there is a large body of evidence that the contractile cells contained within the sinusoids can actively control various functions of the microvasculature [114]. Among them, stellate cells, LSEC (Liver Sinusoidal Endothelial Cells) and Kupffer cells make the sinusoidal network the principal site for the regulation of blood flow and solute exchange.

4.1.1 Sinusoidal vasculature

As previously mentioned, the sinusoids network [112–115, 119, 128] represents the segment of the microcirculation in which the regulation of the hemodynamics, the supply of nutrients and the removal of metabolic products take place. It is heterogeneous in the spatial organization, with sinusoids arranged in interconnecting polygonal networks or as parallel vessels depending on the distance from portal venules and hepatic arterioles. Similarly, the diameter of the sinusoids increases from ~ 5 to ~ 15 μm when moving from the periportal to the pericentral area of the lobule. Four cell types have been recognized in the sinusoidal network [113, 130] (Fig. 4.3): (i) phagocytic Kupffer cells, (ii) extraluminal fat-storing stellate cells, (iii) pit, immunoreactive Natural Killer (NK) cells and (iv) fenestrated endothelial cells. Kupffer cells [131] are macrophages, anchored to the sinusoidal endothelium and exposed therefore to the blood stream, and are mainly responsible for the clearance of toxic or infective particulate. They are unevenly distributed within each hepatic lobule, and exhibit the largest size and greater phagocytic activity in the lobule periportal region. Stellate cells [132], by contrast, are located outside the vessel, in what is called "space of Disse": in addition to their well-documented crucial role in the regulation of the blood flow, they are responsible for retinol metabolism. Part of a population of liver lymphocytes, pit cells [133] are Natural Killers adhering to Kupffer and endothelial cells inside the sinusoids lumen; they exert antitumor functions and probably play a role in the antiviral defense of the liver. Endothelial cells (LSEC) [115, 119] finally constitute nearly half the total number of non-parenchymal sinusoidal cells and form the lining endothelium of the vessels. The structural peculiarities of this endothelium are the absence of a basement membrane and the presence of small fenestrae, approximately 170 nm in diameter, clustered in groups of 10-50 pores known as "sieve plates" (Fig. 4.3).

Sinusoidal fenestrae are of paramount importance in the liver maintenance: they dynamically respond to alterations of the sinusoidal blood flow by contraction or dilatation, they exert scavenger functions and they regulate the exchange of material between the blood and the liver cells [114]. Most importantly, they allow and even facilitate the interactions between lymphocytes and hepatocytes [134].
The lymphocytes population in the liver contains NK and NKT cells (part of the innate immune system), and T and B cells (adaptive immune system); T cells comprise in turn $CD8^+$ and $CD4^+$ T cells, with the former type typically outnumbering the latter [135]. Circulating effector $CD8^+$ T cells determine the pathogenesis and outcome of infection by clinically relevant noncytopathic viruses, such as Hepati-

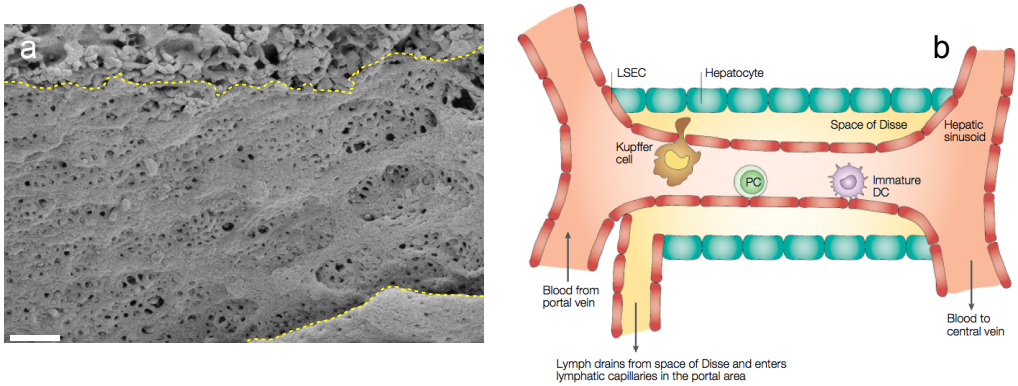

Figure 4.3: *Hepatic sinusoids.* (a): scanning electron micrograph [117] of a murine sinusoid showing the fenestrated endothelial wall and the clustering of fenestrae in Sieve plates. Scale bar=1 μm. (b): schematic of the structure of a hepatic sinusoid [116]. Several cell types are found, including Kupffer cells, lymphocytes (Pit cells), Dendritic Cells (DC) and Liver Sinusoidal Endothelial Cells (LSEC). The sub-endothelial space, known as the space of Disse, is the region from which hepatic lymph originates.

tis B (HBV) or Hepatitis C Virus (HCV) [136]. While in the brain, gut and skin $CD8^+$ T cells perform effector functions following extravasation from post-capillary venules [137, 138], it has been recently experimentally demonstrated [117] by multi-photon intravital microscopy on HBV-expressing murine models that a different mechanism regulates the migration and function of $CD8^+$ T cells in the microcirculation of the liver. Specifically, $CD8^+$ T cells first arrest within liver sinusoids by preferentially docking onto platelet aggregates; after this initial platelet-dependent arrest, they actively crawl along sinusoids and probe sub-sinusoidal hepatocytes for the presence of antigens by extending cytoplasmic protrusions through endothelial fenestrae. Hence the hepato-cellular antigen recognition process takes place before the $CD8^+$ T extravasation into the parenchyma, and T cells perform effector functions (they produce interferon-gamma IFN-γ and kill virus-expressing hepatocytes) while in the intravascular space.

The intra-vascular nature of the antigen recognition processes in the liver suggests the attractive hypothesis that the adhesion and activation of $CD8^+$ T cells may affect the sinusoidal hemodynamics. A reduction of the flow speed is expected, since the slow migration and crawling of T cells along the sinusoids and

their adhesion to platelet aggregates should lead to frequent perturbations and even temporary stasis of the blood flow. Conversely, the adhesion and activation of T cells may be favored by the morphology-dependent hemodynamic properties of specific vessels. Overall, a tight interplay between hemodynamics and T-cells priming is expected to have a pivotal role in regulating the immunological properties of the liver. Together with a systematic comparison, at the level of individual capillaries, of the intrahepatic blood flow velocity in physiological and pathological conditions, the characterization of this interplay represents one of the unanswered fundamental issues pertaining to the pathogenesis of HBV.
Notably, FLICS appears to be the optimal tool to tackle both the issues. On the one hand, it has the potential of allowing to map the blood flow velocity in extended and highly branched portions of the hepatic microcirculation, with the fundamental single-vessel sensitivity. On the other hand, by extension of the approach to multicolor imaging (specifically, by fluorescently labeling flowing particles and circulating effector T cells with spectrally separated dyes), the slow deformation dynamics of cells adhering to the vessel walls can be monitored simultaneously to the blood flow. In these regards, the combination of dynamic and morphological information offered by the exploitation of raster-scanned xy-images is a definite FLICS advantage.
With this in mind, I provide in this Chapter the characterization of the blood flow velocity at the level of individual sinusoids in the hepatic microcirculation of healthy murine models. Besides confirming the effectiveness of the FLICS method in such a complex circulatory network, I provide the baseline values for the future comparison with the blood flow velocity under HBV- or pathological conditions.

4.2 Materials and methods

4.2.1 Intravital microscopy

C57BL/6 mice have been purchased from Charles River, USA, and have been housed under specific pathogen-free conditions until 6-8 weeks of age. A tail vein catheter (VisualSonic, USA) has been inserted into previously shaved mice prior to anesthetization with 5% isoflurane (Abbot, USA) through a nose cone also delivering oxygen at 1 L/min. Then surgery and liver intravital imaging have been carried out with lower concentrations of isoflurane (between 0.8% and 1%). The surgery and the preparation of the liver have been performed as described in [117],

and the mice have been placed in a left lateral position with the left liver lobe exteriorized onto a glass coverslip attached to a custom-made imaging platform. The imaging platform has been sealed to prevent dehydration and continuous body temperature monitoring has been performed to ensure the maintenance of a narrow range of 37-38 C. The blood flow in the sinusoids has been visualized by injecting intravenously non-targeted 5 nm Quantum Dots (Invitrogen, USA) immediately before imaging (λ_{exc}=900 nm, λ_{em}^{peak}=655 nm).
All the experimental procedures have been approved by the Institutional Animal Committees of the San Raffaele Scientific Institute, Milan, Italy.

4.2.2 Experimental setup

All the measurements have been performed on an inverted two-photon microscopy setup based on a commercially available TriM Scope II scan head (LaVision BioTec). Fluorescence excitation is provided by a tunable fs-pulsed Ti:Sa laser (Ultra II, Coherent; λ=680-1080 nm, 120 fs FWHM pulse duration, 80 MHz repetition rate). The beam, for its optimization, passes through a beam-shaping device consisting of a pair of crossed polarizers that control the excitation power, a telescope for adapting the collimation of the laser beam and matching the beam dimension to the size of the objective lens back focal plane, and a prism-based chirp compensation unit that compensates for pulse broadening due to the optical components and the objective lens. The beam alignment is checked thanks to four-quadrant photo diodes placed inside the beam-shaping unit and the scan-head. A high-working distance objective (Zeiss plan-apochromat, 20x / N.A. 1.0, 1.9 mm working distance, water dipping) simultaneously excites the sample and collects the emitted signal in epifluorescence geometry. The fluorescence is steered to a non-descanned unit and split into four channels (blue, green, red and far red). Spectral separation is achieved by dichromatic mirrors and bandpass filters (455/50 nm, 525/50 nm, 590/50 nm and 665/50 nm) in front of each photomultiplier tube (3 Hamamatsu H7422-40 GaAsP High Sensitivity PMTs and 1 Hamamatsu H7422-50 GaAsP High Sensitivity PMT red extended). The entire microscope is surrounded by a custom made thermostatic cabinet in which the temperature is kept at 37 C (air thermostating by ”The Cube”, Life Imaging Services, CH).
The QDs absorption has been primed at 900 nm; the fluorescence signal has been detected through the filter 665/50 nm and the PMT gain has always been adjusted to avoid saturation in the pixels intensity. Details concerning image sizes and formats and the adopted line scan frequencies are reported in the figure captions.

4.2.3 Data analysis softwares

All the acquired images have been visualized, linearly contrast-adjusted for display and exported in *tif* format using ImageJ (U.S. National Institutes of Health, USA). Cross-correlation functions have been computed by means of the same custom-written Python code exploiting Fast Fourier Transform (FFT) routines employed for the FLICS analysis of Chapter 3. The same code has been used to apply the threshold filter to the images, as described later in the text. All the non-linear least-squares fits have been performed by the OriginPro 8.6 software (OriginLab, USA).

4.3 Experimental data

An exemplifying raster-scanned xy-image acquired by two-photon excitation intravital microscopy, at high magnification, on a single sinusoid of the murine hepatic microcirculation is reported in Fig. 4.4a. It has been built by detecting the photo-luminescence signal of 5-nm Quantum Dots (QDs), which appear as the brightest diagonal lines in the image and provide contrast with respect to non-fluorescent flowing RBCs.
Due to autofluorescence contributions and to the scattering processes inevitably occurring in a thick, living biological sample [139], the diagonal lines, alternately produced by photo-luminescent QDs and dark RBCs in the xy-image do not exhibit the high contrast and signal-to-noise ratio of the images analyzed by FLICS in Chapter 3. By estimating the ratio of the maximum detected intensity in the image to the average signal in dark regions within the vessel (i.e., outside the diagonal streaks produced by QDs), a S/N ratio well below the minimum value

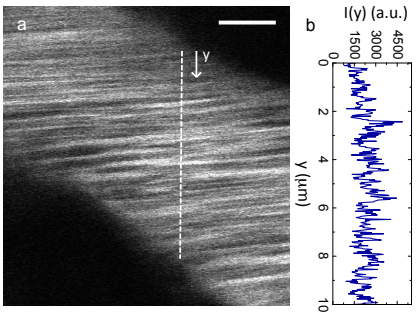

Figure 4.4: In-vivo *FLICS: signal-to-noise ratio.* (a): raw raster-scanned xy-image acquired by detecting the QDs photo-luminescence in a sinusoid of the murine hepatic microcirculatory system; f_{line}=1370 Hz, δx=0.026 μm, scale bar=3 μm. (b): photo-luminescence intensity profile extracted from the dashed white line in panel (a), evidencing the low contrast affecting xy-images acquired by multi-photon excitation intravital microscopy in the liver of living mice.

required for the FLICS analysis and identified in Section 3.5 is found (see the photo-luminescence intensity profile in Fig. 4.4b). The FLICS cross-correlation functions are therefore better computed after a threshold has been applied to the intensity counts in the pixels of the xy-image.

4.3.1 Optimal intensity threshold for the *in-vivo* FLICS analysis

The intensity threshold on the pixels intensity acts as a high-pass filter, defining a minimum photo-luminescence intensity F_{min}: for each pixel, the detected intensity is unaltered if it exceeds the adopted threshold value, and is set to zero otherwise. If the threshold is properly chosen, the background is effectively removed without affecting the estimate of the blood flow speed recovered from the diagonal lines produced by QDs.
Increasing threshold values have been tested for the image in Fig. 4.4a, and the inspection of their effect on the recovered CCFs has been adopted as a guideline for the selection of the optimal F_{min} value. As reported in Fig. 4.5f with the CCFs computed at a fixed column distance $(j-i)$=100 pixels, the higher the threshold, the higher is the amplitude of the CCF and the more discernible is its peak. Notably, no variation in the peak lag time τ_{max} is found, so that the measured flow speed value is not affected by the threshold. On the contrary, the filter on intensity values significantly affects the width of the diagonal lines produced by flowing objects in the image: the higher the adopted F_{min} value, the thinner is each diagonal streak (since pixels on the border are more likely affected by the threshold); this leads in turn to a reduced width of the recovered cross-correlation functions, possibly impacting the estimates of the diffusion coefficient and size of the imaged flowing particles. Looking for a univocal criterion to identify the threshold for the subsequent FLICS analyses, I extracted the histogram of the intensity counts of the image (Fig. 4.5e) and identified the most frequent value for the intensity counts by means of its Gaussian fit. When adopted for the threshold F_{min}, this most frequent value allows suppressing the background and recovering peaked CCFs (inset of Fig. 4.5e) without altering the obtained speed $|\underline{v}|$.

The results reported here for the specific image of Fig. 4.4a have general validity, since they exemplify what has been obtained by testing the threshold effect on a number of images acquired by intravital microscopy in the liver microcirculation (a second example will be reported in Section 4.3.3). I have therefore performed all the FLICS measurements reported in this Chapter after having excluded the intensity levels below the most frequent signal count in the examined images.

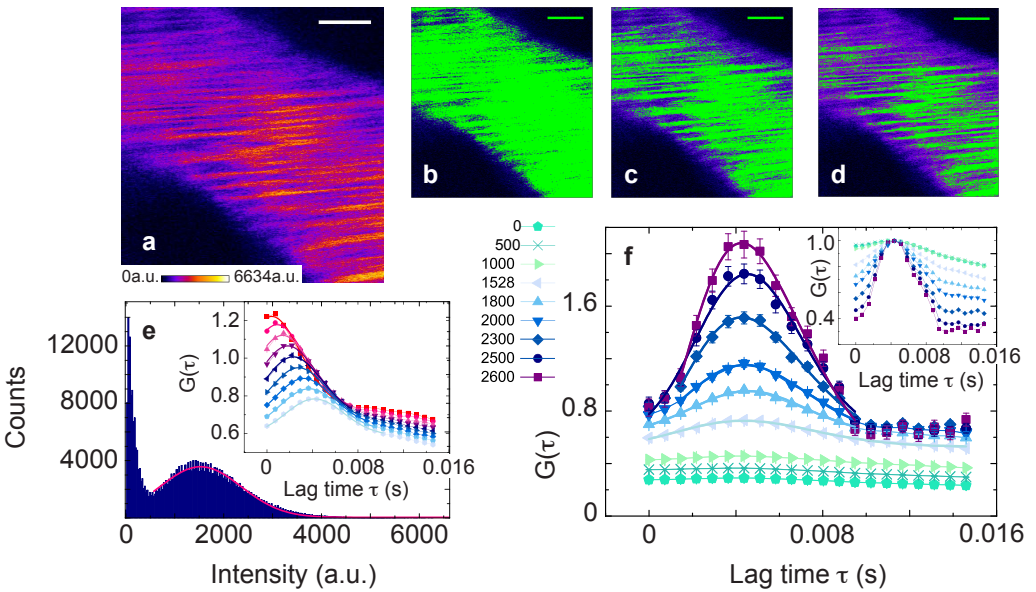

Figure 4.5: *Intensity threshold for the FLICS analysis.* (a)-(d): three exemplifying thresholds are evaluated for the image in Fig. 4.4 and reported here in panel (a) for direct comparison: F_{min}=1000 a.u. in (b), 1528 a.u. in (c) and 2000 a.u. in (d). The pixels in which the intensity exceeds the threshold (and that therefore remain unchanged for the computation of the CCFs) are uniformly green-colored; otherwise they are shown with the same LUT of panel (a). For a too low threshold value (as in b) the background is not suppressed, whereas for a much higher value (panel d) too many pixels acquire a null intensity prior to the derivation of the CCFs. An intermediate reasonable threshold is shown in (c). (e): histogram of the intensity counts for the image in (a); the threshold F_{min}=1528 a.u. adopted in (c) corresponds to the center x_c=(1528±9) a.u. of the histogram, as obtained from its Gaussian best fit (the first peak of the histogram is ascribed to the low intensity values detected outside the vessel and is therefore neglected). Inset: CCFs (mean±s.e.m.) computed on the image in (a) with the threshold F_{min}=1528 a.u. with $(j-i)$=10...90 pixels (10-pixel step). (f): effect of various thresholds (color-coded on the left in arbitrary units) on experimental CCFs (mean±s.e.m.) recovered from the image in (a) with $(j-i)$=100 pixels. The global fit to eq. (2.21) of six CCFs (with 1528 a.u. $< F_{min} <$ 2600 a.u.) provides a shared flow speed $|\underline{v}|$=(494±3) $\mu m/s$. Inset: the CCFs are normalized to highlight the independence of the peak lag time on the F_{min} value. The effect of the threshold on the CCFs width can be quantified by the (narrow) range a=1.9-2.7 μm provided for the radius of the flowing objects by the CCFs fit to eq. (2.21).

4.3.2 Cross-correlation analysis on LUT-inverted xy-images

Upon the background removal, the computation of the FLICS CCFs can be performed either on the QDs signal, or on RBCs upon a LUT inversion. To assess whether the two procedures lead to equivalent results, a LookUp Table inversion has been applied to the same xy-image reported and analyzed in Figs. 4.4 and 4.5. This operation associates the lowest intensity counts to the flowing Quantum Dots, whereas the highest counts are attributed to non-fluorescent flowing erythrocytes and to the regions outside the sinusoid (Fig. 4.6a). For the cross-correlation analysis to be performed on RBCs, a minimum intensity threshold has been adopted to exclude the contribution of QDs; additionally, an upper threshold has been introduced to prevent the areas outside the investigated vessel to interfere in the flow speed measurement. Cross-correlation functions have been computed (Fig. 4.6b) for increasing column distance in the range $(j-i)$=10...90 pixels (with 10-pixel step): their fit to eq. (2.21) provides a flow speed $|\underline{v}|$=(497±10) $\mu m/s$, that well compares with the result $|\underline{v}|$=(494±3) $\mu m/s$ previously obtained by cross-correlating the photoluminescence of QDs. The CCFs derived for $(j-i)$=10, 50, 90 pixels in

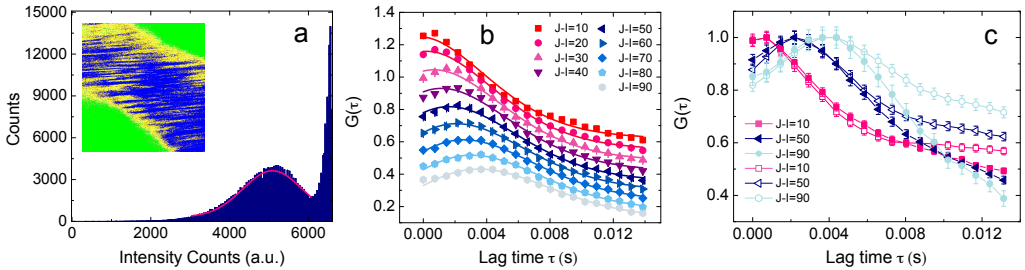

Figure 4.6: *LUT inversion for the FLICS analysis.* (a): histogram of the intensity counts for the image shown in Fig. 4.5a upon a LUT inversion. For the CCFs computation, a minimum intensity threshold F_{min}=5087 a.u., corresponding to the center of the Gaussian peak of the histogram, is adopted to exclude the contribution of QDs, shown in blue in the inset (hence the same criterion described in the previous Subsection is applied); an upper threshold F_{max}=6060 a.u. excludes the regions outside the vessel (shown in green in the inset) from the cross-correlation analysis. (b): the thresholds F_{min}=5087 a.u. and F_{max}=6060 a.u. are adopted to derive the CCFs for $(j-i)$=10...90 pixels (10-pixel step); the CCFs are overlaid to their fit to eq. (2.21). Data are reported as mean±s.e.m. (c): comparison of the normalized CCFs (mean±s.e.m.) derived for $(j-i)$=10, 50, 90 pixels by cross-correlating the signal of QDs (open symbols) and red blood cells (filled symbols).

the two cases (i.e., by the cross-correlation of the signal of QDs and RBCs) have also been directly compared (Fig. 4.6c): no differences have been found in the peak lag time of the CCFs, thereby proving again the equivalency of the two procedures for the measurement of the flow speed. What is actually affected is the width of the CCFs (and hence the diffusion coefficient and the size of the flowing objects potentially recovered by fitting the experimental CCFs). This had to be expected, since the diagonal lines produced by QDs and RBCs have a different width: for the RBCs, the width is assigned by their size and diffusion coefficient; for QDs, it is mainly regulated by the spatial separation between adjacent erythrocytes (we do not observe the diagonal streaks of individual QDs, imaging instead as a diagonal line all the QDs comprised between pairs of red blood cells). I therefore conclude that if D and a have to be estimated by the FLICS cross-correlation function, it is mandatory to cross-correlate the signal of red blood cells; if the measurement mainly aims at recovering the modulus and the direction of the flow velocity, as in this case, the FLICS analysis can be performed without any prior LUT inversion.

4.3.3 FLICS analysis of xyt-stacks

Once identified the criterion to select the optimal intensity threshold for the xy-images acquired *in-vivo* in the hepatic microcirculation, I further extended FLICS to a ROI-based approach and to dynamic studies in time. A raster-scanned xy-image has been acquired on a 50x30 μm^2 field of view, encompassing a bifurcation in the circulatory network, and the image acquisition has been repeated in time-lapse mode to generate an xyt-stack over a time interval of $\sim$ 10 seconds. At each time point, the FLICS measurement of the flow velocity has been performed separately on three Regions of Interest centered on in-focus vessels: for each ROI, the histogram of the intensity counts has been derived to identify the threshold, then the cross-correlation functions have been computed for increasing column distances and have been fit to eq. (2.21) to recover the flow speed.
The results are shown in Fig. 4.7. In panel a, the whole field of view is reported with the schematic of the vessels centerlines: these are color-coded for the retrieved flow speed $|\underline{v}|$, while arrows define the flow direction. In panels b and c, two of the examined ROIs are isolated and magnified in the first five frames of the xyt-stack: the same color-code adopted for panel a allows inspecting the magnitude, as well as the physiological fluctuations, of the flow speed in time. The temporal evolution of the speed $|\underline{v}|$ is also detailed for both the ROIs in panels d and e over the whole sampled 10-s interval; for completeness, both the exact and approximate estimates $|\underline{v}|$ and $|\underline{v}|^0$ have been derived.

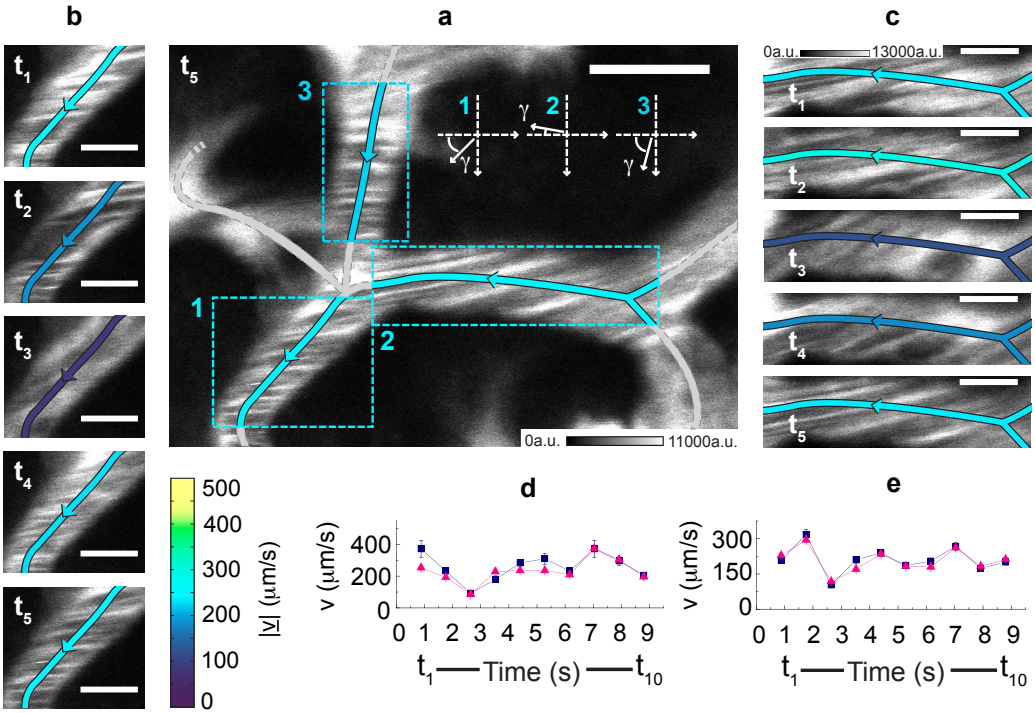

Figure 4.7: *FLICS analysis over time.* (a): raw xy-image acquired in the murine hepatic microcirculation by detecting the photoluminescence of 5-nm QDs; f_{line}=850 Hz, δx=0.05 μm, scale bar=10 μm. The cross-correlation analysis has been performed separately on the evidenced ROIs (ROI 1: 240x210 pixels; ROI 2: 450x120 pixels; ROI 3: 145x250 pixels). The estimates of the blood flow speed obtained from the global fits to eq. (2.21) of experimental CCFs are $|\underline{v}|$=(235±4) μm/s, $|\underline{v}|$=(235±3) μm/s and $|\underline{v}|$=(229±8) μm/s for ROIs 1,2 and 3, respectively; the $|\underline{v}|$ values have been exploited to color-code the vessel centerlines. The angle γ between the scan path and the flow direction is sketched in the Cartesian plane and has been fixed for the fit to 50° in ROI 1, -4° in ROI 2 and 80° in ROI 3, according to the definition of eq. (2.22). The scan frequency, the pixel size, the column distance and the beam waists (ω_0=0.5 μm, ω_{0z}=2 μm) have also been fixed in the fit. (b),(c): ROI 1 and ROI 2 are shown, in (b) and (c) respectively, in the first five consecutive frames of the temporal stack; each frame is identified by its sampling time $t_i = i\Delta t$, Δt=0.88 s being the time interval between the sampling of the same pixel in two consecutive frames i and $i+1$. The same color-code of panel (a) has been adopted for the vessel centerlines. Scale bar=5 μm, same calibration bar in a.u. for panels in (b) and (c). (d),(e): estimates for $|\underline{v}|$ (triangles) and $|\underline{v}|^0$ (squares) versus time obtained in ROIs 1 (d) and 2 (e). An average 15% overestimate of the flow speed is found in ROI 1 when the peak time alone is exploited for the speed measurement, whereas an average 7% overestimate is found in ROI 2.

Exemplifying cross-correlation functions are reported for ROI 2 in Fig. 4.8, where, as previously anticipated, I also compare the effect of several possible threshold values on the results of the FLICS analysis. As in Subsection 4.3.1, the amplitude of the CCFs increases for increasing values of F_{min}, while the peak lag time remains unchanged (Fig. 4.8c,d). Moreover, here even the CCFs computed with F_{min}=0 a.u. allow the recovery of the blood flow speed, thereby providing a reference value to validate the independence of the estimated speed $|\underline{v}|$ on the selected threshold value: the global fit to eq. (2.21) of the CCFs derived for $(j-i)$=20

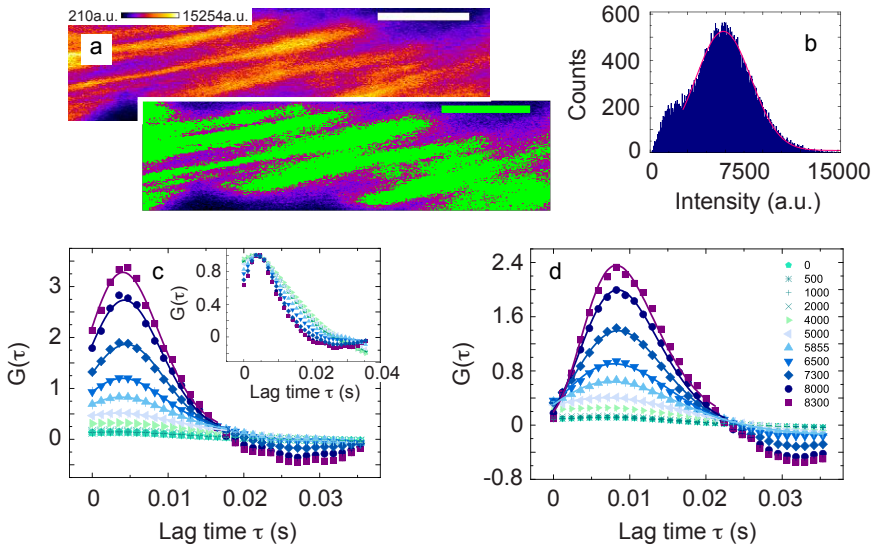

Figure 4.8: *Intensity threshold for the FLICS analysis.* (a): the ROI identified as 2 in Fig. 4.7 is reported (top panel, t_5) to allow the direct comparison with the lower panel, where the pixels having an intensity higher than the adopted threshold F_{min}=5855 a.u. (i.e., pixels kept unchanged for the CCFs derivation) are uniformly green-colored. The threshold is assigned by the center of the histogram of the intensity counts (shown in b with its Gaussian fit) as previously discussed in the text. Scale bar in (a)=5 μm. (c), (d): effect of various threshold values on experimental cross-correlation functions for the image in (a). CCFs (mean±s.e.m.) are computed for $(j-i)$=20 pixels in (c) and $(j-i)$=40 pixels in (d), for increasing F_{min} in the range 0-8300 a.u. (same color code in both panels). In the inset of panel (c), CCFs for $(j-i)$=20 pixels have been normalized to highlight the slight reduction of the correlation width with increasing F_{min} and the independence of the peak lag time on the threshold value.

and 40 pixels with F_{min}=0 a.u. leads to a speed $|\underline{v}|$=(242±8) $\mu m/s$, in agreement with the result $|\underline{v}|$=(235±3) $\mu m/s$ obtained for F_{min}=5855 a.u. (reported in Fig. 4.7). This confirms that, even when not mandatory, the introduction of the threshold does not alter the obtained results.

4.3.4 FLICS analysis on wide fields of view

When studying a larger field of view encompassing a highly intricate, geometrically complex region of the hepatic microvasculature, many sinusoidal branches can be analyzed in parallel by the ROI-based FLICS approach implemented in the previous Subsection. An exemplary result is shown in Fig. 4.9a, where a raw 110x90 μm^2 raster-scanned xy-image is reported at a selected time point along with the

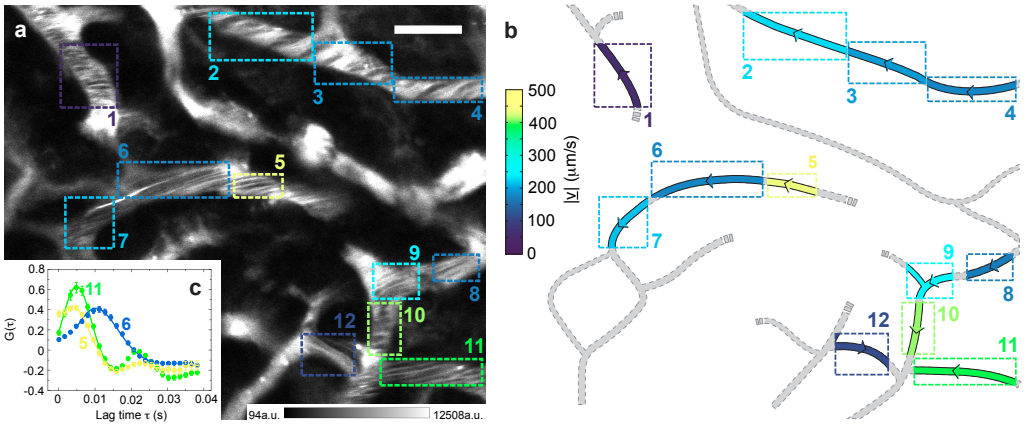

Figure 4.9: *In-vivo flow mapping in a complex vessel network by FLow Image Correlation Spectroscopy.* (a): raw raster-scanned xy-image acquired in the murine hepatic microcirculation by detecting the signal of 5-nm QDs; the lower right corner corresponds to the same region analyzed in Fig. 4.7. f_{line}=627 Hz, δx=0.102 μm, scale bar=15 μm. CCFs have been derived on the selected ROIs (~ 100x50 - 200x100 pixels) for $(j-i)$=0.51-2.55 μm; the estimates $|\underline{v}|$ and $|\underline{v}|^0$, obtained from the CCFs according to the procedures explained in Chapter 2, are reported in Table 4.1. (b): schematic of the vessels centerlines for the image in (a). In each ROI, the arrow defines the flow direction and the color codes for the speed value $|\underline{v}|$. Vessels not analyzed are shown in grey. (c): CCFs (mean±s.e.m.) computed for $(j-i)$=2.04 μm in ROIs 5, 6 and 11; their fit to eq. (2.21) yields $|\underline{v}|$=(499±18) $\mu m/s$ in ROI 5, $|\underline{v}|$=(187±2) $\mu m/s$ in ROI 6 and $|\underline{v}|$=(396±3) $\mu m/s$ in ROI 11.

twelve ROIs on which the CCFs have been derived. Despite the large field of view, the computed CCFs still show the expected peak (three examples are reported in Fig. 4.9c), allowing to recover the blood flow speed either by their fit to eq. (2.21) or by simply taking advantage of their peak lag time (eq. 2.37). Both these exact and approximate estimates $|\underline{v}|$ and $|\underline{v}|^0$, reported in Table 4.1, are comparable with the values obtained for the blood flow speed in Fig. 4.7: this is a clear indication of the possibility of applying the cross-correlation analysis to raster-scanned xy-images irrespectively of the adopted zooming factor. This conclusion is reinforced by the analysis of ROIs 10 and 11, which include the very same vessels examined in Fig. 4.7.

ROI	1	2	3	4	5	6
$\|\underline{v}\|$ [$\mu m/s$]	56±5	226±7	187±10	186±3	499±18	187±2
$\|\underline{v}\|^0$ [$\mu m/s$]	–	260 ±39	235±34	168±16	375±73	192±17

ROI	7	8	9	10	11	12
$\|\underline{v}\|$ [$\mu m/s$]	213±1	163±4	239±13	168±8	396±3	137±1
$\|\underline{v}\|^0$ [$\mu m/s$]	203±6	151±12	332±42	-	406±60	138±7

Table 4.1: *Blood flow speed in the twelve ROIs analyzed in Fig. 4.9.* Data refer to the estimates of the flow speed $|\underline{v}|$ provided by the fit of the experimental CCFs, and to the estimates $|\underline{v}|^0$ recovered directly from the peak time of the same CCFs (eq. 2.37; each estimate is the weighted average of the values obtained from the peak time of the CCFs computed for four column distances in the corresponding ROI). Apart from ROIs 1 and 10, where $|\underline{v}|^0$ could not be obtained due to its singularity (see eq. 2.39), the direct measurement of the flow speed from the cross-correlation peak time was possible in all the ROIs and led to a 0.96 average ratio $|\underline{v}|/|\underline{v}|^0$.

The results of Figs. 4.7 and 4.9 and of Table 4.1 exemplify the typical range 50-500 $\mu m/s$ that I measured for the blood flow speed in the hepatic microcirculation of healthy murine models. These results provide the reference values for a future comparison with the sinusoidal flow speed in pathological conditions. The speed values I measured by FLICS have also been cited already in [117] in the context of

the characterization of the effector $CD8^+$ T cells crawling along the liver sinusoids: following the initial interactions with platelet aggregates, T cells were shown to crawl independently of the blood direction and at a $\sim$ 10-μm/min speed that was 500- to 3.000-fold slower than the sinusoidal flow.

4.4 Conclusions and future perspectives

Throughout Chapters 2-4, I have theorized, developed and experimentally validated FLow Image Correlation Spectroscopy, a novel method to extract *absolute* flow speed values in complex vessel networks from a single raster-scanned optical xy-image acquired *in vivo* by confocal or multi-photon excitation microscopy. Before pointing out the potential future developments and extensions of the method, I now summarize the key advantages FLICS offers with respect to state-of-the-art techniques and correlation analyses:

1. FLICS does not require the scan path being parallel to the flow direction. A *single* xy-image therefore suffices for the recovery of both the modulus and the direction of the (blood) flow velocity in all the vessels within the imaged field of view, irrespectively of their orientation and of the geometrical complexity of the investigated circulatory network. In these regards, FLICS outperforms dual-beam Fluorescence Cross-Correlation Spectroscopy [33,34] and Scanning Laser Image Correlation [57], which impose stricter requirements on the alignment of the flow direction with the pairs of sampled excitation volumes (see Fig. 1.5);

2. A single scan frequency is required for the FLICS analysis, in contrast to the recently-developed RVFS (Relative Velocity Field Scanning) [67], and the choice of this scan speed is easily accomplished by live scanning the sample at decreasing f_{line} until diagonal lines appear. The scan frequencies of standard commercially available scanning microscopes (10-2000 Hz) are suitable to map blood flows, avoiding the implementation of *ad-hoc* setups or of resonant scanning heads. By contrast, given a flow speed $\sim$ 500 $\mu m/s$, a resonant scanning head is mandatory for its measurement by SLIC or by a Single Particle Tracking approach.

3. Since a single xy-frame suffices for FLICS, kinetic studies can be performed in space and time through sequential imaging (xyt- and xyz-stacks) with a typical time step of the order of 0.5-1 s.

4. By relying on image scanning along a raster pattern, FLICS allows monitoring relevant morphological parameters (e.g., the vessel diameter) simultaneously to the flow speed, with the diffraction-limited resolution (200-500 nm in the radial direction, 0.5-2 μm in the axial direction) of fluorescence confocal or intravital microscopy. In a multi-color implementation, the slow deformation dynamics of cells adhering to the vessel walls can be monitored as well. As previously anticipated, I plan to exploit this advantage to investigate the interaction between hemodynamics and the T-cell priming in the murine liver under HBV pathological conditions.

The majority of these advantages have been proven in, or exploited for, the measurements reported in Chapters 3 and 4. Considering instead the FLICS disadvantages, the main drawback of the FLICS method concerns the possibility of characterizing the velocity profile along the vessel diameter and of quantifying the vessel shear rate and shear stress. A minimum width of a few microns is required for the region of interest on which the FLICS measurement is performed: while defining the spatial resolution with which the flow speed can be mapped across the imaged field of view, this minimum required ROI size hampers the recovery of flow speed profiles in vessels less than about 20-30 μm in diameter.

I plan to further extend in the future the FLICS method to the measurement of three-dimensional velocity fields, with the discrimination of all the three components of velocity vectors arbitrarily oriented in a non-planar vascular system. Starting from the general theoretical framework of eq. (2.16), analytical simulations and *in-vitro* validation measurements will be performed to assess the impact on the cross-correlation function of both the radial and azimuthal angles subtended by the vector $\underline{v}$ with the x-, y- and z- axes. If the discrimination of the three main unknowns -namely, the flow speed and the two angles- will appear unfeasible starting from a single image acquired in the xy-plane, I will explore the alternative of sequentially collecting data in both the xy- and xz- planes. A new data analysis protocol will be devised, capable of collectively accounting for the spatio-temporal information encoded in both the images for improved parameter estimation.
I also plan to derive, starting from the same xy-image analyzed by FLICS, relevant hemodynamic parameters other than the flow speed $\underline{v}$ (for example, the hematocrit).

FLow Image Correlation Spectroscopy can be finally extended to the measurement of pulsatile, arterial flows. Efforts are ongoing to determine the effect of the periodicity of the flow on the CCF, which I have already derived analytically under the assumption of a flow speed harmonically varying in time.

Part III

Image Correlation for Intermittent Active Transport

Chapter 5

Anisotropic Gold Nanoparticles

The prefix "*nano*", which is ubiquitous nowadays in science and technology, refers to the ensemble of the peculiar structural, optical, magnetic and electronic properties arising from the confinement of matter to the nanoscale [140, 141]. Electronic confinement and higher surface-to-volume ratios [141,142] with respect to bulk materials induce unique and technologically promising properties in nanostructures and devices, turning them into the target of intense scientific exploration and into versatile tools for a number of applications in physics, biology and medicine [143–150].

In this context, noble-metal - especially gold and silver - NanoParticles (NPs) appear particularly promising for biochemical sensing [151], medical diagnostics [152] and drug or gene delivery [153] thanks to their good biocompatibility [154], the ease in synthesis [155] and the possible conjugation [156] to a variety of biomolecular ligands. Even more importantly, the characteristic 'Surface Plasmon Resonance' (SPR) [157–161] has identified in noble-metal NPs a valid alternative to fluorophore-based labelling for *in-vitro* and *in-vivo* imaging [151,162].

Driven by the nanoparticle interaction with electromagnetic waves with suitable frequency, the SPR consists in the coherent excitation and in-phase oscillation of all the free electrons within the nanoparticle conduction band. It is finely tunable in the visible and infra-red spectral region by acting on the NP size, shape and dielectric environment [163,164], and it endows noble-metal NPs with strongly enhanced extinction: the absorption and scattering cross-sections of commonly employed (40-80 nm) gold nanospheres are ~ 5 orders of magnitude higher than those of standard absorbing and fluorescing dyes [163]. It is therefore clear that these SPR-enhanced

optical properties offer multiple imaging modalities based upon the elastic Rayleigh scattering, the inelastic Raman scattering, the two-photon luminescence and the harmonic generation of noble-metal NPs [162,165–167]. Photo-thermal imaging and therapy are further allowed by the nanoparticles capability of efficiently converting light into heat via non-radiative electron relaxation dynamics [168–171].

The radiative and non-radiative properties of both anisotropic and spherically symmetric gold NPs are the object of this Chapter. By the Mie's and Gans' theories [142, 172, 173], I discuss the physical origin of the Surface Plasmon Resonance; I review the effects of the NP size and shape on the resonance condition and I emphasize the relative contributions of absorption and scattering to the total extinction cross-section, to highlight the suitability of anisotropic gold NPs for the confocal reflectance imaging exploited in the next Chapters.

5.1 The surface plasmon resonance: optical extinction

The very intense color of copper, silver and gold colloidal solutions has fascinated scientists since the turn of the twentieth century [158, 174]. For example, spherical gold nanoparticles exhibit a strong absorption in the visible ($\sim$ 520 nm) region of the electromagnetic spectrum, whereas this absorption is completely absent in bulk gold as well for particles smaller than about 2 nm. Dating back to 1908, Mie was the first to explain the red color of gold nanoparticle solutions by solving Maxwell's equations, with the appropriate boundary conditions, for a spherical metal particle interacting with an incident radiation field [172]. The only material-related quantities that Mie introduced are the frequency-dependent complex dielectric function of the metal and the dielectric constant of the surrounding medium; although not always correctly accounting for the dependence of the extinction peak and bandwidth on the nanoparticle size (Subsection 5.1.1), Mie's theory has the advantage of being conceptually simpler than more recent refined theories and has been employed to explain a number of experimental results with overall success [174, 175].

Challenges to the Mie's theory have been provided by the synthesis of monodisperse nanoparticles with a variety of anisotropic shapes: I cite, for example, cubes, prisms, wires, shells, stars and rods [157, 176–181]. The lack of spherical symmetry precludes their analytical description by Mie's theory, therefore motivating the need for a theory capable of predicting the optical properties of particles of arbitrary size and shape subject to a complex external dielectric environment. On

the one hand, prolate and oblate ellipsoidal particles are properly described by Gans' theory [173], an extension of the framework developed by Mie allowing to quantitatively describe the optical absorption spectra of gold nanorods of varying aspect ratio. On the other hand, numerical techniques -e.g. the Discrete Dipole Approximation [182], the multiple moltipole method [183] and the finite-difference time-domain method [184]- have been recently developed to model (even interacting) anisotropic particles for which the exact analytical solution of Maxwell's equations is prevented.

5.1.1 Spherical nanoparticles: Mie's theory

I begin by considering a spherical nanometer-sized metallic particle interacting with the electric field of an incoming light wave of suitable frequency. The electric field induces a polarization of the free conduction electrons with respect to the much heavier ionic core of the nanoparticle: as a result of this net charge difference, a restoring force arises from the Coulomb attraction between electrons and nuclei, leading to the coherent periodical oscillation of the electron cloud (Fig. 5.1) [142]. The oscillation period is determined by four factors: the density of electrons, the effective electron mass, the size and shape of the charge distribution [158].

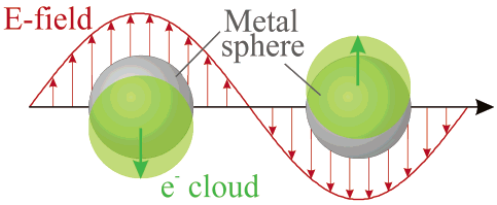

Figure 5.1: *Dipole Surface Plasmon resonance for a spherical nanoparticle.* Schematic of the displacement of the conduction electron charge in a metallic sphere interacting with an incident electric field of suitable frequency [158].

The in-phase oscillation of the conduction electrons is referred to as the 'dipole particle Surface Plasmon Resonance' (SPR) and leads to both absorption and scattering contributions within the total optical extinction of the nanoparticle. Absorption occurs due to electron-hole recombinations of either intra-band type (within the metal conduction band), or of inter-band type (between the conduction band and, for example, the d- band); by contrast, elastic Rayleigh scattering takes place when the plasmonic oscillating electric field radiates energy at the same frequency as that of the exciting incoming radiation [185].
Higher-order modes of plasmon excitation can also be induced: in the quadrupole mode, for example, half of the electron cloud moves parallel to the incident electric

field and half oscillates along the anti-parallel direction [158]. The dipole- and all the multipole- terms are accounted for in Mie's theory, which expresses the extinction, absorption and scattering cross-sections of a spherical metal particle (σ_{ext}, σ_{abs} and σ_{scatt}, respectively) as a function of the incident wave-vector, of the particle radius and of the refractive indices of both the metal and the surrounding medium (or equivalently, of their dielectric functions). Explicitly, by the series expansion of the involved fields into partial waves, the cross-sections σ_{ext}, σ_{abs} and σ_{scatt} are provided as an infinite series of multipole oscillations [142, 163]:

$$\sigma_{ext} = \frac{2\pi}{|\underline{k}|^2} \sum_{L=1}^{+\infty} (2L+1) Re(a_L + b_L) \tag{5.1}$$

$$\sigma_{scatt} = \frac{2\pi}{|\underline{k}|^2} \sum_{L=1}^{+\infty} (2L+1) Re(|a_L|^2 + |b_L|^2) \tag{5.2}$$

$$\sigma_{abs} = \sigma_{ext} - \sigma_{scatt} \tag{5.3}$$

a_L and b_L terms in eqs. (5.1)-(5.3) are given by

$$a_L = \frac{m\psi_L(mx)\psi_L'(x) - \psi_L'(mx)\psi_L(x)}{m\psi_L(mx)\eta_L'(x) - \psi_L'(mx)\eta_L(x)} \tag{5.4}$$

and

$$b_L = \frac{\psi_L(mx)\psi_L'(x) - m\psi_L'(mx)\psi_L(x)}{\psi_L(mx)\eta_L'(x) - m\psi_L'(mx)\eta_L(x)} \tag{5.5}$$

$m = n/n_m$ is the ratio of the complex refractive index n of the particle to the real refractive index n_m of the surrounding medium; $\underline{k}$ is the incident wave-vector, ψ_L and η_L are the Riccati-Bessel cylindrical functions, and the prime symbol denotes their differentiation with respect to the whole argument in parentheses. L denotes the summation over partial waves: $L = 1$ corresponds to the dipole term, $L = 2$ corresponds to the quadrupole term, etcetera. Finally, r is the particle radius and $x = |\underline{k}|r$, leading to the explicit dependence of σ_{ext}, σ_{abs} and σ_{scatt} on the size of the particle.

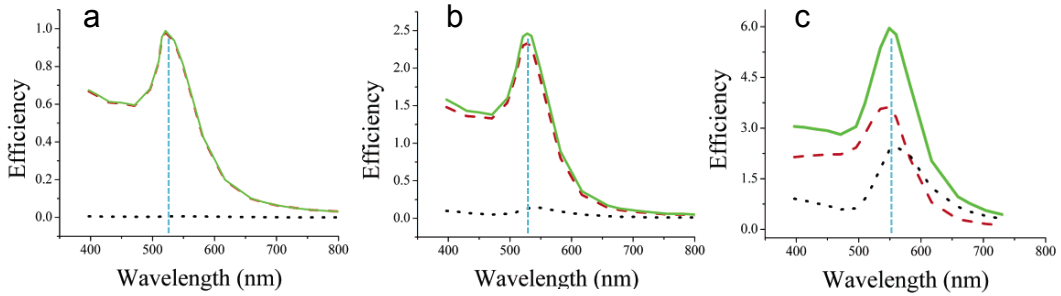

Figure 5.2: *Mie's theory for gold nanospheres.* Calculated spectra of the efficiency of absorption (red dashed), scattering (black dotted) and extinction (green solid) for gold nanospheres with diameter d= 20 nm (a), 40 nm (b) and 80 nm (c) [163]. The values for the complex dielectric function of gold, adopted for the computation, have been derived at the different wavelengths from [186] and corrected for the nanoparticles size. The dimensionless efficiencies can be exploited to recover the corresponding cross-sections σ_{ext}, σ_{abs} and σ_{scatt} by multiplication with the cross-sectional area of the nanospheres.

Extrinsic size effect

The larger the particle, the less homogeneous is the electron polarization induced by the incident electric field; as a result, higher-order (multipole) terms become increasingly important with greater particle sizes. Since higher-order oscillation modes peak at lower energies, the plasmon band blue shifts with decreasing particle radius [142,174]. This direct dependence of the optical extinction spectrum on the size of the nanoparticle is usually referred to as the 'extrinsic size effect' and follows from eqs. (5.1)-(5.5).
The extrinsic size effect has been theoretically investigated, for example, in reference [163], where the absorption, scattering and extinction efficiencies and cross-sections, computed from Mie's theory by the Discrete Dipole Approximation (DDA) method [182], have been reported for gold nanospheres of variable 20-80 nm diameter (Fig. 5.2). Both the extinction efficiency and the relative contribution of scattering increase as the nanosphere size increases. Moreover, at the wavelength λ_{max}=528 nm of the plasmon resonance maximum, 40-nm gold nanospheres have an absorption cross-section σ_{abs} ~10^{-15} m^2, leading to a molar absorption coefficient $\epsilon \sim 10^9$ $M^{-1}cm^{-1}$: common strongly absorbing dyes such as Rhodamine 6G (ϵ=1.16x10^5 $M^{-1}cm^{-1}$ [187]) have 4-orders-of-magnitude lower absorption when

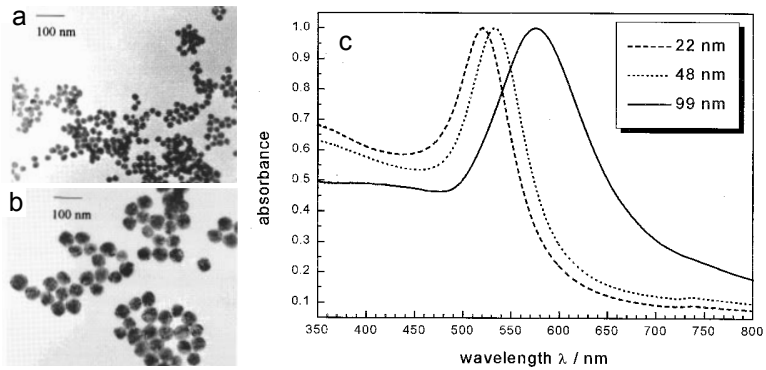

Figure 5.3: *Experimental SPR absorption spectra for gold nanospheres of increasing radius.* (a),(b): TEM (Transmission Electron Microscope) images [174] of 22 nm (a) and 48 nm (b) Au nanospheres (see details in [174] for the synthesis). (c): optical absorption spectra of 22, 48 and 99 nm gold spherical NPs in acqueous solution. All the spectra have been normalized to their maximum value, found at λ_{max}=512, 533 and 575 nm.

compared to spherical gold nanoparticles. Similarly, 80-nm gold NPs display a scattering cross-section $\sigma_{scatt} \sim 10^{-14}$ m^2 at 560 nm, which is comparable to the one of much larger (300 nm) commonly employed polystyrene beads; the same scattering signal is about 5 orders of magnitude higher than the fluorescence emission of fluorescein [187] at 483 nm, where its quantum yield is ~0.98.
The predictions of Mie's theory in the extrinsic size region have been experimentally confirmed; exemplifying results are reported in Fig. 5.3 for 20-100 nm Au nanospheres [142], exhibiting the expected longer plasmon-peak wavelengths for increasing particle radius. The same experimental data also reveal that the plasmon bandwidth decreases for decreasing particle size.

Intrinsic size effect

The investigation of the size dependence of the optical properties is more complex for particles much smaller than the wavelength λ of the incident light. For a particle diameter less than about $\lambda/20$, the electric field can be assumed to be constant over the whole particle size, and only the dipole term contributes significantly to the extinction cross-section [142, 174, 189]. By only retaining the a_1

term in eq. (5.1) [188], the explicit expression for σ_{ext} can be simplified to

$$\sigma_{ext} = 9\frac{\omega}{c}\epsilon_m^{3/2}V\frac{\epsilon_2(\omega)}{[\epsilon_1(\omega)+2\epsilon_m]^2+\epsilon_2(\omega)^2} \tag{5.6}$$

V is the particle volume, ω is the angular frequency of the incoming radiation, c is the speed of light and ϵ_m is the dielectric constant of the surrounding medium, assumed to be frequency independent. $\epsilon(\omega) = \epsilon_1(\omega) + i\epsilon_2(\omega)$ is the complex dielectric function of the nanoparticle metal, obtained phenomenologically or with the help of electrostatics. If $\epsilon_2(\omega)$ is small or weakly dependent on ω, the resonance condition can be cast as $\epsilon_1(\omega) = -2\epsilon_m$; hence the real part ϵ_1 determines the wavelength position of the resonance, while the imaginary part ϵ_2 regulates the bandwidth. I remark that the dependence of the resonance condition $\epsilon_1(\omega) = -2\epsilon_m$ and of eq. (5.6) on ϵ_m also evidences that the dielectric properties of the local environment of the NPs affect the SPR peak wavelength: this is at the basis of the exploitation of NPs as chemical or bio- sensors for (for example, adsorbate-induced) changes in the surrounding medium [185]. This applies to nanospheres and to the anisotropic nanoparticles described in the following Subsections.

Eq. (5.6) evidences that, under this so-called dipole or quasi-static approximation, σ_{ext} no longer significantly depends on the particle radius r: apart from amplitude variations due to the dependence on the volume V, the radius r does not affect the shape of the extinction spectrum. However, by implying that the surface plasmon extinction becomes size-independent for particles smaller than about 20 nm, eq. (5.6) contradicts experimental evidences: a strong absorption damping has been reported for particles smaller than 5 nm, the SPR even disappears for nanospheres smaller than 2 nm in diameter [142, 175, 190] and the SPR bandwidth depends on the particle radius.
The discrepancy probably arises from the assumption of a bulk-like structure for the electronic bands of the nanoparticle and from the introduction of the medium dielectric constant as the only material-related physical quantity entering Mie's derivation. Somehow empirically, a size dependence of the dielectric function $\epsilon=\epsilon(\omega, r)$ has been proposed for the treatment of particles less than 20 nm in diameter [142, 174]. In an alternative approach, a reduction of the electrons mean free path due to the physically limited dimensions of the nanoparticle has been pointed out as a justification of experimental results [191]. Briefly, when electrons scatter with the particle surface elastically and in a random way, the coherence of the plasmon oscillation is lost: the smaller the nanoparticle, the faster is this

coherence loss and the larger is the particle absorption bandwidth. In the formal mathematical derivation, an intra-band contribution is added to the dielectric function $\epsilon(\omega)$; according to the Drude-Sommerfeld free-electron model,

$$\epsilon(\omega) = 1 - \frac{\omega_p^2}{\omega^2 + i\gamma\omega} \tag{5.7}$$

$\omega_p^2 = ne^2/\epsilon_0 m_{eff}$ is the squared bulk plasmon frequency [192]; e, n and m_{eff} are the electron charge, density and effective mass, ϵ_0 is the vacuum permittivity and γ is a phenomenological damping constant. For a bulk metal with infinite boundaries, γ is related to the sum γ_0 of the reciprocal lifetimes of the electron-electron, electron-phonon and electron-defect scattering processes; by contrast, when the particle size turns comparable to the electron mean free path (~ 50 nm in gold [193]), an additional, even dominating, term is added due to the electron-surface scattering events. The damping constant becomes therefore size-dependent:

$$\gamma(r) = \gamma_0 + \frac{A v_F}{r} \tag{5.8}$$

where A depends on the diffusive or isotropic nature of the scattering processes and v_F is the electron velocity at the Fermi energy. By eq. (5.8), the nanoparticle radius r is explicitly inserted into the dielectric function $\epsilon(\omega)$ (in what is called an 'intrinsic size effect') and, in turn, into the extinction cross-section of the modified Mie's theory. Notably, this model predicts the experimentally retrieved $1/r$ dependence of the bandwidth [174] (Fig. 5.4).

While current theories satisfactorily model the size dependence of the plasmon bandwidth, the prediction of the resonance peak wavelength as a function of the

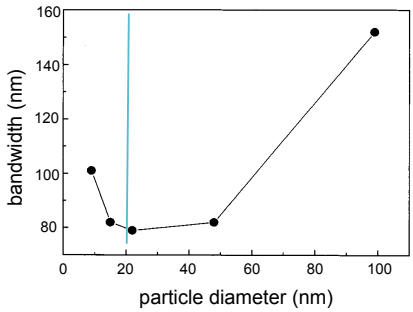

Figure 5.4: *SPR bandwidth for gold nanospheres of increasing radius [174].* The plasmon bandwidth $\Delta\lambda$ increases for increasing sphere diameter in the 'extrinsic size region' (d>20 nm), whereas it is inversely proportional to the particle radius in the 'intrinsic size region' (d<20 nm).

nanoparticle radius in the intrinsic size region is rather complex: different theories predict both a red shift and a blue shift with decreasing NP size, and both the trends have been observed experimentally [142]. Size-dependence studies are complicated by the inhomogeneous band broadening due to the non-perfect monodispersity of real NP samples. Furthermore, most synthesis protocols allow the production of nanoparticles in a limited size range: for example, the chemical reduction with sodium citrate limits to sizes above 5 nm, while reduction with sodium borhydride produces stable nanoparticles with a diameter below 5 nm. Since the matrix (the capping ligands) around the nanoparticle strongly affects the plasmon peak and bandwidth [142, 194], it is rather difficult to discriminate between a size- and a matrix- dependence within the observed experimental results [142].

5.1.2 Ellipsoidal nanoparticles: Gans' theory

The theory developed by Gans [173] in 1915 extends Mie's theory to the description of the peculiar optical properties of asymmetrical, rod-shaped nanoparticles (Fig. 5.5a). These ellipsoidal nanostructures [162], typically a ten of nanometer in width and tens to hundreds of nanometers in length [189], exhibit two separate bands within the plasmon resonance absorption spectrum [142, 151, 163, 164] (Fig. 5.5b). A first higher-energy band corresponds to the oscillation of electrons perpendicularly to the major rod axis, and is usually referred to as the 'transverse plasmon absorption band'; it is spectrally superimposed to the visible surface resonance of nanospheres and it is relatively insensitive to the rod aspect ratio R (simply defined as the ratio of the longer axis to the shorter axis of the rod-like particle). A second lower energy band corresponds instead to the oscillation of electrons perpendicularly to the shorter rod axis, and is known as the 'longitudinal plasmon absorption band'; its peak wavelength linearly red shifts with increasing aspect ratio: hence the higher R, the higher is the energy separation between the resonance frequencies of the two bands (Fig. 5.5b). Notably, the extinction longitudinal band of noble-metal rods favorably lies in the Near-InfraRed (NIR) region, a spectral window where biological tissues exhibit high transmittivity [199]: this has turned rod-like nanoparticles into one of the most widely studied classes of tunable resonant NPs for *in-vivo* imaging and applications.

From the theoretical viewpoint, the optical absorption spectrum of a collection of randomly-oriented gold nanorods, having a mean aspect ratio R, has been treated by Gans under the dipole approximation. By introducing a depolarization factor

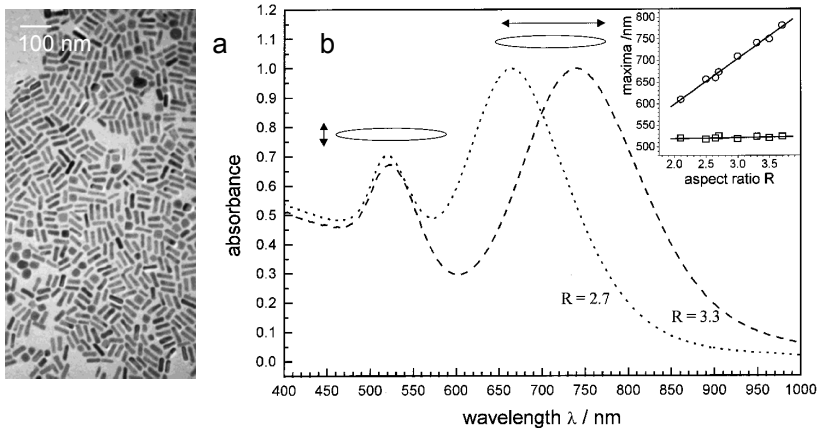

Figure 5.5: *Gold nanorods.* (a): TEM image of gold nanorods, synthesized by seed-mediated surfactant-directed synthesis (adapted from [189,195]). (b): experimental size-dependent optical absorption spectra of gold nanorods with mean aspect ratios R=2.7 and R=3.3; the transverse and the longitudinal plasmon bands are clearly distinguishable. Inset: the peak wavelengths of the two bands (longitudinal band, circles; transverse band, squares) are plotted against the nanorods aspect ratio [142].

along each of the three axes, he provided the explicit expression for the extinction, absorption and scattering cross-sections of elongated ellipsoids [142,151,164,196,197]:

$$\sigma_{abs} = \frac{2\pi}{3\lambda}\epsilon_m^{3/2} V \sum_i \frac{\epsilon_2(\omega)/n_i^2}{\{\epsilon_1(\omega) + [(1-n_i)/n_i]\epsilon_m\}^2 + \epsilon_2(\omega)^2} \tag{5.9}$$

$$\sigma_{scatt} \approx \frac{8\pi^3}{9\lambda^4}\epsilon_m^2 V^2 \sum_i \frac{[\epsilon_2(\omega)^2 + (\epsilon_1(\omega) - \epsilon_m)^2]/n_i^2}{\{\epsilon_1(\omega) + [(1-n_i)/n_i]\epsilon_m\}^2 + \epsilon_2(\omega)^2} \tag{5.10}$$

$$\sigma_{ext} = \sigma_{abs} + \sigma_{scatt} \tag{5.11}$$

As in the previous subsection, ϵ_m is the dielectric constant of the surrounding medium, ϵ_1 and ϵ_2 are the frequency-dependent real and imaginary parts of the particle dielectric function, V is the nanostructure volume, λ and ω are the wavelength and the angular frequency of the incident radiation. $n_{i=A,B,C}$ are the aforementioned depolarization factors along axes A, B and C. By assuming

$A > B = C$ and by denoting with R the rods aspect ratio,

$$\begin{cases} n_A = \dfrac{2}{R^2-1}\left(\dfrac{R}{2\sqrt{R^2-1}}\ln\dfrac{R+\sqrt{R^2-1}}{R-\sqrt{R^2-1}}-1\right) \\ n_B = n_C = \dfrac{1-n_A}{2} \end{cases} \tag{5.12}$$

For aspect ratios in the range 1-4 (practically representing the tuning of the longitudinal plasmon mode from 520 nm to approximately 800 nm), the depolarization factor n_A satisfies $n_A \approx (3R)^{-1}$: by adopting this approximation, σ_{abs} can be rewritten as

$$\sigma_{abs} \approx \frac{6\pi}{\lambda}\epsilon_m^{3/2}\epsilon_2 V R^2\left[\frac{1}{\epsilon_2^2+(\epsilon_1+(3R-1)\epsilon_m)^2}+ \right. \\ \left. + \frac{8}{(3R-1)^2}\frac{1}{\epsilon_2^2+(\epsilon_1+(1+2/(3R-1))\epsilon_m)^2}\right] \tag{5.13}$$

The first and second term in eq. (5.13) represent the longitudinal and the transverse plasmon modes, respectively. Notably, eq. (5.13) predicts the aforementioned linear dependence of the longitudinal band peak wavelength on the aspect ratio, and the practical insensitivity of the transverse band upon the same parameter R [197]. Irrespectively of the adoption of the approximation $n_A \approx (3R)^{-1}$, Gans' theory has been employed to fit the experimental optical extinction spectra of several colloidal gold nanorod samples with varying aspect ratio. Moreover, systematic studies in the optical resonance wavelength, in the extinction cross-section and in the relative scattering contribution with changes in the nanoparticle dimensions have been performed to enable the selection of the optimal NPs for absorption-based or scattering-based biological and biomedical applications.

While the rod aspect ratio affects the plasmon peak wavelength, the absolute size of the rods only modifies the magnitude of absorption, scattering and extinction without affecting the shape of the spectra (eqs. 5.9-5.11): the higher the volume V, the higher are σ_{ext} and the contribution of scattering. The magnitude of the NIR absorption and scattering (σ_{abs}=1.97x10^{-14} m^2 and σ_{scatt}=1.07x10^{-14} m^2) of gold nanorods with a hydrodynamic radius of 22 nm and an aspect ratio of 3.9 has also been shown to be comparable to that of nanospheres and nanoshells, but at a much smaller size or volume [163]: since smaller NPs usually offer better cellular

uptake, rods have been identified in [163] as the most promising nanostructures for localized photo-thermal therapies and live-cell imaging.

I finally remark that the underlying dipole approximation limits the applicability of eqs. (5.9)-(5.11) to rods smaller than about one tenth of the incident wavelength. Although the higher-order resonances of ellipsoidal nanoparticles have been successfully calculated by the Discrete Dipole Approximation method [198], Gans' theory covers the size range in which stable particles can be produced by current high yield synthesis protocols.

5.1.3 Star-shaped nanoparticles

I have already pointed out that moving from spherical to rod-like nanoparticles favorably shifts the SPR longitudinal band to the near-infrared, enabling the employment of noble-metal nanorods for imaging and theranostic applications in living cells and tissues. Beside affecting the SPR peak wavelength, the shape of the employed nanoparticles also plays a crucial role in regulating the extent and the pathways of the NPs cellular internalization [200, 201] or, when aiming at drug-delivery biomedical applications, their intravascular transport within the target organism. Many factors, including the cellular membrane stretching or the membrane bending energy, regulate the so-called 'wrapping time' required by the cell for the nanoparticle enclosure: this wrapping time is usually reduced by the spherical geometry, so that spherically symmetric NPs demonstrate a ~500% more efficient cellular uptake with respect to rod-like ones [201, 202]. A drawback of spherical NPs, of particular concern in the rapidly developing field of nanomedicine, is their limited targeting capability. When transported by the bloodstream (for example, within a vascularizing tumor), spherical NPs expose a small surface - theoretically a single point - to the blood vessel walls: the reduced contact do not support a stable, firm adhesion, thereby hampering the uptake of the drug-containing nanostructure by the target cells. Therefore, disc-like, cylindrical and hemispherical particles outperform spheres in evading uptake by phagocytic cells and in flowing through capillaries [203].

Among cubes, stars, prisms, rods and shells, I focus on star-like NPs (Fig. 5.6). Their sub-cellular dynamics and transport processes will be the object of the next Chapters: hence I refer to Section 6.1 for the description of the specific properties of the employed gold nanostars, and just anticipate here the main features of the Surface-Plasmon-Resonance bands of star-shaped nanostructures.

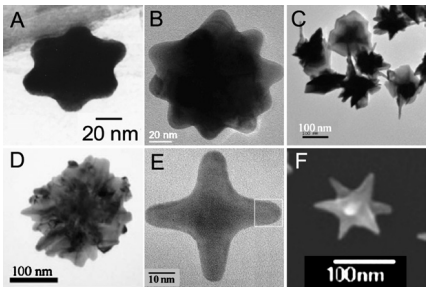

Figure 5.6: *Gold nanostars.* TEM images of different star-shaped nanoparticles (from [189] and references therein).

Stars can be modeled as a central nearly-spherical core with prolate protruding tips [204]. Since no exact analytical solution exists to predict their extinction cross-section, the Surface Plasmon Resonance bandwidth and peak wavelength are usually identified by direct experimental characterization of the nanostar sample. These characterizations, performed by single particle spectroscopy, have already revealed that star-shaped NPs are endowed with multiply peaked absorption and scattering spectra [205]. Each peak is related to a specific tip of the star: exactly as for nanorods, the longitudinal peaks found in the near-infrared for single Au nanostars can be ascribed to the plasmonic oscillation of electrons perpendicularly to the tips. This rather intuitive conclusion has been verified by inspecting the dependence of the amplitude of the individual peaks, within the scattering spectrum of single nanostars, on the polarization of the exciting radiation: the scattered light is linearly polarized at a distinct angle for each peak [205], strongly suggesting that the different plasmon resonances of the star are associated to its different tips [204] (the probability of excitation of each plasmon mode depending on the square of its dipole moment along the incident electric field).[1] All the peaks, corresponding to the individual tips of the nanostars, contribute in defining the overall absorption and scattering spectra of the nanostar solution, which exhibit broad yet well-defined peaks in the visible and NIR [205].

[1]The same polarization dependence applies to the plasmon resonances of nanorods: if rod-like particles are embedded in a matrix and they are parallel to each other, only the longitudinal band appears for an incoming radiation polarized parallel to the long axis of the rods. Conversely, only the transverse mode is excited if the incident beam is polarized perpendicularly to the rods long axis [188].

5.2 Photoluminescence properties of gold nanoparticles

As previously noticed, the SPR-enhanced extinction cross-section of plasmonic nanoparticles make them efficient contrast agents in optical imaging. As the scattering signal is orders-of-magnitude higher than the fluorescence emission from synthetic dye molecules, spherical and anisotropic noble-metal NPs are well suited for biomedical imaging using confocal reflectance or dark-field microscopy [151,162]. Dark field light scattering has been successfully employed, for example, to monitor the receptor-mediated uptake of gold nanorods by HeLa cells [206], or for cancer diagnosis by using anti-EGFR (anti-Epidermal Growth Factor Receptor) antibody-conjugated gold nanorods [170].

A bright alternative to light scattering for biomedical imaging is the detection of the strong photo-luminescence signal emitted by plasmonic NPs.
Even though gold is known to quench the emission of nearby fluorophores due to back-electron transfer, Mooradian reported in 1969 the emission of a weak photoluminescence signal from bulk gold [207]. The photoluminescence from bulk noble metals has been attributed to the radiative recombination of the excited electrons in the sp band with the holes in the d band [142] (Fig. 5.7a). Specifically, a three-step process has been proposed [142,162,208]: at first, electrons are excited from the filled d band to electronic states above the Fermi level in the sp conduction band and generate electron-hole pairs; then, a partial energy transfer to the phonon lattice occurs on the picosecond timescale, followed by the radiative recombination of some electron-hole pairs and photon emission. The quantum efficiency of the single-photon luminescence is typically very low (of the order of 10^{-10}), but is increased by several orders of magnitude on rough surfaces of noble metals [209]; rough surfaces can be regarded as a collection of nanometer-size randomly oriented hemispheroids, which exhibit surface plasmon resonances and lead therefore to the amplification of the incoming and outgoing electric fields. This so-called 'lightning rod effect' [209,210] also occurs for nanoparticle aggregates, or single nanoparticles, strongly enhancing both their Raman scattering signal (thereby referred to as SERS, or Surface-Enhanced Raman Scattering) and their photo-luminescence signal [142].

Even more appealing for imaging applications is the Two-Photon excited Luminescence (TPL) signal of noble-metal NPs [162,167,211,212]. The TPL properties and mechanism have been largely investigated by near-field and far-field optical scanning techniques. Far-field microscopy, employed in [167] to probe the TPL of gold nanorods, has revealed that, when excited at the peak IR wavelength of the

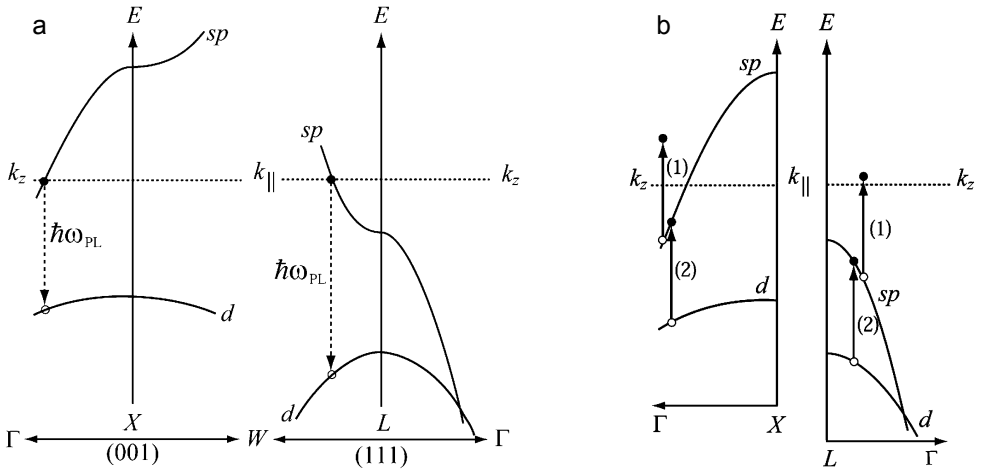

Figure 5.7: *Two-photon luminescence of gold nanoparticles [212].* (a): schematic diagram of the band structure near the X and L symmetry points in the first Brillouin zone of gold. In gold crystals, optical transitions preferentially occur near the X and L points due to the high density of states. $\hbar\omega_{PL}$ denotes the photon energy of the photo-luminescence radiated by filling a hole with an electron from the sp band; dashed lines denote the Fermi surface. (b): excitation scheme of sequential one-photon absorptions near the X and L symmetry points in gold. In both (a) and (b), open and filled circles identify holes and electrons, respectively.

longitudinal plasmon band, gold rod-like nanoparticles emit in the broad 400-650 nm spectral region. Two peaks have been found close to the 520-nm and to the 630-nm wavelengths expected from the electron-hole recombination near the X and L symmetry points of the Brillouin zone, corresponding respectively to the (001) and (111) lattice planes in the gold ffc crystal. The non-linear nature of the excitation process has been confirmed by the quadratic dependence of the emitted intensity on the excitation power, and the dependence of the emitted TPL on the excitation polarization has been demonstrated to follow a cosine function to the fourth power. This dependence resembles the one established for two-photon excited fluorescent molecules, and suggests that a coherent two-photon absorption process is at the basis of the TPL generation. By contrast, the emitted TPL has been shown to be essentially depolarized.

Complementarily, Near-field Scanning Optical Microscopy (NSOM) has been

adopted by Imura *et al.* [212] to perform the same polarization-dependence characterization of the TPL signal of gold nanorods. A dependence on a cosine function to the second power has been revealed on the excitation polarization, and two sequential one-photon processes have been pointed out to explain the TLP emission and the observed results. Initially, a first photon excites via an intra-band transition an electron in the sp conduction band from a level below the Fermi energy to a level above the Fermi energy; at the same time, a hole is created in the sp conduction band below the Fermi level. Then, a second photon excites an electron from the d band to sp band, where the hole was created by the first photon; finally, an electron-hole recombination results in the photo-luminescence emission (Fig. 5.7b). The probability of the first transition is maximized when the exciting radiation is polarized parallel to the rod axis, whereas the second transition is polarization-insensitive. Although questioned by the experimental results of other groups [166, 167], the TPL mechanism proposed in [212] agrees with the peculiar dependence of the two-photon excited luminescence of Au nanostructures on the temporal width of the excitation laser pulses [213].

Chapter 6

Gold Nanostars Intracellular Dynamics: Results in r-Space

The capability of converting the absorbed energy into heat via non-radiative electron relaxation dynamics and of inducing localized heating effects [142,162,168] makes gold NanoParticles (NPs) widely employed for cancer cell photothermal treatments [169–171] or as nanocarriers that can thermally release loaded molecules [214,215]. This especially applies to NPs of asymmetric shapes, such as rods and stars, that - as described in the previous Chapter - exhibit the major plasmon resonance absorption band in the convenient near infrared region of the electromagnetic spectrum. This same absorption band also confers to asymmetric NPs a large luminescence signal upon two-photon excitation in the IR peak, thereby creating an intrinsic optical tool to detect them in living systems [167,216].
For the rational design and optimization of the imaging-based and photo-thermal therapy applications of gold nanoparticles, the characterization of their cellular internalization and of their intracellular trafficking pathways is mandatory: in order to develop nanodevices that can target cell organelles or act on specific cell metabolic paths, it is critical to know how the internalization process occurs and, even most importantly, how the NPs behave once inside the cytoplasm.
To date, no unique model has been devised for the intracellular transport of nanoparticles and, more in general, of organelles, vesicles and cargoes. Experimental results reported in the literature vary form Brownian motion [217,218] to anomalous super- [218–220] and sub- [221,222] diffusion, the latter being usually described with the aid of approximate, effective models [221,223]. Elastic trapping,

obstructions, meshwork-like domains, stalling events and the action of molecular motor proteins [220, 224] contribute to limit or enhance simple sub-cellular Brownian diffusion, producing complex transport dynamics. Overall, due to the heterogeneity of the cytoplasmic environment and to the resulting variability of intracellular transport mechanisms, it would be very useful to derive some sort of 'model-free' analysis protocol capable of quantitatively characterizing the mode of motion (of gold nanostars or biological macromolecules) without any prior assumption on its Brownian or super-diffusive nature. The search and development of such a model is the object of Chapters 6-8, where live-cell time-lapse confocal imaging and the detection of the scattering signal of branched Gold NanoStars (GNSs) are exploited to follow their dynamics upon internalization in HeLa cells.

In this Chapter, I determine at first the characteristic timescale of the GNSs intracellular motion by the TICS (Temporal Image Correlation Spectroscopy [47]) analysis of the acquired xyt- temporal sequences of raster-scanned confocal images; then I identify the different transport mechanisms underlying the GNSs dynamics by STICS (Spatio-Temporal Image Correlation Spectroscopy [48]), and I discuss the possible theoretical models of enhanced diffusion.

6.1 Materials and Methods

6.1.1 Cell culture

The intracellular dynamics of gold nanostars has been investigated in HeLa human cervical cancer cells. The cells have been cultured in complete DMEM (Dulbecco Modified Eagle Medium) with 10% FBS (Fetal Bovine Serum) at 37C with 5% CO_2, and have been routinely split 1:10 in culture dishes when at ~80% confluence. The cells have been incubated for 4 hours at 37 C with a GNSs concentration of 25 $\mu g/ml$, which has been proven by previous viability tests to be non-cytotoxic to cells up to 24 hours [216]. For the incubation process, no FBS has been added; this allows avoiding protein-corona effects and the consequent alteration of the GNSs hydrodynamic size.

6.1.2 Gold nanostars

GNSs have been synthesized by a laurylsulphobetaine (LSB)-driven seed-mediated growth as described in [226, 227], with an LSB concentration [LSB]=0.35 M. They have a moderately negative surface charge, with ζ-potential ζ=(-27$\pm$6)

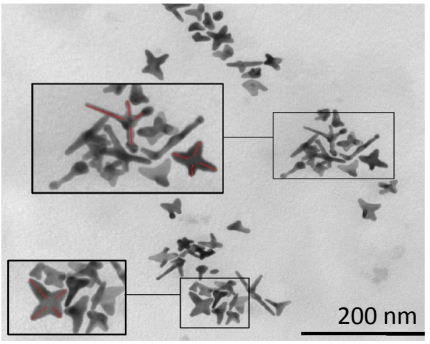

Figure 6.1: *Gold nanostars (I).* Exemplary TEM image of star-shaped nanoparticles synthesized with an LSB concentration [LSB]=0.35 M.

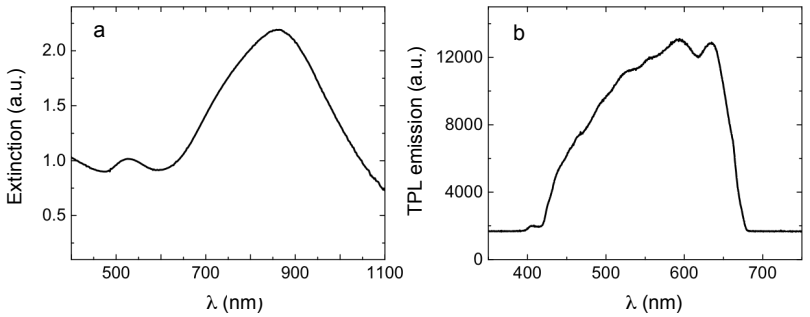

Figure 6.2: *Gold nanostars (II).* (a): extinction spectrum of the GNSs shown in Fig. 6.1. (b): two-photon luminescence spectrum of the GNSs shown in Fig. 6.1; the cut-off at 670 nm is due to the presence of a dichroic filter in the optical path. Excitation wavelength λ_{exc}=800 nm, average excitation power P=2 mW.

mV [216]. As derived from Transmission Electron Microscopy (TEM) images (Fig. 6.1), the GNSs have average branch sizes of (53±12) nm and (9±2) nm, yielding a transverse plasmon extinction band around 530 nm and a longitudinal plasmon band centered at 850 nm (Fig. 6.2a). When subject to two-photon excitation in the infrared peak, the GNSs exhibit a strong photo-luminescence signal as a consequence of electron-hole recombinations near the X and L points of the Au Brillouin zone: the resulting TPL emission spectrum is a broad band at visible wavelengths (Fig. 6.2b).

In order to quantify the extent of the nanoparticles aggregation in solution, that could impact or even inhibit the GNSs cellular internalization, Raster Image Correlation Spectroscopy (RICS) [52] measurements have been performed in the cell culture medium according to the formalism described in Section 1.3.2. A diffusion coefficient D=(2.1±0.2) $\mu m^2/s$ has been recovered (Fig. 6.3), corresponding to a hydrodynamic radius r=(106±10) nm and to an average aggregation number of ~ 3 units.

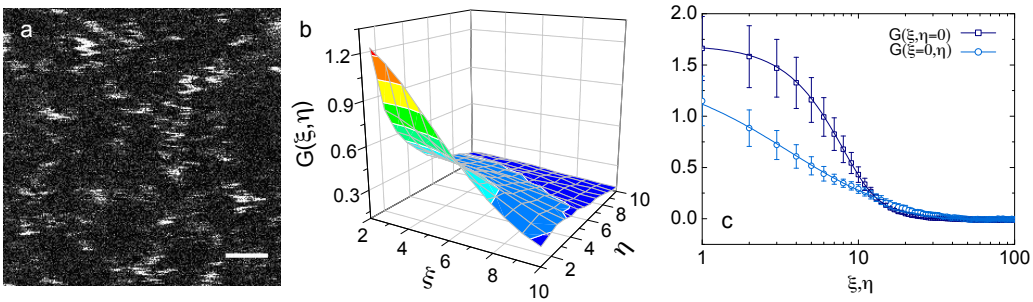

Figure 6.3: *Gold nanostars: RICS measurements in solution.* (a): maximum intensity projection of a 100-frame raster-scanned xyt-stack acquired by detecting the scattering signal of GNSs freely diffusing in the cell culture medium (scale bar=1 μm, δx=0.025 μm, scan frequency per line f_{line}=700 Hz, pixel dwell time τ_p=1.4 μs). As described in Section 1.3.2, GNSs are imaged as irregular streaks, so that the diffusion coefficient can be recovered by the spatial correlation of the detected signal according to eq. (1.50). The correlation function is computed separately for each frame of the stack; then the results are averaged to ensure adequate statistics. (b): exemplifying RICS spatial correlation function $G(\xi,\eta)$ recovered from the xyt-stack reported as maximum projection in panel (a). Only a portion ($\xi,\eta \in [0,10]$ pixels) of the correlation function is shown for the sake of display. (c): $G(\xi,\eta=0)$ and $G(\xi=0,\eta)$ profiles extracted from the RICS correlation function averaged over five 100-frame xyt-stacks. The global fit of the profiles to eq. (1.54) leads to a diffusion coefficient D=(2.1±0.2) $\mu m^2/s$; δx, τ_{line}, τ_p and the excitation laser beam waist ω_0=0.2 μm have been treated as fixed parameters in the fit. I refer to Section 3.2 for the description of the experimental setup, and to Subsection 6.2.1 for the justification of the extension of the fluorescence formalism of eq. (1.54) to the detection of a light-scattering signal.

6.1.3 Confocal reflectance microscopy

For the TICS and STICS analysis described in this Chapter, as well as for the analyses by Single Particle Tracking and by k-Space Image Correlation Spectroscopy

reported in Chapters 7 and 8, data have been acquired in the form of temporal sequences of raster-scanned xy-images by means of a Leica TCS SP5 confocal microscope (Leica Microsystems, Wetzlar, Germany). I refer to Section 3.2 for the description of the available laser lines, objectives and detection units of the set-up. The GNSs scattering signal has been primed by the 488 nm line of the Argon ion laser or by the 633 nm line of the He:Ne laser, with a typical power P=20 μW; the signal has been collected in back-scattering geometry by the 40x plan-apochromat oil immersion objective. The numerical aperture N.A.=1.3, corresponding to a subtended semi-angle θ=60° (refractive index n=1.518), defines the range $120° - 240°$ for the signal-collection angles under the adopted back-scattering geometry. A photomultiplier tube has been employed for the signal detection at 488 nm or 633 nm; no offset has been applied, a 8-bit dynamic range has been selected and the PMT gain has been adjusted to avoid saturation in the pixels intensity.

As justified later in the text, the images have been acquired with a 400 Hz line scan frequency continuously up to 500 frames, on fields of view 30-40 μm in side. With a 1024x1024 resolution, this corresponds to an image acquisition time τ_f=2.5 s and to a typical pixel size δx=0.03-0.04 μm. For the TICS analysis only, pixels have been re-binned to a final size comparable to the microscope point-spread-function (0.2 μm).

Raster-scanned scattered- and transmitted- light images have been acquired simultaneously and the superposition of the first and last frames of both the xyt-stacks has been exploited to exclude the loss of the z- focal plane positioning and the occurrence of whole-cell displacements throughout the acquisition.

6.1.4 Two-photon excitation microscopy

Two-photon excitation microscopy has been employed for comparison with the results of confocal reflectance microscopy. Photo-luminescence imaging has been performed on a BX51-FV300 scanning microscope (Olympus, Japan) modified for direct (non-descanned) detection of the signal and coupled to a femtosecond Titanium:Sapphire laser (Mai Tai, Spectra Physics, USA; repetion rate 80 MHz, pulse Full-Width-Half-Maximum 100 fs). The microscope is equipped with a water immersion objective (N.A. = 1.1, 60x, working distance=1.5 mm; Olympus, Japan). The two-photon luminescence of gold nanostars has been primed by excitation at λ=800 nm, with power P=3 mW, and has been selected by a band-pass filter at 535 nm (HQ535/50, Chroma Inc., USA).

6.1.5 Data analysis softwares and simulation codes

All the acquired images have been visualized, linearly contrast-adjusted for display and exported in *tif* format using ImageJ (U.S. National Institutes of Health, USA). TICS and STICS correlation functions (and the kICS correlation functions in Chapter 8) have been computed by a custom-written Python code exploiting Fast Fourier Transform (FFT) routines, whereas non-linear curve fitting has been performed by the Origin Pro 8.6 software (OriginLab, Northampton, USA). The zero-lag TICS and STICS correlation values have always been excluded from the fitting procedure.

6.2 Reflectance imaging of gold nanostars

The detection of the Two-Photon Luminescence (TPL) of anisotropic noble-metal nanoparticles, and the detection of their scattering signal, represent the two most valuable options for the observation of plasmon-resonant nanostructures in living cells. The benefits of two-photon excitation and TPL-based imaging are manifold [162, 228–230]: (i) the TPL can be excited at near-infrared frequencies between 700 and 1000 nm, the window of greatest transmittivity through biological tissues; (ii) two-photon excitation provides intrinsic optical sectioning and, by drastically reducing the excitation in out-of-focus planes, it reduces the photo-toxicity for the specimen; (iii) the power densities required for TPL imaging are orders of magnitude below the damage threshold of biological tissues [162]. However, a two-photon setup is not always available in most the laboratories, where a scanning confocal microscope exploiting visible laser lines is usually present. This is the major drawback of TPL-based imaging, and suggests the alternative of exploiting the huge scattering cross-section of noble-metal NPs in the visible region of the e.m. spectrum.
When considering excitation and detection at visible wavelengths, scattered light also outperforms the detection of the (one-photon excited) fluorescence signal emitted by nanoparticle-dye constructs: the labeling and functionalization of nanoparticles with fluorescent dyes often lead to the uncontrolled release of dye molecules in the cytoplasm or in the acidic environment of lysosomes and endosomes; moreover, it may alter the NPs surface charge and aggregation state.
Provided these considerations, the detection of the nanoparticles back-scattered radiation shares the dye-free approach of two-photon luminescence, without neces-

sitating the instrumentation and pulsed laser sources required by the TPL excitation. This motivates the adoption of confocal reflectance imaging [231] for the investigation of the GNSs intracellular dynamics.

At first, the possibility of discriminating the scattering signal of gold nanostars from the background reflected signal of cellular structures has been verified. To this aim, raster-scanned xy-images have been acquired by confocal reflectance microscopy on GNSs-treated HeLa cells, upon 4 hours incubation at 37 C, and have been compared with those acquired, under the same condition and acquisition settings, on untreated cells. The comparison (Fig. 6.4a,b) reveals that GNSs are well distinguishable over the background signal scattered by cellular organelles, and are internalized (with what is often described in the literature as an endocytosis process [201,232,233]) within vesicles comparable or larger than the microscope PSF. The typical size of the vesicles, 260$\pm$35 nm, has been determined by the Gaussian fits of the radial intensity profiles extracted from 20 separate objects.

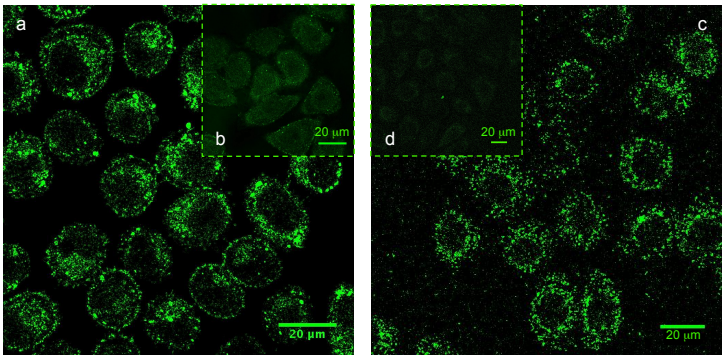

Figure 6.4: *Gold nanostars cellular uptake.* (a): GNSs uptake in HeLa cells monitored by detecting the GNSs scattering signal. λ=488 nm, P=20 μW; the image is a single frame of an xyz-stack, that with the optical sectioning properties of confocal microscopy has been exploited to verify that GNSs are within the cell instead of being located on the upper membrane. (b): image acquired under the same imaging conditions and settings of panel (a) on untreated HeLa cells. (c): GNSs uptake in HeLa cells monitored by detecting the GNSs two-photon excited photo-luminescence; λ_{exc}=800 nm, P=3 mW. Panels (a) and (c) evidence a similar intracellular distribution of gold nanostars and identify scattered light as a powerful alternative to TPL for the GNSs imaging. (d): image acquired under the same imaging conditions and settings of panel (c) on untreated HeLa cells.

The results obtained by confocal reflectance imaging have also been compared with those of two-photon excitation microscopy (Fig. 6.4a,c). The TPL signal, primed by excitation within the near-infrared longitudinal plasmon band of the GNSs, reveals a similar intracellular distribution for the nanoparticles, which accumulate in ~ 250 nm vesicles within the cell cytoplasm without penetrating the nucleus.

6.2.1 Light scattering form factors

The detection of the GNSs scattering signal clearly allows the identification of the nanoparticles over the low background produced by cellular structures. Prior to employing reflected light to probe dynamic transport processes at the sub-cellular level, it is necessary to verify which formalism - the one of Dynamic Light Scattering (DLS) [234–236], or the one of Fluorescence and Image Correlation Spectroscopy [1, 11, 12, 17, 42] - is better suited to describe the experimental data. Specifically, the spatial and temporal variations exhibited by the GNSs scattering signal within the acquired xyt-stacks may be ascribed to number and/or phase fluctuations. Number fluctuations may be produced by the diffusive or directional motion of GNSs-containing endocytotic vesicles in and out of the excitation volume, and are at the basis of the fluorescence-correlation formalism I have extensively treated in Chapter 1; by contrast, the presence of phase fluctuations, and the consequent coherence effects, would largely affect the spatio-temporal correlation functions and would hamper the convenient adoption of the FCS approach for the analysis of confocal-reflectance-imaging data.

Recalling that GNSs are internalized within 200-300 nm vesicles and recalling the hydrodynamic radius r=(106±10) nm of the employed nanostars, a density of 2-3 nanoparticles/vesicle can be expected: hence, in the present case, phase fluctuations may arise from the roughness and internal structure of the vesicles from which the scattering signal being detected originates.

Light scattering form factors can be employed to quantify the extent of these phase fluctuations [235]. I have therefore simulated the form factor $P(\theta)$ of a single sphere 300 nm in radius, and I have compared the result to the form factor $P_3(\theta)$ of an aggregate composed of three smaller spheres, each of them having a 100 nm radius to resemble the hydrodynamic radius of a single GNS. In this notation, θ is the angle defined by the scattered wave-vector $\underline{k}_s$ with respect to the incident wave-vector $\underline{k}_i$; the form factors $P(\theta)$ and $P_3(\theta)$ have been simulated throughout the whole $0° - 360°$ θ range, covering therefore the collection angles ($\theta = 120° - 240°$) of the employed

microscope objective in back-scattering geometry. The reasonable, yet geometrically simple and analytically treatable, configuration that I have assumed for the three spheres is shown in Fig. 6.5a: the spheres are aligned along an arbitrary direction subtending an angle α with the optical z-axis, and are separated by a distance $|\underline{\Delta}|$. As described in the following, the form factors for single and aggregate spheres have been simulated at different values of both α and $|\underline{\Delta}|$.

The scattering form factor of the three-sphere aggregate can be derived analytically by extending the derivation of the factor $P(\theta)$ of a single sphere of radius R and volume V [235], which is given, under the assumption of elastic scattering ($|\underline{k}_i|=|\underline{k}_s|$), by

$$P(\theta) = \int d\underline{r}\rho(\underline{r})e^{i\underline{q}\cdot\underline{r}} \tag{6.1}$$

$|\underline{q}| = |\underline{q}|(\theta) = |\underline{k}_s - \underline{k}_i| = 4\pi n/\lambda \sin(\theta/2)$, where n is the refractive index of the medium and λ is the incident-beam wavelength [234,235]. $\rho(\underline{r})$ is given by

$$\rho(\underline{r}) = \begin{cases} 0, & \text{if } r > R \\ 1, & \text{if } r \leq R \end{cases} \tag{6.2}$$

The computation of the integral in eq. (6.1) over the whole space is straightforward in polar coordinates and leads to

$$\begin{aligned} P(\theta) &= V\frac{3}{(|\underline{q}|R)^3}[\sin(|\underline{q}|R) - (|\underline{q}|R)\cos(|\underline{q}|R)] \\ &= V\frac{3}{\left(4\pi n/\lambda \sin\frac{\theta}{2}R\right)^3}[\sin\left(4\pi n/\lambda \sin\frac{\theta}{2}R\right) - \left(4\pi n/\lambda \sin\frac{\theta}{2}R\right)\cos\left(4\pi n/\lambda \sin\frac{\theta}{2}R\right)] \end{aligned} \tag{6.3}$$

Similarly, for the three-sphere aggregate described by the geometry of Fig. 6.5a $P_3(\theta)$ can be computed as

$$P_3(\theta) = \int d\underline{r}\rho(\underline{r})e^{i\underline{q}\cdot\underline{r}} + \int d\underline{r}\rho(\underline{r}+\underline{\Delta})e^{i\underline{q}\cdot\underline{r}} + \int d\underline{r}\rho(\underline{r}-\underline{\Delta})e^{i\underline{q}\cdot\underline{r}} \tag{6.4}$$

Since

$$\int d\underline{r}\rho(\underline{r}\pm\underline{\Delta})e^{i\underline{q}\cdot\underline{r}} = P(\theta)e^{\mp i\underline{q}\cdot\underline{\Delta}} \tag{6.5}$$

$P_3(\theta)$ is given by

$$\begin{aligned} P_3(\theta) &= P(\theta)\left[1 + 2\cos\left(\underline{q}\cdot\underline{\Delta}\right)\right] \\ &= P(\theta)\left\{1 + 2\cos\left[\frac{2\pi n|\underline{\Delta}|}{\lambda}\left(\cos\alpha(\cos\theta - 1) + \sin\alpha\sin\theta\right)\right]\right\} \end{aligned} \tag{6.6}$$

with $P(\theta)$ provided by eq. (6.3).

As anticipated previously, eqs. (6.3) and (6.6) have been employed to simulate $P(\theta)$ and $P_3(\theta)$ under a geometry capable of mimicking GNSs enclosed in cellular vesicles. Hence a radius R=300 nm has been adopted to simulate $P(\theta)$, whereas a radius R=100 nm has been adopted for each of the three spheres described by $P_3(\theta)$; the distance $|\underline{\Delta}|$ has been varied between 200 and 600 nm, and four possible orientations (α=0°, 30°, 90° and 150°) of the three-sphere aggregate in the xz-plane have been evaluated. The results are reported in Fig. 6.5b,c and evidence that, for $\theta \in [120° - 240°]$, the form factors $P(\theta)$ and $P_3(\theta)$ almost coincide. This strongly suggests that a three-GNSs aggregate practically behaves as a single larger particle, and that the phase fluctuations associated to the enclosure of (possibly multiple) GNSs within the cellular vesicles are negligible in the experimental conditions of the present work.
The presence of phase fluctuations arising from fast sub-vesicle dynamics (i.e., arising from the motion of single GNSs within the vesicles) has been excluded as well: as discussed later in the text, TICS and RICS measurements performed at high temporal resolution ($\sim$ 0.2 s/frame, 1 ms/line, 5 μs/pixel) on selected intra-cellular regions do not reveal any decay in the temporal correlation function (in the case of TICS) and lead to spatial correlation functions coinciding with the microscope PSF (in the case of RICS).

In summary, the results of this Subsection demonstrate that, in the present case, the scattering signal of gold nanostars can be treated, from the theoretical and practical viewpoint, as if was fluorescence: apart from the substitution of the product of the absorption cross-section and of the fluorescence quantum yield by the scattering cross-section, the formalism of Fluorescence Correlation Spectroscopy can be adopted for the description and analytical derivation of the temporal and/or spatial correlation functions employed throughout Chapters 6-8.

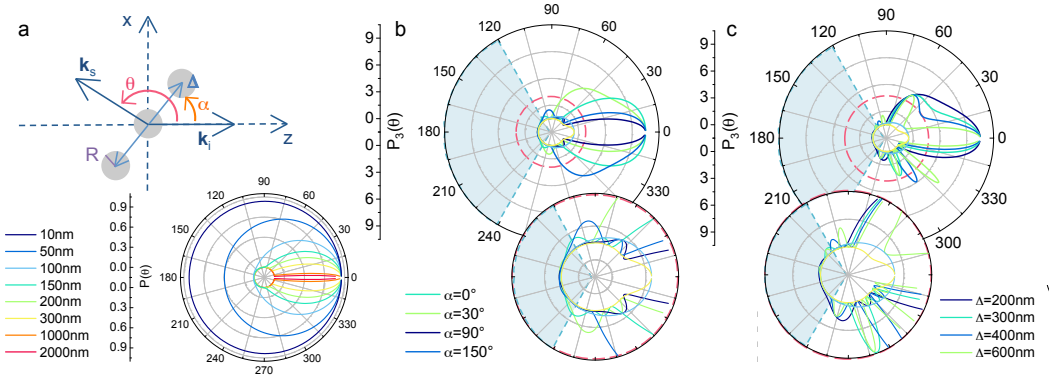

Figure 6.5: *Light scattering form factors.* (a): sketch of the geometrical configuration employed to evaluate the scattering form factor $P_3(\theta)$ for an object made up of three spheres of equal radius R and separated by a distance $|\underline{\Delta}|$. I call α the angle subtended by the vector $\underline{\Delta}$ with the optical z-axis, while θ is the angle defining the direction of the scattered wave-vector $\underline{k}_s$ with respect to the incident wave-vector $\underline{k}_i$. For elastic light scattering, $|\underline{k}_i|=|\underline{k}_s|=2\pi n/\lambda$: in the present case, n=1.518 and a wavelength λ=488 nm is assumed. In the lower panel, the polar plot of the form factor $P(\theta)$ for a single sphere of increasing radius (R=10 nm-2 μm) is reported for the sake of completeness. (b): the form factor $P_3(\theta)$, simulated with R=100 nm and $|\underline{\Delta}|$=200 nm is reported for various possible orientations α of the three-sphere aggregate in the xz-plane. The red dashed circle is magnified on the bottom to evidence that the form factors for a single 100-nm sphere (added in light blue) and for a single 300-nm sphere (yellow) practically coincide with the form factor of the aggregate. (c): form factor for a three-sphere aggregate simulated with fixed R=100 nm, α=30° and variable distance $|\underline{\Delta}|$ between the spheres. As in (b), the red circle is magnified to allow the comparison with the form factors of single 100 nm (light blue) and 300 nm (yellow) spheres. In both (b) anc (c), the grey shaded region in the polar plot corresponds to the light-collection angles defined by the numerical aperture N.A.=1.3 of our microscope objective.

6.3 Temporal Image Correlation Spectroscopy

Within the broad ensemble of the Image Correlation Spectroscopy (ICS) techniques, TICS (Temporal Image Correlation Spectroscopy) [46–48] is the first I adopt to investigate the intra-cellular dynamics of GNSs-containing cellular vesicles. While referring to Chapter 1 (Section 1.3.1) for the detailed treatment of the TICS approach and theoretical framework, I just recall that the raw data for the TICS analysis consist in an xyt- temporal stack of raster-scanned (confocal) images: for each pixel position (x, y), the computation of the temporal Auto-Correlation

Function (ACF) $G(\tau|x,y)$ and its fit to the proper decay model allow recovering the dynamic and kinetic parameters underlying the temporal fluctuations of the detected (fluorescence or scattering) signal.
Explicitly, I denote with $I(x,y,t)$ the scattering intensity detected at pixel coordinates (x,y) at time t, and with $\delta I(x,y,t)$ the fluctuations of the same signal with respect to its average computed over the whole pixel time trace: $\delta I(x,y,t) = I(x,y,t) - < I(x,y,t) >_t$. Notably, the subtraction of $< I(x,y,t) >_t$ acts as an immobile population removal. The TICS auto-correlation function is then computed, for each lag time τ, as

$$G(\tau|x,y) = \frac{< \delta I^*(x,y,t)\delta I(x,y,t+\tau) >_t}{< I(x,y,t) >_t^2} \tag{6.7}$$

Clearly as in FCS the characteristic correlation time (i.e., the lag time at which the correlation amplitude is one half of the maximum $G(\tau = 0)$ value) can only be adequately sampled if it is much smaller than the total acquisition time T, and much longer than the measurement temporal resolution Δt.

At first, TICS measurements have been performed on GNSs-treated HeLa cells at the highest temporal resolution allowed by the experimental setup. Recalling that $\Delta t \equiv \tau_f$ is defined by the inverse of the frame rate, the highest available scan frequency per line (f_{line}=1400 Hz) has been adopted and the frame format has been reduced down to 32x32-128x128 pixels^2, leading to a frame acquisition time Δt=25-90 ms. The TICS correlation functions recovered with these acquisition settings in sub-cellular Regions of Interest (ROIs) do not reveal any decay: fast vesicle motions, as well as the aforementioned sub-cellular dynamics, on the second time scale are therefore to be excluded. Further confirmation has been obtained by the RICS analysis of the same xyt-stacks: the experimental spatial correlation functions coincide with the diffraction-limited point-spread-function, not revealing any dynamic process on the timescale sampled with the 714 μs line scan time and the 6-22 μs pixel dwell time.
Subsequent TICS measurements have been performed therefore at lower temporal resolution and higher acquisition time T: a line scan frequency f_{line}=400 Hz and a 1024x1024 image format have been selected, leading to a frame time Δt=2.5 s. T has been increased to 20-30 minutes (500 frames), to accurately sample dynamic processes on the tens-of-seconds timescale. Conveniently, each xyt-stack has been acquired over one-two whole cells, on a typical field of view 30-40 μm in side:

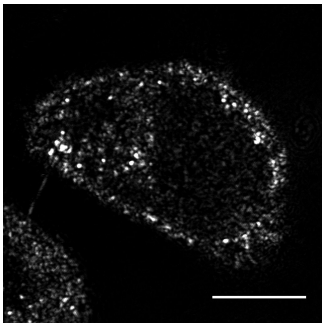

Figure 6.6: *Representative confocal reflectance* xy*-image acquired by detecting the scattering signal of GNSs upon cellular internalization*; the frame is one of 500 images acquired sequentially for the TICS analysis with Δt=2.5 s; scale bar=10 μm.

a representative frame acquired on a GNSs-treated HeLa cell is reported in Fig. 6.6. For the subsequent computation of the TICS ACFs, the xyt-stacks have been re-binned to achieve a final pixel size comparable to the 200-nm spatial resolution of the setup.

Exemplifying results of these TICS experiments are summarized for both treated and untreated cells in Figs. 6.7 and 6.8 [237]. At first, for each pixel of the acquired image stacks the temporal auto-correlation function $G(\tau|x,y)$ has been computed according to eq. (6.7). In order to avoid the ACF computation in regions outside the cell, in the cell nucleus and in the pixels containing the only contribution of the glass coverslip background scattering, a threshold (a high-pass filter) I_{min} has been applied to the time-averaged pixel intensities $< I(x,y,t) >_t$: the ACF has been computed exclusively in the pixels with an averaged intensity $< I(x,y,t) >_t$ exceeding I_{min}. A fast visualization of the typical timescale of the transport processes producing the scattering fluctuations has been obtained by storing and color-coding, for each pixel, the lag-time where the corresponding ACF halves. Large differences have been found between treated and untreated cells (Fig. 6.7a,b and Fig. 6.8): long ($\sim$ 20-50 s) decay-times occur in the cytoplasm around the cell nucleus for GNSs-treated cells, whereas shorter times are systematically found for untreated cells (where the correlation decay-time map is built from the fluctuations affecting the background scattering of cellular structures and organelles). This difference has been made quantitative in Fig. 6.7c by means of the comparison of the decay-time histograms recovered on two treated and control cells.

Once identified the tens-of-seconds timescale of the GNSs dynamics, insight on the specific mode of motion has been gained by inspecting the shape and decay of individual auto-correlation functions over the whole lag-time range. In order to allow the direct comparison with the ROI-based STICS analysis performed in the

next Section, ACFs have been averaged over 2.2x2.2 μm^2 ROIs (64x64 pixels^2, in the raw images) and have been fit to the analytical theoretical expressions predicted by two possible transport models: two-dimensional Brownian diffusion in the focal plane with diffusion coefficient D (eq. 6.8), and 2D Brownian diffusion coupled to a drift velocity $\underline{v} = (v_x, v_y)$ (eq. 6.9) [11,15,26].

$$G(\tau|x,y) = \frac{1}{< N >} \frac{1}{\left(1 + \frac{\tau}{\tau_D}\right)} + G_\infty \tag{6.8}$$

$$G(\tau|x,y) = \frac{1}{< N >} \frac{1}{\left(1 + \frac{\tau}{\tau_D}\right)} exp\left\{ -\left(\frac{\tau}{\tau_v}\right)^2 \frac{1}{\left(1 + \frac{\tau}{\tau_D}\right)} \right\} + G_\infty \tag{6.9}$$

Following the definitions of Chapter 1, in eqs. (6.8) and (6.9) $< N >$ is the average number of scattering objects in the excitation volume, $\tau_D = \omega_0^2/(4D)$ and $\tau_v = \omega_0/|\underline{v}|$; ω_0 is the excitation beam waist. G_∞ is an offset accounting for the computation of the experimental correlation functions on a finite dataset: the finite data integration time T (1200 s, to be compared with the ~ 50 s typical correlation decay time) make experimental ACFs turn negative at large lag-times and deviate from the theoretical ACF defined in the limit $T \to +\infty$ [16,225]. The fit to eqs. (6.8) and (6.9) is shown in Fig. 6.7d for three experimental ACFs:

- the first (left panel) is a purely diffusive ACF that can be fit to eq. (6.8), with best-fit parameter D=(2.64±0.06)x10^{-4} $\mu m^2/s$. The typical 20-50 s decay times of diffusive-like ACFs yield diffusion coefficients in the range (2-5)x10^{-4} $\mu m^2/s$: these are 10^4 smaller than that of the same GNSs in solution, consistently with the uptake of GNSs by large vesicles [218];

- the second ACF (central panel) is well fit by a diffusion+drift model (eq. 6.9), with D=(2.21±0.04)x10^{-4} $\mu m^2/s$ and $|\underline{v}|$=(3.6±0.1)x10^{-3} $\mu m/s$. Typical drift speed values $10^{-2} - 10^{-3}$ $\mu m/s$ are found, comparable to those reported in a variety of studies of internalization of anticancer drugs [238], lipoplexes [239], polyplexes [240] and lipid/DNA nanoparticles [241];

- a third kind of ACF time behavior (right panel) cannot be fitted by either of the previous models. Even a fractional α-exponent in the temporal dependence of the diffusive ACF decay, which is usually introduced to account for anomalous sub-diffusion [223] and which will be treated in more detail in Section 6.5,

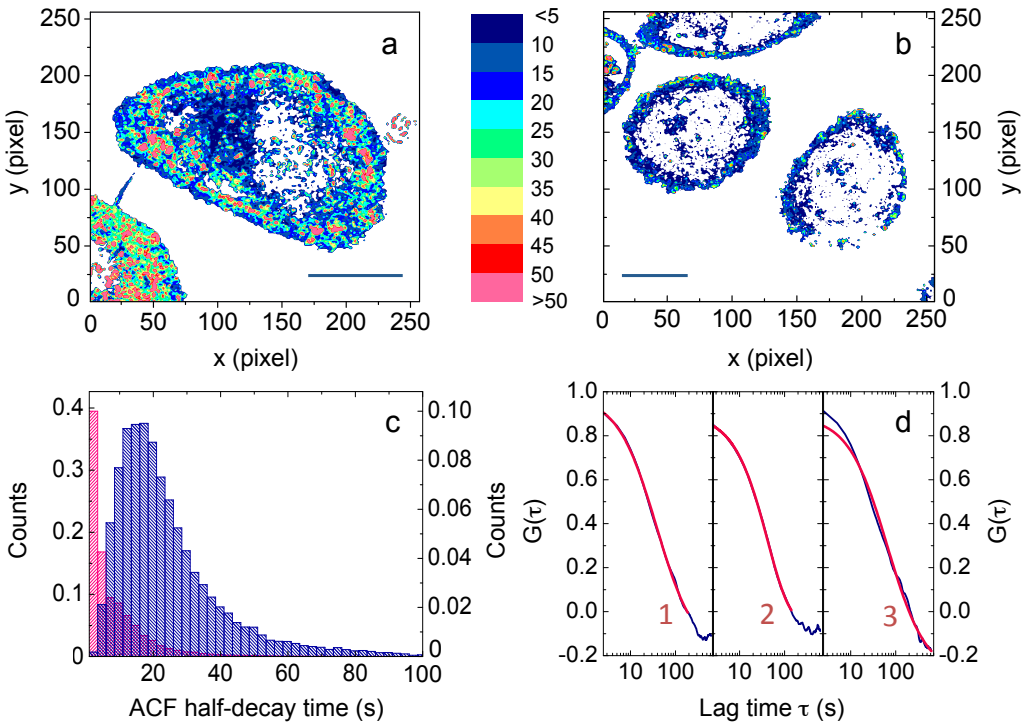

Figure 6.7: *GNSs intracellular dynamics investigated by Temporal Image Correlation Spectroscopy.* (a),(b): whole-cell maps of the TICS correlation half-height decay time obtained in GNSs-treated (a) and untreated (b) HeLa cells; the decay times are color-coded in seconds. The same intensity threshold of 100 a.u. (inserted to avoid the ACF computation in pixels outside the cell, in the cell nucleus and in the pixels containing the only contribution of background scattering in focal planes close to the glass coverslip) has been applied for the analysis of both the xyt-stacks in (a) and (b). Scale bars=10 μm. (c): histogram of the correlation half-height decay times recovered from the TICS maps of panels (a) and (b) (blue and pink, respectively). Each histogram has been normalized to the corresponding total number of counts (thereby excluding the pixels with a time-averaged intensity lower than the applied threshold, shown in white in a and b). (d): exemplifying ACFs recovered on separate 2.2μmx2.2μm ROIs on the xyt-stack analysed in panel (a). Curve 1, fit to eq. (6.8) with D=(2.64$\pm$0.06)x10^{-4} $\mu m^2/s$; curve 2, fit to eq. (6.9) with D=(2.21$\pm$0.04)x10^{-4} $\mu m^2/s$ and $|\underline{v}|$=(3.6$\pm$0.1)x10^{-3} $\mu m/s$. For curve 3 the best-fit to eq. (6.9) is shown, evidencing that the ACF can not be satisfactorily fit by either a diffusion+drift or a purely diffusive model.

does not lead to a satisfactory fit of the data. The more refined analysis performed by spatio-temporal correlation and shown in the next Section is therefore required.

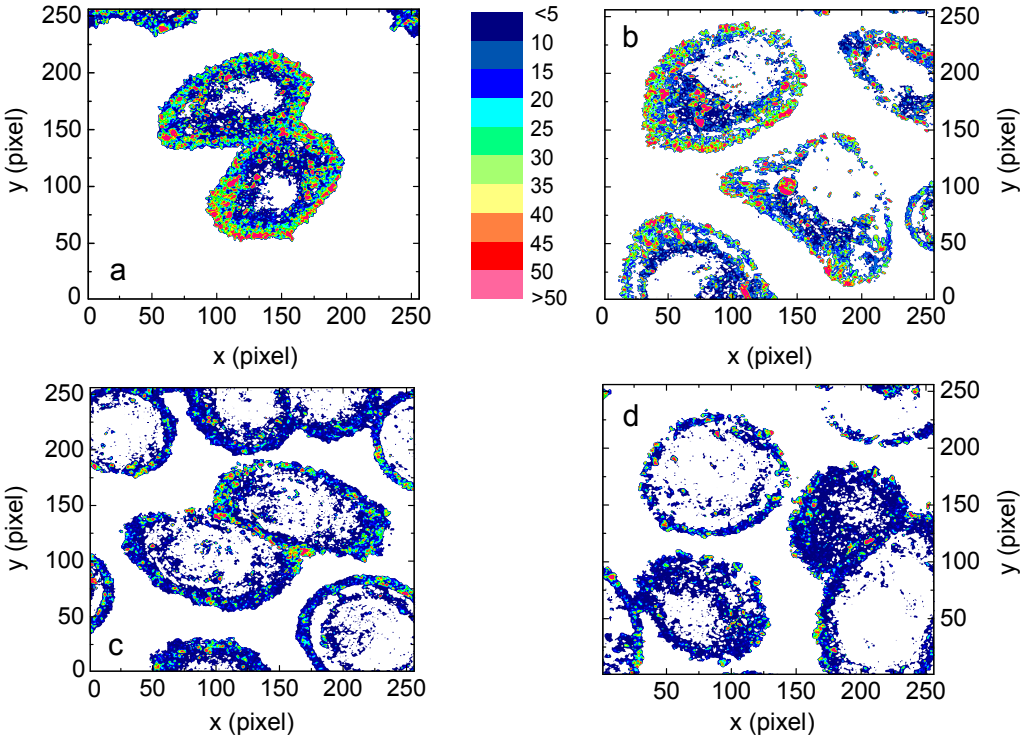

Figure 6.8: *GNSs intracellular dynamics investigated by Temporal Image Correlation Spectroscopy.* (a)-(d): whole-cell maps of the TICS correlation half-height decay time obtained in GNSs-treated HeLa cells (a and b) and in untreated HeLa cells (c and d); the same color-code (in seconds) is adopted for all the panels. In order to avoid the ACF computation in pixels containing the only contribution of background scattering, a 100 a.u. threshold has been applied to the time-averaged pixel intensities $< I(x, y, t) >_t$, as in Fig. 6.7. Image side=60 μm in (a), 62 μm in (b), 57 μm in (c) and 50 μm in (d).

6.4 Spatio-Temporal Image Correlation Spectroscopy

The xyt-stacks examined by TICS in Section 6.3 can also be analyzed by means of the spatio-temporal correlation (STICS) formalism [48] described in Chapter 1, Section 1.3.3. The 1024x1024 images of the selected cells have been divided in 64x64 ROIs, and the STICS Spatio-Temporal Correlation Function (STCF) has been computed in each one according to

$$G(\xi,\eta,\tau)=\left\langle \frac{<\delta i^{*}(x,y,t)\delta i(x+\xi,y+\eta,t+\tau)>_{xy}}{<i(x,y,t)>_{xy}<i(x,y,t+\tau)>_{xy}}\right\rangle_{t} \tag{6.10}$$

where

$$\begin{cases} i(x,y,t)=I(x,y,t)-<I(x,y,t)>_{t}+<I(x,y,t)>_{xyt} \\ \\ \delta i(x,y,t)=i(x,y,t)-<i(x,y,t)>_{xy} \end{cases} \tag{6.11}$$

For each pixel location (x,y) at a given time point t, $i(x,y,t)$ defines a corrected (immobile population filtered) pixel intensity, obtained by subtracting to the detected scattering signal $I(x,y,t)$ the average intensity of the pixel time trace, and by subsequently adding the average intensity of the entire xyt-stack (see Section 1.3.2). For each ROI, the compatibility of the computed STCF with the two simple transport models (pure diffusion and diffusion+drift) previously considered for TICS has been tested: by recalling the explicit expression

$$G(\xi,\eta,\tau)\propto\left[1+\frac{4D(\xi\tau_{p}+\eta\tau_{l}+\psi\tau_{f})}{\omega_{0}^{2}}\right]^{-1}\cdot$$

$$\cdot\exp\left\{-\frac{1}{\omega_{0}^{2}}\frac{[\xi\delta x-v_{x}(\xi\tau_{p}+\eta\tau_{l}+\psi\tau_{f})]^{2}}{1+\frac{4D(\xi\tau_{p}+\eta\tau_{l}+\psi\tau_{f})}{\omega_{0}^{2}}}\right\}\cdot\exp\left\{-\frac{1}{\omega_{0}^{2}}\frac{[\eta\delta x-v_{y}(\xi\tau_{p}+\eta\tau_{l}+\psi\tau_{f})]^{2}}{1+\frac{4D(\xi\tau_{p}+\eta\tau_{l}+\psi\tau_{f})}{\omega_{0}^{2}}}\right\} \tag{6.12}$$

derived in Chapter 1 for the STCF, the presence of a non-zero drift velocity can be identified by inspecting the dependence, on the lag time τ, of the coordinates $(\xi,\eta)_{max}$ of the peak of the correlation function. Under the experimentally-satisfied condition $\tau=\xi\tau_{p}+\eta\tau_{l}+\psi\tau_{f}\approx\psi\tau_{f}$, for each τ value the STCF can be regarded as a 2D Gaussian in the lag variables ξ and η: the peak value is located at $(\xi,\eta)_{max}\delta x=(0,0)\ \forall\tau$ if $v_{x},v_{y}=0$, whereas it shifts at $(\xi,\eta)_{max}\delta x=(v_{x}\tau,v_{y}\tau)$ when $|\underline{v}|\neq 0$ [48].

Again, as in TICS, different behaviors have been found in the peak coordinates of the experimental STCFs. This is exemplified in Fig. 6.9 for the same cell shown in Fig. 6.6 and analyzed by TICS in Fig. 6.7. For the very same three ROIs discussed by TICS, STCFs are reported at three different time delays and the ξ and η coordinates of the STCF peak $(\xi,\eta)_{max}$ are plotted versus the lag time τ:

- for ROI 1 (panels b-e) the peak of the STCF remains located at the origin of the axes becoming broader at later times, as expected for the diffusive case;
- for ROI 2 (panels f-i) the STCF peak coordinates vary linearly with the time delay, in agreement with a 2D diffusion+ drift model, and allow to recover the x- and y- components of the drift velocity: v_x=(1.20±0.02)x10^{-3} $\mu m/s$ and v_y=(1.96±0.03)x10^{-3} $\mu m/s$;
- for ROI 3, the peak of the STCF broadens in an asymmetric fashion for increasing lag time values and its position varies non linearly with the lag time τ.

From the temporal displacement of the STCFs peak in all the ROIs, the GNSs dynamics has been mapped across the whole cell: in Fig. 6.9a, circles denote the regions of diffusive motion, arrows define the ROIs where a non-zero drift speed has been recovered (arrows are color-coded for the modulus $|\underline{v}|$ and oriented according to the drift direction) and squares are employed to identify the ROIs where an anomalous behavior of the STCF has been found. Note that in the upper left quadrant of the cell, a finer grid has been adopted - by a 32-pixels shift along x and y of the 64x64 ROIs - to map the dynamic processes with more details [242]. The map highlights that: (i) the direction of the arrows representing the recovered drift velocities indicates that there is not a preferential flux, suggesting that although described by a drift model, the motion of the GNSs collected in large vesicles can be related to transport events in the cytoplasm or along the randomly-oriented F-actin filaments; (ii) a large fraction (40%) of the ROIs show the anomalous behavior; (iii): values of the same order of magnitude have been recovered by TICS and STICS for $|\underline{v}|$: the $\sim 10^{-2}$-10^{-3} $\mu m/s$ $|\underline{v}|$ values, with the diffusion coefficients $\sim 10^{-4}$ $\mu m^2/s$, are very low, suggesting that the observed vesicles mainly move in the focal plane during the whole data acquisition time; the validity of this 2D approximation will be considered and proven at the end of the kICS analysis.

To exclude the presence of artifacts in the STCF peak sampling and in the measurement of low speeds and diffusion coefficients, the microscope stage drift

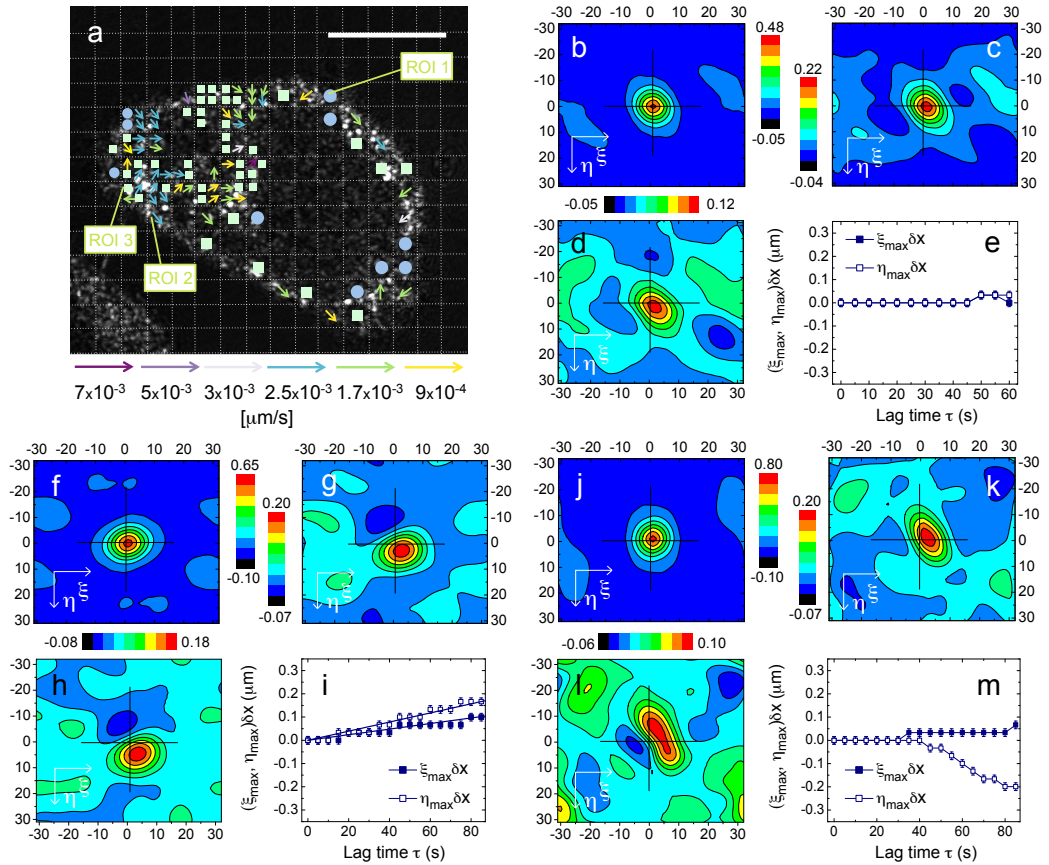

Figure 6.9: *STICS analysis of the GNSs intracellular dynamics (I) [237].* (a): whole-cell STICS map classifying the scattering vesicles dynamics in each ROI as purely diffusive (circles), diffusive with a drift component (arrows, defining the velocity direction and color-coded according to the speed $|\underline{v}|$) and anomalous (squares); the classification is based on the $(\xi,\eta)_{max}$-vs-τ plot as described in the text. 200 frames of the raw xyt-stack have been employed for the computation of the STCFs. Scale bar=10 μm. (b)-(d): contour plots of the STICS correlation function $G(\xi,\eta,\tau)$ at fixed lag times (τ=0 in b, 25 s in c and 35 s in d) for the ROI identified as 1 in panel (a); the calibration bars color-code for the correlation amplitude. (e): $(\xi,\eta)_{max}$-vs-τ plot for ROI 1 in panel a. (f)-(h), (j)-(l): contour plots of the STICS correlation function $G(\xi,\eta,\tau)$ at fixed lag times (τ=0 s in f and j, 50 s in g and k, 75 s in h and l) for ROIs 2 (panels f-h) and 3 (panels j-l). (i),(m): $(\xi,\eta)_{max}$-vs-τ plot for ROIs 2 (i) and 3 (m). For ROI 2, the $(\xi,\eta)_{max}$ coordinates allow to recover v_x=(1.20±0.02)x10^{-3} μm/s and v_y=(1.96±0.03)x10^{-3} μm/s as best-fit parameters. For panels (e), (i) and (m), the experimental uncertainty on the STCF peak coordinates is equal to half the pixel size.

over an integration time T=20 minutes has been evaluated by STICS analyses on immobile 0.1 μm fluorescent spheres: no displacement (less than a pixel) has been detected in the STCF peak under the same imaging conditions adopted for the investigation of the GNSs dynamics. Finally, the results presented in Fig. 6.9 do not depend critically on the specific examined cell (Fig. 6.10), on the total data acquisition time T (Fig. 6.11a) and on the size of the ROI on which STICS is performed: anomalous peak displacements have been recovered by both reducing the ROI side to 32 pixels and increasing it to 128 pixels (Fig. 6.11b,c) .

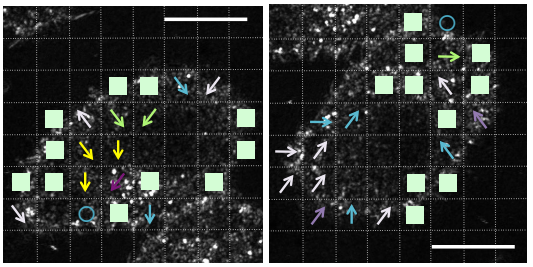

Figure 6.10: *STICS analysis of the GNSs intracellular dynamics (II).* The STICS analysis is reported for two more GNSs-treated HeLa cells to show the generality of the results of Fig. 6.9. The same code for circles, squares and arrows of Fig. 6.9 is adopted. f_{line}=400 Hz, τ_f=2.5 s, ROI size=64x64 pixels^2, scale bar=10 μm.

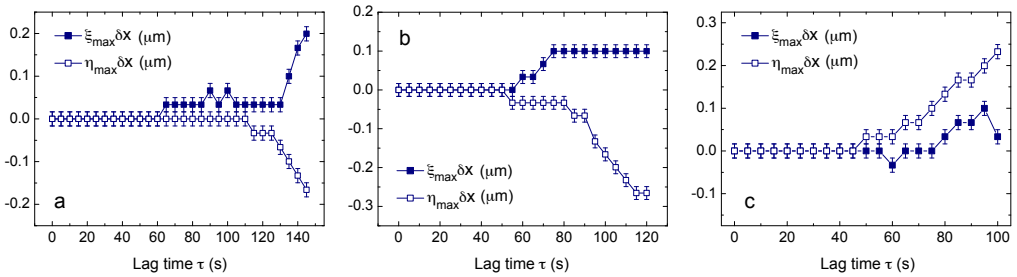

Figure 6.11: *STICS analysis of the GNSs intracellular dynamics (III).* (a): $(\xi,\eta)_{max}$-vs-τ plot recovered on the same cell analyzed in Fig. 6.9, on a 64x64 pixels^2 ROI, by exploiting all the 500-frames of the temporal stack (note that only 200 frames have been employed for the computation of the STCFs shown in Fig. 6.9). (b), (c): $(\xi,\eta)_{max}$-vs-τ plot recovered on the same cell analyzed in Fig. 6.9 (200 frames exploited) on a exemplifying 32x32 ROI (in b) and on a 128x128 ROI (in c). The anomalous non-linear peak displacement is retrieved irrespectively of the ROI size and of the data integration time.

The TICS and STICS analyses reveal that neither simple Brownian diffusion, nor the coupling of free diffusion with a drift velocity vector, are sufficient to completely describe the complex sub-cellular dynamics of endocytotic GNSs-containing

scattering vesicles. In particular STICS suggests an enhancement of Brownian diffusion. In fact, the peak coordinates of the STCF do not remain located at the origin of the Cartesian axes for all τ values - thereby excluding free diffusion - but typically exhibit a non-linear dependence on the lag time - equally excluding a diffusion+drift model. Therefore, a so-called super-diffusive, sub-ballistic behavior is evidenced.

Diffusion within complex media, like a living cell, may be hindered or enhanced by molecular crowding, transient binding events, interaction with obstacles and meshwork-like domains: in these cases, the mobility of molecules and tracer particles is classified as 'anomalous', and it cannot be described by the usual diffusion coefficient and drift speed derived from the Fick's equation any more. Since hindered and enhanced diffusion are observed in a variety of experimental systems, theoretical models capturing anomalous dynamics represent a topic of general interest and of ongoing research developments [243, 244]. Aiming at explaining the physical origin of the anomalous diffusion observed in the GNSs experimental data, I review in the nest Section different possible models of enhanced diffusion, especially evaluating their applicability to the formalism of Correlation Spectroscopy and to the derivation of the analytical expression of spatial and/or temporal correlation functions.

6.5 Theoretical models of enhanced diffusion

The physical properties of diffusive motion are conveniently characterized by a probability density function $P(\underline{x}, t)$, defining the probability $P(\underline{x}, t)d\underline{x}$ of finding the particle between $\underline{x}$ and $\underline{x} + d\underline{x}$ at time t provided it was at the origin $\underline{x} = 0$ at time $t = 0$ [223, 245]. The probability density function, also called the propagator, solves the Fick's equation I have already introduced in Chapter 1:

$$\frac{\partial P(\underline{x}, t)}{\partial t} = D\nabla^2 P(\underline{x}, t) \tag{6.13}$$

where D is the diffusion coefficient satisfying the Stokes-Einstein's equation ($D = KT/(6\pi\eta R)$; T is the temperature, K is the Boltzmann's constant, η is the medium viscosity and R is the particle hydrodynamic radius). For simple Brownian motion in d-dimensions, the solution of eq. (6.13) is a Gaussian distribution [245–247]:

$$P(\underline{x}, t) = \frac{1}{(4\pi Dt)^{d/2}} \exp\left(-\frac{|\underline{x}|^2}{4Dt}\right) \tag{6.14}$$

Hence a Brownian trajectory consists in a sequence of N successive particle displacements, with every displacement along each dimension distributed normally (according to eq. 6.14) with zero mean and a variance σ^2 that depends on the diffusion coefficient as $\sigma^2 = 2Dt$ [247,248]. The particle Mean-Square-Displacement (MSD), computed as

$$MSD(t) = \int_{-\infty}^{+\infty} |\underline{x}|^2 P(\underline{x}, t)\, d\underline{x} \tag{6.15}$$

takes - for isotropic diffusion - the form

$$MSD(t) = 2dDt \tag{6.16}$$

The footmark of Brownian diffusion is therefore a mean-square-displacement growing linearly with time [245, 249–255]. Experimental deviations from this linear behavior have been reported in many systems (including, just to name a few, amorphous semiconductors, turbulent fluids, cells and actin networks [220,246,256,257]), where the MSD exhibits a power-law scaling with time:

$$MSD(t) = D_\alpha t^\alpha \tag{6.17}$$

The exponent α determines whether the mobility is called anomalous sub-diffusion ($0<\alpha<1$) or anomalous super-diffusion ($\alpha>1$). D_α has now dimensions of length-squared per fractional time: hence the standard diffusion coefficient defined by the Fick's law (eq. 6.13) cannot reproduce the non-linear τ-dependence of the MSD [223]. This has motivated the development of various models that, starting from specific assumptions about the physical basis of anomalous mobility or starting from considerations of mathematical convenience, try to achieve a comprehensive description of complex diffusive dynamics. In Fluorescence Correlation Spectroscopy, a time-dependent diffusion coefficient is usually assumed.

6.5.1 Time-dependent diffusion coefficients

The most widely used model for anomalous diffusion in FCS takes advantage of an approximate, mathematically simple approach: a time-dependent diffusion coefficient $D(t)$ is introduced in a generalized Fick's equation of the type

$$\frac{\partial P(\underline{x}, t)}{\partial t} = D(t)\nabla^2 P(\underline{x}, t) \tag{6.18}$$

Two possible definitions for $D(t)$ have been adopted [223]:

$$\begin{cases} D(t) = \dfrac{1}{2d}\dfrac{MSD(t)}{t} = \dfrac{1}{2d}D_\alpha t^{\alpha-1} \quad (i) \\ \\ D(t) = \dfrac{1}{2d}\dfrac{\partial MSD(t)}{\partial t} = \dfrac{\alpha}{2d}D_\alpha t^{\alpha-1} \quad (ii) \end{cases} \tag{6.19}$$

Differently from definition (i), when substituted into eq. (6.18) eq. (6.19ii) has the advantage of allowing a simple derivation of an anomalous propagator that rigorously solves the diffusion equation and simultaneously captures the correct power-law scaling of the MSD [223]:

$$P(\underline{x}, t) = \frac{1}{(2\pi D_\alpha t^\alpha/d)^{d/2}} exp\Big(-\frac{|\underline{x}|^2}{2D_\alpha t^\alpha/d}\Big) \tag{6.20}$$

The propagator of eq. (6.20) has been employed already for the derivation of the FCS temporal auto-correlation function $G(\tau)$. For $\flat$-photon excitation, by introducing the beam waists ratio $\zeta = \omega_0/\omega_{0z}$ and the diffusion time τ_D, $G(\tau)$ is given [221,223] by

$$\begin{cases} G(\tau) \propto \dfrac{1}{1+\big(\dfrac{\tau}{\tau_D}\big)^\alpha}\dfrac{1}{\Big[1+\zeta^2\big(\dfrac{\tau}{\tau_D}\big)^\alpha\Big]^{(d-2)/2}} \\ \\ \tau_D = \Big(\dfrac{\omega_0^2}{4\flat D_\alpha/2d}\Big)^{1/\alpha} \end{cases} \tag{6.21}$$

Even though the propagator (6.20) is simpler than others proposed to model sub-diffusion in the context of time-fractional diffusion equations [246] (see Subsection 6.5.2), the corresponding correlation functions have at least two disadvantages for the purpose of this work. First, the fit to eq. (6.21) of the experimental TICS ACFs (like the one shown in Fig. 6.7d) does not always lead to satisfactory results. Second, the non-linear displacement of the peak coordinates of the STICS correlation function reported in Section 6.4 cannot be retrieved starting from a time-dependent diffusion coefficient. In fact, I derived the explicit expression of the STICS STCF starting from the anomalous propagator of eq. (6.20), revealing that the α-exponent does not appear in the numerator of the quasi-Gaussian terms:

$$G(\xi, \eta, \tau) \propto \left[1 + \frac{D_\alpha(\xi\tau_p + \eta\tau_l + \psi\tau_f)^\alpha}{\omega_0^2}\right]^{-1}.$$

$$\cdot exp\left\{-\frac{1}{\omega_0^2}\frac{[\xi\delta x-\nu_x(\xi\tau_p+\eta\tau_l+\psi\tau_f)]^2}{\left(1+\frac{D_\alpha(\xi\tau_p+\eta\tau_l+\psi\tau_f)^\alpha}{\omega_0^2}\right)}\right\}\cdot exp\left\{-\frac{1}{\omega_0^2}\frac{[\eta\delta x-\nu_y(\xi\tau_p+\eta\tau_l+\psi\tau_f)]^2}{\left(1+\frac{D_\alpha(\xi\tau_p+\eta\tau_l+\psi\tau_f)^\alpha}{\omega_0^2}\right)}\right\} \tag{6.22}$$

Modelled with eq. (6.20), anomalous diffusion impacts the width of the spatio-temporal correlation function rather than the peak position, showing the incompatibility of the GNSs experimental data with a simple model based on the time dependence of the diffusion coefficient. This also suggests that eq. (6.20) is suited to describe sub-diffusion more than super-diffusive processes.

Equally difficult is the application of the alternative model that has been proposed [258] recently in the framework of Fluorescence Correlation Spectroscopy starting from the non-linear Fokker-Planck equation. The Einstein's mean field equation for the random walk has been generalized by allowing the particles concentration to impact the probability for the jump from one site to another: even though sub-diffusion and super-diffusion have been tackled (with a rather cumbersome formalism), only an integral, non-analytical expression has been provided for the temporal FCS auto-correlation function in both the cases.

Aiming at deriving analytically the TICS and STICS correlation functions to quantify the dynamic parameters underlying the nanostars dynamics, I explored the possibility of extending to FCS and ICS the enhanced-diffusion models provided by statistical mechanics.

6.5.2 Lévy flights

The first model I consider is the one of Lévy flights. I introduce their general formalism by recalling the previously defined probability density function $P(\underline{x},t)$, denoting the probability $P(\underline{x},t)d\underline{x}$ of finding the particle between $\underline{x}$ and $\underline{x}+d\underline{x}$ at time t provided it was at the origin $\underline{x}=0$ at time $t=0$. $P(\underline{x},t)$ can be fully specified by introducing a jump length distribution $\lambda(|\underline{x}|)$ and a waiting time distribution $\psi(t)$: each jump of the random walk has jump length $\underline{x}$ drawn from the distribution λ, and the time interval between two consecutive jumps is distributed according to ψ. In the absence of external bias, the theory of Continuous Time Random Walk (CTRW) relates λ and ψ to the Fourier-Laplace transform $P(\underline{k},u)$ of $P(\underline{x},t)$ [246,255]:

$$P(\underline{k},u)=\frac{1-\psi(u)}{u}\frac{1}{1-\lambda(|\underline{k}|)\psi(u)} \tag{6.23}$$

Three cases can be distinguished:

- $\psi(t) = \delta(t - \tau)$ and $\lambda(|\underline{x}|)$ is Gaussian with variance σ^2: the Gaussian probability density function of eq. (6.14) is found, with the corresponding linear time-dependence of the mean square displacement. This is therefore the case of regular Brownian motion;

- $\lambda(|\underline{x}|)$ is Gaussian, while $\psi(t)$ is a so-called Lévy stable density [1] with index $0<\alpha<1$: $\psi(t) \sim t^{-1-\alpha}$. In this case the characteristic waiting time $\int_0^{+\infty} t\psi(t)dt$ diverges, while $P(\underline{k}, t)$ is of the type

$$P(\underline{k}, t) = \sum_0^{+\infty} \frac{(-D_\alpha |\underline{k}|^2 t^\alpha)^n}{\Gamma(1 + \alpha n)} \tag{6.24}$$

  with Γ being the Mittag-Leffler function. $P(\underline{k}, t)$ turns from an initial stretched-exponential behavior to a power-law behavior, and satisfies in $\underline{x}$,t space the time-fractional diffusion equation

$$\frac{\partial P(\underline{x}, t)}{\partial t} = D_\alpha \Delta_t^{1-\alpha} \nabla^2 P(\underline{x}, t) \tag{6.25}$$

  where $\Delta_t^{1-\alpha}$ is the fractional Riemann-Liouville operator defined as

$$\Delta_t^{1-\alpha} P(\underline{x}, t) = \frac{1}{\Gamma(\alpha)} \frac{\partial}{\partial t} \int_0^t \frac{P(\underline{x}, t')}{(t - t')^{1-\alpha} dt'} \tag{6.26}$$

  The diffusing particle can get stuck at a certain position for very long times, resulting in an MSD exhibiting power-law sub-diffusive time dependence [246];

- $\psi(t) = \delta(t - \tau)$ and $\lambda(|\underline{x}|)$ is a Lévy stable density with index $0<\mu<2$: $\lambda(|\underline{x}|) \sim |\underline{x}|^{-1-\mu}$. This is the case of super-diffusive Lévy flights [246, 255, 259, 260], described in more detail in the following.

[1] Lévy stable laws are introduced by the generalized central limit theorem: it states that the sum of independent identically distributed random variables with infinite variance converges to a Lévy limit distribution. Lévy stable laws exhibit a power-law asymptotic $p(x) \sim |x|^{-1-\mu}$. The sum of independent identically distributed random variables with finite variance converges instead to a Gaussian distribution, recovered from the Lévy case with $\mu=2$.

Provided the jump length and waiting time distributions $\lambda(|\underline{x}|) \sim |\underline{x}|^{-1-\mu}$ and $\psi(t) = \delta(t-\tau)$, the probability density function $P(\underline{x}, t)$ can be obtained from eq. (6.23) as a Lévy stable law with Fourier transform

$$P(\underline{k}, t) = exp\{-D^{(\mu)}|\underline{k}|^{\mu} t\} \tag{6.27}$$

I remark that in this case $D^{(\mu)}$ has dimensions of space$^{\mu}$/time. Back-transformed into position space, $P(\underline{k}, t)$ yields an analytical solution in terms of the Fox H-function, expanded in series as

$$P(\underline{x}, t) = \frac{1}{\mu (D^{(\mu)} t)^{1/\mu}} \sum_{\nu=0}^{\infty} \frac{\Gamma([1+\nu]/\mu)}{\Gamma([1+\nu]/2)\Gamma(1-[1+\nu]/2)} \cdot \frac{(-1)^{\nu}}{\nu!} \left(\frac{|\underline{x}|}{(D^{(\mu)} t)^{1/\mu}} \right)^{\nu} \tag{6.28}$$

$P(\underline{x}, t)$ is plotted for μ=1 at selected time points in Fig. 6.12, where it is compared with the Gaussian probability density function recovered in the limiting case μ=2. Contrasting with the time-fractional diffusion equation valid for sub-diffusion (eq. 6.25), $P(\underline{x}, t)$ satisfies a space-fractional diffusion equation:

$$\frac{\partial P(\underline{x}, t)}{\partial t} = D^{(\mu)} \frac{\partial^{\mu}}{\partial |\underline{x}|^{\mu}} P(\underline{x}, t) \tag{6.29}$$

where the fractional Riesz-Weyl operator is defined by the Fourier transform $F\{\partial^{\mu}/\partial|\underline{x}|^{\mu} P(\underline{x}, t)\} = -|\underline{k}|^{\mu} P(\underline{k}, t)$ [246, 255].

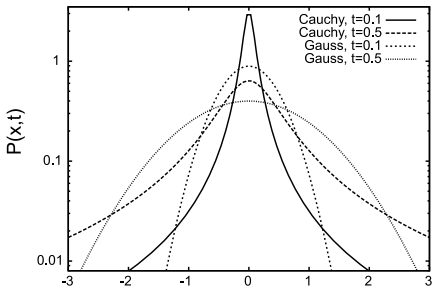

Figure 6.12: *Lévy flights propagator [246].* The probability density function of eq. (6.28) with μ=1 (i.e., the Chauchy-Lévy stable density) is plotted in the one-dimensional case versus x at two time points; the Lévy propagator is compared with the Gaussian distribution recovered from eq. (6.28) with μ=2. The propagator peaks at x=0 due to the initial condition $P(x, 0)=\delta(x)$ at t=0; $D=D^{(1)}=1$ has been assumed for the simulation.

In the course of a random walk governed by the long-tailed jump length distribution $\lambda(|\underline{x}|) \sim |\underline{x}|^{-1-\mu}$, steps of all sizes may occur and a trajectory of fractal dimension μ is obtained. As I show in Fig. 6.13a-c, Lévy-flights trajectories exhibit local explorations as well as long excursions, so that clusters of small steps are separated by a single much longer jump [246, 255, 259, 261]. When compared to a typical Brownian trajectory (Fig. 6.13d) with the same number of steps, Lévy flights clearly reveal their super-diffusive nature. These properties of the Lévy flights have been shown to represent a better search strategy with respect to Brownian diffusion, so that animals like albatross, monkeys, jackals and plankton have been claimed to behave in a Lévy fashion when looking for food [246, 262]. Lévy flights have also

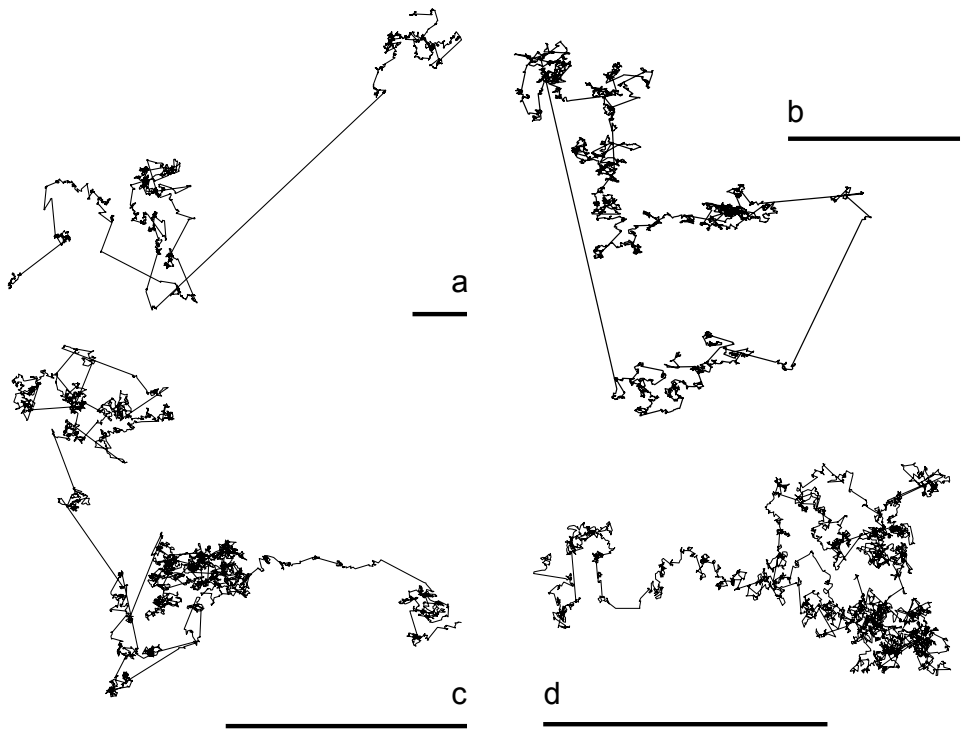

Figure 6.13: *Lévy flights.* Comparison of the trajectories of Lévy processes with index μ=1.3 (a), 1.5 (b) and 1.8 (c). In (d) a simulated Brownian trajectory (i.e., a Lévy flight with index μ=2) is reported for comparison. 5000 steps have been drawn for all the trajectories; the scale bar represents 200 pixels in all the panels.

been found in a multitude of systems ranging from turbulent plasmas [263] and earthquakes [264] to human travels [265], the evolution of the stock market [266] and the diffusion of banknotes [267].

With proper values of the Lévy index μ, trajectories closely resembling the one reported in the next Chapter for GNSs diffusing in the cell cytoplasm can be reproduced. Moreover, when a STICS analysis is performed, the super-diffusive behaviour exhibited by trajectories simulated according to the formalism of Lévy flights leads to an anomalous non-linear peak displacement in the spatio-correlation correlation function. As described in the next subsection, this strongly supports the compatibility of the Lévy-flights model with the experimental data of Figs. 6.9 and 6.11.

Lévy flights: numerical simulations and STICS analysis

Confocal laser scanning microscopy images of ideal, non-interacting particles diffusing in a Lévy-flight fashion have been simulated by a custom-written Python code to test whether the resulting super-diffusive behavior is compatible with the non-linear displacement of the STICS correlation peak. For the simulation of individual trajectories, randomly generated initial x- and y-coordinates are assigned to each particle; then, at each time step, two pseudo-random numbers are extracted to assign the particle direction and the jump length: the angle is drawn from a uniform distribution in the interval $[0, 2\pi]$, while the jump length is extracted from the Lévy stable distribution $\lambda(|\underline{x}|) \sim |\underline{x}|^{-1-\mu}$ with the chosen value for μ. Particle positions are subsequently converted to pixel-unit coordinates and convolved with a 2D Gaussian function with given e^{-2} radius, to simulate the excitation of equally bright point emitters by a focused TEM_{00} laser beam. The image matrix obtained at each time point is normalized, and each pixel value is rounded to the closest integer; than the same STICS Python code and procedure adopted for the analysis of the experimental data of Fig. 6.9 are employed to inspect the peak-coordinates plot.
An exemplary result is shown in Fig. 6.14, for a Lévy trajectory simulated with index μ=1.3: the recovered $(\xi, \eta)_{max}$-vs-τ plot is non-linear, resembling the typical STICS results obtained when analyzing the intracellular dynamics of GNSs-containing vesicles. Similar non-linear trends have been recovered for various values of the power-law exponent μ, suggesting that a Lévy dynamics may underly the experimentally observed super-diffusion.

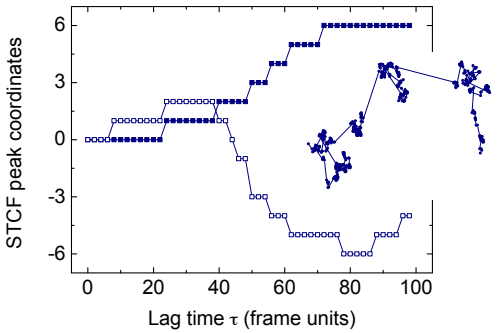

Figure 6.14: *Lévy flights: STICS analysis.* Peak coordinates ξ_{max} and η_{max} (filled and open symbols, in pixel units) versus the lag time (in frame units) provided by the STICS analysis of a simulated Lévy flight with μ=1.3; the same trajectory is reported as inset.

The results of Fig. 6.14 confirm the previously hypothesized sub-ballistic but super-diffusive nature of the vesicles dynamics within the cytoplasm of HeLa cells. However, the mathematics of Lévy flights hampers the exploitation of the model for the description of experimental data and for the quantification of physically-relevant transport parameters starting from the same data. First, the variance of the Lévy jump-length distribution is infinite: hence, the mean square displacement cannot be formally defined, and it cannot be exploited for the analysis of Single Particle Tracking data like those presented in Chapter 7. Second, the Fourier transform $P(\underline{k}, t)$ of eq. (6.27) contains a μ exponent for the $\underline{k}$ vector. Recalling the derivation of the STICS correlation function I reported in Chapter 1 (eqs. 1.56-1.68), integration over the Fourier-space vector $\underline{k}$ must be performed for the STCF to be explicitly derived: μ can be fractional, and the integral containing -in addition to other terms- $exp(-D^{(\mu)}|\underline{k}|^{\mu}t)$ cannot be computed analytically. Third, the index μ does not give particular insight into the physical basis of the observed super-diffusive dynamics: it does not coincide with the exponent α derived from an experimentally-computed MSD (eq. 6.17) and it can only provide an estimate of the extent of the deviation of the observed dynamics from a purely Brownian one. Summarizing, despite the solid mathematical foundations of Lévy flights in the generalized central limit theorem and despite their broad affinity with a number of biological and non-biological systems, Lévy flights tend to discourage practical applications [268, 269].

I finally mention that the long-standing complication of the diverging variance has been tackled by two variants of Lévy flights, known as Lévy walks [246, 255, 259, 269] and Truncated Lévy Flights (TLF) [270]. In truncated Lévy flights, the

arbitrarily long steps are eliminated by introducing a cut-off length for the extraction of jumps from the long-tailed power law distribution λ. In Lévy walks, instead of the decoupled jump length and waiting time distributions used in the continuous-time-random-walk description of Lévy flights, a coupling is introduced between $\lambda(|\underline{x}|)$ and $\psi(t)$. By coupling space and time into, for example, a distribution $\psi(\underline{x}, t) \sim \lambda(\underline{x})\delta(|\underline{x}| - vt)$, steps of arbitrary lengths are allowed, but long steps are penalized by requiring longer time to be performed; v represents therefore a velocity [246, 255, 259]. Even though both TLFs and Lévy walks solve the second moment divergence, they do not help in simplifying the derivation of spatial and/or temporal correlation functions.

6.5.3 Intermittent active transport

Difficulties in the derivation of ICS correlation functions are also found when attempting to exploit the formalism of the Generalized Langevin Equation (GLE). The GLE for a particle of mass m, subject to a random force $F(t)$, reads

$$m x''(t) + \int_0^t \gamma(t - t') x'(t') dt' = F(t) \tag{6.30}$$

where $\gamma(t)$ is a dissipative term. Under specific assumptions for $\gamma(t)$ and $F(t)$, eq. (6.30) has been employed to model the mean-square-displacement of intracellular super-diffusion: specifically, an experimentally-observed crossover from a sub-diffusive regime to a super-diffusive regime (with $t^{3/2}$-dependence for the MSD) has been modeled by the GLE [220]. To this aim, the random force $F(t)$ has been regarded as the sum of two uncorrelated contributions: (i) an internal noise due to thermal activity that, once related to the dissipative term $\gamma(t)$, allows accounting for the viscoelastic properties of the cell cytoplasm and for the resulting hindered diffusion; (ii) an external random force, responsible for the enhancement of diffusion. Two power laws have been assumed for the autocorrelation functions of both the force contributions, so that, by proper adjustment of the power-law exponents, the aforementioned transition between sub- and super- diffusion can be retrieved [220]. Interestingly, a quantitative interpretation of the physics underlying the observed transport processes has been achieved by linking the parameters identifying the forces correlation functions to a macroscopic effective diffusion coefficient; moreover, a physical and biological basis for the external random force has been identified in the role of cellular molecular motor proteins [220, 224].

Molecular motors are responsible for the intracellular active transport of organelles, vesicles and cargoes along the semi-flexible oriented filaments of the cytoskeleton [224]. Capable of converting the chemical fuel provided by Adenosine-TriPhosphate (ATP) into mechanical work, myosin motors regulate the active transport along actin filaments, while dynein and kinesin motors carry cargoes toward the plus and minus ends of the microtubules [273]. When cellular vesicles, lysosomes, endosomes or mytochondria randomly bind and unbind to motor proteins, Brownian diffusion in the cytoplasm alternates with directed, ballistic displacements along actin filaments and microtubules [271,272]: hence the overall dynamics of tracer particles within the complex cellular environment can be regarded as an intermittency between phases of free diffusion and phases of active directed transport mediated by molecular motor proteins.
The role of molecular-motor mediated active transport in defining an overall intracellular super-diffusive dynamics is nowadays largely accepted. Furthermore, the idea of intermittent active transport suggests a formalism which is mathematically easier to handle than the one of Lévy flights and of the generalized Langevin equation in statistical mechanics. This formalism, described in the following, combines the approach usually adopted to model search and target-finding processes [274,275] with the traditional formalism proposed by Magde *et al.* for the description of chemical reactions in point-FCS [3].

Hypothesizing that cytoskeleton-based transport is responsible for the enhanced diffusion revealed by TICS and STICS, the GNSs intracellular motion can be modeled by a sequence of jumps between a purely diffusive Brownian regime and an active transport regime. Hence, I consider a GNSs-containing vesicle freely diffusing in a d-dimensional space (d=2 in the present case [2]), that randomly binds to molecular motor proteins with association and dissociation rates k_{12}^* and k_{21}. A binding/unbinding reaction of the form

$$A + B \underset{k_{21}}{\overset{k_{12}^*}{\rightleftharpoons}} C \tag{6.31}$$

is therefore considered, where B identifies the binding sites (molecular motor proteins, in our case) and the A and C species identify endocytotic vesicles in their

[2] As anticipated previously, the validity of the 2D approximation will be confirmed with the kICS analysis in Chapter 8.

free and bound forms, respectively. The binding kinetics is completely determined by the bimolecular forward rate constant k_{12}^* and by the first-order dissociation rate constant k_{21}.
By denoting with A_{eq}, B_{eq} and C_{eq} the equilibrium concentrations of the three species and with δA, δB and δC the fluctuations of the concentrations about their temporal average, the dynamics and kinetics of the system are governed by the following system of differential equations:

$$\begin{cases} \dfrac{\partial(A_{eq}+\delta A)}{\partial t} = D\nabla^2(A_{eq}+\delta A) - k_{12}^*(A_{eq}+\delta A)(B_{eq}+\delta B) + k_{21}(C_{eq}+\delta C) \\ \dfrac{\partial(B_{eq}+\delta B)}{\partial t} = -k_{12}^*(A_{eq}+\delta A)(B_{eq}+\delta B) + k_{21}(C_{eq}+\delta C) \\ \dfrac{\partial(C_{eq}+\delta C)}{\partial t} = D\nabla^2(C_{eq}+\delta C) - \underline{v}\cdot\underline{\nabla}(C_{eq}+\delta C) + k_{12}^*(A_{eq}+\delta A)(B_{eq}+\delta B) \\ \qquad\qquad - k_{21}(C_{eq}+\delta C) \end{cases} \tag{6.32}$$

D is the diffusion coefficient of nanoparticles-containing cellular vesicles and $\underline{v}$ is the constant velocity of the molecular motor-mediated active transport; no change in the diffusion coefficient D is assumed upon the occurrence of a binding or unbinding event: this allows minimizing the number of free parameters in the model, while allowing - as described in Chapter 7- a satisfactory description of the experimental data. Without loss of generality, no diffusive term is inserted in the rate equation for the free binding sites, assuming that molecular motor proteins are immobile prior to the binding process.
Recalling that equilibrium concentrations are space- and time- independent and that they satisfy the equilibrium condition $k_{12}^* B_{eq} A_{eq} = k_{21} C_{eq}$, eqs. (6.32) reduce to

$$\begin{cases} \dfrac{\partial\delta A}{\partial t} = D\nabla^2\delta A - k_{12}^*(A_{eq}\delta B + B_{eq}\delta A + \delta A\delta B) + k_{21}\delta C \\ \dfrac{\partial\delta B}{\partial t} = -k_{12}^*(A_{eq}\delta B + B_{eq}\delta A + \delta A\delta B) + k_{21}\delta C \\ \dfrac{\partial\delta C}{\partial t} = D\nabla^2\delta C - \underline{v}\cdot\underline{\nabla}\delta C + k_{12}^*(A_{eq}\delta B + B_{eq}\delta A + \delta A\delta B) - k_{21}\delta C \end{cases} \tag{6.33}$$

If the number of binding sites is assumed to be much larger than the number of

freely diffusing vesicles, the concentration fluctuations δA affecting species A are likely to be much larger than the fluctuations δB affecting the concentration of molecular motor proteins in their unbound form. The condition $\delta A/A_{eq} >> \delta B/B_{eq}$ leads to

$$\begin{aligned} k_{12}^*(A_{eq}\delta B + B_{eq}\delta A + \delta A\delta B) &= k_{12}^* A_{eq} B_{eq}(\delta B/B_{eq} + \delta A/A_{eq} + \delta A\delta B/A_{eq}B_{eq}) \\ &\approx k_{12}^* B_{eq}\delta A \end{aligned} \tag{6.34}$$

yielding in turn

$$\begin{cases} \dfrac{\partial \delta A}{\partial t} = D\nabla^2\delta A - k_{12}^* B_{eq}\delta A + k_{21}\delta C \\ \dfrac{\partial \delta B}{\partial t} = -k_{12}^* B_{eq}\delta A + k_{21}\delta C \\ \dfrac{\partial \delta C}{\partial t} = D\nabla^2\delta C - \underline{v}\cdot\underline{\nabla}\delta C + k_{12}^* B_{eq}\delta A - k_{21}\delta C \end{cases} \tag{6.35}$$

The temporal derivatives $\partial\delta A/\partial t$ and $\partial\delta C/\partial t$ do not depend on the concentration fluctuation δB; hence the differential equations can be solved for δA and δC independently from the concentration fluctuation of free binding sites, reducing eq. (6.35) to

$$\begin{cases} \dfrac{\partial \delta A}{\partial t} = D\nabla^2\delta A - k_{12}^* B_{eq}\delta A + k_{21}\delta C \equiv D\nabla^2\delta A - k_{12}\delta A + k_{21}\delta C \\ \dfrac{\partial \delta C}{\partial t} = D\nabla^2\delta C - \underline{v}\cdot\underline{\nabla}\delta C + k_{12}^* B_{eq}\delta A - k_{21}\delta C \equiv D\nabla^2\delta C - \underline{v}\cdot\underline{\nabla}\delta C + k_{12}\delta A - \\ \qquad - k_{21}\delta C \end{cases} \tag{6.36}$$

Under the approximation of eq. (6.34), the binding reaction is therefore a first-order reaction, with forward rate constant $k_{12} \equiv k_{12}^* B_{eq}$. In the following, I will denote the free and bound states as (1) and (2), respectively, and schematically depict the effective unimolecular reaction as

$$(1) \quad D \underset{k_{21}}{\overset{k_{12}}{\rightleftharpoons}} D + \underline{v} \quad (2) \tag{6.37}$$

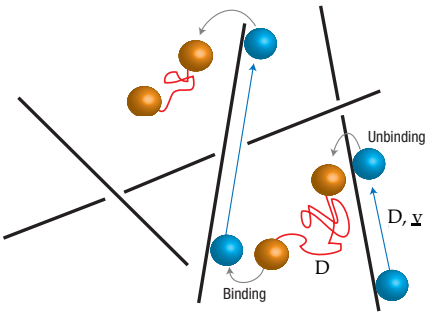

Figure 6.15: *Schematic of intermittent active transport [271].* A particle undergoing intermittent active transport alternates phases of Brownian diffusion (in red) with diffusion coefficient D, and phases of molecular motor-mediated active transport (in blue) along the cytoskeletal filaments (sketched in black) with diffusion coefficient D and drift velocity $\underline{v}$.

identifying each state by the mode of motion exhibited by the investigated particles.

The two-state dynamics described by eq. (6.37) is expected to produce a super-diffusive but sub-ballistic behavior: the presence of a non-zero drift speed in state (2) should be responsible for the enhancement of diffusion, whereas the presence of state (1), and the consequent reduction of the time spent by the particles in the drift state, should make the overall observed dynamics deviate from a purely ballistic one. I also expect the formalism of eqs. (6.31)-(6.37) to be analytically treatable for the derivation of FCS and ICS correlation functions. In fact, similar approaches have been adopted in the literature to describe the binding/unbinding of fluorescently labeled macromolecules to immobile cellular substrates or to unlabeled diffusing receptors in the plasma membrane [8, 276]. When implemented in the framework of fluorescence or scattering correlation methods, the two-state intermittent dynamics of eq. (6.37) has the advantage of allowing the recovery of physically meaningful parameters: the diffusion coefficient, the drift speed and the transition rates between the active and the passive regime; in these regards, intermittency outperforms Lévy flights.

Prior to adopting the formalism of eqs. (6.31)-(6.37) for the ICS-based analysis of the GNSs intracellular dynamics (Chapter 8), I report in Chapter 7 the Single Particle Tracking experiments I performed to unambiguously attribute to intermittent active transport the super-diffusive behavior of endocytosed nanostars; numerical simulations are reported as well, to verify the compatibility of the intermittent-transport model with the experimental anomalous displacement of the STICS spatio-temporal correlation functions.

Chapter 7

Single Particle Tracking Experiments

By imposing order and directionality onto the naturally stochastic behavior of Brownian diffusion, molecular motors mediate intracellular drift phenomena and support the transport of vesicles and organelles along microtubules and actin filaments [219, 224, 271, 277–279]. This interplay between diffusion and active transport often makes the overall dynamics exhibited by tracer particles in the cellular environment neither ballistic nor purely diffusive [273, 279]: different mobility states, differing in the magnitude of the diffusion coefficient and in the eventual presence of a non-zero drift velocity, might alternate and produce extremely complex transport pathways [271]. Methods capable of an automated and reliable time-resolved identification of mobility states, and capable of dissecting the presence of directionality within an otherwise diffusive motion, are therefore required and continuously developed [219,248,252,280,281].
Among these techniques, Single Particle Tracking (SPT) [249,252] provides access to single-particle trajectories with sub-diffraction ~ 10 nm resolution [249,254] and, by the statistical analysis of these trajectories, potentially yields the distribution of active and passive state durations as well as the distributions of the state parameters (namely, the velocity during the active phases and the diffusion coefficient of the passive motion). Even though the computation of the estimator to the second-order moment of the displacement (the Mean-Square-Displacement, or MSD) represents the most widely adopted approach for the analysis of SPT data [249,252], alternative methods for the advanced analysis of particle trajectories have been

recently introduced. Some of them characterize the mode of motion by inspecting the directional persistence [280] or the self-similarity [282] of the trajectories, the trajectory radius of gyration, asymmetry and spread in space [247, 272], or the deviation of individual displacements from Gaussian statistics [283]; others recover transport parameters by exploiting the principles of Bayesian inference [248,281,284]. In this Chapter, the analysis of the intracellular SPT trajectories of nanostars-containing cellular vesicles is reported. The computation of the experimental MSDs and the Bayesian analysis of the whole trajectories, modeled as Hidden Markov Models, allow not only to verify the compatibility of the experimental data with the super-diffusion model based on intermittent active transport, but also to unambiguously attribute to the very same intermittent dynamics the super-diffusive behavior pointed out by STICS in Chapter 6. The results obtained here by Single Particle Tracking will finally complement and strengthen the transport parameters recovered by image correlation in Fourier space in Chapter 8.

7.1 Principles of Single Particle Tracking: MSD analysis

I begin by reviewing the basic principles of Single Particle Tracking and of the MSD-based analysis. SPT is based on the measurement of the trajectory, i.e. the sequence of positions $\underline{x}(t_j) = (x(t_j), y(t_j))$ (or $(x(t_j), y(t_j), z(t_j))$ in the three-dimensional case) at times $t_{j=1\ldots N}$, of individual (fluorescent or scattering) mobile particles imaged in time-lapse mode [249, 254]. Starting for example from an xyt-stack of raster-scanned confocal images, the particle coordinates are determined at each time point with ~ 10 nm accuracy by centroid calculations; then they are reassembled to reconstruct the whole trajectory that, when analyzed by the proper statistical approach, allows the extraction of transport parameters (e.g., diffusion coefficients, drift velocities) and the motion classification (as directed, constrained, diffusive, intermittent, etc.).
The possibility of performing such a classification relies on relating each displacement $\Delta\underline{x}$ travelled by the particle in a time interval τ to a well-defined probability density function; for example, for a particle undergoing 2D Brownian diffusion (with diffusion coefficient D) and uniform planar drift (with velocity $\underline{v} = (v_x, v_y)$), each displacement can be regarded as extracted from a Gaussian probability density function

$$P(\Delta\underline{x}, \tau) = \frac{1}{(4\pi D\tau)} \exp\left(-\frac{|\Delta\underline{x} - \underline{v}\tau|^2}{4D\tau}\right) \tag{7.1}$$

The Gaussian distribution has a variance that depends on the diffusion coefficient as $\sigma^2 = 2D\tau$ and it is centered at $(v_x\tau, v_y\tau)$; hence it recalls the zero-centered Gaussian distribution of eq. (6.14) in the simple case of free thermal diffusion ($|\underline{v}| = 0$). Depending on D and $\underline{v}$, the diffusion propagator randomly assigns at each time step the length and direction of the particle jump: hence by observing, by an SPT experiment, a sequence of displacements, insight can be gained on the ensemble of transport parameters that fully characterize the underlying probability density function. This obviously applies not only to the trajectories arising from a simple combination of diffusion and drift, but also to purely diffusive or intermittent trajectories for which a reasonable assumption on the underlying probability distribution can be made.

The simplest strategy by which the measurement of the transport parameters and the classification of the mode of motion can be performed consists in computing the trajectory mean-square-displacement and in comparing the experimental MSD with the theoretical analytical expressions predicted for the different possible modes of motion:

- *Experimentally* (on a discrete data-set) and in the hypothesis of two-dimensional transport, the MSD is computed [249] as

$$MSD(\tau) \equiv MSD(n\Delta t) = \frac{1}{N-n} \sum_{j=0}^{N-n-1} \left\{ \left[x(t_{j+n}) - x(t_j) \right]^2 + \left[y(t_{j+n}) - y(t_j) \right]^2 \right\} \tag{7.2}$$

  $MSD(\tau)$ defines therefore the average squared distance travelled by the particle in a time $\tau = n\Delta t$, the lag time τ being an integer multiple of the temporal separation Δt between consecutively sampled points in the trajectory.[1]

- *Theoretically*, the analytical expression for the MSD (to be employed for the fit of the experimental MSD-vs-τ plot) is derived by averaging, over the expected transport propagator, the square of the position random variable. Recalling again simple Brownian diffusion (case (i)) and the combination of 2D diffusion and drift (case (ii)), integration of the squared position over the

[1] For practical purposes, n is usually limited to $\sim 20\%$ of the total number N of the recorded positions: in fact, the uncertainty associated to the MSD values increases with the lag time τ, since the higher τ, the smaller is the number of data points available for the averaging operation of eq. (7.2) [249, 254].

propagator of eq. (7.1) translates into the computation of a Gaussian integral, yielding

$$\begin{cases} MSD(\tau) = 4D\tau \quad (i) \\ \\ MSD(\tau) = 4D\tau + |\underline{v}|^2\tau^2 \quad (ii) \end{cases} \tag{7.3}$$

A linear MSD-vs-τ plot is found in the presence of Brownian diffusion, with a slope proportional to the diffusion coefficient D [245, 249–254]; by contrast, the coupling of thermal diffusion and planar uniform drift endows the MSD plot with positive curvature due to a quadratic dependence of the square travelled distance on the lag time τ [249, 252, 254].[2] With a similar procedure, starting form the appropriate propagator $P(\underline{x}, \tau)$, the MSD for more complex and transient dynamics can be explicitly derived: in the next Subsection, the derivation of the MSD for intermittent active transport is reported.

When no prior information is given on the kind of motion the particle experiences, the curvature of the experimental MSD-vs-τ plot and its fit to the possible MSD theoretical models can identify its diffusive, directional or (as shown in the next Subsection) intermittent nature.

7.1.1 MSD for intermittent active transport

I consider the two-state dynamics of eq. (6.37), describing a particle switching between a diffusive state with diffusion coefficient D and a diffusion+drift state with diffusion coefficient D and drift velocity $\underline{v} = (v_x, v_y)$. I denote with k_{12} and k_{21} the transition rates regulating the probability for the particle to switch from one state to the other. I also denote with $p_{\alpha\beta}(\underline{x}, t)$ the probability density of finding the particle in state α (α=1,2) at point $\underline{x}$ at time t, provided it was in state β (β=1,2) at time t=0. $p_{\alpha\beta}(\underline{x}, t)$ satisfies the system of differential equations previously introduced as eq. (6.36):

$$\begin{cases} \dfrac{\partial p_{1\beta}(\underline{x}, t)}{\partial t} = D\nabla^2 p_{1\beta}(\underline{x}, t) - k_{12} p_{1\beta}(\underline{x}, t) + k_{21} p_{2\beta}(\underline{x}, t) \\ \\ \dfrac{\partial p_{2\beta}(\underline{x}, t)}{\partial t} = D\nabla^2 p_{2\beta}(\underline{x}, t) - \underline{v} \cdot \underline{\nabla} p_{2\beta}(\underline{x}, t) + k_{12} p_{1\beta}(\underline{x}, t) - k_{21} p_{2\beta}(\underline{x}, t) \end{cases} \tag{7.4}$$

[2] The MSD expressions of eq. (7.3) are valid as long as the characteristic dimension L of the space available for diffusion and drift is sufficiently large to make the measurement time interval much smaller than $L^2/4D$. For cell measurements, $L \sim 10\mu m$ and $D \sim 10^{-4}\mu m^2/s$, so that $L^2/4D > 10^6 s$ [249].

Initial conditions can be cast as $p_{\alpha\beta}(\underline{x},0) = \delta_{\alpha\beta}\delta(\underline{x})$ (with α,β=1,2). It is also convenient to introduce the equilibrium probabilities, hereafter referred to as P_1^{eq} and P_2^{eq}, of finding the particle in states (1) and (2) respectively: in terms of the transition rates k_{12} and k_{21},

$$P_1^{eq} = \frac{k_{21}}{k_{12}+k_{21}} \quad , \quad P_2^{eq} = \frac{k_{12}}{k_{12}+k_{21}} \tag{7.5}$$

This allows evaluating the probability density $p_\alpha(\underline{x},t)$ of finding the particle in state α (α=1,2) at point $\underline{x}$ at time t, provided it was in state β (β=1,2) at time t=0 with equilibrium probability P_β^{eq}: by summing over the two propagators $p_{\alpha 1}(\underline{x},t)$ and $p_{\alpha 2}(\underline{x},t)$ [285],

$$p_\alpha(\underline{x},t) = p_{\alpha 1}(\underline{x},t)P_1^{eq} + p_{\alpha 2}(\underline{x},t)P_2^{eq} \tag{7.6}$$

Densities $p_\alpha(\underline{x},t)$ satisfy in turn

$$\begin{cases} \dfrac{\partial p_1(\underline{x},t)}{\partial t} = D\nabla^2 p_1(\underline{x},t) - k_{12}p_1(\underline{x},t) + k_{21}p_2(\underline{x},t) \\ \dfrac{\partial p_2(\underline{x},t)}{\partial t} = D\nabla^2 p_2(\underline{x},t) - \underline{v}\cdot\underline{\nabla}p_2(\underline{x},t) + k_{12}p_1(\underline{x},t) - k_{21}p_2(\underline{x},t) \end{cases} \tag{7.7}$$

with initial conditions $p_1(\underline{x},0) = P_1^{eq}\delta(\underline{x})$ and $p_2(\underline{x},0) = P_2^{eq}\delta(\underline{x})$.

The derivation of the MSD proceeds, in 2D, with the computation of the second-order moments

$$< |\underline{x}_\alpha(t)|^2 >= \iint_{-\infty}^{+\infty} (x^2+y^2)p_\alpha(x,y,t)\,dx\,dy \tag{7.8}$$

where the subscript α in the right-hand term denotes the distribution $p_\alpha(x,y,t)$ over which the two moments are computed: $< |\underline{x}_1(t)|^2 >$ is the mean-square-displacement after a time t travelled during the particle residence in state (1), whereas $< |\underline{x}_2(t)|^2 >$ is the mean-square-displacement after a time t travelled during the particle residence in state (2). With these definitions, the total MSD at time t is simply the sum $< |\underline{x}(t)|^2 >=< |\underline{x}_1(t)|^2 > + < |\underline{x}_2(t)|^2 >$ [285].
In order to derive $< |\underline{x}(t)|^2 >$, I multiply eq. (7.7) by (x^2+y^2) and I integrate with

respect to $\underline{x}$ from minus to plus infinity [285]. This leads to

$$\begin{cases} \dfrac{d<|\underline{x}_1(t)|^2>}{dt} = 4DP_1^{eq} - k_{12}<|\underline{x}_1(t)|^2> + k_{21}<|\underline{x}_2(t)|^2> \\ \dfrac{d<|\underline{x}_2(t)|^2>}{dt} = 4DP_2^{eq} + 2(v_x<x_2(t)> + v_y<y_2(t)>) + \\ \qquad\qquad + k_{12}<|\underline{x}_1(t)|^2> - k_{21}<|\underline{x}_2(t)|^2> \\ \dfrac{d<|\underline{x}(t)|^2>}{dt} = 4D(P_1^{eq} + P_2^{eq}) + 2(v_x<x_2(t)> + v_y<y_2(t)>) \end{cases} \tag{7.9}$$

with the initial conditions $<|\underline{x}_\alpha(0)|^2>=0$ (α=1,2). In obtaining eq. (7.9), I have employed the relation $P_\alpha(t) = P_\alpha^{eq}$ (α=1,2): this condition can be derived by integrating eq. (7.7) with respect to $\underline{x}$ from minus to plus infinity, and by solving the resulting differential equations

$$\frac{dP_1(t)}{dt} = -\frac{dP_2(t)}{dt} = -k_{12}P_1(t) + k_{21}P_2(t) \tag{7.10}$$

with the initial conditions $P_\alpha(t=0) = P_\alpha^{eq}$. $P_1(t) = \iint_{-\infty}^{+\infty} p_1(\underline{x},t)dxdy$ and $P_2(t) = \iint_{-\infty}^{+\infty} p_2(\underline{x},t)dxdy$ are the probabilities of finding the particle in state (1) and in state (2) at time t.

Prior to integrate, with respect to time, the equation for $<|\underline{x}(t)|^2>$, it is necessary to compute $<x_2(t)>$ and $<y_2(t)>$, i.e. the mean displacement at time t, along the x- and y- directions, travelled by the particle when in state (2). Again, $<x_2(t)>=\iint_{-\infty}^{+\infty} x p_2(x,y,t)dxdy$ is obtained by multiplying by x eq. (7.7), by then integrating with respect to $\underline{x}$ from minus to plus infinity, and by finally solving the system of coupled differential equations for $<x_1(t)>$ and $<x_2(t)>$ with the initial conditions $<\underline{x}_\alpha(0)>=0$; the same procedure is applied to $<y_2(t)>=\iint_{-\infty}^{+\infty} y p_2(x,y,t)dxdy$, leading to

$$\begin{cases} <x_2(t)> = \tau_{rel}v_x^{eff}(1-k_{12}\tau_{rel})(1-e^{-t/\tau_{rel}}) + v_x^{eff}P_2^{eq}t \\ <y_2(t)> = \tau_{rel}v_y^{eff}(1-k_{12}\tau_{rel})(1-e^{-t/\tau_{rel}}) + v_y^{eff}P_2^{eq}t \end{cases} \tag{7.11}$$

The system relaxation time and the effective velocity components have been introduced according to the definitions $\tau_{rel} = (k_{12}+k_{21})^{-1}$, $v_x^{eff} = v_x P_2^{eq}$ and $v_y^{eff} = v_y P_2^{eq}$.

By substituting eq. (7.11) into eq. (7.9) (third eq.), one obtains

$$\frac{d<|\underline{x}(t)|^2>}{dt} = 4D + 2\Big[\tau_{rel}(1-k_{12}\tau_{rel})(1-e^{-t/\tau_{rel}})\{v_x v_x^{eff} + v_y v_y^{eff}\} + \\ + P_2^{eq}(v_x v_x^{eff} + v_y v_y^{eff})t\Big] \tag{7.12}$$

The derivation of the MSD ends with the integration of eq. (7.12) with respect to time from $t = 0$ to a generic time τ, yielding

$$<|\underline{x}(\tau)|^2> = MSD(\tau) = \\ = 4D\tau + |\underline{v}^{eff}|^2\tau^2 + 2\tau_{rel}\frac{k_{21}}{k_{12}}|v^{eff}|^2\Big(\tau - \tau_{rel}(1-e^{\tau/\tau_{rel}})\Big) \tag{7.13}$$

$|\underline{v}^{eff}| = P_2^{eq}|\underline{v}|$ is the modulus of the effective drift velocity, obtained by weighting the drift speed $|\underline{v}|$ with the equilibrium probability of finding the particle in the active state.
Globally, eq. (7.13) evidences that the MSD for intermittent active transport is the superposition of three terms: the first term linearly depends on the lag time and on the diffusion coefficient D, and recalls the MSD of a purely diffusive process (eq. 7.3 i); the second term depends quadratically on the lag time and recalls the MSD of directional transport (eq. 7.3 ii), with a reduced speed equal to $|\underline{v}^{eff}|$; the third term contains the dependence on the kinetic parameters of the model (the relaxation time and the transition rates k_{12} and k_{21}).

Together with eq. (7.3), the MSD expression of eq. (7.13) can be employed for the fit of experimental mean-square-displacement plots. Both the mode of motion and the underlying transport parameters could be recovered from the MSD fit: in the presence of intermittent active transport, the diffusion coefficient, the effective drift speed, the system relaxation time and the ratio of the two transition rates can in principle be recovered; then by combining τ_{rel} and the ratio k_{21}/k_{12}, the transition rates k_{12} and k_{21} can be derived as well.
In this context, I remark that the derivation of eqs. (7.3) and eq. (7.13) does not take into account any source of experimental uncertainty. Although a few attempts in deriving analytically the standard deviation of MSD plots have been performed for free diffusion [249], static errors arising from the uncertainty on particle localizations are usually accounted for by adding a constant term (a baseline) into the adopted MSD fit equation; when static errors are not taken into

account, free diffusion may be incorrectly categorized as anomalous sub-diffusion due to an erroneous non-linear dependence of the MSD-vs-τ plot [254, 272, 286].

7.2 Bayesian analysis of particle trajectories

The main drawback of an MSD-based analysis relies in the MSD being a temporally-averaged quantity. When the mean-square-displacement is computed by an average over the whole trajectory length, the statistics with which the mean value is determined increases at the expense of temporal resolution: short-lived phases of an intermittent dynamics might get lost in the averaging operation, so that, for example, intermittent directional transport may be mistaken for a permanent diffusion or drift process with erroneous values for the drift speed or diffusion coefficient. Such a problem has been reported already for the analysis of hop-diffusion, which can be identified by inspecting the whole trajectory but leads to a linear τ-dependence in the experimental MSD [254, 287]. Similarly, intermittency between two diffusion states, with diffusion coefficients D_1 and D_2, might produce a linear MSD-vs-τ plot with a slope proportional to the weighted average (weighted on the equilibrium probabilities of the two states) of the D_1 and D_2 values [248]. In this case the MSD describes the overall average dynamics of the particle but lacks to give insight into the microscopic and transient features of the true transport phenomenon.

Two possible strategies can be adopted to overcome this limitation affecting the MSD computation and analysis. The first consists in deriving the MSD by averaging the square-displacement over limited portions of the experimental trajectory: by restricting the number of data points over which the MSD is computed, and by subsequently sliding the window of interest throughout the trajectory length, temporal variations experienced by the mode of motion and/or by the transport parameters (and hence by the MSD curvature) can be identified [219,272]. Especially when combined to the measurement of the angular correlation of consecutive steps, local MSDs help in identifying and quantifying directional persistence at a sub-trajectory level. The drawback is that a certain extent of subjectiveness is introduced by the choice of the window size; moreover, the window size must remain narrower than the minimum duration of the specific transient motion under investigation, which is usually not known a priori.

The second strategy, described in detail in the following, exploits the principles of Bayesian statistics and the formalism of Hidden Markov Models to simulta-

neously account for the whole observed trajectory, while achieving single-step temporal resolution in the detection of state changes.

7.2.1 Modeling a particle trajectory as a Hidden Markov Model

I have already pointed out the role of the Gaussian diffusion propagator $P(\underline{x}, t)$ in assigning the length of the displacement travelled during a time interval Δt by a particle exhibiting Brownian diffusion and uniform drift: each displacement along the x- and the y- direction is distributed normally, with a variance proportional to the diffusion coefficient and with mean value assigned by the drift speed. More in general, when an SPT trajectory is collected (whether diffusive, ballistic or intermittent), each observed displacement obeys a well-defined probability distribution: hence, the observation of the sequence of *individual* particle displacements should allow inferring the parameters characterizing the corresponding probability density function (i.e., the transport parameters) and the temporal variations this probability density function undergoes (i.e., the changes in the motion state) with increased sensitivity. Accurate statistics is still achieved by taking advantage of the whole trajectory but, since the averaging operation intrinsic in the MSD computation is not performed any more, short-lived motion phases (i.e., phases lasting for a few time-steps in the SPT experiment) can now be detected.

From the theoretical and mathematical viewpoint, the idea of extracting motion parameters and state changes from entire SPT trajectories can be formalized by the statistical framework of Hidden Markov Models [248, 284, 288, 289].
Let $\underline{x}(t_j) = (x(t_j), y(t_j))$ (for $j = 1...N$) be a single-particle trajectory measured by an SPT experiment. For the sake of generality, the observed particle is assumed to experience stochastic transitions between m motion states, with the i^{th} state ($i = 1...m$) parameterized by specific transport properties: a diffusion coefficient D_i and a drift velocity $\underline{v}_i$ are considered here. At each time point $t_{j=1...N}$, the particle is in one of the m states, so that, for a trajectory of length N, a sequence of N state occupancies is assigned: I denote this state sequence with

$$\mathbf{s} = s(t_1)s(t_2)...s(t_N) \tag{7.14}$$

with each $s(t_j)$ belonging to $[1, 2, ..., m]$. The state occupied by the particle at time t_j is assumed to depend only on the state the particle occupies at time t_{j-1}: hence

$$p\big(s(t_j) = i \big| s(t_{j-1}), s(t_{j-2})...\big) = p\big(s(t_j) = i \big| s(t_{j-1})\big) \tag{7.15}$$

$\forall j$, where $p\big(s(t_j) = i \big| s(t_{j-1}), s(t_{j-2})...\big)$ is the conditional probability that the particle is in state i at time t_j provided it has before experienced the sequence state $s(t_{j-1}), s(t_{j-2})...$. The random transitions between the states are regulated by probabilities p_{ik}, with each p_{ik} defined ($\forall j$ and with $i, k = 1...m$) by

$$p_{ik} = p\big(s(t_{j+1}) = k \big| s(t_j) = i\big) \tag{7.16}$$

Experimentally, the exact state sequence **s** is clearly not observed: what is observed is the sequence of the particle displacements. However, the length and direction of each displacement $\Delta\underline{x}(t_{j+1}) = \underline{x}(t_{j+1}) - \underline{x}(t_j)$ is assigned by the state the particle occupies at the corresponding time point t_j through the relative (diffusion) propagator: therefore, although the N-step state sequence **s** underlying the trajectory (and hence the exact state the particle occupies at time t_j) is unknown (hidden), the experimental measurement of all the particle displacements assigned by **s** allows inferring information on the sequence **s** itself, as well as on the transport parameters of the constituent states and on the rates of transition between them. To this aim, the likelihood maximization strategy described in the following is adopted.

7.2.2 Maximum-likelihood approach

Let $\theta = \{D_{i=1...m}, \underline{v}_{i=1...m}, p_{i,k=1...m}\}$ be the set of unknown parameters for a d-dimensional trajectory described by an m-state Markov chain. For d=2 (2D tracking experiment) and m=2 (as in two-state dynamics of eq. 6.37), the transition probabilities for the particle to undergo a state switch in a time interval Δt (equal to the time resolution of the SPT data acquisition) are related to the rate constants k_{12} and k_{21} [248] by

$$\begin{cases} p_{12} = \dfrac{k_{12}}{k_{12} + k_{21}}\big\{1 - exp[-(k_{12} + k_{21})\Delta t]\big\} \\ p_{21} = \dfrac{k_{21}}{k_{12} + k_{21}}\big\{1 - exp[-(k_{12} + k_{21})\Delta t]\big\} \\ p_{11} = 1 - p_{12} \\ p_{22} = 1 - p_{21} \end{cases} \tag{7.17}$$

The set of independent parameters reduces in this case to $\theta = \{D_{i=1,2}, \underline{v}_{i=1,2}, p_{12}, p_{21}\}$. Equivalently, $\theta = \{D_{i=1,2}, |\underline{v}|_{i=1,2}, \alpha_{i=1,2}, p_{12}, p_{21}\}$, where α_i is the angle defining

the x- and y- components of the drift velocity vector $\underline{v}_i$ ($v_{xi} = |\underline{v}_i| \cos \alpha_i$, $v_{yi} = |\underline{v}_i| \sin \alpha_i$).
According to Bayes' theorem, the likelihood of a parameter set θ given an experimental trajectory $\underline{x}(t_{j=1...N})$ can be expressed as

$$\ell\Big(\theta\big|\underline{x}(t_1), \underline{x}(t_2), ..., \underline{x}(t_N)\Big) = \frac{p\big(\underline{x}(t_1), \underline{x}(t_2), ..., \underline{x}(t_N)\big|\theta\big)p(\theta)}{p\big(\underline{x}(t_1), \underline{x}(t_2), ..., \underline{x}(t_N)\big)} \tag{7.18}$$

By assuming a uniform prior probability $p(\theta)$ (the less informative prior) and by marginalizing the likelihood over all possible hidden state sequences $\mathbf{s}$, eq. (7.18) can be re-written as

$$\begin{aligned} \ell\Big(\theta\big|\underline{x}(t_1), \underline{x}(t_2), ..., \underline{x}(t_N)\Big) &\propto p\big(\underline{x}(t_1), \underline{x}(t_2), ..., \underline{x}(t_N)\big|\theta\big) = \\ &= \sum p\big(\underline{x}(t_1), \underline{x}(t_2), ..., \underline{x}(t_N)\big|\mathbf{s}, \theta\big)p(\mathbf{s}|\theta) \\ &\equiv \sum p\big(\mathbf{x}|\mathbf{s}, \theta\big)p(\mathbf{s}|\theta) \end{aligned} \tag{7.19}$$

In the last equation, $\mathbf{x} \equiv \underline{x}(t_1), \underline{x}(t_2), ..., \underline{x}(t_N)$ has been introduced for the sake of compactness, denoting the observed sequence of coordinates.
The summation over state sequences can be performed efficiently by the forward-backward algorithm [248, 284, 289, 290]. It relies on evaluating the probability $\phi_i(j)$ of observing the partial sequence of coordinates $\underline{x}(t_1), \underline{x}(t_2), ..., \underline{x}(t_{j+1})$ up to the $(j+1)^{th}$ step and of being in state i at time t_j, given the model parameters θ:

$$\phi_i(j) = p\big(\underline{x}(t_1), \underline{x}(t_2), ..., \underline{x}(t_{j+1}), s(t_j) = i\big|\theta\big) \tag{7.20}$$

At first, $\phi_i(1)$ corresponds to the probability that $s(t_1) = i$ and that the first displacement $\Delta\underline{x}(t_2) = \underline{x}(t_2) - \underline{x}(t_1)$ is observed:

$$\begin{aligned} \phi_i(1) &= p\big(\underline{x}(t_1), \underline{x}(t_2), s(t_1) = i\big|\theta\big) = \\ &= p\big(\underline{x}(t_1), \underline{x}(t_2)\big|s(t_1) = i, \theta\big)p\big(s(t_1) = i\big|\theta\big) \\ &= p\big(\underline{x}(t_1), \underline{x}(t_2)\big|s(t_1) = i, \theta\big)\pi_i \end{aligned} \tag{7.21}$$

Here $\pi_i = P_i^{eq}$ defines the probability of starting in state i at time t_1. Since each state i is parameterized by a diffusion coefficient D_i and a planar drift velocity $\underline{v}_i$, the diffusion+drift propagator of eq. (7.1) can be exploited to obtain

$$p\big(\underline{x}(t_1), \underline{x}(t_2)\big|s(t_1) = i, \theta\big) = \frac{1}{(4\pi D_i \Delta t)} exp\Big(-\frac{|\Delta\underline{x}(t_2) - \underline{v}_i\Delta t|^2}{4D_i\Delta t}\Big) \tag{7.22}$$

Then at subsequent time points $\phi_i(j)$ can be evaluated recursively [289] according to

$$\begin{aligned}\phi_i(j) =& p\big(\underline{x}(t_j), \underline{x}(t_{j+1})\big|s(t_j) = i, \theta\big) \sum_{k=1}^{2} \phi_k(j-1)p_{ki} \\ &= \frac{1}{(4\pi D_i \Delta t)} exp\Big(-\frac{|\Delta\underline{x}(t_{j+1}) - \underline{v}_i\Delta t|^2}{4D_i\Delta t}\Big) \sum_{k=1}^{2} \phi_k(j-1)p_{ki}\end{aligned} \tag{7.23}$$

Hence by recursion all the ϕ terms up to $\phi_i(N-1)$ can be computed. Note that $\phi_i(N-1)$ corresponds to the probability that $s(t_{N-1}) = i$ and that all the displacements up to $\underline{x}(t_N)$ have been observed. Therefore a final summation over the two possible states i=1,2 yields the probability of having observed all the trajectory for a given parameter set θ:

$$\begin{aligned}\ell\Big(\theta\big|\underline{x}(t_1),&\underline{x}(t_2), ..., \underline{x}(t_N)\Big) \propto p\big(\underline{x}(t_1), \underline{x}(t_2), ..., \underline{x}(t_N)\big|\theta\big) = \\ &= \sum p\big(\mathbf{x}\big|\mathbf{s}, \theta\big)p(\mathbf{s}\big|\theta) = \sum_{i=1}^{2} \phi_i(N-1) = \\ &= \sum_{i=1}^{2} \left\{ \frac{1}{(4\pi D_i \Delta t)} exp\Big(-\frac{|\Delta\underline{x}(t_N) - \underline{v}_i\Delta t|^2}{4D_i\Delta t}\Big) \sum_{k=1}^{2} \phi_k(N-2)p_{ki} \right\}\end{aligned} \tag{7.24}$$

I remark that due to the recursive structure of eq. (7.24), *all* the displacements enter explicitly in the likelihood evaluation.

Given the experimental observation of the sequence $\mathbf{x}$ of the particle coordinates, by means of eq. (7.24) the likelihood of any parameter set θ can be quantified; since the most probable parameter set - hereafter referred to as Θ - is the one that maximizes the likelihood, the Bayesian inference of dynamic and kinetic parameters from the observed SPT trajectory ends with the maximization of $\ell\Big(\theta\big|\underline{x}(t_1), \underline{x}(t_2), ..., \underline{x}(t_N)\Big)$ with respect to θ.

7.2.3 Markov Chain Monte Carlo algorithm

The maximization of the likelihood (eq. 7.24) with respect to θ is intractable analytically, so that numerical methods must be employed to obtain the most

probable parameter set Θ:

$$\Theta = \text{argmax}_{\theta}\left\{\ell\left(\theta\middle|\underline{x}(t_1),\underline{x}(t_2),...,\underline{x}(t_N)\right)\right\} = \text{argmax}_{\theta}\left\{\phi_1(N-1)+\phi_2(N-1)\right\} \tag{7.25}$$

A possible method to be adopted for the likelihood maximization relies on the Markov Chain Monte Carlo algorithm [248, 289, 291]. Briefly, at each iteration the likelihood of a proposed parameter set θ_p is computed and compared to the likelihood of the actual parameter set θ: according to a Metropolis rejection criterion, θ_p is accepted with probability $p = 1$ if it produces an increase in the likelihood value, and with probability assigned by the ratio of the likelihoods $\ell(\theta_p|\mathbf{x})$ and $\ell(\theta|\mathbf{x})$ otherwise. More in detail, the steps of the MCMC maximization procedure can be described as follows:

1. An initial parameter set θ is proposed. In the present case, initial parameter guesses for the diffusion coefficient and the drift speed are randomly selected within the orders of magnitude suggested by image correlation and MSD analyses; the drift direction and the transition probabilities are extracted as pseudo-random numbers from uniform distributions in the interval $[0, 2\pi]$ and $[0, 1]$, respectively. The extracted probabilities are checked against the summation conditions (e.g., $\sum_k p_{ik} = 1$ and $\sum_i P_i^{eq} = 1$) and extracted again if necessary;

2. A new guess θ_p for the parameter set is randomly extracted from a suitable probability distribution. The detailed-balance condition of Markov chains (stating that the average number of transitions from θ to θ_p should be equal to the average number of transitions from θ_p to θ) requires the probability distributions to be either uniform or Gaussian: practically, a random-walk is performed in the parameters space. Each distribution is parameterized by a step-width or variance δ to control the extent by which a parameter can vary. In the present case, a multivariate Gaussian distribution centered at the previous parameter estimate is employed for all the parameters, and each variance is adjusted to achieve a $\sim$ 30-60% acceptance rate at the end of the whole MCMC run. No constraints other than the probability normalization conditions and the non-negativeness of diffusion coefficients and drift speeds are imposed during MCMC successive iterations. Finally, at each MCMC step sequential separate likelihood updates are performed for dynamic parameters

(diffusion coefficient, drift speed and drift angle), whereas a block approach is adopted for probabilities (displacements are simultaneously proposed for all unknown probabilities leading to a joint likelihood update);

3. The proposed set θ_p is accepted or rejected according to a Metropolis rejection criterion. The move is accepted with probability $\min(1, \ell(\theta_p|\mathbf{x})/\ell(\theta|\mathbf{x}))$: hence all the moves that increase the likelihood are immediately accepted, while moves that decrease the likelihood get accepted with a probability assigned by the ratio of the new and the old likelihood values. Again, this criterion is adopted to satisfy the detailed-balance condition of Markov chains. The aforementioned acceptance rate ~ 30-60% usually allows to sufficiently explore the parameter space; too high acceptance rates are associated to a too small width for the proposal distribution (hence the parameter space is not adequately explored), whereas too low acceptance rates denote that the majority of the parameter proposals move far from the region of maximum likelihood;

4. Steps 1-3 are repeated until the algorithm convergence. At the end of the MCMC run, the results are output as a plot of the values of the likelihood and of the values of all the model parameters[3] as a function of the iteration step. The typical likelihood-vs-iteration plot shows an initial monotonic increase, reaching then a plateau where the likelihood fluctuates around its maximum value; similarly, after initial abrupt variations, all the parameter estimates maintain relatively constant values as a function of the iteration step. The most probable parameter set Θ is assigned by fitting to a Gaussian trial function the histograms of the values explored by each parameter within the final plateau.
   To avoid being stuck in local maxima and to ensure that the likelihood global maximum is found, ~ 10-20 independent MCMC runs (with different initial parameter guesses and different seed for the pseudo-random number generator) are performed for each trajectory; individual runs typically consist in 10-20x10^3 iterations.

[3]For each iteration step, the new parameter value is reported if the move is accepted, while the old parameter estimate is reported if is is kept unchanged with the move.

7.3 Experimental results

Having outlined the theoretical framework for both the MSD-based and the Bayesian analyses of Single Particle Tracking data, I report the experimental results [237] obtained when investigating by means of SPT the intracellular transport of endocytosed gold nanostars.

SPT raw data have been collected on the same xyt-stacks of raster-scanned confocal images analyzed by TICS and STICS in Chapter 6 (hence I refer to the Materials and Methods Section of Chapter 6 for the details concerning image acquisition settings). The trajectories of individual GNSs-containing scattering vesicles have been computed by the tracking software Imaris (Bitplane, Zurich, CH) and have been subsequently analyzed by a custom-written Python code to yield the mean-square-displacement $MSD(\tau)$ according to the definition of eq. (7.2).
As shown in Fig. 7.1 with exemplary trajectories and MSD-vs-τ plots, like Temporal and Spatio-Temporal Image Correlation Spectroscopy, Single Particle Tracking reveals the presence of different motion types. The first MSD plot exhibits a linear dependence on the lag time τ, classifying the corresponding trajectory as purely diffusive (eq. 7.3i). The second MSD-vs-τ plot requires the coupling of Brownian diffusion and a non-zero drift speed, and can be fit to the MSD expression of eq. (7.3ii). The third MSD is not compatible with eq. (7.3) and, due to the positive curvature, suggests the presence of super-diffusive dynamics. Hypothesizing therefore that cytoskeleton-based transport is responsible for the enhancement of diffusion, I have tested the compatibility of the MSD with a sequence of jumps between a purely diffusive motion regime and an active transport regime: in agreement with the intermittent transport model of eq. (6.37), the curve can be fit to the MSD expression I derived in eq. (7.13). Out of a total of thirty trajectories and MSD plots examined, ~75% of them were not compatible with the simple diffusive and ballistic models.

It is worth underlying that the intermittent transport model of eq. (6.37) hypothesizes a single value for the diffusion coefficient of cellular vesicles when freely diffusing in the cytoplasm and when bound to molecular motor proteins: no change in the diffusion coefficient is introduced upon the binding/unbinding events regulating the transitions from the active to the passive motion state. Furthermore, a non-zero drift velocity is assumed to characterize only state (2), state (1) exhibiting purely diffusive dynamics. Therefore, the set of model parameters $\theta = \{D_{i=1,2}, |\underline{v}|_{i=1,2}, \alpha_{i=1,2}, p_{12}, p_{21}\}$ reduces to $\theta = \{D, |\underline{v}|, \alpha, p_{12}, p_{21}\}$, with

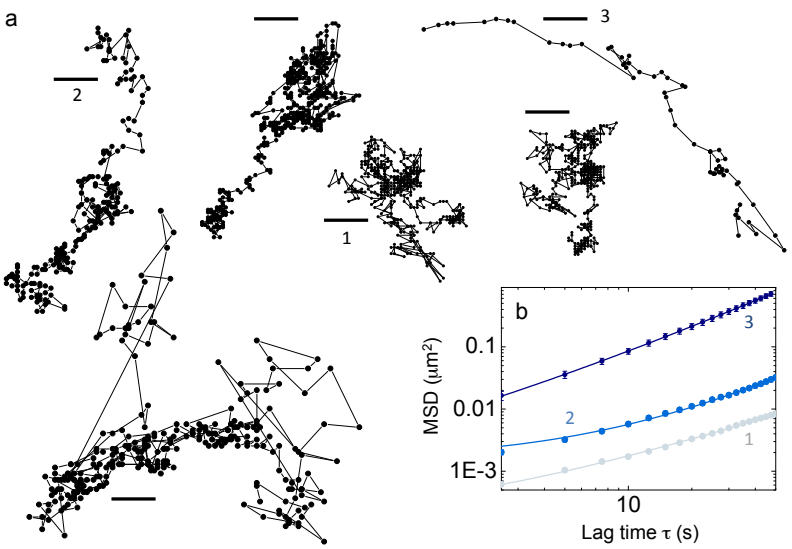

Figure 7.1: *Single Particle Tracking: trajectories and MSD analysis.* (a): exemplary SPT trajectories obtained by tracking GNSs-containing scattering vesicles in HeLa cells; the scale bar corresponds to 0.2 μm for all the trajectories, except for track #3, for which the scale bar corresponds to 0.4 μm. The trajectories exhibit purely diffusive, directional and intermittent dynamics as shown with the MSD plots in panel (b). (b): MSD-vs-τ plots for the trajectories identified as #1,2 and 3 in (a); at each lag time τ, the MSD is reported as mean ± standard deviation over the whole trajectory length; error bars are within the size of data points. Curve 1 has been fit to eq. (7.3i), with best-fit parameter D=(3.87± 0.05)x10^{-5} $\mu m^2/s$; curve 2 has been fit to eq. (7.3ii), with best-fit parameter D=(8.9± 0.3)x10^{-5} $\mu m^2/s$ and $|\underline{v}|$=(2.26± 0.04)x10^{-3} $\mu m/s$; curve 3 has been fit to eq. (7.13), with D=(1.4±0.1)x10^{-3} $\mu m^2/s$, $|\underline{v}^{eff}|$=(1.12±0.04)x10^{-2} $\mu m/s$, τ_{rel}=(8±3) s and k_{21}/k_{12}=2.1±0.5.

$D_1 = D_2 \equiv D$, $|\underline{v}|_1 = 0$ and $|\underline{v}|_2 \equiv |\underline{v}|$. This configuration corresponds to the *simplest* possible intermittent transport model deviating from purely diffusive and ballistic behaviors: it avoids over-parameterization and, according to the MSD analysis, it is sufficient to describe the GNSs experimental data.

To further strengthen the results of the MSDs fit, and to allow a more reliable estimate of all the dynamic and kinetic parameters the model involves, the Bayesian maximum-likelihood analysis described in Section 7.2 has been implemented. A custom-written Python code has been employed for the Markov Chain Monte Carlo

(MCMC) maximization according to eqs. (7.17)-(7.24): the procedure outlined in Subsection 7.2.3 has been followed, but for the sake of computational convenience the logarithm of the likelihood has been maximized, instead of directly maximizing $\ell(\theta|\mathbf{x})$.
The outcome of the MCMC algorithm on an exemplary trajectory exhibiting intermittency between diffusion and active transport is reported in Fig. 7.3. In panel (a), the log-likelihood is plotted as a function of the iteration step for five separate MCMC runs on the same intermittent-type trajectory, evidencing the code convergence to the likelihood global maximum. Similarly, the trend of the model parameters is reported, as a function of the iteration step, in the insets of panels (b)-(f). In the same panels, for D, $|\underline{v}|$, α, p_{12} and p_{21}, I report the histogram of the values each parameter assumes during the MCMC run after the initial monotonic increase of the log-likelihood: these histograms, representing the parameter values explored in the region of the parameters space close to likelihood maximum, can be fit to a Gaussian trial function to derive the most probable parameter set $\Theta = \{D=(6.1\pm0.6)x10^{-5}\ \mu m^2/s,\ |\underline{v}|=(1.2\pm0.4)x10^{-2}\ \mu m/s,\ \alpha=(241^\circ \pm 12^\circ),\ p_{12}=(0.04\pm0.03),\ p_{21}=(0.18\pm0.09)\}$. The corresponding equilibrium probabilities are $P_1^{eq}=(0.8\pm0.1)$ and $P_2^{eq}=(0.2\pm0.1)$ and strongly support that an intermittent model can be adopted to describe the GNSs experimental intracellular SPT data.

The just-described analysis (Fig. 7.3) refers to a single portion of a longer trajectory, shown entirely in Fig. 7.2. In fact, by relying on the two-state dynamics of eq. (6.37), the implemented Monte Carlo code requires a single drift direction for the active transport state: taking into account abrupt changes in the drift direction (like those apparent in Fig. 7.2) would require the introduction of at least a third state (differing in the angle α) within the model, remarkably complicating the parameters recovery. It is therefore convenient to manually segment the trajectory and to apply the Bayesian analysis separately on each of the portions identified. The results reported in Fig. 7.3 refer to the segment denoted as (i) in Fig. 7.2, whereas the results for segments (ii) and (iii) are shown in Fig. 7.4.
Importantly, while intermittent active transport well describes portion (iii) with $P_1^{eq}=(0.92\pm0.02)$ and $P_2^{eq}=(0.08\pm0.02)$, segment (i) is classified as purely diffusive by the MCMC Bayesian analysis (a vanishing probability $p_{12}=0.00\pm0.02$ is retrieved). Therefore, the proposed intermittent model also includes the single-state purely diffusive behavior (and, similarly, the diffusion+drift case): no prior assumption on the Brownian or super-diffusive nature of the investigated dynamics is required, and the simplest stochastic transport model accurately describing the experimental data can be identified.

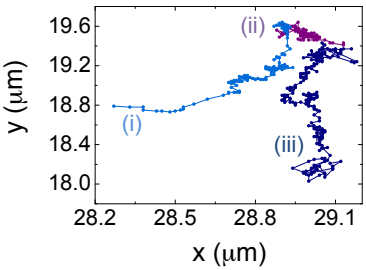

Figure 7.2: *Single Particle Tracking: Bayesian analysis (I).* SPT trajectory exhibiting intermittent active transport, collected in the same HeLa cell analyzed by TICS and STICS in Figs. 6.7 and 6.9. The Bayesian analysis of the trajectory is reported in Figs. 7.3,7.4 and has been performed separately on segments (i), (ii) and (iii) as described in the text.

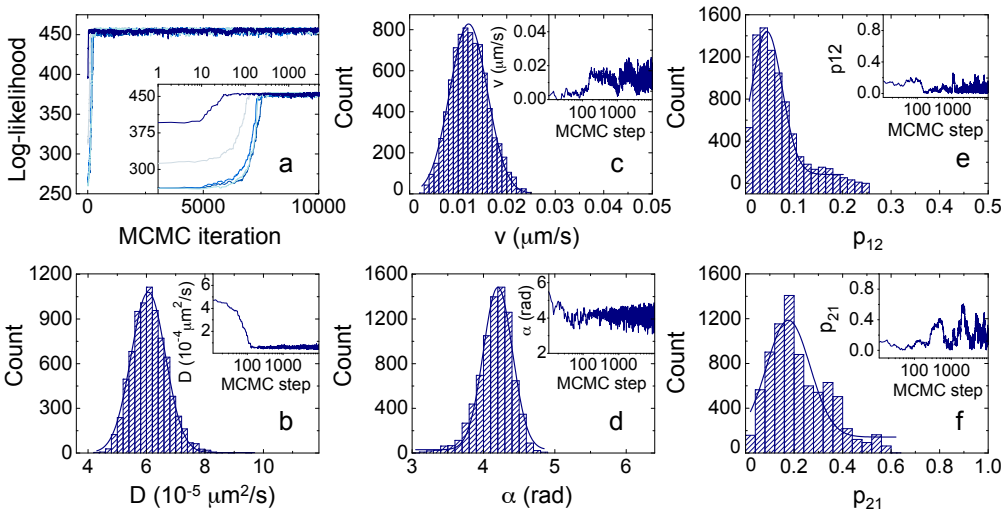

Figure 7.3: *Single Particle Tracking: Bayesian analysis (II).* The results of the MCMC likelihood maximization are reported for portion (i) of the trajectory shown in Fig. 7.2. (a): log-likelihood as a function of the MCMC iteration step for five independent runs; the log-scale is adopted in the inset to magnify the code convergence to the same likelihood global maximum. (b)-(f): histograms of the parameter values explored during the log-likelihood maximization after the initial convergence steps. Data refer to D, $|\underline{v}|$, α, p_{12} and p_{21} (panels b, c, d, e and f, respectively). The mean values recovered by the Gaussian fits identify the most probable parameter set $\Theta = \{D=(6.1\pm0.6)x10^{-5}\ \mu m^2/s,\ |\underline{v}|=(1.2\pm0.4)x10^{-2}\ \mu m/s,\ \alpha=(241^\circ \pm 12^\circ),\ p_{12}=(0.04\pm0.03),\ p_{21}=(0.18\pm0.09)\}$ given the experimental trajectory (P_1^{eq}=(0.8±0.1), P_2^{eq}=(0.2±0.1)). In the inset of each panel, the value proposed for the corresponding parameter as a function of the maximum-likelihood iteration is reported.

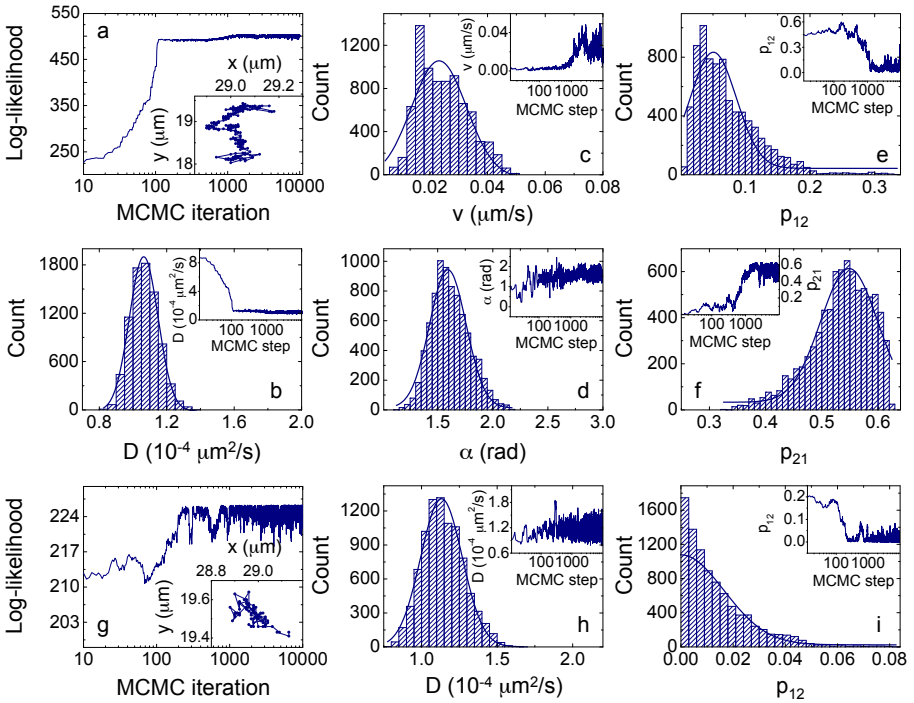

Figure 7.4: *SPT: Bayesian analysis (III).* (a)-(f): Bayesian analysis of portion (iii) of the trajectory shown in Fig. 7.2. The same segment of the trajectory is reported here in the inset of panel (a). (a): exemplifying log-likelihood plot as a function of the MCMC iteration step. (b)-(f): histograms of the parameter values explored during the log-likelihood maximization after the initial convergence steps of a single run. Data refer to D, $|\underline{v}|$, α, p_{12} and p_{21} (b, c, d, e and f, respectively). The mean values and standard deviations recovered by the Gaussian fits identify $\Theta = \{D=(1.06\pm0.09)x10^{-4}\ \mu m^2/s$, $|\underline{v}|=(2.3\pm0.9)x10^{-2}\ \mu m/s$, $\alpha=(91^\circ \pm 10^\circ)$, $p_{12}=(0.05\pm0.04)$, $p_{21}=(0.55\pm0.05)\}$ given the experimental trajectory ($P_1^{eq}=(0.92\pm0.02)$, $P_2^{eq}=(0.08\pm0.02)$). In the insets, the values proposed for the parameters as a function of the iteration are also reported. (g)-(i): MCMC analysis of portion (ii) of the trajectory shown Fig. 7.2. The same segment of the trajectory is reported here in the inset of panel (g). (g): exemplifying log-likelihood plot as a function of the MCMC iteration step. (h),(i): histograms of the values of D and p_{12} explored during the log-likelihood maximization after the initial convergence steps of a single run. The most probable values recovered as means and standard deviations of the Gaussian fits are $D=(1.1\pm0.1)x10^{-4}$ $\mu m^2/s$ and $p_{12}=(0.00\pm0.02)$. Due to the diffusive nature of the investigated trajectory, the histograms related to $|\underline{v}|$, α and p_{21} have not been reported. In the insets of panels (g) and (i), the values proposed for the corresponding parameter (D and p_{12}, respectively) are shown as a function of the iteration step.

The results of the MCMC Bayesian analysis of nineteen SPT trajectories are summarized in Tables 7.1 and 7.2, with the recovered diffusion coefficients, drift speeds, transition rates, transition probabilities, equilibrium probabilities for states (1) and (2) and effective drift speeds.
The typical diffusion coefficients $\sim 10^{-4}$ $\mu m^2/s$ agree with the results of Temporal Image Correlation Spectroscopy. The probabilities p_{12} an p_{21} retrieved by SPT (Table 7.1) correspond to an equilibrium probability P_2^{eq} typically varying between 0 and 0.2 (Table 7.2): SPT identifies therefore short-lived phases of directed transport, with a typical duration of a few seconds. Notably, this typical residence time in

trajectory	D $(\mu m^2/s)$	$\lvert\underline{v}\rvert$ $(\mu m/s)$	p_{12}	p_{21}
1	$(1.3\pm0.1)x10^{-4}$	0.06 ± 0.01	0.01 ± 0.01	0.8 ± 0.2
2	$(7\pm1)x10^{-4}$	0.21 ± 0.02	0.03 ± 0.02	0.6 ± 0.2
3	$(9\pm1)x10^{-4}$	0.09 ± 0.01	0.02 ± 0.02	0.4 ± 0.1
4	$(9.7\pm0.1)x10^{-4}$	0.052 ± 0.004	0.04 ± 0.02	0.8 ± 0.1
5	$(1.12\pm0.01)x10^{-4}$	0.026 ± 0.004	0.07 ± 0.03	0.3 ± 0.1
6	$(8\pm1)x10^{-5}$	0.04 ± 0.01	0.02 ± 0.01	0.7 ± 0.1
7	$(1.0\pm0.1)x10^{-3}$	0.08 ± 0.03	0.1 ± 0.1	0.7 ± 0.1
8	$(7\pm1)x10^{-4}$	0.13 ± 0.02	0.03 ± 0.02	0.7 ± 0.1
9	$(6.3\pm0.4)x10^{-4}$	0.28 ± 0.01	0.005 ± 0.003	0.93 ± 0.04
10	$(3.0\pm0.2)x10^{-4}$	0.16 ± 0.02	0.000 ± 0.003	0.9 ± 0.1
11	$(1.5\pm0.1)x10^{-4}$	0.08 ± 0.01	0.01 ± 0.01	0.6 ± 0.1
12	$(1.0\pm0.2)x10^{-4}$	0.02 ± 0.01	0.07 ± 0.07	0.8 ± 0.1
13	$(6\pm1)x10^{-5}$	0.012 ± 0.004	0.04 ± 0.03	0.2 ± 0.1
14	$(1.1\pm0.3)x10^{-4}$	0.11 ± 0.01	0.00 ± 0.03	0.2 ± 0.1
15	$(5\pm1)x10^{-5}$	0.003 ± 0.001	0.6 ± 0.2	0.1 ± 0.1
16	$(5\pm1)x10^{-5}$	0.06 ± 0.01	0.000 ± 0.002	0.91 ± 0.04
17	$(8\pm1)x10^{-5}$	0.028 ± 0.003	0.02 ± 0.01	0.8 ± 0.1
18	$(2.0\pm0.1)x10^{-4}$	0.05 ± 0.01	0.02 ± 0.01	0.7 ± 0.1
19	$(5\pm1)x10^{-5}$	0.09 ± 0.01	0.03 ± 0.02	0.5 ± 0.1

Table 7.1: *Bayesian analysis of Single Particle Tracking data.* Diffusion coefficient, drift speed and transition probabilities recovered by the Bayesian analysis of nineteen SPT trajectories collected in GNSs-treated HeLa cells. The corresponding transition rates, equilibrium probabilities and effective drift speed are reported in Table 7.2.

trajectory	k_{12} (s^{-1})	k_{21} (s^{-1})	P_1^{eq}	P_2^{eq}	$\lvert\underline{v}^{eff}\rvert$ $(\mu m/s)$
1	0.01±0.01	0.6±0.3	0.98±0.01	0.02±0.01	(9±8)x10^{-4}
2	0.02±0.01	0.4±0.3	0.95±0.05	0.05±0.05	(1.0±0.9)x10^{-2}
3	0.01±0.01	0.20±0.05	0.95±0.05	0.05±0.05	(4±3)x10^{-3}
4	0.03±0.02	0.7±0.3	0.96±0.03	0.04±0.03	(2±1)x10^{-3}
5	0.03±0.02	0.2±0.1	0.8±0.1	0.2±0.1	(4±2)x10^{-3}
6	0.02±0.01	0.5±0.2	0.97±0.02	0.03±0.02	(1.3±0.8)x10^{-3}
7	0.08±0.05	0.5±0.2	0.87±0.08	0.13±0.08	(1.1±0.8)x10^{-2}
8	0.02±0.01	0.5±0.2	0.96±0.03	0.04±0.03	(6±5)x10^{-3}
9	0.006±0.004	1.1±0.2	0.99±0.01	0.01±0.01	(2±1)x10^{-3}
10	0.005±0.004	1.0±0.2	0.99±0.01	0.01±0.01	(9±6)x10^{-4}
11	0.006±0.004	0.4±0.1	0.99±0.01	0.01±0.01	(1.2±0.9)x10^{-3}
12	0.07±0.07	0.8±0.3	0.9±0.1	0.1±0.1	(2±1)x10^{-3}
13	0.02±0.01	0.08±0.05	0.8±0.1	0.2±0.1	(2±1)x10^{-3}
14	0.00±0.01	0.11±0.05	1.0±0.1	0.0±0.1	–
15	0.5±0.4	0.07±0.06	0.1±0.1	0.9±0.1	(2.6±0.9)x10^{-3}
16	0.003±0.002	1.0±0.2	1.00±0.01	0.00 ±0.01	–
17	0.02±0.01	0.7±0.2	0.97±0.02	0.03±0.02	(8±5)x10^{-4}
18	0.014±0.007	0.4±0.1	0.97±0.02	0.03±0.02	(1.4±0.8)x10^{-3}
19	0.01±0.01	0.2±0.1	0.95±0.04	0.05±0.04	(5±4)x10^{-3}

Table 7.2: *Bayesian analysis of Single Particle Tracking data.* Transition rates, equilibrium probabilities and effective drift speed recovered by the Bayesian analysis of nineteen SPT trajectories collected in GNSs-treated HeLa cells. The trajectories compatible with a purely diffusive dynamics (P_1^{eq}=0) are those corresponding to a dwell time in state (2) $\tau_2=1/k_{21}$ less than, or close to, the detection limit of 2.5 s defined by the temporal resolution of the SPT experiment.

state (2), defined as $\tau_2=1/k_{21} \sim 10$ s, agrees with the duration of the force generated by molecular motor proteins along microtubules, as reported in the literature [273]. During their dwell in state (2), vesicles typically exhibit a relatively high drift speed $|\underline{v}| \sim 10^{-2}$ $\mu m/s$: even though the active transport regime lasts for a few trajectory steps, the drift speed allows imparting sufficient directionality to the particle trajectories to produce the overall super-diffusive behavior observed experimentally. When weighted by the equilibrium probability P_2^{eq} of the active transport state

(according to the definition of effective drift velocity previously introduced), the drift speed recovered by SPT reduces to the $\sim 10^{-3}$ $\mu m/s$ drift speed I have obtained by TICS and STICS.
The discrepancy between the drift speeds obtained by SPT and fluctuation-based Image Correlation analyses is, however, the result of a limited comparison between the Bayesian analysis of *intermittent* trajectories and the TICS and STICS analyses of the only regions of interest exhibiting a simpler *diffusion+drift* dynamics (up to this Chapter, no estimate for the drift speed has been recovered by Image Correlation in the presence of intermittent active transport) . Anticipated here, the comparison between the drift speed values measured by TICS, STICS and Single Particle Tracking will be deepened and considered in more detail in Chapter 8, once accomplished the measurement of the intermittent-model parameters by Fourier-space Image Correlation Spectroscopy.

7.4 Numerical simulations

The results presented so far in this Chapter suggest the compatibility of the two-state intermittent dynamics (eq. 6.37) with the GNSs intracellular transport. An additional confirmation of the compatibility of the experimental data with the assumed transport model can be achieved by verifying that the very same intermittency might produce the anomalous, non-linear displacement of the peak of the spatio-temporal correlation function when a STICS analysis is performed. As in the case of Lévy flights, numerical simulations can be of help in performing such a validation.
In order to simulate single-particle trajectories arising from a two-state intermittent dynamics with given D, $|\underline{v}|$, α, p_{12} and p_{21} values, a discrete Markov chain is initially generated from the p_{12} and p_{21} probabilities to assign the sequence of state occupancies [248]. Specifically, the particle state at the first time point is assigned by comparing a pseudo-random number r, extracted in the interval $(0,1)$, with the equilibrium probabilities: if $r \leq P_1^{eq}$, $s(t_1)$=1; otherwise, $s(t_1)$=2. Then at each time point t_j a new random number r is extracted within the same interval $(0,1)$: if $s(t_{j-1})$=1 and $r \leq p_{12}$, $s(t_j)$=2; if $s(t_{j-1})$=2 and $r \leq p_{21}$, $s(t_j)$=1; otherwise $s(t_{j-1})$=$s(t_j)$ and the state is kept unchanged.
Once the state sequence **s** has been generated, it is employed to define the particle displacements at each time point. When the particle is in state (1) at time t_j, a Brownian jump l_j is extracted from a Gaussian distribution with variance $2D\Delta t$

and zero mean, and an arbitrary jump direction γ_j is assigned by extracting a pseudo-random number from a flat distribution in the interval $[0, 2\pi]$; when the particle is in state (2), the displacement is computed by vectorially adding a term $\underline{v}\Delta t$ to a Brownian jump. Formally, the coordinates update starts from randomly assigned initial coordinates (x_0, y_0) and proceeds according to

$$\begin{cases} x(t_{j+1}) = x(t_j) + l_j \cos\gamma_j & \text{if} \quad s(t_j) = 1 \\ \\ y(t_{j+1}) = y(t_j) + l_j \sin\gamma_j & \text{if} \quad s(t_j) = 1 \end{cases} \tag{7.26}$$

$$\begin{cases} x(t_{j+1}) = x(t_j) + l_j \cos\gamma_j + |\underline{v}| \cos\alpha\Delta t & \text{if} \quad s(t_j) = 2 \\ \\ y(t_{j+1}) = y(t_j) + l_j \sin\gamma_j + |\underline{v}| \sin\alpha\Delta t & \text{if} \quad s(t_j) = 2 \end{cases} \tag{7.27}$$

Finally, particle positions are converted to pixel-units coordinates and convolved with a 2D Gaussian function with given e^{-2} radius to simulate the excitation of equally bright point emitters by a focused TEM_{00} laser beam. The image matrix obtained at each time point is normalized and pixel values are rounded to the closest integer, ranging from 0 to either 255 or 4095, to simulate an 8- or 12-bit A/D converter. Typically, 500-1000 steps are simulated for each trajectory with a time step Δt=2.5 s, and 64x64 or 128x128 image sizes are employed to resemble the 2-16 μm^2 square ROIs on which the experimental image correlation analyses have been performed.

The results of the numerical simulations for intermittent active transport are exemplified in Fig. 7.5. Trajectories simulated with fixed D=2x10^{-4} $\mu m^2/s$, $|\underline{v}|$=2x10^{-3} $\mu m/s$, α=330°, p_{21}=0.05 and increasing values of the probability p_{12} are reported. p_{12} varies from 0 to 0.5, leading to an equilibrium probability P_2^{eq} for the active transport state varying between 0 and 0.9. When the xyt-stacks of images generated from these trajectories are analyzed by Spatio-Temporal Image Correlation Spectroscopy, the displacement of the peak coordinates $(\xi, \eta)_{max}$ from the origin increases with the probability P_2^{eq} of the molecule being in state (2) but, differently from what is expected for a simple diffusion+drift single-state system, a non-linear trend is detected in the $(\xi, \eta)_{max}$-vs-τ plot (Fig. 7.5g-k). Equivalently, a TICS analysis (Fig. 7.5l) of the same image stacks leads to temporal correlation functions $G(\tau)$ that, when forced fit to the simple diffusion+drift model (eq. 6.9), show the same discrepancy exhibited by the experimental TICS correlation function in Fig.

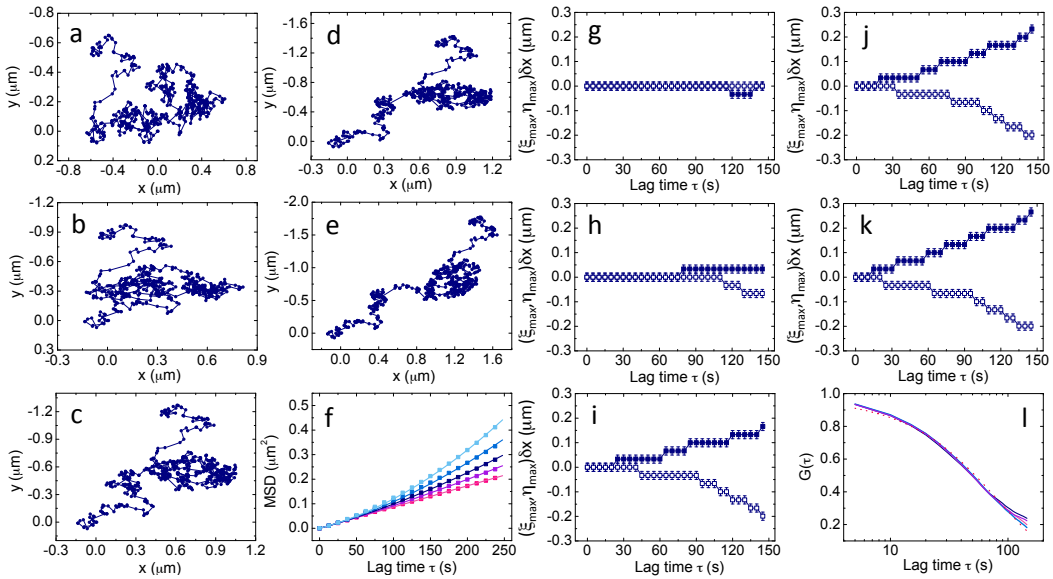

Figure 7.5: *Intermittent active transport: numerical simulations.* (a)-(e): single-particle trajectories simulated with the formalism of Hidden Markov Models applied to the two-state dynamics of eq. (6.37), with fixed p_{21}=0.05 and increasing values for p_{12}: p_{12}=0 in (a), 0.025 in (b), 0.05 in (c), 0.1 in (d) and 0.5 in (e). The corresponding equilibrium probabilities for the diffusion+drift state are P_2^{eq}=0, 0.33, 0.5, 0.67 and 0.9, respectively. D, $|\underline{v}|$ and α have been fixed to D=2x10^{-4} $\mu m^2/s$, $|\underline{v}|$=2x10^{-3} $\mu m/s$ and α=330° for all the simulations. For the sake of display, each trajectory has been translated to make the first generated data point coincide with the origin of the Cartesian axes and only 500 steps out of a total of 5000 simulated data points are shown. (f): MSDs for the 5000-steps long trajectories of panels (a)-(e), with p_{12} increasing from the bottom to the top. Each MSD(τ) plot is superimposed to the fit to eq. (7.13) with D, $|\underline{v}|$, k_{21}/k_{12} and τ_{rel} fixed to the simulation input parameters. (g): coordinates $(\xi_{max}, \eta_{max})\delta x$ ($\xi_{max}\delta x$ filled squares, $\eta_{max}\delta x$ open squares) of the peak of the STICS correlation function computed on a 1000-frames long xyt-stack of images simulated starting from the single particle trajectory of panel (a). (h)-(k): peak coordinates of the STICS STCF computed on the trajectories of panels (b)-(e) (with panels h,i,j,k corresponding to panels b,c,d,e, respectively). (l): TICS correlation functions (solid lines) computed on the same simulated xyt-stacks analyzed by STICS in panels (g)-(k). Almost perfectly overlapping, correlation curves hamper the recovery of transport parameters and kinetic rate constants by means of TICS. The dotted line is the forced fit to the simpler diffusion+drift model (eq. 6.9) with the diffusion coefficient D=2x10^{-4} $\mu m^2/s$ and the drift speed $|\underline{v}|$=2x10^{-3} $\mu m/s$ fixed to the simulation input parameters.

6.7d. Globally, although not exhaustive of the full parameter space for the transition probabilities p_{12} and p_{21}, these simulations confirm again the compatibility between the experimental data reported in Fig. 6.9 and a model for the intracellular dynamics of gold nanostars based upon intermittent active transport.

7.4.1 Effect of multiple velocity directions

I conclude this Chapter by evaluating, for the sake of completeness, a last possible explanation for the non-linear peak displacement found in the STICS spatio-temporal correlation functions. This explanation was not considered and included among the theoretical models of enhanced diffusion in Chapter 6 for two reasons: (i) this model does not rely on a super-diffusive sub-ballistic dynamics, concerning instead the vectorial composition of multiple velocity directions in a simple diffusive+drift process; (ii) it is only by the analysis of Single Particle Tracking data of Figs. 7.1-7.4 that the attribution, of the anomalous STICS results, to the simple experimental configuration described in the following can be excluded. More in details, an anomalous displacement of the STCF peak resembling the one found experimentally can be easily reproduced hypothesizing that the N particles within the Region Of Interest analyzed by STICS exhibit free diffusion and uniform drift along different directions: recalling the formalism of eq. (7.26), a different angle α_k with respect to the x-axis is considered for the drift velocity of each k^{th} particle. Numerical simulations can therefore be performed according to the procedure outlined previously: each particle, now always residing in state (2), travels at each time step a random Brownian jump, plus a jump $\underline{v}\Delta t$ proportional to its drift speed. As shown in Fig. 7.6, the higher the number of the velocity directions averaged in the computation of the spatio-temporal correlation function, the more asymmetric the STCF becomes. This is consistent with the explicit analytical expression of the STCF predicted for multiple populations of diffusing and drifting objects:

$$g(\xi,\eta,\tau) \propto \sum_{k=1}^{N} \left\{ \left[1 + \frac{4D(\xi\tau_p + \eta\tau_l + \psi\tau_f)}{\omega_0^2} \right]^{-1} \cdot \right.$$

$$\left. \cdot exp\left\{ -\frac{1}{\omega_0^2} \frac{[\xi\delta x - v_{kx}(\xi\tau_p + \eta\tau_l + \psi\tau_f)]^2}{\left(1 + \frac{4D(\xi\tau_p + \eta\tau_l + \psi\tau_f)}{\omega_0^2}\right)} - \frac{1}{\omega_0^2} \frac{[\eta\delta x - v_{ky}(\xi\tau_p + \eta\tau_l + \psi\tau_f)]^2}{\left(1 + \frac{4D(\xi\tau_p + \eta\tau_l + \psi\tau_f)}{\omega_0^2}\right)} \right\} \right\} \tag{7.28}$$

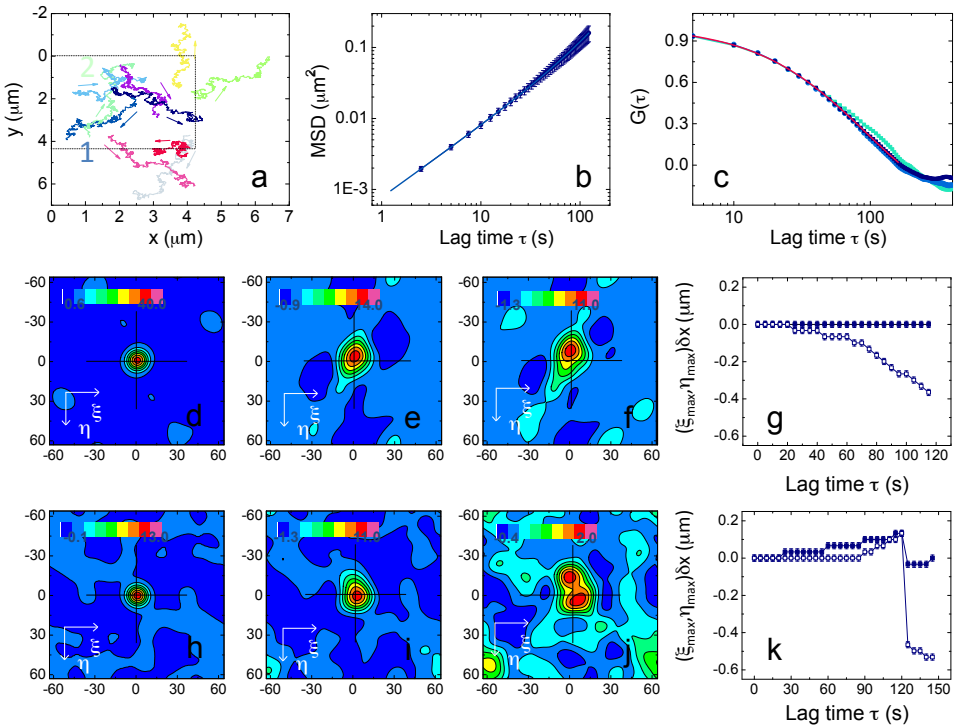

Figure 7.6: *STICS: effect of multiple velocity directions.* (a): 500-step trajectories simulated for a D+$\underline{v}$ model with D=2x10^{-4} μm^2/s, $|\underline{v}|$=2x10^{-3} μm/s. Drift directions are sketched as arrows. (b): MSD (mean ± s.t.d.) for all the trajectories in panel (a), fitted to eq. (7.3 ii) with D=(1.92±0.01)x10^{-4} μm^2/s and $|\underline{v}|$=(2.08±0.01)x10^{-3} μm/s. (c): TICS ACFs computed (eq. 6.10 with ξ, η=0) on simulated 500-frames long, 64x64 xyt-stacks encompassing the only particle labelled as 1 in panel (a) (grey curve), particles 1 and 2 (light blue curve) and all the particles within the bounded box in (a) (blue curve). The fit to eq. (6.9) yields D=(1.87±0.03)x10^{-4} μm^2/s and $|\underline{v}|$=(1.6±0.2)x10^{-3} μm/s; as expected, TICS is insensitive to the direction of drift motions while allowing the recovery of the modulus of the drift velocity. (d)-(f): STICS correlation functions (eq. 1.56) for τ=0, 75 and 100 s (d, e, f) computed on a simulated xyt-stack encompassing the particles labelled as 1 and 2 in panel (a). Analytically, the STCF is a linear combination of two quasi-Gaussian terms describing free diffusion and drift along the two directions α_1=127° and α_2=299°. The peak position plotted in panel (g) is a non-linear function of τ, hampering the recovery of the modulus and direction of drift velocity vectors (on experimental data, the analytical derivation of the peak position of the superposition of an unknown number of quasi-Gaussian terms would be required). (h)-(k): results of the STICS analysis on an xyt-stack encompassing the 4.2x4.2 μm^2 ROI in panel (a) (τ=0,75,125 s in h,i,j). The multiple STCF peaks resulting from the linear combination of ten quasi-Gaussian terms are evident at τ=125 s.

Clearly, the STCF resulting from the superposition of N single-population correlation functions may exhibit different extent of asymmetry and, depending on the peak position of the constituent Gaussian terms, might show more than one resolved peak. Nevertheless, even if the STCF peak coordinates [4] vary non-linearly with increasing lag time τ (Fig. 7.6), the MSDs of all the particles still show the quadratic time-dependence expected from eq. (7.3 ii). The comparison with the sub-ballistic MSDs reported in Fig. 7.1 confirms that the superposition of multiple velocity directions cannot completely justify the experimental results presented so far.

[4]The STCF is not literally a single-peak function any more, but it is still possible to track the coordinates of the *maximum* value of the STCF versus the lag time τ.

Chapter 8

Gold Nanostars Intracellular Dynamics: Results in k-Space

Single Particle Tracking provides direct insight into an appropriate effective dynamic model to describe the intracellular transport of endocytosed gold nanoparticles. However, while offering single-particle sensitivity and the possibility of identifying even short-lived phases of active transport, SPT is time consuming and computationally expensive in both the trajectory reconstruction and in the Bayesian Markov Chain Monte Carlo likelihood maximization. Moreover, it requires the identification of individual objects inside the cell, preventing therefore a ROI-by-ROI analysis.
Since a straightforward approach to be applied on a whole-cell basis is desirable, in this Chapter I extend the formalism of Image Correlation Spectroscopy to the investigation of intermittent transport phenomena. I start from the two-state intermittent dynamics previously considered for SPT and, once demonstrated that the spatio-temporal correlation function cannot be analytically derived in the direct r-space, I move to Fourier space and provide explicitly the correlation function of k-space Image Correlation Spectroscopy (kICS) [42, 292]. At first, I evaluate the influence of the dynamic and kinetic parameters (the diffusion coefficient, the drift velocity and the transition rates between the active and the passive transport regimes) on simulated kICS correlation functions. Then I outline the protocol for data analysis and employ it to derive whole-cell maps for the parameters underlying the GNSs intracellular dynamics.

8.1 Derivation of the spatio-temporal correlation function for 2D intermittent active transport

A few attempts have been made in the literature [8,276] in deriving the analytical expression of the TICS and STICS correlation functions in the presence of complex transport phenomena, resulting from the binding/unbinding of fluorescently-labeled macromolecules to immobile cellular substrates or to unlabeled diffusing receptors in the plasma membrane. In the first case the particle motion occurs intermittently, with phases of Brownian motion alternating with periods of immobility. The theoretical framework, which has been derived for point-FCS [8], can be readily extended to the TICS analysis. The second case, where the overall transport can be modeled by two diffusive states characterized by different diffusion coefficients, has been treated [276] for k-space Image Correlation Spectroscopy [42,292].
As suggested by the experimental results of Chapters 6 and 7, I derive here the theoretical framework - for both STICS and its k-space version kICS - for the intermittent transport (eq. 6.37) that best describes the switching between phases of planar thermal diffusion and phases of 2D active transport mediated by molecular motors inside living cells. While previous derivations for Particle Image Correlation Spectroscopy (PICS) [241,293] require numerical data fitting, I find for kICS an analytical solution to the problem to be employed for the analysis of the experimental data.

I focus therefore on the unimolecular reaction of eq. (6.37),

$$(1) \quad D \underset{k_{21}}{\overset{k_{12}}{\rightleftarrows}} D + \underline{v} \quad (2) \tag{8.1}$$

and derive the STICS spatio-temporal correlation function

$$G(\xi,\eta,\tau) \approx \frac{< \delta I^*(x,y,t)\delta I(x+\xi, y+\eta, t+\tau) >_{xyt}}{(< I(x,y,t) >_{xy})^2} \tag{8.2}$$

assuming that fluctuations $\delta I(x,y,t)$ are due to the transport phenomena undergone by molecules switching between a diffusive state (1) and a diffusion+drift bound state (2). Throughout the derivation, I adopt the formalism of fluorescence microscopy: under the hypothesis of negligible phase fluctuations (as pointed out

in Chapter 6) the derivation is unchanged when fluctuations in a detected scattering signal are considered.

I express the signal intensity detected at spatial coordinates $\underline{x} = (x, y)$ at time t as a sum of the individual contributions $I_{i=1,2}(\underline{x}, t)$ of the molecules in the i^{th} state [17]:

$$\begin{cases} I(\underline{x}, t) = \sum_{i=1}^{2} I_i(\underline{x}, t) \\ \\ I_i(\underline{x}, t) = \phi_i \int_{-\infty}^{+\infty} d\underline{r} W(\underline{r} - \underline{x}) C_i(\underline{r}, t) \end{cases} \tag{8.3}$$

As in Chapter 1, ϕ_i is the product of the detection efficiency and of the quantum yield and absorption cross-section of the particles in state i; if $I_i(\underline{x}, t)$ represents a scattering intensity, ϕ_i is the product of the detection efficiency and of the scattering cross-section. $C_i(\underline{r}, t)$ is the local concentration of the particles in state i, while $W(\underline{r})$ is the product of the spatial distribution of the excitation intensity times the dimensionless optical transfer function of the objective-pinhole combination. For negligible spatial and temporal fluctuations affecting, on the second-to-minute timescale sampled in STICS, the molecular quantum yield and the absorption/scattering cross-section,

$$\delta I(\underline{x}, t) = \sum_{i=1}^{2} \phi_i \int_{-\infty}^{+\infty} d\underline{r} W(\underline{r} - \underline{x}) \delta C_i(\underline{r}, t) \tag{8.4}$$

The substitution of eq. (8.4) into the numerator of the spatio-temporal correlation function (8.2) yields

$$g(\underline{\Delta}, \tau) \equiv < \delta I^*(\underline{x}, t) \delta I(\underline{x} + \underline{\Delta}, t + \tau) >_{xyt} =$$

$$\lim_{R \to +\infty} \frac{1}{R^2} \int_{-R/2}^{R/2} d\underline{x} \iint_{-\infty}^{+\infty} d\underline{r} d\underline{r}' W^*(\underline{r} - \underline{x}) W(\underline{r}' - \underline{x} - \underline{\Delta}) \sum_{i,j=1}^{2} \phi_i \phi_j < \delta C_i^*(\underline{r}, t) \delta C_j(\underline{r}', t+\tau) >_t$$

$$= \lim_{R \to +\infty} \frac{1}{R^2} \int_{-R/2}^{R/2} d\underline{x} \iint_{-\infty}^{+\infty} d\underline{r} d\underline{r}' W^*(\underline{r} - \underline{x}) W(\underline{r}' - \underline{x} - \underline{\Delta}) \sum_{i,j=1}^{2} \phi_i \phi_j < \delta C_i^*(\underline{r}, 0) \delta C_j(\underline{r}', \tau) > \tag{8.5}$$

The vector $\underline{\Delta}$ has been introduced according to $\underline{\Delta} = (\xi, \eta)\delta x$ (δx being the pixel size) and the spatial average has been replaced by the integral over an area R^2, following the notation of eq. (1.2) and of Subsection 1.3.3.

I proceed by deriving the concentration correlation term $< \delta C_i^*(\underline{r}, 0) \delta C_j(\underline{r}', \tau) >$,

recalling that, near equilibrium, concentrations $\delta C_{i=1,2}(\underline{r}, t)$ satisfy the previously introduced system of differential equations

$$\begin{cases} \dfrac{\partial \delta C_1(\underline{r}, t)}{\partial t} = D\nabla^2 \delta C_1(\underline{r}, t) - k_{12}\delta C_1(\underline{r}, t) + k_{21}\delta C_2(\underline{r}, t) \\ \dfrac{\partial \delta C_2(\underline{r}, t)}{\partial t} = D\nabla^2 \delta C_2(\underline{r}, t) - \underline{v} \cdot \underline{\nabla}\delta C_2(\underline{r}, t) + k_{12}\delta C_1(\underline{r}, t) - k_{21}\delta C_2(\underline{r}, t) \end{cases} \tag{8.6}$$

These differential equations are conveniently solved in Fourier space; their Fourier transforms[1] yield

$$\begin{cases} \dfrac{\partial \delta \widehat{C_1}(\underline{q}, t)}{\partial t} = -D|\underline{q}|^2 \delta \widehat{C_1}(\underline{q}, t) - k_{12}\delta \widehat{C_1}(\underline{q}, t) + k_{21}\delta \widehat{C_2}(\underline{q}, t) \\ \dfrac{\partial \delta \widehat{C_2}(\underline{q}, t)}{\partial t} = -D|\underline{q}|^2 \delta \widehat{C_2}(\underline{q}, t) + i\underline{q} \cdot \underline{v}\delta \widehat{C_2}(\underline{q}, t) + k_{12}\delta \widehat{C_1}(\underline{q}, t) - k_{21}\delta \widehat{C_2}(\underline{q}, t) \end{cases} \tag{8.7}$$

or equivalently, for $i = 1, 2$,

$$\frac{\partial \delta \widehat{C_i}(\underline{q}, t)}{\partial t} = \sum_{j=1}^{2} M_{ij} \delta \widehat{C_j}(\underline{q}, t) \tag{8.8}$$

with the matrix M defined as

$$M = \begin{bmatrix} -D|\underline{q}|^2 - k_{12} & k_{21} \\ k_{12} & -D|\underline{q}|^2 + i\underline{q} \cdot \underline{v} - k_{21} \end{bmatrix} \tag{8.9}$$

Following the formalism of Chapter 1, the solutions for $\delta \widehat{C}_{i=1,2}(\underline{q}, t)$ are found by the computation of the two eigenvalues $\lambda^{(s=1,2)}$ and of the two eigenvectors $\chi^{(s=1,2)}$ of the matrix M [17]:

$$\delta \widehat{C}_i(\underline{q}, t) = \sum_{s=1}^{2} \chi_i^{(s)} exp(\lambda^{(s)} t) \sum_{k=1}^{2} \chi_k^{-1(s)} \delta \widehat{C}_k(\underline{q}, 0) \tag{8.10}$$

Prior to derive $\lambda^{(s=1,2)}$ and $\chi^{(s=1,2)}$ and to explicitly substitute them into eq. (8.10), it is convenient to compute implicitly the concentration correlation term. As for

[1] The same convention $\widehat{f}(\underline{q}) = (2\pi)^{-d/2} \int f(\underline{x}) e^{i\underline{q}\cdot\underline{x}} d^d\underline{x}$ for the Fourier transform definition of Chapter 1 is adopted.

eqs. (1.15)-(1.17), in the two-dimensional case one gets

$$< \delta C_i^*(\underline{r},t)\delta C_j(\underline{r}',t+\tau) >_t =< \delta C_i^*(\underline{r},0)\delta C_j(\underline{r}',\tau) >= \\ = \frac{1}{(2\pi)} \int_{-\infty}^{+\infty} < \delta C_i^*(\underline{r},0)\delta \widehat{C}_j(\underline{q},\tau) > e^{-i\underline{q}\cdot\underline{r}'}\, d\underline{q} \\ = \frac{1}{(2\pi)} \int_{-\infty}^{+\infty} \sum_{s=1}^{2} \chi_j^{(s)} exp(\lambda^{(s)}\tau) \sum_{k=1}^{2} \chi_k^{-1(s)} < \delta C_i^*(\underline{r},0)\delta \widehat{C}_k(\underline{q},0) > e^{-i\underline{q}\cdot\underline{r}'}\, d\underline{q} \\ = \frac{1}{(2\pi)^2} \iint_{-\infty}^{+\infty} \sum_{s=1}^{2} \chi_j^{(s)} exp(\lambda^{(s)}\tau) \sum_{k=1}^{2} \chi_k^{-1(s)} < \delta C_i^*(\underline{r},0)\delta C_k(\underline{r}'',0) > e^{-i\underline{q}\cdot(\underline{r}'-\underline{r}'')}\, d\underline{q} d\underline{r}'' \tag{8.11}$$

For an ideal solution, denoted with $< C_i >$ the ensemble average concentration of the particles in state i, the zero-lag time concentration correlation can be evaluated [11,17] as

$$< \delta C_i^*(\underline{r},0)\delta C_k(\underline{r}'',0) >=< C_i > \delta_{ik}\delta(\underline{r}-\underline{r}'') \tag{8.12}$$

so that, by carrying out the integration over $\underline{r}''$ in eq. (8.11) I obtain

$$< \delta C_i^*(\underline{r},0)\delta C_j(\underline{r}',\tau) >= \frac{< C_i >}{(2\pi)^2} \int_{-\infty}^{+\infty} \sum_{s=1}^{2} \chi_j^{(s)} exp(\lambda^{(s)}\tau) \chi_i^{-1(s)} e^{i\underline{q}\cdot(\underline{r}-\underline{r}')}\, d\underline{q} \tag{8.13}$$

By substituting eq. (8.13) and the Fourier transforms of the intensity distributions $W^*(\underline{r}-\underline{x})$ and $W(\underline{r}'-\underline{x}-\underline{\Delta})$ into eq. (8.5) I obtain

$$g(\underline{\Delta},\tau) = \lim_{R\to+\infty} \frac{1}{R^2} \int_{-R/2}^{R/2} d\underline{x} \iint_{-\infty}^{+\infty} d\underline{r} d\underline{r}' \int_{-\infty}^{+\infty} d\underline{q} W^*(\underline{r}-\underline{x}) W(\underline{r}'-\underline{x}-\underline{\Delta}) \cdot \\ \cdot \sum_{i,j=1}^{2} \left\{ \frac{< C_i > \phi_i\phi_j}{(2\pi)^2} \sum_{s=1}^{2} \chi_j^{(s)} exp(\lambda^{(s)}\tau) \chi_i^{-1(s)} \right\} e^{i\underline{q}\cdot(\underline{r}-\underline{r}')} \quad \to \tag{8.14}$$

$$g(\underline{\Delta},\tau) = \frac{1}{(2\pi)^4} \lim_{R\to+\infty} \frac{1}{R^2} \int_{-R/2}^{R/2} d\underline{x} \iint_{-\infty}^{+\infty} d\underline{r} d\underline{r}' \int_{-\infty}^{+\infty} d\underline{q} \iint_{-\infty}^{+\infty} d\underline{q}' d\underline{q}'' \widehat{W}^*(\underline{q}') \widehat{W}(\underline{q}'') \cdot \\ \cdot \sum_{i,j=1}^{2} \left\{ < C_i > \phi_i\phi_j \sum_{s=1}^{2} \chi_j^{(s)} exp(\lambda^{(s)}\tau) \chi_i^{-1(s)} \right\} e^{i\underline{q}\cdot(\underline{r}-\underline{r}')+i\underline{q}'\cdot(\underline{r}-\underline{x})-i\underline{q}''\cdot(\underline{r}'-\underline{x}-\underline{\Delta})} \tag{8.15}$$

By now recalling eq. (1.61), and that the Dirac delta is even, $g(\underline{\Delta},\tau)$ can be written as

$$g(\underline{\Delta},\tau) = \frac{1}{2\pi R^2}\iiint_{-\infty}^{+\infty} d\underline{q}d\underline{q}'d\underline{q}''\widehat{W}^*(\underline{q}')\widehat{W}(\underline{q}'')\cdot$$

$$\cdot\sum_{i,j=1}^{2}\left\{< C_i > \phi_i\phi_j\sum_{s=1}^{2}\chi_j^{(s)}exp(\lambda^{(s)}\tau)\chi_i^{-1(s)}\right\}e^{i\underline{q}''\cdot\underline{\Delta}}\delta(\underline{q}+\underline{q}')\delta(\underline{q}+\underline{q}'')\delta(\underline{q}''-\underline{q}') \tag{8.16}$$

Equivalently,

$$g(\underline{\Delta},\tau) = \frac{1}{2\pi R^2}\iiint_{-\infty}^{+\infty} d\underline{q}d\underline{q}'d\underline{q}''\widehat{W}^*(\underline{q}')\widehat{W}(\underline{q}'')R(\underline{q},\tau)e^{i\underline{q}''\cdot\underline{\Delta}}\delta(\underline{q}+\underline{q}')\delta(\underline{q}+\underline{q}'')\delta(\underline{q}''-\underline{q}') \tag{8.17}$$

where, for the sake of compactness, sums have been replaced by the $\underline{q}$- and τ-function $R(\underline{q},\tau)$.
The successive integrations over $\underline{q}$ and $\underline{q}''$ and a final 2D change of variable $\underline{k} = -\underline{q}'$ lead to

$$g(\underline{\Delta},\tau) = \frac{1}{2\pi R^2}\iint_{-\infty}^{+\infty} d\underline{q}'d\underline{q}''\widehat{W}^*(\underline{q}')\widehat{W}(\underline{q}'')R(-\underline{q}',\tau)e^{i\underline{q}''\cdot\underline{\Delta}}\delta(\underline{q}''-\underline{q}')\delta(\underline{q}''-\underline{q}') =$$

$$= \frac{1}{2\pi R^2}\int_{-\infty}^{+\infty} d\underline{q}'\left|\widehat{W}(\underline{q}')\right|^2R(-\underline{q}',\tau)e^{i\underline{q}'\cdot\underline{\Delta}}\delta(0) =$$

$$= \lim_{R\to+\infty}\frac{1}{2\pi R^2}\int_{-\infty}^{+\infty} d\underline{q}'\left|\widehat{W}(\underline{q}')\right|^2R(-\underline{q}',\tau)e^{i\underline{q}'\cdot\underline{\Delta}}\frac{R^2}{2\pi} =$$

$$= \frac{1}{(2\pi)^2}\int_{-\infty}^{+\infty} d\underline{q}'\left|\widehat{W}(\underline{q}')\right|^2R(-\underline{q}',\tau)e^{i\underline{q}'\cdot\underline{\Delta}} =$$

$$= \frac{1}{(2\pi)^2}\int_{-\infty}^{+\infty} d\underline{k}\left|\widehat{W}(-\underline{k})\right|^2R(\underline{k},\tau)e^{-i\underline{k}\cdot\underline{\Delta}} \tag{8.18}$$

Eq. (8.18) requires now the explicit expression of $R(\underline{k},\tau)$ and of the Fourier transform of the excitation intensity distribution. $R(\underline{k},\tau)$, as previously anticipated, can be obtained by computing the eigenvalues and eigenvectors of the matrix M.

Following the notation of eqs. (1.12)-(1.14) and (8.10),

$$\begin{cases} \lambda^{(1)} = \dfrac{-2D|\underline{k}|^2 - (k_{12}+k_{21}) + i\underline{k}\cdot\underline{v} + \sqrt{\Lambda}}{2} \\ \lambda^{(2)} = \dfrac{-2D|\underline{k}|^2 - (k_{12}+k_{21}) + i\underline{k}\cdot\underline{v} - \sqrt{\Lambda}}{2} \\ \Lambda = (k_{12}+k_{21})^2 - |\underline{k}\cdot\underline{v}|^2 + 2i\underline{k}\cdot\underline{v}(k_{12}-k_{21}) \end{cases} \tag{8.19}$$

and

$$\begin{cases} \chi_1^{(1)} = 1 \\ \chi_2^{(1)} = \dfrac{D|\underline{k}|^2 + k_{12} + \lambda^{(1)}}{k_{21}} \\ \chi_1^{(2)} = 1 \\ \chi_2^{(2)} = \dfrac{D|\underline{k}|^2 + k_{12} + \lambda^{(2)}}{k_{21}} \end{cases} \quad \begin{cases} \chi_1^{-1(1)} = \dfrac{D|\underline{k}|^2 + k_{12} + \lambda^{(2)}}{\lambda^{(2)} - \lambda^{(1)}} \\ \chi_2^{-1(1)} = -\dfrac{k_{21}}{\lambda^{(2)} - \lambda^{(1)}} \\ \chi_1^{-1(2)} = -\dfrac{D|\underline{k}|^2 + k_{12} + \lambda^{(1)}}{\lambda^{(2)} - \lambda^{(1)}} \\ \chi_2^{-1(2)} = \dfrac{k_{21}}{\lambda^{(2)} - \lambda^{(1)}} \end{cases} \tag{8.20}$$

By assuming that for particles in states (1) and (2) $\phi_1 = \phi_2 \equiv \phi$, and by further expressing the equilibrium concentrations as

$$\begin{cases} < C_1 > = < C > \dfrac{k_{21}}{k_{12}+k_{21}} \\ < C_2 > = < C > \dfrac{k_{12}}{k_{12}+k_{21}} \end{cases} \tag{8.21}$$

$R(\underline{k}, \tau)$ can be expressed as

$$R(\underline{k}, \tau) \equiv \sum_{i,j=1}^{2} \left\{ < C_i > \phi_i \phi_j \sum_{s=1}^{2} \chi_j^{(s)} exp(\lambda^{(s)}\tau) \chi_i^{-1(s)} \right\} = < C > \phi^2 \frac{\mathbb{A} e^{\lambda^{(1)}\tau} + \mathbb{B} e^{\lambda^{(2)}\tau}}{\mathbb{C}} \tag{8.22}$$

with

$$\begin{cases} \mathbb{A} = k_{12}k_{21} + k_{12}(D|\underline{k}|^2 + k_{12} + \lambda^{(1)}) - k_{21}(D|\underline{k}|^2 + k_{12} + \lambda^{(2)}) - \\ \quad - (D|\underline{k}|^2 + k_{12} + \lambda^{(1)})(D|\underline{k}|^2 + k_{12} + \lambda^{(2)}) \\ \mathbb{B} = -k_{12}k_{21} - k_{12}(D|\underline{k}|^2 + k_{12} + \lambda^{(2)}) + k_{21}(D|\underline{k}|^2 + k_{12} + \lambda^{(1)}) + \\ \quad + (D|\underline{k}|^2 + k_{12} + \lambda^{(1)})(D|\underline{k}|^2 + k_{12} + \lambda^{(2)}) \\ \mathbb{C} = (k_{12} + k_{21})(\lambda^{(1)} - \lambda^{(2)}) \end{cases} \tag{8.23}$$

If a 2D Gaussian (with amplitude W_0 and $1/e^2$ distance ω_0, as in eq. 1.65) is assumed for the excitation intensity distribution, and if is substituted into eq. (8.18) along with the expression for $R(\underline{k}, \tau)$,

$$g(\underline{\Delta}, \tau) = \frac{< C > \phi^2 (W_0 \omega_0^2)^2}{16(2\pi)^2} \int_{-\infty}^{+\infty} d\underline{k} \left\{ \frac{\mathbb{A} e^{\lambda^{(1)}\tau} + \mathbb{B} e^{\lambda^{(2)}\tau}}{\mathbb{C}} \right\} exp\left\{ -\frac{\omega_0^2 |\underline{k}|^2}{4} - i\underline{k} \cdot \underline{\Delta} \right\} \tag{8.24}$$

The normalized STICS correlation function of eq. (8.2) is finally obtained by dividing eq. (8.24) by the squared spatially-averaged intensity $< I(x, y, t) >_{xy}^2 = \phi^2 \widehat{W}(0)^2 (< C_1 > + < C_2 >)^2$:

$$G(\underline{\Delta}, \tau) \approx \frac{1}{< C > (2\pi)^2} \int_{-\infty}^{+\infty} d\underline{k} \left\{ \frac{\mathbb{A} e^{\lambda^{(1)}\tau} + \mathbb{B} e^{\lambda^{(2)}\tau}}{\mathbb{C}} \right\} exp\left\{ -\frac{\omega_0^2 |\underline{k}|^2}{4} - i\underline{k} \cdot \underline{\Delta} \right\} \tag{8.25}$$

Due to the complex $\underline{k}$-dependence of the $\mathbb{A}$, $\mathbb{B}$ and $\mathbb{C}$ terms and of the eigenvalues $\lambda^{(1)}$ and $\lambda^{(2)}$, the integral over the $\underline{k}$ variable cannot be performed analytically. Hence eq. (8.25) provides the STICS theoretical framework for the investigation of intermittent active transport: the dynamic parameters D and $\underline{v}$ and the association / dissociation rates k_{12} and k_{21} can only be recovered by employing eq. (8.25) for a non-linear least-squares numerical fit in the complex field of experimental correlation functions.

As described in the following, a much more convenient alternative, having the main advantage of not requiring the numerical integration of eq. (8.25), is offered by the Fourier-space version [42, 292] of STICS.

8.1.1 2D intermittent active transport in Fourier space

k-space Image Correlation Spectroscopy (kICS) [42,292] relies on computing the two dimensional spatial Fourier transform of each image of the same raster-scanned xyt-stack analyzed by STICS, and in spatio-temporally correlating these Fourier transforms to extract information regarding the dynamic and kinetic processes underlying the detected signal fluctuations. Practically, the definition of eq. (8.2) is employed for the computation of the kICS correlation function, with $I(x,y,t)$ now denoting the pixel value at spatial coordinates (x,y) at time t after the 2D frame Fourier transform. As a consequence, the kICS correlation function, hereafter referred to as $G(\underline{k},\tau)$, coincides with the Fourier transform of the STICS correlation function $G(\underline{\Delta},\tau)$, and vice versa:

$$G(\underline{\Delta},\tau) = \frac{1}{2\pi}\int_{-\infty}^{+\infty} G(\underline{k},\tau)e^{-i\underline{k}\cdot\underline{\Delta}}d\underline{k} \tag{8.26}$$

If eq. (8.25) is recalled, its comparison with eq. (8.26) directly yields the normalized kICS correlation function in the form

$$G(\underline{k},\tau) \propto \frac{\mathbb{A}e^{\lambda^{(1)}\tau} + \mathbb{B}e^{\lambda^{(2)}\tau}}{\mathbb{C}} exp\left\{-\frac{\omega_0^2|\underline{k}|^2}{4}\right\} \tag{8.27}$$

As before, the eigenvalues $\lambda^{(1)}$ and $\lambda^{(2)}$ and the $\mathbb{A}$, $\mathbb{B}$ and $\mathbb{C}$ terms are given by eqs. (8.19) and (8.23).

8.2 Limits of the kICS correlation function

I now verify that the kICS correlation function I derived for intermittent active transport correctly reduces to the expected functional forms when a single purely diffusive state or a single diffusion+drift state are considered.

- A single purely diffusive state is recovered from the two-state dynamics of eq. (8.1) in the limit $|\underline{v}| \to 0$: in this case, having assumed that the diffusion coefficient D does not vary upon binding of molecular motor proteins and cellular vesicles, states (1) and (2) coincide (exhibit equal transport properties).

The eigenvalues of the matrix M satisfy

$$\begin{cases} \lambda^{(1)} \xrightarrow[|\underline{v}|\to 0]{} -D|\underline{k}|^2 \\ \lambda^{(2)} \xrightarrow[|\underline{v}|\to 0]{} -D|\underline{k}|^2 - (k_{12} + k_{21}) \end{cases} \tag{8.28}$$

This leads to

$$\begin{cases} \mathbb{A} \xrightarrow[|\underline{v}|\to 0]{} (k_{12} + k_{21})^2 \\ \mathbb{B} \xrightarrow[|\underline{v}|\to 0]{} 0 \\ \mathbb{C} \xrightarrow[|\underline{v}|\to 0]{} \mathbb{A} \end{cases} \tag{8.29}$$

When substituted into eq. (8.27), eqs. (8.28) and (8.29) yield the kICS correlation function reported in the literature [292] for the simple diffusive case:

$$G(\underline{k}, \tau) \xrightarrow[|\underline{v}|\to 0]{} exp\left\{ -|\underline{k}|^2 \left[\frac{\omega_0^2}{4} + D\tau \right] \right\} \tag{8.30}$$

- In the limit $k_{12} \to +\infty$ and $k_{21} \to 0$, molecules tend to exclusively populate state (2), exhibiting Brownian diffusion and uniform drift. Since

$$\Lambda = (k_{12} + k_{21})^2 - |\underline{k} \cdot \underline{v}|^2 + 2i\underline{k} \cdot \underline{v}(k_{12} - k_{21}) \xrightarrow[k_{12}\to+\infty,\, k_{21}\to 0]{}$$

$$\xrightarrow[k_{12}\to+\infty,\, k_{21}\to 0]{} (k_{12} + k_{21})^2 - |\underline{k} \cdot \underline{v}|^2 + 2i\underline{k} \cdot \underline{v}(k_{12} + k_{21}) =$$

$$= (k_{12} + k_{21} + i\underline{k} \cdot \underline{v})^2 \approx (k_{12} + i\underline{k} \cdot \underline{v})^2 \tag{8.31}$$

the eigenvalues of the matrix M turn into

$$\begin{cases} \lambda^{(1)} \xrightarrow[k_{12}\to+\infty,\, k_{21}\to 0]{} -D|\underline{k}|^2 + i\underline{k} \cdot \underline{v} \\ \lambda^{(2)} \xrightarrow[k_{12}\to+\infty,\, k_{21}\to 0]{} -D|\underline{k}|^2 - k_{12} \end{cases} \tag{8.32}$$

The $\mathbb{A}$ and $\mathbb{B}$ terms can therefore be rewritten as

$$\begin{cases} \mathbb{A} \xrightarrow[k_{12}\to+\infty,\, k_{21}\to 0]{} k_{12}(k_{12} + i\underline{k}\cdot\underline{v}) \\ \\ \mathbb{B} \xrightarrow[k_{12}\to+\infty,\, k_{21}\to 0]{} 0 \\ \mathbb{C} \xrightarrow[k_{12}\to+\infty,\, k_{21}\to 0]{} \mathbb{A} \end{cases} \tag{8.33}$$

This yields, in agreement with the literature [292],

$$G(\underline{k},\tau) \xrightarrow[k_{12}\to+\infty,\, k_{21}\to 0]{} exp\left\{ -\frac{\omega_0^2|\underline{k}|^2}{4} - \left[D|\underline{k}|^2 - i\underline{k}\cdot\underline{v} \right]\tau \right\} \tag{8.34}$$

8.3 Extension to 3D intermittent active transport

Throughout Section 8.1, I have assumed that the fluctuations in the detected scattering signal originate from the two-dimensional Brownian diffusion and drift undergone by particles switching between a free state (1) and a bound state (2) while in the focal plane. I now attempt to extend the same formalism to the more general case of three-dimensional diffusion and directional transport: I maintain therefore an isotropic diffusion coefficient D, and I introduce a 3D drift velocity $\underline{v} = (v_x, v_y, v_z)$. I call α and ϕ the angles subtended by the vector $\underline{v}$ in the xy-plane and with the z-axis, respectively (with $\phi = 90°$ corresponding to a vanishing z-component $v_z = 0$), so that $\underline{v} = (|\underline{v}|\cos\alpha\sin\phi, |\underline{v}|\sin\alpha\sin\phi, |\underline{v}|\cos\phi)$.
I derive the STICS correlation function $G(\underline{\Delta},\tau)$ by assuming at first a three-dimensional shift vector $\underline{\Delta} = (\xi,\eta,\zeta)\delta x$. Eq. (8.5) (i.e., the numerator of the STICS correlation function) turns into

$$\begin{aligned} g(\underline{\Delta},\tau) = \lim_{R\to+\infty} \frac{1}{R^3} \int_{-R/2}^{R/2} d\underline{x} \iint_{-\infty}^{+\infty} d\underline{r} d\underline{r}' W^*(\underline{r}-\underline{x}) W(\underline{r}'-\underline{x}-\underline{\Delta}) \cdot \\ \cdot \sum_{i,j=1}^{2} \phi_i\phi_j < \delta C_i^*(\underline{r},0)\delta C_j(\underline{r}',\tau) > \end{aligned} \tag{8.35}$$

with three-dimensional vectors $\underline{\Delta}$, $\underline{x}$, $\underline{v}$, $\underline{r}$ and $\underline{r}'$ replacing the same vectors previously defined in 2D. By the same substitution of all the 2D vectors with the

corresponding 3D counterparts, the Fick's equation, the eigenvalues and eigenvectors of the matrix M and the concentration fluctuations $\delta\widehat{C}_{i=1,2}(\underline{q},t)$ can be directly obtained from eqs. (8.6)-(8.10) and (8.19)-(8.20). Hence, similarly to eq. (8.13),

$$< \delta C_i^*(\underline{r},0)\delta C_j(\underline{r}',\tau) >= \frac{< C_i >}{(2\pi)^3}\int_{-\infty}^{+\infty}\sum_{s=1}^{2}\chi_j^{(s)}exp(\lambda^{(s)}\tau)\chi_i^{-1(s)}e^{i\underline{q}\cdot(\underline{r}-\underline{r}')}\,d\underline{q} \tag{8.36}$$

By substituting eq. (8.36) and the Fourier transforms of the 3D intensity distributions $W^*(\underline{r}-\underline{x})$ and $W(\underline{r}'-\underline{x}-\underline{\Delta})$ into eq. (8.35), I obtain

$$\begin{aligned} g(\underline{\Delta},\tau) = \frac{1}{(2\pi)^6}\lim_{R\to+\infty}\frac{1}{R^3}\int_{-R/2}^{R/2}d\underline{x}\iint_{-\infty}^{+\infty}d\underline{r}d\underline{r}'\int_{-\infty}^{+\infty}d\underline{q}\iint_{-\infty}^{+\infty}d\underline{q}'d\underline{q}''\widehat{W}^*(\underline{q}')\widehat{W}(\underline{q}'')\cdot \\ \cdot\sum_{i,j=1}^{2}\left\{< C_i > \phi_i\phi_j\sum_{s=1}^{2}\chi_j^{(s)}exp(\lambda^{(s)}\tau)\chi_i^{-1(s)}\right\}e^{i\underline{q}\cdot(\underline{r}-\underline{r}')+i\underline{q}\cdot(\underline{r}-\underline{x})-i\underline{q}''\cdot(\underline{r}'-\underline{x}-\underline{\Delta})} \end{aligned} \tag{8.37}$$

By extending the procedure outlined in eqs. (8.16)-(8.18) to the 3D case,

$$g(\underline{\Delta},\tau) = -\frac{1}{(2\pi)^3}\int_{-\infty}^{+\infty}d\underline{k}|\widehat{W}(-\underline{k})|^2R(\underline{k},\tau)e^{-i\underline{k}\cdot\underline{\Delta}} \tag{8.38}$$

As previously anticipated, $R(\underline{k},\tau)$ has the functional form of eq. (8.22) with three-dimensional vectors $\underline{k}$ and $\underline{v}$. For the excitation intensity distribution, the 3D Gaussian with amplitude W_0 and $1/e^2$ distances ω_0 and ω_{0z} of eq. (1.19) is assumed. When it is substituted with $R(\underline{k},\tau)$ into eq. (8.38), it leads to

$$\begin{aligned} G(\underline{\Delta},\tau) &\propto \int_{-\infty}^{+\infty}d\underline{k}\left\{\frac{\mathbb{A}e^{\lambda^{(1)}\tau}+\mathbb{B}e^{\lambda^{(2)}\tau}}{\mathbb{C}}\right\}exp\left\{-\frac{\omega_0^2(k_x^2+k_y^2)+\omega_{0z}^2k_z^2}{4}-i\underline{k}\cdot\underline{\Delta}\right\} \\ &\propto \int_{-\infty}^{+\infty}d\underline{k}F(\underline{k},\tau)e^{-i\underline{k}\cdot\underline{\Delta}} \end{aligned} \tag{8.39}$$

with

$$F(\underline{k},\tau) \equiv \left\{\frac{\mathbb{A}e^{\lambda^{(1)}\tau}+\mathbb{B}e^{\lambda^{(2)}\tau}}{\mathbb{C}}\right\}exp\left\{-\frac{\omega_0^2(k_x^2+k_y^2)+\omega_{0z}^2k_z^2}{4}\right\} \tag{8.40}$$

All the k-independent constant terms and the normalization factors have been included in the proportionality symbol.

As in Section 8.1, the integral over the $\underline{k}$-variable in eq. (8.39) can not be performed analytically, preventing the recovery of the explicit expression for the STICS correlation function. Moreover, since the images are acquired in the xy-plane only, no spatial lag can be introduced along the z-axis, and the shift vector $\underline{\Delta}$ in eq. (8.39) necessarily has a null component along the z-axis: $\underline{\Delta} = (\xi, \eta, 0)\delta x$. Eq. (8.39) yields therefore

$$G(\underline{\Delta}, \tau) = G(\xi, \eta, 0, \tau) \propto \iiint_{-\infty}^{+\infty} dk_x dk_y dk_z F(k_x, k_y, k_z, \tau) e^{-i(k_x \xi \delta x + k_y \eta \delta x)}$$

$$= \iint_{-\infty}^{+\infty} dk_x dk_y e^{-i(k_x \xi \delta x + k_y \eta \delta x)} \int_{-\infty}^{+\infty} dk_z F(k_x, k_y, k_z, \tau) \tag{8.41}$$

Recalling that the kICS correlation function is computed by the two-dimensional spatial Fourier transform of the xyt-stack of the raw data (the images are acquired in the xy-plane only, so that no Fourier transform can be performed along the z-direction) [292], the integral

$$\int_{-\infty}^{+\infty} dk_z F(k_x, k_y, k_z, \tau) \equiv G(k_x, k_y, \tau) \tag{8.42}$$

appearing in eq. (8.41) provides the kICS correlation function for the intermittent three-dimensional dynamics. Unfortunately, the complexity of $F(\underline{k}, \tau)$ (eq. 8.40) prevents the analytical solution of the integral.[2]

Summarizing, no analytical solution can be obtained within the formalism of Spatio-Temporal Image Correlation Spectroscopy when investigating intermittent active transport, neither in 2D nor in 3D; by contrast, starting from an xyt-stack of images, an analytical solution can be found in the reciprocal Fourier-space when the diffusion and drift motion exhibited by the imaged particles mainly occur in

[2]If the experimental data are acquired in the form of $xyzt$-stacks - so that 3D volumes are repeatedly acquired in time - a three-dimensional Fourier transform can in principle be computed. The STICS correlation function can be computed in the direct space as a function of three spatial delays ξ, η and ζ, while the kICS correlation function would depend on a 3D $\underline{k}$-vector, with non-zero z component. Under this condition, an analytical solution for the kICS correlation function can be obtained, and it is provided directly by eq. (8.40).

the focal plane. I adopt therefore the 2D approximation for the investigation of the intermittent dynamics of nanostars-containing vesicles in HeLa cells (exactly as for the Single Particle Tracking analysis), and I finally verify, at the end of this Chapter, that the hypothesis of 2D motion is sufficient for the accurate description of the experimental data.

8.4 Simulated kICS correlation functions

The kICS correlation function $G(\underline{k},\tau)$ is effectively a time-series in the complex field, with each frame being the average 2D spatial correlation of the Fourier transforms of pairs of images a lag time τ apart in the experimental dataset. Therefore, two choices are possible for data fitting: either analyzing the $G(\underline{k},\tau)$-vs-τ profiles at fixed $\underline{k}$ delays, or fitting the $G(\underline{k},\tau)$-vs-$\underline{k}$ surfaces at fixed lag time τ.
In order to assess which option offers the greater sensitivity and gives the better estimate of the parameters (diffusion coefficient D, drift velocity $\underline{v}$, association/dissociation rates k_{12} and k_{21}), I have investigated separately the effect of D, $|\underline{v}|$, k_{12} and k_{21} on simulated kICS correlation functions in both the representations. Since $G(\underline{k},\tau)$ is defined in the complex field, for both $G(\underline{k},\tau)$-vs-τ profiles and $G(\underline{k},\tau)$-vs-$\underline{k}$ surfaces I have evaluated the real and imaginary parts: these will be hereafter referred to as $Re(G(\tau))$, $Im(G(\tau))$ (in the case of $G(\underline{k},\tau)$-vs-τ profiles), or as $Re(G(\underline{k}))$, $Im(G(\underline{k}))$ (in the case of $G(\underline{k},\tau)$-vs-$\underline{k}$ surfaces).[3]

8.4.1 kICS profiles

I begin by considering $G(\underline{k},\tau)$-vs-τ profiles. These have been simulated, according to eq. (8.27), for a fixed Fourier-space vector $\underline{k} = (k_x, k_y)$=(-2,0) μm^{-1} and for τ comprised in the broad range 0-250 s. In order to probe the sensitivity of the kICS correlation profiles toward the transition rates (or equivalently, the transition probabilities defined in eq. 7.17), $Re(G(\tau))$ and $Im(G(\tau))$ profiles have been initially simulated with D=2x10^{-4} $\mu m^2/s$, $|\underline{v}|$=0.08 $\mu m/s$ and with an arbitrary direction α=290° for the drift velocity; several probability combinations have been evaluated:

- p_{12}=0.05 and p_{21}=0.05, 0.1, 0.3, 0.5, 0.7, 0.9;

[3] I remark that, although the real and imaginary parts of the kICS correlation function (eq. 8.27) cannot be analytically separated, they can be simulated separately: a custom-written Python code is employed to compute, for any given parameter set, $G(\underline{k},\tau)$ and to evaluate, given the complex number, its real and imaginary parts.

- p_{12}=0.2 and p_{21}=0.05, 0.1, 0.3, 0.5, 0.7;
- p_{12}=0.5 and p_{21}=0.05, 0.1, 0.2, 0.3, 0.4.

These probability combinations correspond to an equilibrium probability for the active transport state P_2^{eq} varying in the range 0.05-0.9, so that the kICS correlation profiles could be evaluated for all the possible intermittent transport modes ranging from nearly diffusive to almost totally active.
The results of these simulations are reported in Fig. 8.1. Simulated $Re(G(\tau))$ profiles and $Im(G(\tau))$ profiles are separated (with $Re(G(\tau))$ profiles in the left column, and $Im(G(\tau))$ profiles in the right column) and color-coded according to the probability p_{12}: p_{12}=0.05 for dashed blue curves, p_{12}=0.2 for dotted pink curves and p_{12}=0.5 for solid light blue curves. In each panel, at fixed p_{12}, the probability p_{21} increases in the direction of the arrow. The comparison of all the $Re(G(\tau))$ profiles (panels a, c and e) highlights they are significantly affected by the probability combinations: the higher the probability p_{12}, the more oscillatory is the behavior of the simulated curves. The same applies to $Im(G(\tau))$ profiles, as apparent when comparing panels b, d and f.

The same $\underline{k}$ vector, diffusion coefficient, drift angle and probability combinations have been subsequently employed for the simulation of $Re(G(\tau))$ and $Im(G(\tau))$ profiles at lower $|\underline{v}|$ values. Drift speeds $|\underline{v}|$=0.01 $\mu m/s$ and 0.001 $\mu m/s$ have been adopted, to include in the explored range of speed values those previously measured by TICS, STICS and SPT.
The $Re(G(\tau))$ and $Im(G(\tau))$ profiles simulated with $|\underline{v}|$=0.01 $\mu m/s$ are reported in Fig. 8.2, while Fig. 8.3 shows the profiles simulated with $|\underline{v}|$=0.001 $\mu m/s$. The same color code of Fig. 8.1 is adopted, with blue, pink and light blue curves corresponding to p_{12}=0.05, 0.2 and 0.5 respectively; as before, for each value of p_{12} the direction of the arrow codes for increasing values of the transition probability p_{21}. Looking globally at Figs. 8.1, 8.2 and 8.3, it is apparent that: (i) especially at low drift speed, the imaginary part ($Im(G(\tau))$ profiles) exhibit the highest sensitivity toward p_{12} and p_{21} values; (ii) the oscillatory behavior of the $Re(G(\tau))$ and $Im(G(\tau))$ plots is mainly regulated by the modulus $|\underline{v}|$ of the drift speed, and it disappears for low $|\underline{v}|$ values; (iii) the higher the speed $|\underline{v}|$, the higher is the sensitivity of the $Re(G(\tau))$ and $Im(G(\tau))$ profiles toward variations in the probability values.
In general, the possibility of recovering the speed $|\underline{v}|$ and the probabilities p_{12} and p_{21} from $Re(G(\tau))$ or $Im(G(\tau))$ profiles seem to increase for higher values of the drift speed and of the probability p_{12}. This can be explained by recalling that the

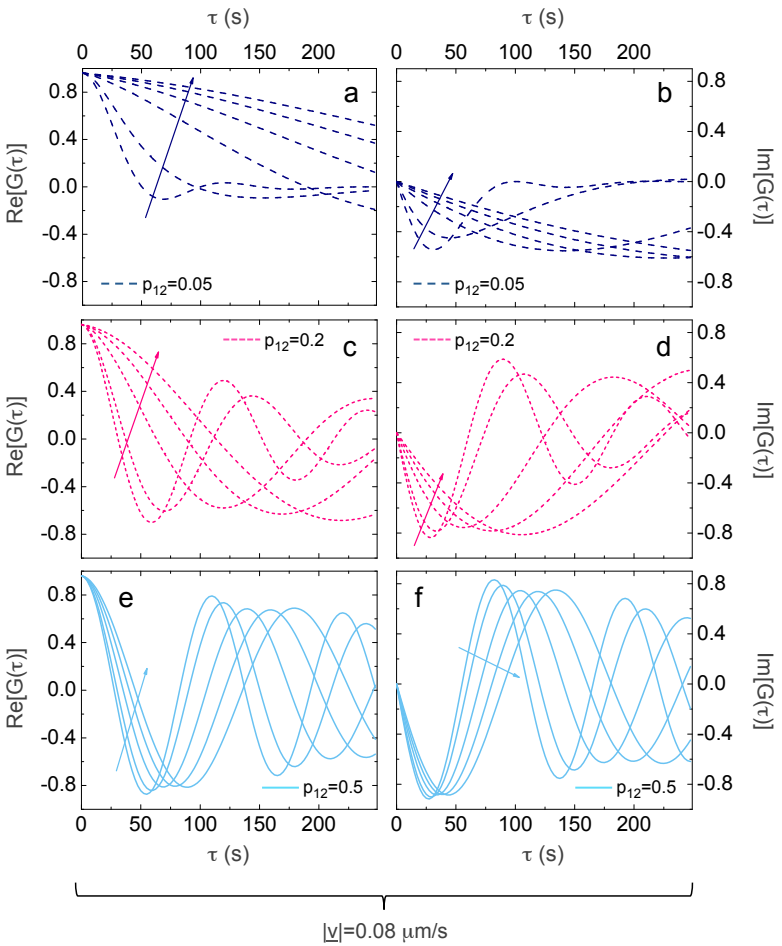

Figure 8.1: *kICS simulations: effect of the transition probabilities (I).* (a), (b): simulated $\mathrm{Re}(G(\tau))$ and $\mathrm{Im}(G(\tau))$ profiles (in a and b respectively) for fixed $\underline{k}$=(-2,0) μm^{-1}, D=2x10^{-4} $\mu m^2/s$, $|\underline{v}|$=0.08 $\mu m/s$ and α=290°. p_{12}=0.05 and p_{21}=0.05, 0.1, 0.3, 0.5, 0.7, 0.9; p_{21} increases in the direction of the arrow. (c), (d): $\mathrm{Re}(G(\tau))$ and $\mathrm{Im}(G(\tau))$ profiles (in c and d respectively) simulated with the same parameters of panels (a) and (b), apart from the transition probabilities: here p_{12}=0.2 and p_{21}=0.05, 0.1, 0.3, 0.5, 0.7, increasing in the direction of the arrow. (e), (f): $\mathrm{Re}(G(\tau))$ and $\mathrm{Im}(G(\tau))$ profiles (in e and f respectively) simulated with the same parameters of panels (a) and (b), apart from p_{12}=0.5 and p_{21}=0.05, 0.1, 0.2, 0.3, 0.4; p_{21} increases in the direction of the arrow. Probability values have been provided as simulation input parameters; then a time step Δt=2.5 s has been employed to derive the corresponding transition rates k_{12} and k_{21}, inserted into eq. (8.27) for the profiles simulation.

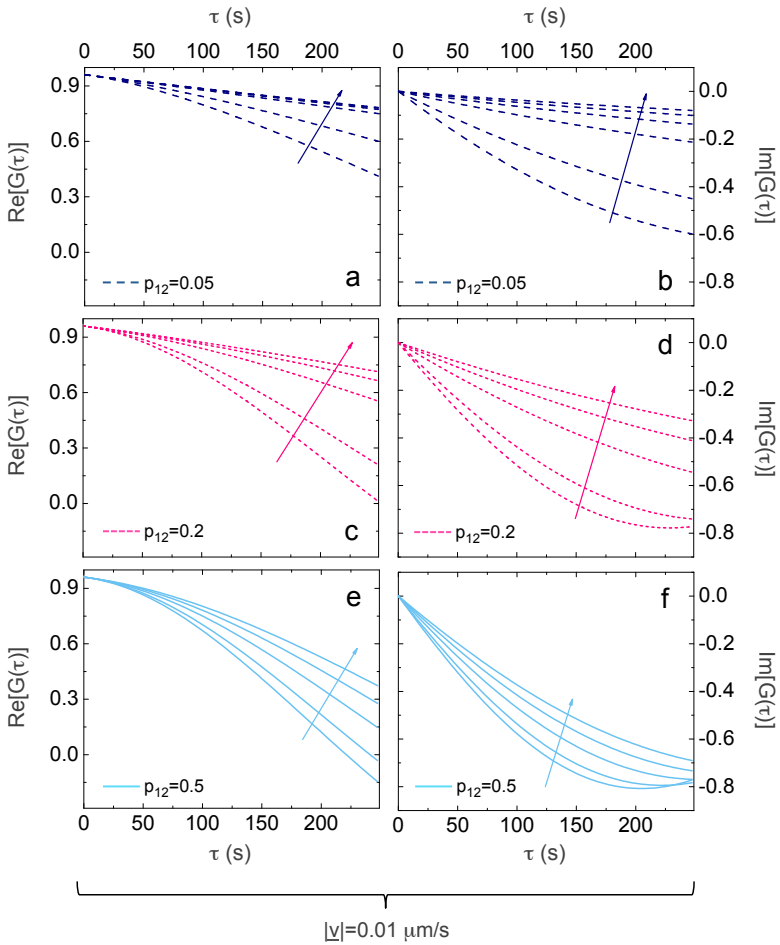

Figure 8.2: *kICS simulations: effect of the transition probabilities (II).* (a)-(f): simulated $\mathrm{Re}(G(\tau))$ and $\mathrm{Im}(G(\tau))$ profiles (real parts in a, c and e; imaginary parts in b, d and f) for fixed $\underline{k}$=(-2,0) μm^{-1}, D=2x10^{-4} $\mu m^2/s$, α=290° and $|\underline{v}|$=0.01 $\mu m/s$. The same color code of Fig. 8.1 is adopted: p_{12}=0.05 and p_{21}=0.05, 0.1, 0.3, 0.5, 0.7, 0.9 for blue dashed curves; p_{12}=0.2 and p_{21}=0.05, 0.1, 0.3, 0.5, 0.7 for pink dotted curves; p_{12}=0.5 and p_{21}=0.05, 0.1, 0.2, 0.3, 0.4 for light blue solid curves; p_{21} always increases in the direction of the arrow. As in Fig. 8.1, probability values have been provided as simulation input parameters; then a time step Δt=2.5 s has been employed to derive the corresponding transition rates k_{12} and k_{21}, inserted into eq. (8.27) for the profiles simulation.

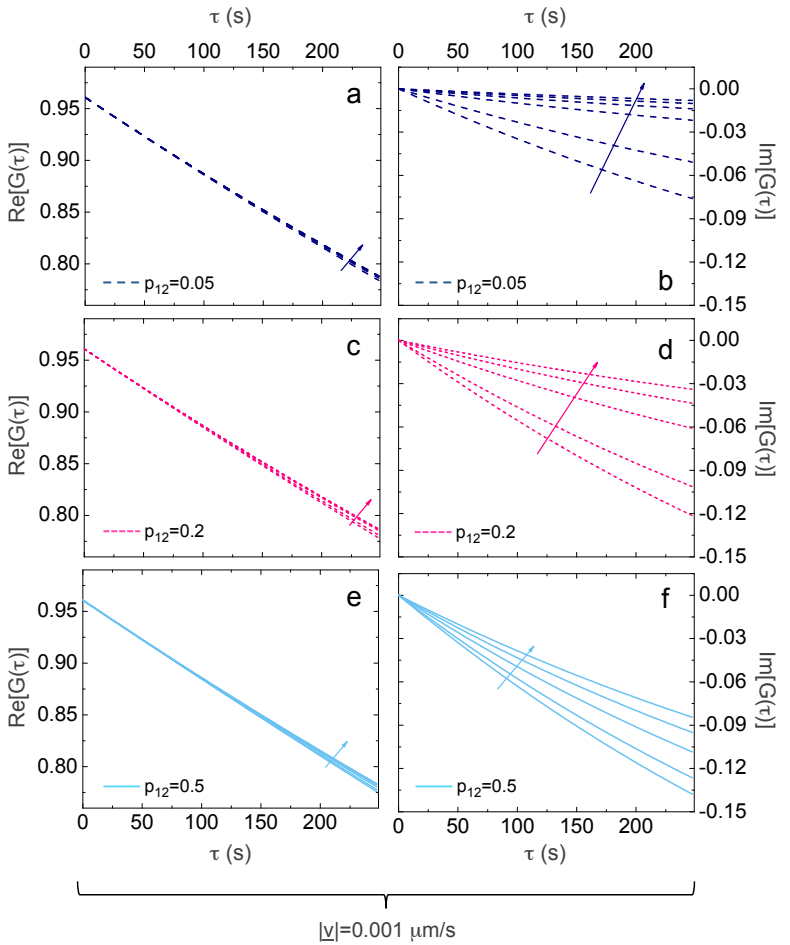

Figure 8.3: *kICS simulations: effect of the transition probabilities (III).* (a)-(f): simulated $\mathrm{Re}(G(\tau))$ and $\mathrm{Im}(G(\tau))$ profiles (real parts in a, c and e; imaginary parts in b, d and f) for fixed $\underline{k}$=(-2,0) μm^{-1}, D=2x10^{-4} $\mu m^2/s$, α=290° and $|\underline{v}|$=0.001 $\mu m/s$. The same color code of Fig. 8.1 is adopted: p_{12}=0.05 and p_{21}=0.05, 0.1, 0.3, 0.5, 0.7, 0.9 for blue dashed curves; p_{12}=0.2 and p_{21}=0.05, 0.1, 0.3, 0.5, 0.7 for pink dotted curves; p_{12}=0.5 and p_{21}=0.05, 0.1, 0.2, 0.3, 0.4 for light blue solid curves; p_{21} always increases in the direction of the arrow. As in Fig. 8.1, probability values have been provided as simulation input parameters; then a time step Δt=2.5 s has been employed to derive the corresponding transition rates k_{12} and k_{21}, inserted into eq. (8.27) for the profiles simulation.

lower $|\underline{v}|$, the more similar are the transport properties of states (1) and (2); similarly, the lower the transition probability p_{12}, the smaller are the effect of the drift speed and the deviation of the particle motion from a purely diffusive one.

Having evaluated the effect of $|\underline{v}|$ and of the transition probabilities, I now turn to the diffusion coefficient. Like $|\underline{v}|$, also the diffusion coefficient D significantly affects the simulated $Re(G(\tau))$ and $Im(G(\tau))$ plots. This is shown in Fig. 8.4 for D in the range 2x10^{-5}-2x10^{-3} $\mu m^2/s$, with exemplifying profiles simulated with fixed $\underline{k}$=(-2,0) μm^{-1}, $|\underline{v}|$=0.001 $\mu m/s$, α=290°, p_{12}=0.05 and p_{21}=0.5.

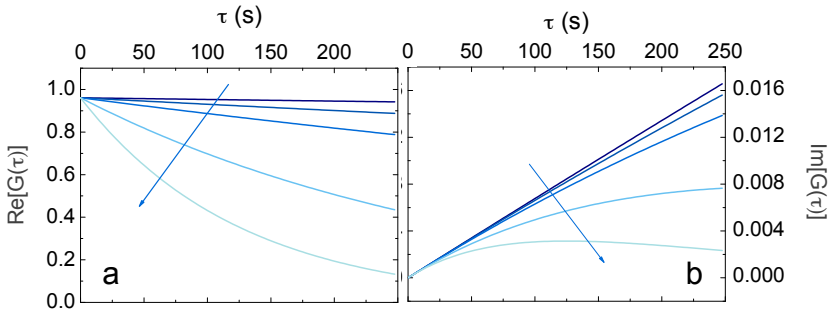

Figure 8.4: *kICS simulations: effect of the diffusion coefficient.* (a), (b): simulated $Re(G(\tau))$ and $Im(G(\tau))$ profiles (in a and b respectively), for fixed $\underline{k}$=(-2,0) μm^{-1}, $|\underline{v}|$=0.001 $\mu m/s$, α=290°, p_{12}=0.05 and p_{21}=0.5. D=2x10^{-5}, 8x10^{-5}, 2x10^{-4}, 8x10^{-4} and 2x10^{-3} $\mu m^2/s$, increasing in the direction of the arrow.

8.4.2 Fitting real and imaginary parts

The sensitivity of $G(\underline{k},\tau)$-vs-τ profiles toward the model parameters, explored in Figs. 8.1-8.4 for the real and imaginary parts, suggests that the non-linear fit of experimental temporal kICS profiles should allow the recovery of D, $|\underline{v}|$, k_{12} and k_{21}.

The obvious way to simultaneously account for both the real and imaginary parts of these $G(\underline{k},\tau)$-vs-τ kICS plots would consist in performing a non-linear global fit in the complex field. Alternatively, in order to fasten and simplify the fitting procedure, a combination (for example the ratio, or the product) of the $Re(G(\tau))$ and $Im(G(\tau))$ profiles can be exploited.

In Fig. 8.5 (panels a-c), the product $Re(G(\tau)) \cdot Im(G(\tau))$ has been simulated for fixed $\underline{k}$=(-2,0) μm^{-1}, D=2x10^{-4} $\mu m^2/s$, $|\underline{v}|$=0.08 $\mu m/s$ and α=290°. The same probability combinations, and the same color code, of Figs. 8.1-8.3 have been adopted, to evidence that the product of the real and imaginary parts depends sensibly upon the transition rates of the intermittent model. The same applies when the drift speed is reduced to 0.01 $\mu m/s$ (Fig. 8.5, panels d-f) and to 0.001 $\mu m/s$ (Fig. 8.5, panels g-i).

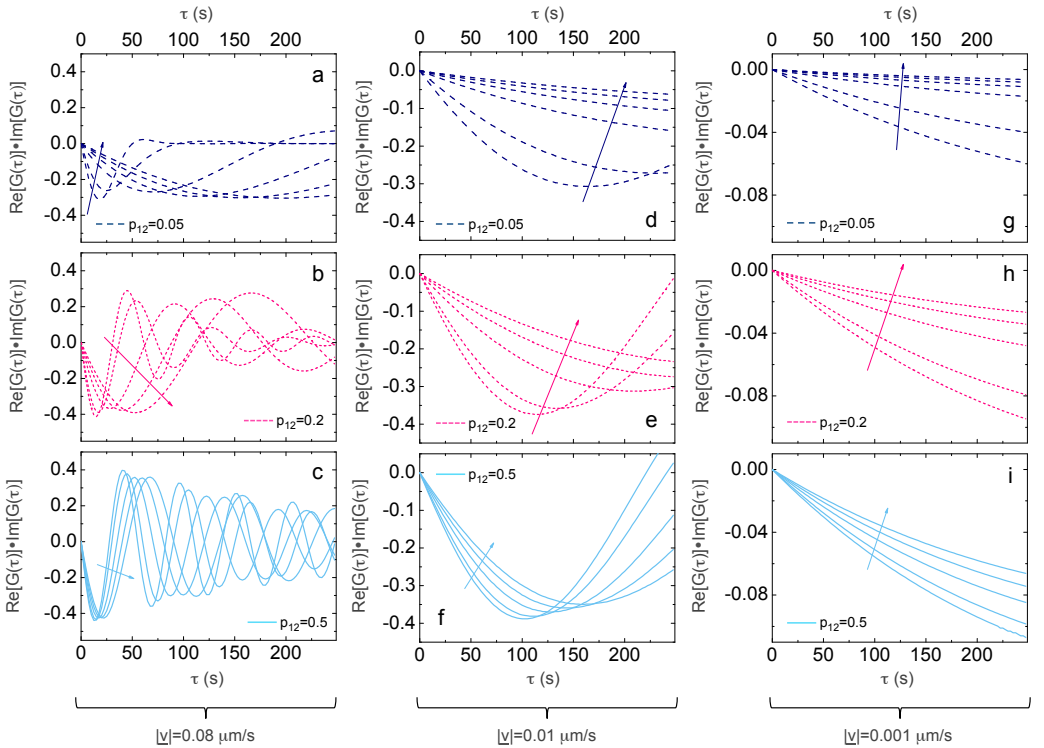

Figure 8.5: *kICS simulations: product of the real and imaginary parts of* $G(\underline{k},\tau)$*-vs-*τ *profiles.* (a)-(c): $Re(G(\tau)) \cdot Im(G(\tau))$ profiles simulated according to eq. (8.27) for fixed $\underline{k}$=(-2,0) μm^{-1}, D=2x10^{-4} $\mu m^2/s$, α=290° and $|\underline{v}|$=0.08 $\mu m/s$. The same probability combinations and color code of Figs. 8.1-8.3 are employed: p_{12}=0.05 for blue curves (in a), p_{12}=0.2 for pink curves (in b) and p_{12}=0.05 for light blue curves (in c); for each p_{12}, the probability p_{21} increases along the arrow according to the probability combinations previously defined. (d)-(f): same simulation parameters and color code of (a)-(c), apart from $|\underline{v}|$=0.01 $\mu m/s$. (g)-(i): same simulation parameters and color code of (a)-(c), apart from $|\underline{v}|$=0.001 $\mu m/s$.

In the sensitivity toward the transition rates of the intermittent model, the product $Re(G(\tau)) \cdot Im(G(\tau))$ outperforms the ratio $Im(G(\tau))/Re(G(\tau))$: the ratio corresponds to the tangent of the phase of the complex number $G(\tau)$, and exhibits the periodic divergences of a tangent function. Equivalently, the modulus $|G(\tau)|^2$, given by $Re(G(\tau))^2 + Im(G(\tau))^2$, is always positive and flattens the behavior of the curves becoming less sensitive to the parameters. Both the ratio $Im(G(\tau))/Re(G(\tau))$ and the modulus $|G(\tau)|^2$ are simulated in Fig. 8.6, with the same simulation input parameters adopted for the product $Re(G(\tau)) \cdot Im(G(\tau))$ in Fig. 8.5a-c.

8.4.3 Fourier-space vectors selection

All the $G(\underline{k}, \tau)$-vs-τ profiles in Figs. 8.1-8.6 have been simulated for a fixed arbitrary $\underline{k}$ vector $\underline{k}$=(-2,0) μm^{-1}. As a rule of thumb, no particular $\underline{k}$ vector is preferable for the extraction of kICS temporal profiles. This is shown in Fig. 8.7, with an exemplary simulated $Re(G(\underline{k})) \cdot Im(G(\underline{k}))$ surface (at fixed lag time τ=75 s) and with the $Re(G(\tau)) \cdot Im(G(\tau))$ profiles extracted in several $\underline{k}$ coordinates: the k_x and k_y components affect the amplitude and shape of the $Re(G(\tau)) \cdot Im(G(\tau))$ profiles but, these variations being explicitly accounted for in the analytical expression of the kICS correlation function, no specific $\underline{k}$ value is identified as better than others for the curves fitting procedure and for the consequent recovery of transport and kinetic parameters.

8.4.4 kICS surfaces

Once inspected the dependence of $G(\underline{k}, \tau)$-vs-τ profiles on the parameters of the intermittent model, I evaluate $G(\underline{k}, \tau)$-vs-$\underline{k}$ surfaces. In Fig. 8.8a-b, I report the product of the real and imaginary parts of the $G(\underline{k}, \tau)$-vs-$\underline{k}$ surfaces simulated, according to eq. (8.27), for a fixed lag time τ=25 s with D=2x10^{-4} $\mu m^2/s$, α=290° and $|\underline{v}|$=0.08 $\mu m/s$; the probability combination $\{p_{12} = 0.5, p_{21} = 0.05\}$ is adopted for panel (a), whereas $\{p_{12} = 0.05, p_{21} = 0.9\}$ is employed in panel (b). These two combinations for the transition probabilities are those producing the largest difference in the temporal $Re(G(\tau))$ and $Im(G(\tau))$ profiles shown in Fig. 8.1. Correspondingly, a large difference in the surfaces is found here (Fig. 8.8a-b), suggesting that a reliable recovery of transition rates is also allowed when fitting $G(\underline{k}, \tau)$-vs-$\underline{k}$ surfaces. However, when all the simulation parameters are kept unchanged apart from a reduction of the drift speed $|\underline{v}|$ to 0.001 $\mu m/s$, the differences in the simulated surfaces practically disappear (Fig. 8.8c-d): this makes $G(\underline{k}, \tau)$-vs-$\underline{k}$ surfaces much less

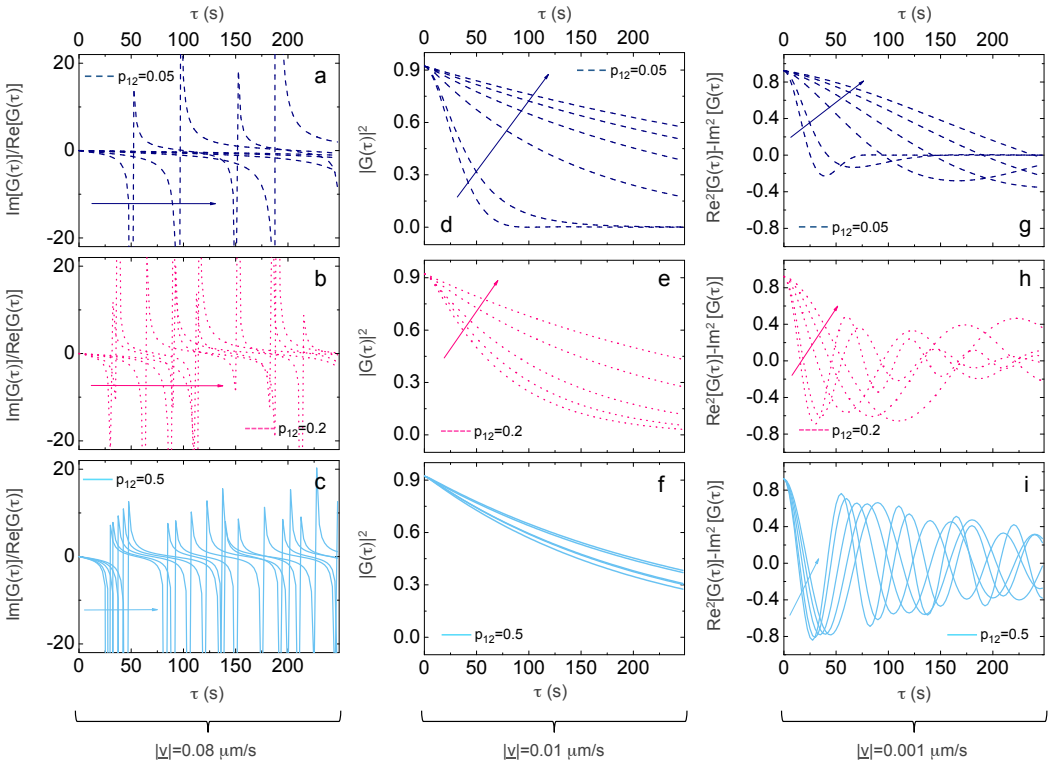

Figure 8.6: *kICS simulations: options for data fitting.* (a)-(c): simulated $\mathrm{Im}(G(\tau))/\mathrm{Re}(G(\tau))$ for fixed $\underline{k}$=(-2,0) μm^{-1}, D=2x10^{-4} $\mu m^2/s$, $|\underline{v}|$=0.08 $\mu m/s$ and α=290°. The same probability combinations of Figs. 8.1-8.3 are employed, with color-coded p_{12}, and with p_{21} increasing in the direction of the arrow. The periodic diverges make the ratio $\mathrm{Im}(G(\tau))/\mathrm{Re}(G(\tau))$ an inconvenient choice when aiming at the fit of experimental data. (d)-(f): modulus $|G(\tau)|^2$ simulated with the same parameters and color code of panels (a)-(c). In (f) an irregular trend is found for varying p_{21}, and no arrow is reported. (g)-(i): $\mathrm{Re}(G(\tau))^2 - \mathrm{Im}(G(\tau))^2$ profiles simulated with the same parameters and color code of panels (a)-(c). $\mathrm{Re}(G(\tau))^2 - \mathrm{Im}(G(\tau))^2$ (equal to the real part of $G^2(\tau)$) resembles $\mathrm{Re}(G(\tau)) \cdot \mathrm{Im}(G(\tau))$ (half the imaginary part of $G^2(\tau)$) in its sensitivity to variations in the probability values. Globally, it is convenient to employ either $\mathrm{Re}(G(\tau))^2 - \mathrm{Im}(G(\tau))^2$ or $\mathrm{Re}(G(\tau)) \cdot \mathrm{Im}(G(\tau))$ profiles for the recovery of probability combinations from the kICS experimental data.

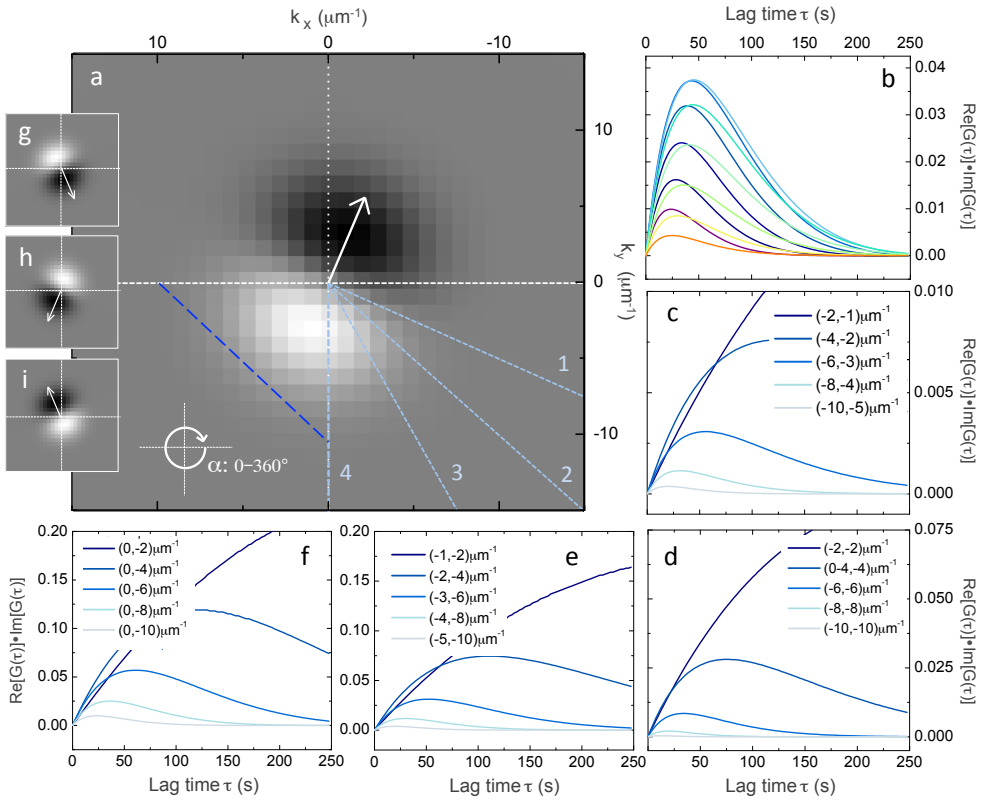

Figure 8.7: *kICS simulations:* $\underline{k}$ *vector selection.* (a): product of the real and imaginary parts, reported for τ=75 s, of the kICS correlation function $G(\underline{k},\tau)$ simulated for D=2x10^{-4} $\mu m^2/s$, $|\underline{v}|$=0.001 $\mu m/s$, α=290° (indicated by the arrow), p_{12}=0.4 and p_{21}=0.05. For the sake of display, the 64x64 pixels^2 correlation function has been cropped to only show its non-vanishing central portion. (b): $Re(G(\tau)) \cdot Im(G(\tau))$ profiles extracted for different k_x and k_y values along the dashed blue line in panel (a): $\underline{k}$ varies (from purple to orange) from (0,-10), (1,-9), (2,-8)... to (9,-1), (10,0) μm^{-1}. (c)-(f): $Re(G(\tau)) \cdot Im(G(\tau))$ profiles extracted for different k_x and k_y values along the light blue dashed lines denoted as 1 (c), 2 (d), 3 (e) and 4 (f) in panel (a); k_x and k_y are reported in each panel. (g)-(i): product of the real and imaginary parts, reported for τ=75 s, of the kICS correlation function $G(\underline{k},\tau)$ simulated for D=2x10^{-4} $\mu m^2/s$, $|\underline{v}|$=0.001 $\mu m/s$, p_{12}=0.4 and p_{21}=0.05; α=67° in (g), 113° in (h) and 247° in (i) (see inset of panel a for the angle α definition). As remarked later in the text, since the separation of the correlation lobes appears orthogonal to the flow direction, $G(\underline{k},\tau)$ correlation surfaces at fixed lag time directly provide an estimate of the angle subtended by the drift direction and the horizontal x-axis.

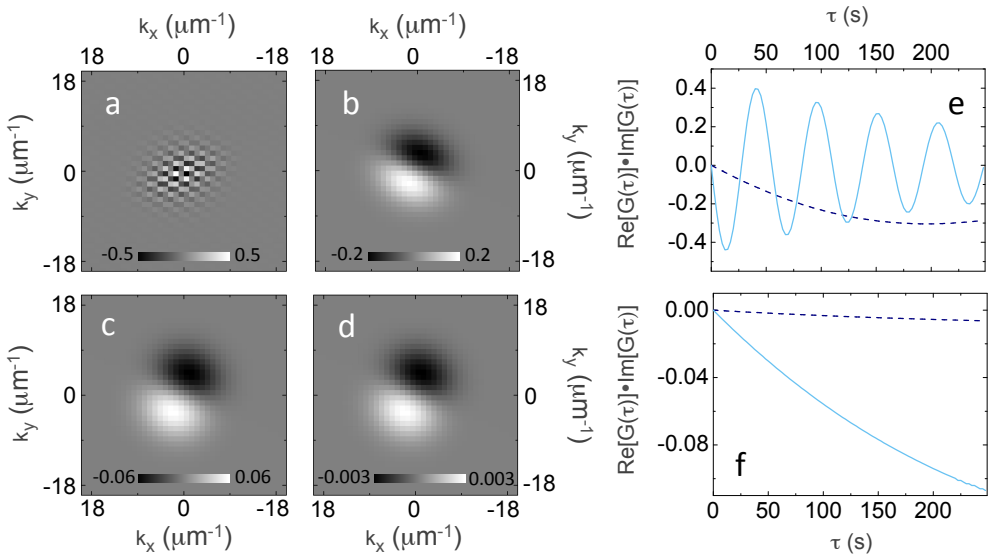

Figure 8.8: *kICS simulations:* $G(\underline{k},\tau)$*-vs-*$\underline{k}$ *surfaces.* (a), (b): product of the real and imaginary parts of the $G(\underline{k})$ surface simulated for τ=25 s with D=2x10^{-4} $\mu m^2/s$, $|\underline{v}|$=0.08 $\mu m/s$ and α=290°; $\{p_{12} = 0.5, p_{21} = 0.05\}$ in (a), $\{p_{12} = 0.05, p_{21} = 0.9\}$ in (b). (c), (d): product of the real and imaginary parts of the $G(\underline{k})$ surface simulated for τ=25 s with D=2x10^{-4} $\mu m^2/s$, $|\underline{v}|$=0.001 $\mu m/s$ and α=290°; $\{p_{12} = 0.5, p_{21} = 0.05\}$ in (c), $\{p_{12} = 0.05, p_{21} = 0.9\}$ in (d). (e): $Re(G(\tau)) \cdot Im(G(\tau))$ plots simulated in $\underline{k}$=(-2,0) μm^{-1} with the same D=2x10^{-4} $\mu m^2/s$, $|\underline{v}|$=0.08 $\mu m/s$ and α=290°; $\{p_{12} = 0.5, p_{21} = 0.05\}$ for the light blue curve, $\{p_{12} = 0.05, p_{21} = 0.9\}$ for the blue curve. (f): $Re(G(\tau)) \cdot Im(G(\tau))$ plots simulated in $\underline{k}$=(-2,0) μm^{-1} with the same D=2x10^{-4} $\mu m^2/s$, $|\underline{v}|$=0.001 $\mu m/s$ and α=290°; $\{p_{12} = 0.5, p_{21} = 0.05\}$ for the light blue curve, $\{p_{12} = 0.05, p_{21} = 0.9\}$ for the blue curve. The comparison of panels (c), (d) and (f) clearly suggests exploiting temporal profiles rather than kICS surfaces.

sensitive to the probability values with respect to the temporal $Re(G(\tau)) \cdot Im(G(\tau))$ plots (shown with the same simulation parameters in Fig. 8.8e-f).
The only advantage of $G(\underline{k},\tau)$-vs-$\underline{k}$ surfaces is that they allow the immediate detection of the drift direction, which is orthogonal to the displacement between the positive and the negative lobes: previously shown in Fig. 8.7, this is also evidenced in Fig. 8.8a-d.

Fig. 8.8 also reveals that $Re(G(\underline{k})) \cdot Im(G(\underline{k}))$ surfaces de-correlate, for the typical D and $|\underline{v}|$ values recovered by TICS, STICS and SPT, in the 0-10 μm^{-1}

$\underline{k}$-range. When a confocal xyt-stack is Fourier transformed, the pixel size and the ROI size determine the obtained $\underline{k}$ vectors [42]: an adequate sampling of 0-10 μm^{-1} reciprocal-space vectors starting from a 64x64 ROI would require a pixel size of ~ 0.2 μm. This coarse spatial sampling required by $G(\underline{k},\tau)$-vs-$\underline{k}$ surfaces could be obtained on the same experimental dataset analyzed by STICS by pixel re-binning, at the expense of the number of pixels on which the correlation function is averaged. Alternatively the ROI size can be increased, thereby lowering the number of ROIs into which the image (the cell, in the present case) is divided. By contrast, as demonstrated with Fig. 8.7, even a single $\underline{k}$ vector can be exploited to extract the corresponding $G(\underline{k},\tau)$-vs-τ plot, with the same temporal sampling suitable for STICS.

Summarizing, provided the considerations of Subsections 8.4.1-8.4.4 and taking into account the computationally heavier effort in performing surface fitting of a complex function, I suggest to fit the experimental $G(\underline{k},\tau)$-vs-τ plots due to the higher sensitivity towards the model probabilities and the less strict requirements concerning spatial sampling. To increase the precision in the parameters recovery and to decrease the degree of cross-correlation among the parameters in the fit, a global fit over several $Re(G(\tau)) \cdot Im(G(\tau))$ profiles at different $\underline{k}$ values can eventually be performed.

8.5 kICS analysis of the nanostars intermittent dynamics

Once investigated the effect of D, $|\underline{v}|$, p_{12} and p_{21} on the kICS correlation function, I have employed reciprocal-space correlation spectroscopy for the analysis of the same xyt-stacks previously examined by TICS, STICS and SPT. Each 64x64 ROI has been Fourier-transformed to yield $G(\underline{k},\tau)$; then, $Re(G(\tau))\cdot Im(G(\tau))$ profiles have been extracted for selected components k_x and k_y and fitted according to the 2D model of eq. (8.27) to recover the dynamic and kinetic parameters.

Exemplary results are reported in Figs. 8.9-8.10 for the same three ROIs examined in Sections 6.3 and 6.4, exhibiting Brownian diffusion (ROI 1), Brownian diffusion coupled to directed motion (ROI 2) and intermittent active transport (ROI 3).

- For ROI 1, a $Re(G(\tau))$ profile only is reported (Fig. 8.9b, curve 1) since, according to eq. (8.30), an identically zero imaginary part is predicted for the kICS correlation function of a purely diffusive system. The profile can

be equally fit to eq. (8.30) with $|\underline{v}|=0$ (corresponding to the simple single-state diffusive dynamics) and to eq. (8.27), with best-fit diffusion coefficient $D=(1.55\pm0.06)\text{x}10^{-4}$ $\mu m^2/s$. I remark that when the fit is performed according to the 2D intermittent model of eq. (8.27), the dynamics is correctly categorized as diffusive, since the rates $k_{12} \to 0$ and $k_{21} \to +\infty$ obtained through the fit yield $P_1^{eq}=1$.

- For ROI 2, the $Re(G(\tau)) \cdot Im(G(\tau))$ profile extracted in $\underline{k}=(0,-8.9)$ μm^{-1} is shown, fitted to eq. (8.30) with best-fit parameters $D=(3.1\pm0.3)\text{x}10^{-4}$ $\mu m^2/s$, $|\underline{v}|=(2.47\pm0.03)\text{x}10^{-3}$ $\mu m/s$ and $\alpha=(59° \pm 1°)$. Again, the fit can also be performed according to eq. (8.27), leading to transition rates $k_{12} \to +\infty$ and $k_{21} \to 0$ and identifying the existence of a single diffusion+drift state; this confirms that easier transport modes can be easily discriminated and no prior information about the mode of motion is required for the fitting function selection.

- Finally for ROI 3 the $Re(G(\tau)) \cdot Im(G(\tau))$ profile extracted in $\underline{k}=(0,-11.8)$ μm^{-1} is shown, with the fit to the intermittent model of eq. (8.27); best-fit parameters are $D=(7\pm4)\text{x}10^{-5}$ $\mu m^2/s$, $|\underline{v}|=(6.1\pm0.1)\text{x}10^{-3}$ $\mu m/s$, $\alpha=(295° \pm 2°)$, $k_{12}=(0.007\pm0.004)$ s^{-1} and $k_{21}=(0.013\pm0.004)$ s^{-1}, with resulting equilibrium probabilities $P_1^{eq}=(0.6\pm0.2)$ and $P_2^{eq}=(0.4\pm0.2)$.

For all the three ROIs, exemplary $G(\underline{k},\tau)$-vs-$\underline{k}$ surfaces at fixed τ=30 s are also reported (Fig. 8.9a for ROI 1, Fig. 8.9c-d for ROI 2 , Fig. 8.10a-b for ROI 3). The corresponding $Re(G(\underline{k}))$ and $Im(G(\underline{k}))$ profiles extracted along the $k_x = 0$ and $k_y = 0$ axes are shown as well for completeness, with their forced-fit to the parameters recovered from the temporal $Re(G(\tau)) \cdot Im(G(\tau))$ plots.

When the same analysis is performed in all the ROIs within the imaged field of view, whole cell maps can be derived for all the parameters underlying the nanostars dynamics. In Fig. 8.11, panel (a), the map for the equilibrium probability of the active transport state, P_2^{eq}, is shown for the same cell analyzed in Figs. 6.7 and 6.9. D e $|\underline{v}|$ maps are shown in Fig. 8.11b-c and highlight the variability of both diffusion coefficients (in the range $\sim10^{-5}$-10^{-3} $\mu m^2/s$) and speed values (in the range $\sim 10^{-4}$-10^{-2} $\mu m/s$).
The maps for P_2^{eq}, D and $|\underline{v}|$ exemplify the double advantage of the kICS analysis: (i) contrarily to SPT, kICS can be extended (and, to a certain extent, automated) to all the ROIs within the cell, without requiring the identification and tracking

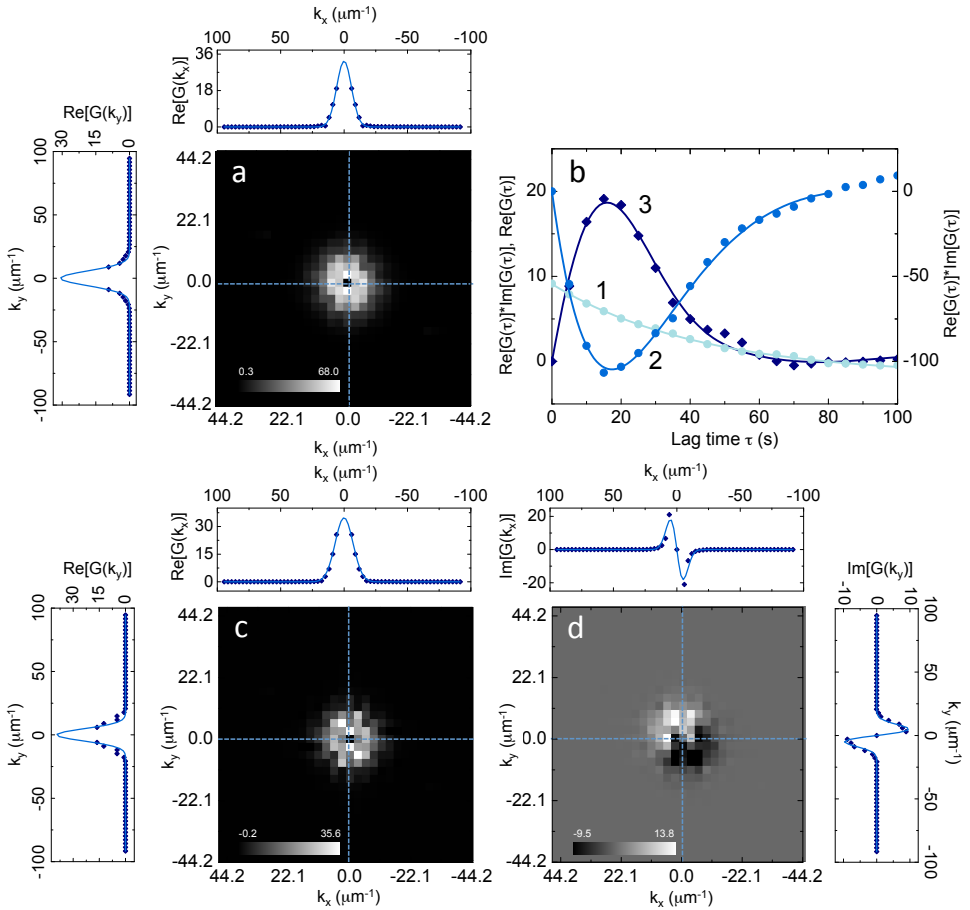

Figure 8.9: *kICS analysis of the GNSs intracellular transport (I).* (a): real part of the kICS surface $G(\underline{k},\tau)$ at τ=30 s computed on Fig. 6.9, ROI 1; profiles along the dashed lines ($k_x = 0$ and $k_y = 0$ axes) are shown with the forced fit to eq. (8.30) with the parameters extracted from panel (b). (b): exemplifying $Re(G(\tau)) \cdot Im(G(\tau))$ profiles for ROI 2 (k_x=0, k_y=-8.9 μm^{-1}; right axis, curve 2) and ROI 3 (k_x=0, k_y=-11.8 μm^{-1}; left axis, curve 3); best fit parameters are reported in the text. The $Re(G(\tau))$ plot is shown for ROI 1 (k_x=-11.8 μm^{-1}, k_y=-17.7 μm^{-1}; left axis, curve 1) with the best fit to eq. (8.30). Error bars are within the size of data points. (c)-(d): real and imaginary parts $Re(G(\underline{k}))$ and $Im(G(\underline{k}))$ (in c and d, respectively) for τ=30 s computed on Fig. 6.9, ROI 2. Profiles along the dashed lines ($k_x = 0$ and $k_y = 0$ axes) are shown with the forced fit to the parameters extracted from panel (b). All the $Re(G(\underline{k}))$ and $Im(G(\underline{k}))$ panels have been computed on a 200-frame stack (total acquisition time 500 s) and cropped (32x32 pixels instead of 64x64) for the sake of display.

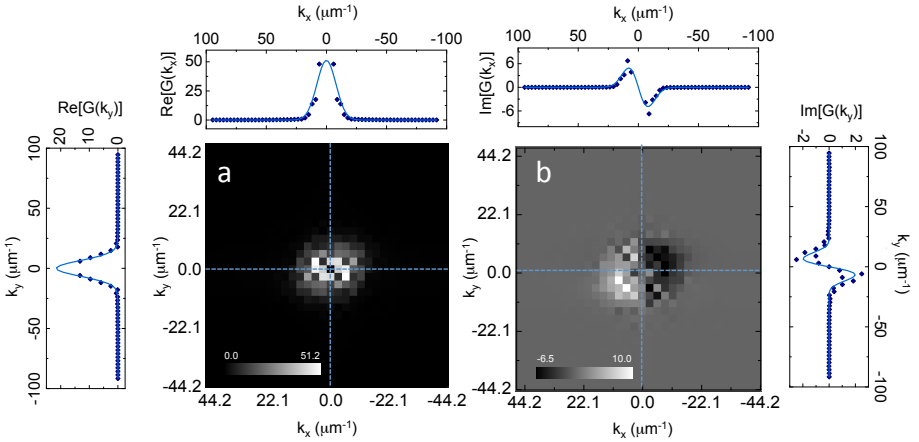

Figure 8.10: *kICS analysis of the GNSs intracellular transport (II).* (a), (b): real and imaginary parts $Re(G(\underline{k}))$ and $Im(G(\underline{k}))$ (in a and b, respectively) for τ=30 s computed on Fig. 6.9, ROI 3. Profiles along the dashed lines ($k_x = 0$ and $k_y = 0$ axes) are shown with the forced fit to the parameters extracted from Fig. 8.9, panel (b). The $Re(G(\underline{k}))$ and $Im(G(\underline{k}))$ panels have been computed on a 200-frame stack (total acquisition time 500 s) and cropped (32x32 pixels instead of 64x64) for the sake of display.

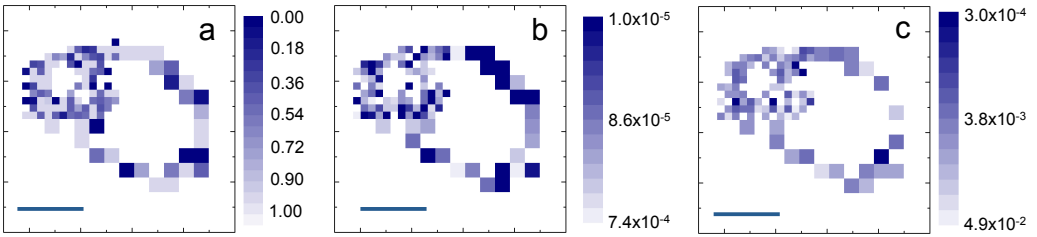

Figure 8.11: *kICS analysis of the GNSs intracellular transport (III).* P^2_{eq} (a) , D (b) and $\underline{v}$ (c) color-coded maps obtained by kICS on the same cell analyzed in Figs. 6.7 and 6.9. Scale bar=10 μm. D and $\underline{v}$ are color-coded in $\mu m^2/s$ and μm/s, respectively. In the upper left quarter of each map, a 32 pixels shift for all the 64x64 ROIs has been adopted along the x- and y- directions to increase the detail in the parameters recovery.

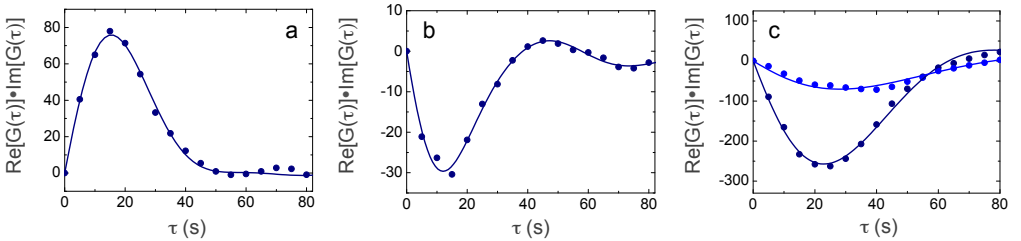

Figure 8.12: *kICS analysis of the GNSs intracellular transport (IV).* Exemplifying $Re(G(\tau)) \cdot Im(G(\tau))$ profiles are shown for three more ROIs analyzed by kICS within the cell examined in Figs. 8.9-8.11. In (a), k_x=0, k_y=-17.7 μm^{-1}; the fit of the profile to eq. (8.27) yields D=(5±1)x10^{-6} $\mu m^2/s$, $|\underline{v}|$=(3.8±0.1)x10^{-3} $\mu m/s$, α=(90° ± 5°), k_{12}=(0.032±0.001) s^{-1} and k_{21}=(0.046±0.002) s^{-1}. In (b), k_x=0, k_y=-5.9 μm^{-1}; the fit of the profile to eq. (8.27) yields D=(3.3±0.5)x10^{-4} $\mu m^2/s$, $|\underline{v}|$=(1.73±0.02)x10^{-2} $\mu m/s$, α=(84° ± 4°), k_{12}=(0.003±0.0003) s^{-1} and k_{21}=(0.013±0.001) s^{-1}. In (c), k_x=0, k_y=-8.9 μm^{-1} for the navy curve, whereas k_x=0, k_y=-11.8 μm^{-1} for the blue curve. The global fit to eq. (8.27) is shown, with shared parameters D=(2±1)x10^{-6} $\mu m^2/s$, $|\underline{v}|$=(6.8±0.5)x10^{-2} $\mu m/s$, α=(6° ± 2°), k_{12}=(0.055±0.002) s^{-1} and k_{21}=(0.061±0.002) s^{-1}. Error bars are within the size of data points.

of individual objects; (ii) contrarily to TICS and STICS, it allows quantifying the transport parameters not only in the presence of purely diffusive or active transport phenomena, but also when a more complex intermittent dynamics is present. This also allows concluding the comparison of the TICS, STICS and SPT results which was anticipated at the end of Chapter 7. On the one hand, Single Particle Tracking usually identifies short-lived phases of active transport, with a relatively high (~ 10^{-2} $\mu m/s$) drift speed $|\underline{v}|$ and with a typical duration of a few seconds (I recall that the majority of the recovered equilibrium probabilities P_2^{eq} vary between 0 and 0.2). On the other hand, as evidenced by the maps of Fig. 8.11, kICS also identifies higher equilibrium probabilities for the active transport regime, and lower values (down to ~ 10^{-4}-10^{-3} $\mu m/s$) for the drift speed.

I argue the reason of this discrepancy may lie in the temporal and spatial averages performed by fluctuation-based methods like TICS, STICS and kICS. The correlation function is averaged over the trajectory length for each particle (and over all the particles included in the region of interest): if active transport events last for a few time points, they may impart sufficient directionality to the trajectory to produce an overall super-diffusive behavior, but the resulting dynamics may be mistaken for an intermittent process with higher equilibrium probability for the active regime and

with lower modulus for the drift velocity (a similar problem has been pointed out before for the Mean-Square-Displacement analysis). This conclusion is reinforced by the fact that the effective drift speeds $|\underline{v}|^{eff}$ measured by SPT, and obtained by weighting $|\underline{v}|$ with P_2^{eq}, precisely resemble the $\sim 10^{-3}$ $\mu m/s$ speed obtained by kICS.

8.6 Effect of the 2D approximation

The typical diffusion coefficients and drift speed values recovered by TICS, STICS, SPT and kICS for the GNSs-containing cellular vesicles suggest that their motion is mostly limited to the focal plane, and that the employment of a 2D model (eqs. 8.3-8.27) suffices for the analysis of the experimental data.
A possible procedure to further demonstrate the applicability of the 2D approximation would require the simulation of the kICS correlation function describing a 3D intermittent dynamics, and the subsequent evaluation of the discrepancy between the parameter values adopted as simulation input and the parameters recovered by a fit of the simulated curves to the approximate 2D model of eqs. (8.3)-(8.27). Since no analytical expression is available for the 3D intermittent active transport, I have considered the simpler coupling of three-dimensional Brownian diffusion and uniform drift. Even though the evaluation of the impact of the 2D approximation on the transition rates k_{12} and k_{21} is prevented, this choice brings two advantages: (i) I expect that the simple $D + \underline{v}$ model provides an estimate of the largest possible error on the recovered D and $|\underline{v}|$ values; indeed, the displacement along the *z*-axis associated to the drift velocity becomes smaller and smaller as the equilibrium probability of the diffusive state (1) increases; (ii) in the absence of intermittency, the kICS correlation function can be analytically derived both in 2D (eq. 8.34) and in 3D (eq. 8.43) [292]:

$$G(\underline{k},\tau) \propto \frac{exp\left\{-\frac{\omega_0^2(k_x^2+k_y^2)}{4} - [D(k_x^2+k_y^2) - i(k_x v_x + k_y v_y)]\tau\right\} exp\left\{-\frac{-v_z^2\tau^2}{4D\tau+\omega_{0z}^2}\right\}}{\sqrt{4D\tau+\omega_{0z}^2}} \tag{8.43}$$

Specifically, I have simulated the product of the real and the imaginary parts of the 3D kICS correlation function versus the lag time, for specific values of the $\underline{k}$ vector components k_x and k_y (I have followed therefore the same procedure adopted for the analysis of the kICS experimental data). I have adopted a diffusion coefficient

$D=2x10^{-4}$ $\mu m^2/s$ and a drift speed $|\underline{v}|=2x10^{-3}$ $\mu m/s$, in order for the simulations to resemble the typical experimental conditions reported previously; once defined the direction of the drift speed in the xy-plane ($\alpha=45°$), I have varied the angle subtended by the drift velocity $\underline{v}$ and the z-axis in the broad range $\phi=20° - 160°$ (90° corresponding to a velocity $\underline{v}$ lying in the focal xy-plane). For each value of the angle ϕ, I have evaluated the discrepancy between the known D, $|\underline{v}|$ and α values set for the simulation and the estimates D_{2D}, $|\underline{v}|_{2D}$ and α_{2D} recovered from the fit of the simulated curves to the product of the real and imaginary parts of the 2D kICS correlation function (eq. 8.34).
As shown in Fig. 8.13b-c, the diffusion coefficient and the drift speed can be determined within a 10% and a 20% discrepancy, respectively. The angle is the parameter that is more significantly affected by the adoption of the 2D approximation (Fig. 8.13d). By inspecting the exemplifying simulated profiles shown in Fig. 8.13a, it is apparent that the curves simulated by the exact 3D model deviate from the corresponding 2D profile in their width more than in the position, along the lag time axis, of the peak. The drift speed, which mainly regulates the peak position of the simulated profiles, is therefore accurately recovered even under the 2D approximation; by contrast a biased estimate of the angle, which affects the width of the correlation profiles, is obtained when employing the 2D model.
I have finally investigated the effect of the same 2D approximation for higher values of the drift speed $|\underline{v}|$. I have simulated the product of the real and the imaginary parts of the kICS correlation function for 3D motion with $D=2x10^{-4}$ $\mu m^2/s$, $\alpha=45°$, $\phi=40°$ and increasing $|\underline{v}|$ up to 10^{-2} $\mu m/s$: by fitting the simulated curves to the 2D model of eq. (8.34), an overestimate of the diffusion coefficient has been obtained, while the speed has been recovered within a 10-20% discrepancy with respect to the reference value (Fig. 8.13e,f).

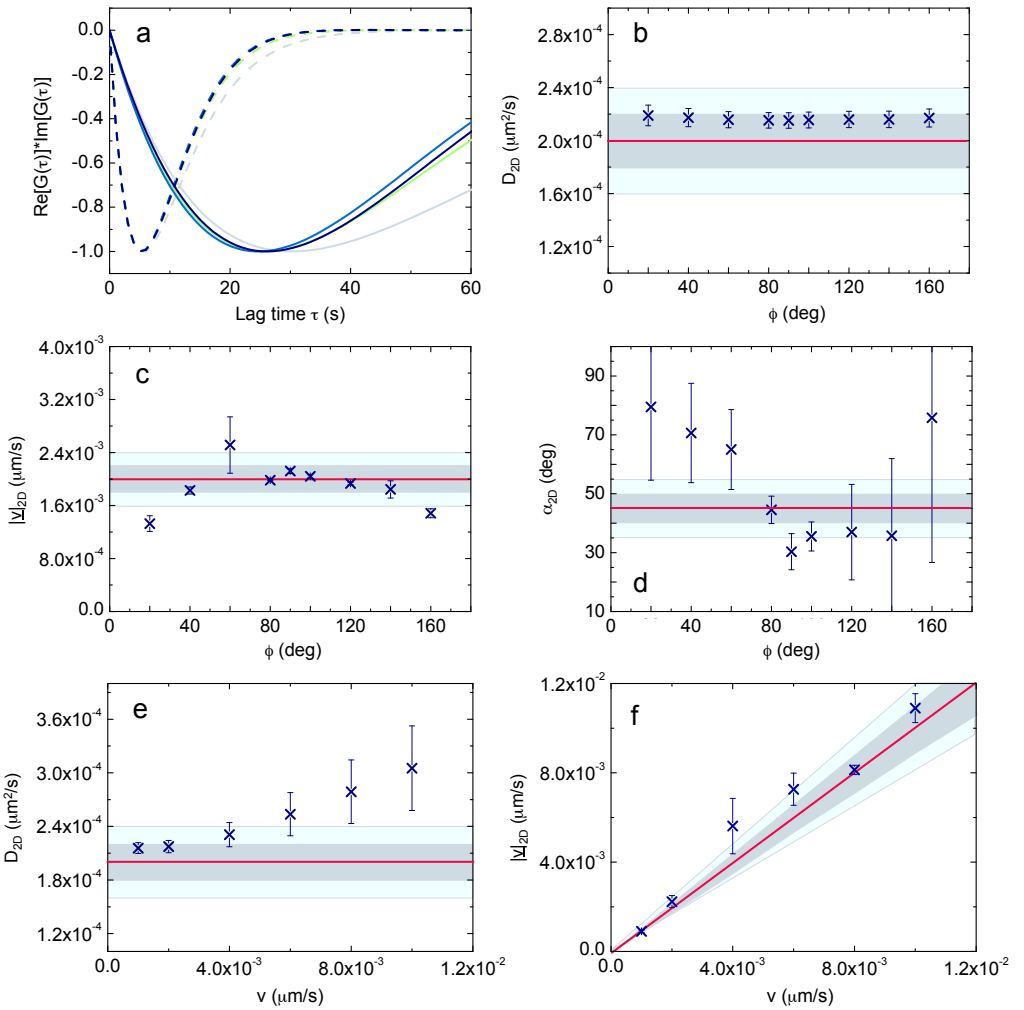

Figure 8.13: *kICS: effect of the 2D approximation on the recovery of the model parameters.* (a): $\mathrm{Re}(G(\tau)) \cdot \mathrm{Im}(G(\tau))$ profiles simulated for 3D diffusion and drift (eq. 8.43) with D=2x10^{-4} $\mu m^2/s$, $|\underline{v}|$=2x10^{-3} $\mu m/s$, α=45° and variable ϕ: ϕ=20° (grey), 60° (green) and 90° (blue). k_x=k_y=-14.8 μm^{-1} for dotted lines, k_x=k_y=-5.9 μm^{-1} for solid lines. In both the cases, the $\mathrm{Re}(G(\tau)) \cdot \mathrm{Im}(G(\tau))$ plot for 2D diffusion and drift (eq. 8.34) is reported in black for comparison. Note that the effect of a non-vanishing z-component for the drift velocity and of 3D diffusion diminishes as the lag time decreases. *the figure caption ends on the next page*

Figure 8.13: (b): estimates (mean $\pm$ standard deviation) of the diffusion coefficient obtained by fitting with the 2D model the profiles simulated for 3D diffusion and drift with variable ϕ in the range $20° - 160°$. The 10% and 20% discrepancies with respect to the simulation input value are marked by the grey and light-blue boxes, respectively. (c), (d): estimates (mean $\pm$ standard deviation) of the drift speed and of the drift angle (in c and d, respectively) obtained by fitting with the 2D model the profiles simulated for 3D diffusion and drift. ϕ varies in the range $20° - 160°$. Again the 10% and 20% discrepancies with respect to the simulation input values are marked by the grey and light-blue boxes, respectively. (e), (f): estimates (mean $\pm$ standard deviation) of the diffusion coefficient (e) and of the drift speed (f) obtained by fitting with the 2D model the profiles simulated (in k_x=k_y=-5.9 μm^{-1} and in k_x=k_y=-14.8 μm^{-1}, as in panel a) for 3D diffusion and drift with D=2x10^{-4} $\mu m^2/s$, α=45°, ϕ=40° and $|\underline{v}|$ variable in the range 10^{-3}-10^{-2} $\mu m/s$.

Conclusions

Unique specialized mechanisms have evolved in biological systems for the regulation of molecular transport both at the sub-cellular level and on the larger spatial scale of whole organs and tissues. The efficient delivery of proteins, nutrients, signaling molecules and growth regulators to their correct location within a cell, the removal of toxins from the bloodstream, blood circulation and drug-delivery events provide just a few examples of the critical role played by transport phenomena in defining the proper functioning of cells, tissues, and whole organisms. Motivated therefore by the relevance of transport phenomena in fields ranging from cell biology to immunology, and by the quest for novel methods aimed at their investigation, in this work I have adopted and extended the approach of Fluorescence Image Correlation Spectroscopy for the study of diffusive, directional and intermittent transport processes in living biological systems.

At first, I have focused on the measurement of blood flow velocities in microcirculatory vessel networks. I have developed, theorized and experimentally validated a novel image-processing method, which I have called FLICS or FLow Image Correlation Spectroscopy, capable of measuring the flow speed and direction, with sub-second temporal resolution and at the level of individual capillaries, even in the presence of a geometrically complex vessel network. To this aim, FLICS exploits a *single* raster-scanned xy-image, acquired by confocal or two-photon excitation fluorescence microscopy, and the computation of the Cross-Correlation Function (CCF) of the signal fluctuations detected in pairs of columns of the image.

The analytical derivation of the CCF explicit expression has been reported for two-dimensional uniform flow in the focal xy-plane, but also for the general case of diffusion and flow in a three-dimensional space. Then the correctness of the newly-developed theoretical framework has been verified with *in-vitro* experiments in a simple microfluidic device, and with *in-vivo* blood flow measurements in the

circulatory system of living zebrafish embryos. By demonstrating that experimental correlation functions exhibit the expected functional dependence on the image acquisition parameters and on the transport properties of the imaged flowing objects, these measurements have validated the CCF analytical expression. Additionally, the speed values recovered by FLICS have been confirmed by their comparison with the results of line-scan based (SLIC, Scanning Laser Image Correlation) measurements on the same samples.

Validation experiments have paved the way for the subsequent application of the FLICS method to blood flow measurements in the intricate murine hepatic microcirculatory system, where the blood flow speed has been characterized and mapped at the level of individual sinusoids. On the one hand, the results obtained here in healthy murine models provide the reference speed values - of the order of hundreds of microns per second - for the future comparison with the sinusoidal flow speed under pathological conditions. On the other hand, the FLICS measurements in zebrafish embryos and in the hepatic microcirculation have allowed to outline and demonstrate the advantages offered by the FLICS approach with respect to alternative state-of-the-art techniques and correlation-based analyses.
The first advantage relies in the fact that the scan path is not required to be parallel to the flow direction: starting from a single xy-image, the flow velocity can be measured in all the vessels within the imaged field of view, irrespectively of their orientation and of the geometrical complexity of the investigated circulatory network. Since a *single* xy-image suffices for FLICS, kinetic studies can also be performed in both space and time by the acquisition of xyz- and xyt- stacks, with a typical sub-second time step. Secondly, in its exploitation of image scanning along a raster pattern, FLICS enables the diffraction-limited imaging of immobile vascular cells simultaneously to the blood flow measurement; relevant morphological parameters (for example, the vessel diameter) can be monitored simultaneously to the flow speed, with the diffraction-limited spatial resolution (0.2-0.5 μm in the radial direction, 0.5-2 μm in the axial direction) of fluorescence confocal and intravital microscopy. Finally, the scan frequencies of standard commercially available scanning microscopes (10-2000 Hz) are suitable to map blood flows up to ~ 1 mm/s, avoiding the implementation of *ad-hoc* setups or of resonant scanning heads.

Applied here to the measurement of flow velocities in planar circulatory systems, FLICS will be extended in the next future to the measurement of three-dimensional velocity fields, with the discrimination all the three components of arbitrarily oriented velocity vectors; I also plan to extend Flow Image Correlation Spectroscopy to the measurement of pulsatile (arterial) flows, and to the extraction -starting from

the same raster-scanned xy-images- of relevant hemodynamic parameters other than the flow speed (for example, the hematocrit and the flow volume).

On a much smaller spatial scale, the exploitation of image correlation spectroscopy has been directed to the investigation of the complex intermittent dynamics exhibited by branched, star-shaped nanoparticles (GNSs, or Gold NanoStars) in HeLa human cancer cells. By taking advantage of the huge scattering cross-section of the employed anisotropic noble-metal nanostars, the principles of image correlation in both the direct and the reciprocal space have been applied to xyt-stacks of images acquired by live-cell time-lapse confocal microscopy in reflectance mode. Provided the light scattering form factors for GNSs internalized in cellular (endocytotic) vesicles, the presence of phase fluctuations and of coherence effects has been excluded, thereby confirming the possibility of extending the fluorescence formalism to the detection of the GNSs back-scattered radiation.

Image stacks have been initially analyzed by Temporal and Spatio-Temporal Image Correlation Spectroscopy. The presence of different transport mechanisms, spanning from pure Brownian diffusion to (sub-)ballistic super-diffusion, has been revealed on the tens-of-seconds timescale. Even more importantly, a metrics for super-diffusion has been identified in the non-linear displacement of the peak coordinates of the two-dimensional STICS correlation function at increasing lag times.
In agreement with the STICS results and with numerical simulations, the super-diffusive sub-ballistic behavior underlying the GNSs dynamics has been ascribed to a two-state intermittency between passive and active transport regimes: cellular vesicles alternate Brownian diffusion in the cytoplasm and directed ballistic displacements, presumably due to the action of molecular motors along the semi-flexible oriented filaments of the cytoskeleton. This model advantageously stems from physically meaningful parameters: namely, the diffusion coefficient and the drift velocity of GNSs-containing vesicles and the transition rates between the diffusive and the active transport regimes. Furthermore, in its compatibility with the theoretical and mathematical formalism of correlation spectroscopy, it outperforms several models of enhanced diffusion previously reported in the literature (Lévy flights, models based on time-dependent diffusion coefficients, or models derived from modifications of the generalized Langevin equation, just to mention a few).

A novel analytical theoretical framework for the investigation of intermittent-type transport phenomena has been therefore proposed for Fourier-space Image Correlation Spectroscopy (kICS). The optimal procedure for the analysis of experi-

mental data has been devised starting from simulated kICS correlation functions, and the possibility of identifying simpler (purely diffusive or ballistic) transport phenomena has been demonstrated. The same data analysis protocol has been finally adopted to derive whole-cell maps of the dynamic and kinetic parameters underlying the GNSs intracellular dynamics.
Strengthened by a Bayesian (Hidden Markov Model based) analysis of single particle tracking data, the results obtained here for the intracellular trafficking of gold nanostars will be of help in the rational design of their drug delivery and photo-thermal therapy applications.

Publications and acknowledgments

Portions of this Ph. D. thesis have been previously published in:

- **Bouzin, M.**, Sironi, L., Chirico, G., D'Alfonso, L., Inverso, D., Pallavicini, P., Collini, M. (2015)
  An Intermittent-Model Fourier-Space Analysis of the Intracellular Motion of Gold Nanostars by Scattering Image Correlation
  Biophys. J. - In press

- Sironi, L.*, **Bouzin, M.***, Inverso, D., D'Alfonso, L., Pozzi, P., Cotelli, F., Guidotti, L. G., Iannacone, M., Collini, M., Chirico, G. (2014)
  In Vivo Flow Mapping in Complex Vessel Networks by Single Image Correlation
  Sci. Rep. 4:7341
  * co-first authors

- Chirico, G., Sironi, L., **Bouzin, M.**, D'Alfonso, L., Collini, M., Ceffa, N. G., Marquezin, C. A. (2015)
  Single Image Correlation for Blood Flow Mapping in Complex Vessel Networks
  Proceedings of SPIE, Vol. 2529, 2529F

Closely related publications and conference presentations include:

- Sironi, L., Borzenkov, M., Collini, M., D'Alfonso, L., **Bouzin, M.**, Chirico, G. (2015)
  Interactions of Gold Nanostars with Cells
  Chapter 4 in *Gold Nanostars: Synthesis, Properties and Biomedical Application*
  Springer Briefs in Materials, Springer International Publishing

- Pozzi, P., Sironi, L., D'Alfonso, L., **Bouzin, M.**, Collini, M., Chirico, G., Pallavicini, P., Cotelli, F., Foglia, E. A. (2014)
Electron Multiplying Charge-Coupled Device-Based Fluorescence Cross-Correlation Spectroscopy for Blood Velocimetry on Zebrafish Embryos
J. Biomed. Opt. 19(6):067007

- Pozzi, P., Rossetti, L., Sironi, L., Freddi, S., D'Alfonso, L., Caccia, M., **Bouzin, M.**, Collini, M., Chirico, G. (2013)
Structured Illuminations Fluorescence Correlation Spectroscopy for Velocimetry in Zebrafish Embryos
Proceedings of SPIE, Vol. 8580, 85899V

- Collini, M., **Bouzin, M.**, Sironi, L., D'Alfonso, L., Pallavicini, P., Chirico, G. (2015)
Reflection Image Correlation Methods Applied to Gold Nanostars Slow Motions in Living Cells
Focus on Microscopy 2015, Gottingen, Germany
International Workshop on Imaging 2015, Varenna, Italy

- Marquezin, C. A., Ceffa, N. G., **Bouzin, M.**, Collini, M., Chirico, G. (2015)
Study of Complex Flow Regimes in Micro-Channels via Image Cross-Correlation microscopy
10^{th} European Biophysics Congress (EBSA), Dresden, Germany

- **Bouzin, M.,** Pozzi, P., Sironi, L., D'Alfonso, L., Collini, M., Chirico, G., Pallavicini, P. (2014)
Dynamics of Gold Nanostars in Cells by Reflection Image Correlation Methods
SIBPA 2014, XXII Conference of the Italian Biophysical Society, Palermo, Italy

- **Bouzin, M.**, D'Alfonso, L., Sironi, L., Chirico, G., Collini, M. (2014)
Fluorescence Cross-Correlation for In-Vivo Hemodynamics Measurements
School of Photonics 2014, Cortona, Italy

- **Bouzin, M.**, Collini, M., Pozzi, P., Sironi, L., D'Alfonso, L., Chirico, G., Bassi, A. (2013)
Blood Fluxes Studies in Zebrafish Embryos by Cross-Correlation Spectroscopy
FisMat 2013, Milano, Italy

I finally acknowledge the precious help of the research groups actively collaborating with the Biophotonics and Biophysics group of Universitá degli Studi di Milano-Bicocca. I especially thank Prof. L. G. Guidotti, Dr. Matteo Iannacone and Dr. Donato Inverso (Division of Immunology, Transplantation and Infectious Diseases, IRCCS San Raffaele Scientific Institute) for providing access to the murine models and to the imaging facility where all the experiments described in Chapter 4 were performed. I am also particularly grateful to Prof. Piersandro Pallavicini (General Chemistry Department, Universitá degli Studi di Pavia) for the synthesis of gold nanostars, to Prof. Franco Cotelli and Dr. Efrem Foglia (Life Sciences Department, Universitá degli Studi di Milano) for providing us with zebrafish embryos, and to Prof. Edoardo Milotti (Physics Department, Univesitá degli Studi di Trieste) for the useful discussions on Bayesian methods.

Bibliography

[1] Magde, D., Elson, E. L., Webb, W. W. (1972) *Thermodynamic fluctuations in a reacting system - measurement by fluorescence correlation spectroscopy*, Phys. Rev. Lett. 29:705-708

[2] Haustein, E., Schwille, P. (2004) *Single-molecule spectroscopic methods*, Curr. Opin. Struct. Biol. 14:531-540

[3] Magde, D., Elson, E. L., Webb, W. W. (1974) *Fluorescence correlation spectroscopy. II. An experimental realization*, Biopolymers 13:29-61

[4] Ehrenber, M., Rigler, R. (1974) *Rotational Brownian-motion and fluorescence intensity fluctuation*, Chem. Phys. 4:390-401

[5] Tsay, J. M., Doose, S., Weiss, S. (2006) *Rotational and translational diffusion of peptide-coated Cd-Se/CdS/ZNS nanorods studied by fluorescence correlation spectroscopy*, J. Am. Chem. Soc. 128:1639-1647

[6] Magde, D., Elson, E. L., Webb, W. W. (1978) *Fluorescence correlation spectroscopy. III. Uniform translation and laminar flow*, Biopolymers 17:361-376

[7] Gosch, M., Blom, H., Holm, J., Heino T., Rigler, R. (2000) *Hydrodynamic flow profiling in microchannel structures by single molecule fluorescence correlation spectroscopy*, Anal. Chem. 72:3260-3265

[8] Michelman-Ribeiro, A., Mazza, D., Rosales, T., Stasevich, T., Boukari, H., Rishi, V., Vinson, C., Knutson, J. R., McNally, J. C. (2009) *Direct measurement of association and dissociation rates of DNA binding in live cells by fluorescence correlation spectroscopy*, Biophys. J. 97:337-346

[9] Widengren, J., Metz, U., Rigler, R. (1995) *Fluorescence correlation spectroscopy of triplet states in solution: a theoretical and experimental study*, J. Phys. Chem. 99:13368-13379

[10] Widengren, J., Rigler, R. (1996) *Mechanisms of photobleaching investigated by fluorescence correlation spectroscopy*, Bioimaging 4:149-157

[11] Elson, E. L. (2011) *Fluorescence correlation spectroscopy: past, present, future*, Biophys. J. 101:2855-2870

[12] Schwille, P. (2001) *Fluorescence correlation spectroscopy and its potential for intracellular applications*, Cell. Biochem. Biophys. 34:383-408

[13] Kubo, R. (1966) *Fluctuation-dissipation theorem*, Rep. Prog. Phys. 29:255-284

[14] Chiantia, S., Ries, J., Schwille, P. (2009) *Fluorescence correlation spectroscopy in membrane structure elucidation*, Biochim. Biophys. Acta 1788:225-233

[15] Haustein, E., Schwille, P. (2002) *Ultrasensitive investigations of biological systems by fluorescence correlation spectroscopy*, Methods 29:153-166

[16] Saffarian, S., Elson, E. L. (2002) *Statistical analysis of fluorescence correlation spectroscopy: the standard deviation and bias*, Biophys. J. 84:2030-2042

[17] Krichevsky, O., Bonnet, G. (2002) *Fluorescence correlation spectroscopy: the technique and its applications*, Rep. Prog. Phys. 65:251-297

[18] Rigler, R., Mets, U., Widengren, J., Kask, P. (1993) *Fluorescence correlation spectroscopy with high count rate and low background: analysis of translational diffusion*, Eur. Biophys. J. 22:169-175

[19] Haustein, E., Schwille, P. (2007) *Fluorescence correlation spectroscopy: novel variations of an established technique*, Annu. Rev. Biophys. Biomol. Struct. 36:151-169

[20] Berland, K. M., So, P. T. C., Gratton, E. (1995) *Two-photon fluorescence correlation spectroscopy: method and application to the intracellular environment*, Biophys. J. 68:694-701

[21] Schwille, P., Haupts, U., Maiti, S., Webb, W. W. (1999) *Molecular dynamics in living cells observed by fluorescence correlation spectroscopy with one- and two-photon excitation*, Biophys. J. 77:2251-2265

[22] He, H., Marguet, D. (2011) *Detecting nanodomains in living cell membrane by fluorescence correlation spectroscopy*, Annu. Rev. Phys. Chem. 62:417-436

[23] Meseth, U., Wohland, T., Rigler, R., Vogel, H. (1999) *Resolution of fluorescence correlation measurements*, Biophys. J. 76:1619-1631

[24] Shi, X., Teo, L. S., Pan, X., Chong, S., Kraut, R., Korzh, V., Wohland, T. (2009) *Probing events with single molecule sensitivity in zebrafish and drosophila embryos by fluorescence correlation spectroscopy*, Dev. Dynam. 238:3156-3167

[25] Brister, P. C., Kuricheti, K. K., Buschmann, V., Weston, K. D. (2005) *Fluorescence correlation spectroscopy for flow rate imaging and monitoring: optimization, limitations and artifacts*, Lab Chip 5:785-791

[26] Collini, M., D'Alfonso, L., Caccia, M., Sironi, L., Panzica, M., Chirico, G., Rivolta, I., Lettiero, B., Miserocchi, G. (2011) *In-vitro - in-vivo fluctuation spectroscopies*. Chapter 10 In: A. Diaspro, *Optical Fluorescence Microscopy: From the Spectral to the Nano Dimension*, Springer-Verlag Berlin Heidelberg

[27] Kinjo, M., Rigler, R. (1995) *Ultrasensitive hybridization analysis using fluorescence correlation spectroscopy*, Nucleic Acids Res. 23(10):1795-1799

[28] Schwille, P., Oehlenschlager, F., Walter, N. G. (1996) *Quantitative hybridization kinetics of DNA probes to RNA in solution followed by diffusional fluorescence correlation analysis*, Biochem. 35:10182-10193

[29] Schwille, P., Meyer-Almes, F., Rigler, R. (1997) *Dual-color fluorescence cross-correlation spectroscopy for multicomponent diffusional analysis in solution*, Biophys. J. 72:1878-1886

[30] Bacia, K., Schwille, P. (2003) *A dynamic view of cellular processes by in vivo fluorescence auto- and cross-correlation spectroscopy*, Methods 29:74-85

[31] Schwille, P., Bieschke, J., Oehlenschlager, F. (1997) *Kinetic investigations by fluorescence correlation spectroscopy: the analytical and diagnostic potential of diffusion studies*, Biophys. Chem. 66:211-228

[32] Arbour, T. J., Enderlein, J. (2010) *Application of dual-focus fluorescence correlation spectroscopy to microfluidic flow-velocity measurements*, Lab Chip 10:1286-1292

[33] Brinkmeier, M., Dorre, K., Stephan, J., Eigen, M. (1999) *Two-beam cross-correlation: a method to characterize transport phenomena in micrometer-sized structures*, Anal. Chem. 71:609-616

[34] Dittrich, P. S., Schwille, P. (2002) *Spatial two-photon fluorescence cross-correlation spectroscopy for controlling molecular transport in microfluidic structures*, Anal. Chem. 74:4472-4479

[35] Pozzi, P., Sironi, L., D'Alfonso, L., Bouzin, M., Collini, M., Chirico, G., Pallavicini, P., Cotelli, F., Foglia, E. A. (2014) *Electron multiplying charge-coupled device-based fluorescence cross-correlation spectroscopy for blood velocimetry on zebrafish embryos*, J. Biomed. Opt. 19(6):067007

[36] Petrasek, Z., Schwille, P. (2009) *Fluctuations as a source of information in fluorescence microscopy*, J. R. Soc. Interface 6:S15-S25

[37] Digman, M. A., Gratton, E. (2011) *Lessons in fluctuation correlation spectroscopy*, Annu. Rev. Phys. Chem. 62:645-668

[38] Petrasek, Z., Ries, J., Schwille, P. (2010) *Scanning FCS for the characterization of protein dynamics in live cells*, Methods Enzymol. 472:317-343

[39] Berland, K. M., So, P. T. C., Chen, Y., Mantulin, W. W., Gratton, E. (1996) *Scanning two-photon fluctuation correlation spectroscopy: particle counting measurements for detection of molecular aggregation*, Biophys. J. 71:410-420

[40] Ruan, Q., Cheng, M. A., Levi, M., Gratton, E., Mantulin, W. W. (2004) *Spatial-temporal studies of membrane dynamics: scanning fluorescence correlation spectroscopy (SFCS)*, Biophys. J. 87:1260-1267

[41] Petrasek, Z., Schwille, P. (2008) *Photobleaching in two-photon scanning fluorescence correlation spectroscopy*, Chem. Phys. Chem. 9:147-158

[42] Wiseman, P. W. (2013) *Image correlation spectroscopy: mapping correlations in space, time, and reciprocal space*, Methods Enzymol. 518:245-267

[43] Bag, N., Wohland, T. (2014) *Imaging fluorescence fluctuation spectroscopy: new tools for quantitative bioimaging*, Annu. Rev. Phys. Chem. 65:225-248

[44] Singh, A. P., Wohland, T. (2014) *Applications of imaging fluorescence correlation spectroscopy*, Curr. Opin. Struct. Biol. 20:29-35

[45] Wiseman, P. W., Brown, C. M., Webb, D. J., Hebert, B., Johnson, N. L., Squier, J. A., Ellisman, M. H., Horwitz, A. F. (2004) *Spatial mapping of integrin interactions and dynamics during cell migration by Image Correlation Microscopy*, J. Cell Sci. 117:5521-5534

[46] Wiseman, P. W., Squier, J. A.,Ellisman, M. H., Wilson, K. R. (2000) *Two-photon image correlation spectroscopy and image cross-correlation spectroscopy*, J. Microsc. 200:14-25

[47] Kolin, D. L., Costantino, S., Wiseman, P. W. (2006) *Sampling effects, noise, and photobleaching in temporal image correlation spectroscopy*, Biophys. J. 90:628-639

[48] Hebert, B., Costantino, S., Wiseman, P. W. (2005) *Spatiotemporal Image Correlation Spectroscopy (STICS) theory, verification, and application to protein velocity mapping in living CHO cells*, Biophys. J. 88:3601-3614

[49] Petersen, N. O., Hoddelius, P. L., Wiseman, P. W., Seger, O., Magnusson, K. (1993) *Quantitation of membrane receptor distribution by image correlation spectroscopy: concept and application*, Biophys. J. 65:1135-1146

[50] Digman, M. A., Brown, C. M., Sengupta, P., Wiseman, P. W., Horwitz, A. R., Gratton, E. (2005) *Measuring fast dynamics in solutions and cells with a laser scanning microscope*, Biophys. J. 89:1317-1327

[51] Digman, M. A., Sengupta, P., Wiseman, P. W., Brown, C. M., Horwitz, A. R., Gratton, E. (2005) *Fluctuation correlation spectroscopy with a laser-scanning microscope: exploiting the hidden time structure*, Biophys. J.: Biophys. Lett. L33-L36

[52] Brown, C. M., Dalal, R. B., Hebert, B., Digman, M. A., Horwitz, A. R., Gratton, E. (2005) *Raster image correlation spectroscopy (RICS) for measuring fast protein dynamics and concentrations with a commercial laser scanning confocal microscope*, J. Microsc. 229:78-91

[53] Rossow, M. J., Sasaki, J. M., Digman, M. A., Gratton, E. (2010) *Raster image correlation spectroscopy in live cells*, Nat. Protoc. 5(11):1761-1774

[54] Digman, M. A., Wiseman, P. W., Horwitz, A. R., Gratton, E. (2009) *Detecting protein complexes in living cells from laser scanning confocal image sequences by the cross correlation raster image spectroscopy method*, Biophys. J. 96:707-716

[55] Coppola, S., Pozzi, D., Candeloro De Sanctis, S., Digman, M. A., Gratton, E., Caracciolo, G. (2013) *Quantitative measurement of intracellular transport of nanocarriers by spatio-temporal image correlation spectroscopy*, Methods Appl. Fluoresc. 1:015005

[56] Potvin-Trottier, L., Lingfeng, C., Horwitz, A. R., Wiseman, P. W. (2013) *A nuspace for image correlation spectroscopy: characterization and application to measure protein transport in live cells*, New J. Phys 15:085006

[57] Rossow, M. J., Mantulin, W. W., Gratton, E. (2010) *Scanning laser image correlation for measurement of flow*, J. Biomed. Opt. 15(2):026003

[58] Digman, M. A., Gratton, E. (209) *Imaging barriers to diffusion by pair correlation functions*, Biophys. J. 97:665-673

[59] Stone, H. A., Stroock, A. D., Ajdari, A. (2004) *Engineering flows in small devices: microfluidics toward a lab-on-a-chip*, Annu. Rev. Fluid Mech. 36:381-411

[60] Kumar, C. S. S. R. (Editor) (2006) *Microfluidic devices in nanotechnology: applications*, Wiley

[61] Minteer, S. D. (Editor) (2006) *Microfluidic techniques: reviews and protocols*, Methods Mol. Biol.

[62] Weigl, B. H., Bardell, R. L., Cabrera, C. R. (2003) *Lab-on-a-chip for drug development*, Adv. Drug Delivery Rev. 55:349-377

[63] Dittrich, P. S., Schwille, P. (2003) *An integrated microfluidic system for reaction, high-sensitivity detection, and sorting of florescent cells and particles*, Anal. Chem. 75:5767-5774

[64] Schulte., T. H., Bardell, R. L., Weigl, B. H. (2002) *Microfluidic technologies in clinical diagnostics*, Clin. Chim. Acta 321 (1-2):1-10

[65] Tuma, R. F., Duran, W. N., Ley, K. (2002) *Microcirculation. Handbook of Physiology*, Second Edition, Elsevier Science

[66] Carmeliet, P. (2003) *Angiogenesis in health and disease*, Nat. Med. 9:653-660

[67] Kamoun, W. S., Chae, S., Lacorre, D. A., Tyrell, J. A., Mitre, M., Gillissen, M. A., Fukumura, D., Jain, R. K. J., Munn, L. L. (2010) *Simultaneous measurement of RBC velocity, flux, hematocrit and shear rate in vascular networks*, Nat. Meth. 7(8):655-660

[68] Kim, T. N., Goodwill, P. W., Chen, Y., Conolly, S. M., Schaffer, C. B., Liepmann, D., Wang, R. A. (2012) *Line-scanning particle image velocimetry: an optical approach for quantifying a wide range of blood flow speeds in live animals*, PLoS One. 7(6):e38590

[69] Sironi, L.*, Bouzin, M.*, Inverso, D., D'Alfonso, L., Pozzi, P., Cotelli, F., Guidotti, L. G., Iannacone, M., Collini, M., Chirico, G. (2014) *In vivo flow mapping in complex vessel networks by single image correlation*, Sci. Rep. 4:7341

[70] Chirico, G., Sironi, L., Bouzin, M., D'Alfonso, L., Collini, M., Ceffa, N. G., Marquezin, C. A. (2015) *Single Image Correlation for Blood Flow Mapping in Complex Vessel Networks*, Proceedings of SPIE, Vol. 2529, 2529F

[71] Frerichs, K. U., Feuerstein, G. Z. (1990) *Laser-Doppler Flowmetry: a review of its application for measuring cerebral and spinal cord blood flow*, Mol. Chem. Neuropathol. 12(1):55-70

[72] Shih, A. Y., Driscoll, J. D., Drew, P. J., Nishimura, N., Schaffer, C. B., Kleinfeld, D. (2012) *Two-photon microscopy as a tool to study blood flow and neurovascular coupling in the rodent brain*, J. Cerebr. Blood F. Met. 32:1277-1309

[73] Briers, J. D. (2001) *Laser Doppler, speckle and related techniques for blood perfusion mapping and imaging*, Physiol. Meas. 22:R35-R66

[74] Shepherd, A. P., Oberg, P. A. (1990) *Laser-Doppler blood flowmetry*, Hingham, MA:Kluwer

[75] Obeid, A. N., Barnett, N. J., Dougherty, G., Ward, G. (1990) *A critical review of laser Doppler flowmetry*, J. Med. Eng. Technol. 14 178-181

[76] Starukhin, P., Ulyanovm, S., Galanzha, E., Tuchin, V. (2000) *Blood-flow measurements with a small number of scattering events*, Appl. Opt. 39:2823-30

[77] Lauritzen, M., Fabricius, M. (1995) *Real time laser-Doppler perfusion imaging of cortical spreading depression in rat neocortex*, Neuroreport 6(9):1271-1273

[78] Chen, Z., Zhao, Y., Srinivas, S. M., Nelson, J. S., Prakash, N., Frostig, R. D. (1999) *Optical Doppler Tomography*, IEEE J. Sel. Top. Quantum Electron. 5(4):1134-1142

[79] Huang, D., Swanson, E. A., Lin, C., Schuman, J. S., Stinson, W. G., Chang, W., Hee, M. R., Flotte, T., Gregory, K., Puliafito, C. A., Fujimoto, J. G. (1991) *Optical Coherence Tomography*, Science 254:1178-1180

[80] Wang, L. Xu, W., Bachman, M., Li, G. P., Chen, Z. (2004) *Phase-resolved optical Doppler tomography for imaging flow dynamics in microfluidic channels*, Appl. Phys. Lett. 85:1855

[81] Chen, Z., Milner, T. E., Srinivas, S., Wang, X., Malekafzali, A., van Gemert, M. J. C., Nelson, J. S. (1997) *Noninvasive imaging of in vivo blood flow velocity using optical Doppler tomography*, Opt. Expr. 22(14):1119-1121

[82] Mace', E., Montaldo, G., Cohen, I., Baulac, M., Fink, M., Tanter, M. (2011) *Functional ultrasound imaging of the brain*, Nat. Meth. 8(8):662-664

[83] Tabrizchi, R., Pugsley, M. K. (2000) *Methods of blood flow measurement in the arterial circulatory system*, J. Pharmacol. Toxicol. Meth. 44:375-384

[84] Loossa, B., Lhuillierb, C., Jeanneau, H. (2002) *Numerical simulation of transit-time ultrasonic flowmeters: uncertainties due to flow profile and fluid turbulence*, Ultrasonics 40(9):1009-1015

[85] Fercher, A: F., Briers, J. D. (1981) *Flow visualization by means of single-exposure speckle photography*, Opt. Commun. 37:326-330

[86] Briers, D., Duncan, D. D., Hirst, E., Kirkpatick, S. J., Larsson, M., Steenbergen, W., Stromberg, T., Thompson, O. B. (2013) *Laser speckle contrast imaging: theoretical and practical limitations*, J. Biomed. Opt. 18(6):066018

[87] Briers, J. D., Webster, S. (1996) *Laser speckle contrast analysis (LASCA): a nonscanning, full-field technique for monitoring capillary blood flow*, J. Biomed. Opt.1:174-179

[88] Dunn, A. K., Bolay, H., Moskovitz, M. A., Boas, D. A. (2001) *Dynamic imaging of cerebral blood flow using laser speckle*, J. Cereb. Blood Flow Metab. 21:195-201

[89] Duncan, D. D., Kirkpatrick, S. J. (2008) *Can laser speckle flowmetry be made a quantitative tool?*, J. Opt. Soc. Am. A Opt. Image Sci. Vis. 25:2088-2094

[90] Koutsiaris, A. G., Mathioulakis, D. S., Tsangaris, S. (1999) *Microscope PIV for velocity-field measurement of particle suspensions flowing inside glass capillaries*, Meas. Sci. Technol. 10:1037-1046

[91] Lindken, R., Rossi, M., Groβe, S., Westerweel, J. (2009) *Micro-Particle Image Velocimetry (μPIV): recent developments, applications, and guidelines*, Lab Chip 9:2551-2567

[92] Wereley, S. T., Meinhart, C. D. (2010) *Recent advances in micro-Particle Image Velocimetry*, Annu. Rev. Fluid Mech. 42:557-76

[93] Helmchen, F., Kleinfeld, D. (2008) *Blood flow and glial cell function with two-photon laser-scanning microscopy*, Chapter 10 in Meth. Enzymol. 444:231-254

[94] Drew, P. J., Blinder, P., Cauwernberghs, G., Shih, A. Y., Kleinfeld, D. (2009) *Rapid determination of particle velocity from space-time images using the Radon transform*, J. Comput. Neurosci. 29(1-2):5-11

[95] Adrian, R. J. (2005) *Twenty years of particle image velocimetry*, Exp. Fluids 39:159-169

[96] Raffel, M., Willert, C., Wereley, S. T., Kompenhans, J. (2007) *Particle Image Velocimetry: a practical guide*, Second edition, Springer

[97] Santiago, J. G., werely, S. T., Meinhart, C. D., Beebe, D. J., Adrian, R. J. (1998) *A micro particle image velocimetry system*, Exp. Fluids 25:316-19

[98] Qian, H., Sheetz, M. P., Elson, E. L. (1991) *Single particle tracking: analysis of diffusion and flow in two-dimensional systems*, Biophys. J. 60:910-921

[99] Wu, B., Chen, Y., Müller, J. D. (2008) *Fluorescence correlation spectroscopy of finite-sized particles*, Biophys. J. 94:2800-2808

[100] Lieschke, G. J., Currie. P. D. (2007) *Animal models of human disease: zebrafish swim into view*, Nat. Rev. 8:353-367

[101] Dooley, K., Zon, L. I. (2000) *Zebrafish: a model system for the study oh human disease*, Curr. Opin. Genet. Dev. 10.252-256

[102] Yoder, J. A., Nielsen, M. E., Amemiya, C. T., Litman, G. W. (2002) *Zebrafish as an immunological model system*, Microb. Infect. 4:1469-1478

[103] Feitsma, H., Cuppen, E. (2008) *Zebrafish as a cancer model*, Mol. Cancer Res. 6(5):685-694

[104] Chico, T. J. A., Ingham, P. W., Crossman, D. C. (2008) *Modeling cardiovascular disease in the zebrafish*, Trends Cardiovasc. Med. 18(4):150-155

[105] Gore, A. V., Monzo, K., Cha, Y. R., Pan, W., Weinstein, B. M. (2012) *Vascular development in the zebrafish*, Cold Spring Harb. Perspect. Med. 2:a006684

[106] Isogai, S., Horiguchi, M., Weinstein, B. M. (2001) *The vascular anatomy of the developing zebrafish: an atlas of embryonic and early larval development*, Dev. Biol. 230:278-301

[107] Higgins, J. M., Eddington, D. T., Bhatia, S. N., Mahadevan, L. (2009) *Statistical dynamics of flowing red blood cells by morphological image processing*, PLoS Comp. Biol. 5(2):e1000288

[108] Denvir, M. A., Tucker, C. S., Mullins, J. J. (2008) *Systolic and diastolic ventricular function in zebrafish embryos: Influence of norepenephrine, MS-222 and temperature*, BMC Biotechnol. 8:21

[109] Malone, M. H., Sciaky, N., Stalheim, L., Hahn, K. M., Linney, E., Johnson, G. L. (2007) *Laser-scanning velocimetry: a confocal microscopy method for quantitative measurement of cardiovascular performance in zebrafish embryos and larvae*, BMC Biotechnol. 7:40

[110] Bruus, H. (2008) *Theoretical Microfluidics*, pp. 48-51, 123-136, Oxford University Press, United Kingdom

[111] Costantino, D., Comeau, J. W. D., Kolin, D. L., Wiseman, P. W. (2005) *Accuracy and dynamic range of spatial image correlation and cross-correlation spectroscopy*, Biophys. J. 89:1251-1260

[112] Hwang, S. (2011) *Microcirculation of the liver*. Chapter 2 In: Madoff, D. C. *et al.* (eds.), *Venous embolization of the liver*, Springer-Verlag London

[113] McCuskey, R. S. (2008) *The hepatic microvascular system in health and its response to toxicants*, Anat. Rec. 291:661-671

[114] Vollmar, B., Menger, M. D.(2009) *The hepatic microcirculation: mechanistic contributions and therapeutic targets in liver injury and repair*, Physiol. Rev. 89:1269-1339

[115] Braet, F., Wisse, E. (2002) *Structural and functional aspects of liver sinusoidal endothelial cell fenestrae: a review*, Comp. Hepatol. 1:1-17

[116] Crispe, I. N. (2003) *Hepatic T cells and liver tolerance*, Nat. Rev. Immunol. 3:51-62

[117] Guidotti, L. G., Inverso, I., Sironi, L., Di Lucia, P., Fioravanti, J., Ganzer, L., Fiocchi, A., Vacca, M., Aiolfi, R., Sammicheli, R., Mainetti, M., Cataudella, T., Raimondi, A., Gonzales-Asegionolaza, G., Protzer, U., Ruggeri, Z. M., Chisari, F. V., Isogawa, M., Sitia, G., Iannacone, M. (2015) *Immunosurveillance of the liver by intravascular effector $CD8^+$ T cells*, Cell 161:486-500

[118] Zuxing, K., Madoff, D. C. (2008) *Liver anatomy: microcirculation of the liver*, Semin. Intervent. Radiol. 25:77-85

[119] Wisse, E., de Zanger, R. B., Charels, K., van der Smissen, P., McCuskey, R. S. (1985) *The liver sieve: considerations concerning the structure and function of endothelial fenestrae, the sinusoidal wall and the space of Disse*, Hepatology 5:683-692

[120] Burkel, W. E. (1970) *The fine structure of the terminal branches of the hepatic arterial system of the rat*, Anat. Rec. 167:329-349

[121] Menger, M. D., Marzi, I., Messmer, K. (1991) *In vivo fluorescence microscopy for quantitative analysis of the hepatic microcirculation in hamsters and rats*, Eur. Surg. Res. 23:158-169

[122] Yamamoto, K., Sherman, I., Phillips, M. J., Fisher, M. M. (1985) *Three-dimensional observations of the hepatic arterial terminations in rat, hamster and human liver by scanning electron microscopy of microvascular casts*, Hepatology 5:452-456

[123] Kardon, R. H., Kessel, R. G. (1980) *Three-dimensional organization of the hepatic microcirculation in the rodent as observed by scanning electron microscopy of corrosion casts*, Gastroenterology 79:72-81

[124] Cabrera, M., frevert, U. (2012) *Novel in vivo imaging techniques for the liver microvasculature*, Intravital 1(2):107-114

[125] Young, B., Lowe, J. S., Stevens, A., Heath, J. W. (2006) *Wheater's functional histology: a text and colour atlas*. 4^{th} Ed. Ofxord, UK: Churchill Livingstone. 288-301

[126] Malarkey, D. E., Johnson, K., Ryan, L., Boorman, G., Maronpot, R. R. (2005) *New insights into functional aspects of liver morphology*, Toxicol. Pathol. 33:27-34

[127] Oda, M., Yokomori, H., Han, J. Y. (2003) *Regulatory mechanisms of hepatic microcirculation*, Clin. Hemorheol. Microcirc. 29:167-182

[128] McCuskey, R. S. (2000) *Morphological mechanisms for regulating blood flow through hepatic sinusoids*, Liver 20:3-7

[129] Nakata, K., Leong, G. F., Brauer, R. W. (1961) *Direct measurement of blood pressures in minute vessels of the liver*, Am. J. Physiol. 199:1181-1188

[130] Bouwens, L., De Bleser, P., Vanderkerken, K., Geerts, B., Wisse, E. (1992) *Liver cell heterogeneity: functions of non-parenchymal cells*, Enzyme 46(1-3):155-168

[131] Bilzer, M., Roggel, F., Gerbes, A. L. (2006) *Role of Kupffer cells in host defense and liver disease*, Liver Int. 26(10):1175-1186

[132] Friedman, S. L. (2008) *Hepatic stellate cells: protean, multifunctional, and enigmatic cells of the liver*, Physiol. Rev. 88(1):125-172

[133] Nakatani, K., Kaneda, K., Seki, S., Nakajima, Y. (2004) *Pit cells as liver-associated natural killer cells: morphology and function*, Med. Electron Microsc. 37:29-36

[134] Warren, A., Le Couteur, D. G., Fraser, R., Bowen, D. G., McGaughan, G. W., Bertolino, P. (2006) *T lymphocytes interact with hepatocytes through fenestrations in murine liver sinusoidal endothelial cells*, Hepatology 44(5):1182-1190

[135] Racanelli, V., Rehermann, B. (2006) *The liver as an immunological organ*, Hepatology 43(2):S54-S62

[136] Guidotti, G., Chisari, F. V. (2006) *Immunobiology and pathogenesis of viral hepatitis*, Annu. Rev. Pathol. 1:23-61

[137] Von Andrian, U. H., Mackay, C. R. (2000) *T-cell function and migration. Two sides of the same coin*, N. Engl. J. Med. 343:1020-1034

[138] Mueller, S. N. (2013) *Effector T-cell responses in non-lymphoid tissues: insights from in vivo imaging*, Immunol. Cell. Biol. 91:290-296

[139] Caccia, M., Sironi, L., Collini, M., Chirico, G., Zanoni, I., Granucci, F. (2008) *Image filtering for two-photon deep imaging of lymphnodes*, Eur. Biophys. J. 37(6):979-987

[140] Lieber, C. M. (2003) *Nanoscale science and technology: building a big future from small things*, MRS Bulletin 28(7):486-491

[141] Kalinin, S. V., Borisevich, A., Fong, D. (2012) *Beyond condensed matter physics on the nanoscale: the role of ionic and electrochemical phenomena in the physical functionalities of oxide materials*, ACS Nano 6(12):10423-10437

[142] Link, S., El-Sayed, M. A. (2000) *Shape and size dependence of radiative, non-radiative and photothermal properties gold nanocrystals*, Int. Rev. Phys. Chem. 19(3):409-453

[143] Rao, C. N. R., Cheetham, A. K. (2001) *Science and technology of nanomaterials: current status and future prospects*, J. Mater. Chem. 11:2887-2894

[144] Ferrari, M. (2005) *Cancer nanotechnology: opportunities and challenges*, Nat. Rev. 5:161-171

[145] Sanhai, W. R., Sakamoto, J. H., Canady, R., Ferrari, M. (2008) *Seven challenges for nanomedicine*, Nat. Nanotechnol. 3:242-244

[146] Alivisatos, A. P. (1996) *Perspectives on the physical chemistry of semiconductor nanocrystals*, J. Phys. Chem. 100:13226-13239

[147] Schmid, G. (2004) *Nanoparticles: from theory to application*, Wiley-VCH

[148] Davis, S. S. (1997) *Biomedical applications of nanotechnology - Implications for drug targeting and gene therapy*, Trends Biotechnol. 15(6):217-224

[149] Emerich, D. F., Thanos, C. G. (2005) *Nanotechnology and medicine*, Expert Opin. Biol. Ther. 3(4):665-663

[150] Vo-Dinh, T. (2007) *Nanotechnology in biology and medicine: methods, devices, and applications*, CRC Press

[151] Huang, X., Neretina, S., El-Sayed, M. A. (2009) *Gold nanorods: from synthesis and properties to biological and biomedical applications*, Adv. Mater. 21:1-31

[152] Sokolov, K., Follen, M., Aaron, J., Pavlova, I., Malpica, A., Lotan, R., Richards-Kortum, R. (2003) *Real-time vital optical imaging of precancer using anti-epidermal growth factor receptor antibodies conjugated to gold nanoparticles*, Cancer Res. 63:1999-2004

[153] Takahashi, H., Niidome, Y., Yamada, S. (2005) *Controlled release of plasmid DNA from gold nanorods induced by pulsed near-infrared light*, Chem. Commun. (Camb). 7(17):2247-2249

[154] Lewinski, N., Colvin, V., Drezek, R. (2008) *Cytotoxicity of nanoparticles*, Small 4:26-49

[155] Burda, C., Chen, X., Narayanan, R., El-Sayed, M. A. (2005) *Chemistry and properties of nanocrystals of different shapes*, Chem. Rev. 195(4):1025-102

[156] Katz, E., Willner, I. (2004) *Integrated nanoparticle-biomolecule hybrid systems: synthesis, properties, and applications*, Angew. Chem. Int. Ed. 43(45):6042-6118

[157] Eustis, S., El-Sayed, M. A. (2005) *Why gold nanoparticles are more precious than pretty gold: Noble metal surface plasmon resonance and its enhancement of the radiative and nonradiative properties of nanocrystals of different shapes*, Chem. Soc. Rev. 35:209-217

[158] Kelly, K. L., Coronado, E., Zhao, L. L., Schatz, G. C. (2003) *The optical properties of metal nanoparticles: the influence of size, shape, and dielectric environment*, J. Phys. Chem. B. 107:668-677

[159] Klar, T., Perner, M., grosse, S., von Plessen, G., Spirkl, W., Feldmann, J. (1998) *Surface-plasmon resonances in single metallic nanoparticles*, Phys. Rev. Lett. 80:4249-4252

[160] Kerker, M. (1969) *The scattering of light and other electromagnetic radiation*, Academic Press, New York

[161] Bohren, C. F., Huffman, D. R. (1983) *Absorption and scattering of light by small particles*, Wiley, New York

[162] Tong, L., Wei, Q., Wei, A., Cheng, J. (2009) *Gold nanorods as contrast agents for biological imaging: optical properties, surface conjugation, and photothermal effects*, Photochem. Photobiol. 85(1):21

[163] Jain, P. K., Lee, K. S., El-Sayed, I. H., El-Sayed, M. A. (2006) *Calculated absorption and scattering properties of gold nanoparticles of different size, shape, and composition: applications in biological imaging and biomedicine*, J. Phys. Chem. B 110:7238-7248

[164] Link, S., Mohamed, M. B., El-Sayed, M. A. (1999) *Simulation of the optical absorption spectra of gold nanorods as a function of their aspect ratio and the effect of the medium dielectric constant*, J. Phys. Chem. B 103:3073-3077

[165] El-Sayed, I. H., Huang, X., El-Sayed, M. A. (2005) *Surface plasmon resonance scattering and absorption of anti-EGFR antibody conjugated gold nanoparticles in cancer diagnostics: applications in oral cancer*, Nano Lett. 5(5):829-834

[166] Durr, N. J., Larson, T., Smith, D. K., Korgel, B. A., Sokolov, K., Ben-Yakar A. (2007) *Two-photon luminescence imaging of cancer cells using molecularly targeted gold nanorods*, Nano Lett. 7(4):941-945

[167] Wang, H., Huff, T. B., Zweifel, D. A., Hei, W., Low, P. S., Wei, A., Cheng, J. (2005) *In vitro and in vivo two-photon luminescence imaging of single gold nanorods*, Proc. Natl. Acad. Sci. 102(44):15752-15756

[168] Chou, C., Chen, C., Wang, C. R. C. (2005) *Highly efficient, wavelength-tunable, gold nanoparticle based optothermal nanoconvertors*, J. Phys. Chem. B 109:11135-11138

[169] Hirsch, L. R., Stafford, R. J., Bankson, A. J., Sershen, S. R., Rivera, B., Price, R. E., Hazle, J. D., Halas, N. J., West, J. L. (2003) *Nanoshell-mediated near-infrared thermal therapy of tumors under magnetic resonance guidance*, Proc. Natl. Acad. Sci. 100(23):13549-13554

[170] Huang, X., El-Sayed, I. H., Qian, W., El-Sayed, M. A. (2006) *Cancer cell imaging and photothermal therapy in the near-infrared region by using gold nanorods*, J. Am. Chem. Soc. 128:2115-2120

[171] Loo, C., Lowery, A., Halas, N., West, J., Drezek, R. (2005) *Immunotargeted nanoshells for integrated cancer imaging and therapy*, Nano Lett. 5(4):709-711

[172] Mie, G. (1908) *Beitrage zur Optik truber Medien, speziell kolloidaler Metallosungen*, Ann. Phys. 330(3):377-445

[173] Gans, R. (1915) *Uber die Form ultramikroskopischer silberteilchen*, Ann. Phys. 352(10):270-284

[174] Link, S., El-Sayed, M. A. (1999) *Size and temperature dependence of the plasmon absorption of colloidal gold nanoparticles*, J. Phys. Chem. B 103:4212-4217

[175] Kreibig, U., Vollmer, M. (1995) *Optical properties of metal clusters*, Springer Speries in Material Science, 25, Springer, Berlin

[176] Skrabalak, S. E., Chen, J., Au, L., Lu, X. M., Li, X., Xia, Y. (2007) *Gold nanocages for biomedical applications*, Adv. Mater. 19:3177-3184

[177] Guerrero-Martinez, A., Barbosa, S., Pastoriza-Santos, I., Liz-Marzan, L. M. (2011) *Nanostars shine bright for you: colloidal synthesis, properties and applications of branched metallic nanoparticles*, Curr. Opin. Colloid Interface Sci. 16:118-127

[178] Huang, C., Wang, Y., Chiu, P., Shih, M. (2006) *Electrochemical synthesis of gold nanocubes*, Mat. Lett. 60(15):1896-1900

[179] Ha, T. W., Koo, H., Chung, B. H. (2007) *Shape-controlled synthesis of gold nanoprisms and nanorods influenced by specific adsorption of halide ions*, J. Phys. Chem. C 111(3):1123-1230

[180] Feng, H., Yang, Y., You, Y., Li, G., Guo, J., Yu, T., Shen, Z., Wu, T., Xing, B. (2009) *Simple and rapid synthesis of ultrathin gold nanowires, their self-assembly and application in surface-enhanced Raman scattering*, Chem. Commun. 1984-1986

[181] Pallavicini, P., Chirico, G., Collini, M., Dacarro, G., Donà, A., D'Alfonso, L., Falqui, A., Diaz-Fernandez, Y., Freddi, S., Garofalo, B., Genovese, A., Sironi, L., Taglietti, A. (2011) *Synthesis of branched Au nanoparticles with tunable near-infrared LSPR using a zwitterionic surfactant*, Chem. Commun. 47:1315-1317

[182] Draine, B. T., Flatau, P. J. (1994) *Discrete-dipole approximation for scattering calculations*, J. Opt. Soc. Am. 11(4):1491-1499

[183] Moreno, E., Erni, D., Hafner, C. (2002) *Band structure computations of metallic photonic crystals with the multiple multipole method*, Phys. Rev. B 65:155120

[184] Taflove, A. (1995) *Computational electrodynamics: the finite-difference time-domain method*, Artech House, Boston, pp. 559

[185] Jain, P. K., Huang, X., El-Sayed, I. H., El-Sayed, M. A. (2007) *Review of some interesting surface plasmon resonance-enhanced properties of noble metal nanoparticles and their applications to biosystems*, Plasmonics 2:107-118

[186] Johnson, P. B., Christy, R. W. (1972) *Optical constants of the noble metals*, Phys. Rev. B 6(12):4370

[187] Du, H., Fuh, R. A., Li, J., COrkan, L. A., Lindsey, J. S. (1998) *PhotochemCAD: a computer-aided design and research tool in photochemistry*, Photochem. Photobiol. 68(2):141-142

[188] Perez-Juste, J., Pastoriza-Santos, I., Liz-Marzan, L. M., Mulvaney, P. (2005) *Gold nanorods: synthesis, characterization and applications*, Coord. Chem. Rev. 249:1870-1901

[189] Nehl, C. L., Hafner, J. H. (2008) *Shape-dependent plasmon resonances of gold nanoparticles*, J. Mater. Chem. 18:2415-2419

[190] Kreibig, U., Genzel, L. (1985) *Optical absorption of small metallic particles*, Surf. Sci. 156(2):678-700

[191] Kreibig, U., Fragstein, C. V. (1969) *The limitation of electron mean free path in small silver particles*, Z. Physik 224:307-323

[192] Moores, A., Goettmann, F. (2006) *The plasmon band in noble metal nanoparticles: an introduction to theory and applications*, New J. Chem. 30:1121-1132

[193] Ashcroft, N. W., Mermin, N. D. (1976) *Solid state physics*, Saunders College, Philadelphia

[194] Mulvaney, P. (1995) *Surface plasmon spectroscopy of nanosized metal particles*, Langmuir 12:788-800

[195] Sau, T. K., Murphy, C. J. (2004) *Seeded high yield synthesis of short Au nanorods in aqueous solution*, Langmuir 20:6414-6420

[196] Papavassiliou, G. C. (1980) *Optical properties of small organic and organic metal particles*, Prog. Solid St. Chem. 12:185-271

[197] Qiu, L., Larson, T. A., Smith, D. K., Vitkin, E., Zhang, S., Modell, M. D., Itzkan, I., Hanlon, E. B., Korgel, B. A., Sokolov, K. V., Perelman, L. T. (2007) *Single gold nanorod detection using confocal light absorption and scattering spectroscopy*, IEEE J. Sel. Top. Quantum Electron. 13:1730-1737

[198] Payne, E. K., Shuford, K. L., Park, S., Scahtz, G. C., Chad, A. (2006) *Multipole plasmon resonances in gold nanorods*, J. Phys. Chem. B 110(5):2150-2154

[199] Weissleder, R. (2001) *A clearer vision for in vivo imaging*, Nat. Biotechnol. 19:316-317

[200] Gratton, S. A., Ropp, P. A., Pohlhaus, P. D., Luft, J. C., Madden, V. J., Napier, M. E., DeSimone, J. M. (2008) *The effect of particle design on cellular internalization pathways*, Proc. Natl. Acad. Sci. 105(33):11613-11618

[201] Verma, A., Stellacci, F. (2012) *Effect of surface porperties on nanoparticle-cell interactions*, Small 6(1):12-21

[202] Chithrani, B. D., Ghazani, A. A., Chan, W. C. W. (2006) *Determining the size and shape dependence of gold nanoparticle uptake into mammalian cells*, Nano Lett. 6:662-668

[203] Ferrari, M. (2008) *Beyond drug delivery*, Nat. Nanotechnol. 3:131-132

[204] Hao, F., Nehl, C. L., Hafner, J. H., Nordlander, P. (2007) *Plasmon resonances of a gold nanostars*, Nano Lett. 7(3):729-732

[205] Nehl, C. L., Liao, H., Hafner, J. H. (2006) *Optical properties of star-shaped gold nanoparticles*, Nano Lett. 6(4):683-688

[206] Ding, H., Yong, K., Roy, I., Pudavar, H. E., Law, W. C., Bergey, E. J., Prasad, P. N. (2007) *Gold nanorods coated with multilayer polyelectrolyte as contrast agents for multimodal imaging*, J. Phys. Chem. C 111(34):12552-12557

[207] Mooradian, A. (1969) *Photoluminescence of metals*, Phys. Rev. Lett. 22:185

[208] Mohamed, M. B., Volkov, V., Link, S., El-Sayed. M. A. (1999) *The ÔlightningÕ gold nanorods: fluorescence enhancement of over a million compared to the gold metal*, Chem. Phys. Lett. 317:517-523

[209] Boyd, G. T., Yu, Z. H., Shen, Y. R. (1986) *Photoinduced luminescence from the noble metals and its enhancement on roughened surfaces*, Phys. Rev. B Consens. Matter 33(12):7923-7936

[210] Boyd, G. T., Rasing, Th, Leite, J. R. R., Shen, Y. R. (1984) *Local-field enhancement on rough surfaces of metals, semimetals, and semiconductors with the use of optical second-harmonic generation*, Phys. Rev. B 30:519

[211] Bouhelier, A., Bachelot, R., Lerondel, G., Kostcheev, S., Rpyer, P., Wiederrecht, G. P. (2005) *Surface plasmon characteristics of tunable photoluminescence in single gold nanorods*, Phys. Rev. Lett. 95:267405

[212] Imura, K., Nagahara, T., Okamoto, H. (2005) *Near-field two-photon-induced photoluminescence from single gold nanorods and imaging of plasmon modes*, J. Phys. Chem. B 109:13214-13220

[213] Biagioni, P., Celebrano, M., Savoini, M., Grancini, G., Brida, D., Matefi-Tempfli, S., Matefi-Tempfli, M., Duó, L., Hecth, B., Cerullo, G., Finazzi, M. (2009) *Dependence of the two-photon photoluminescence yield of gold nanostructures on the laser pulse duration*, Phys. Rev. B 80:045411

[214] Khandelia, R., Jaiswal, A., Ghosh, S. S., Chattopadhyay, A. (2013) *Gold nanoparticle-protein agglomerates as versatile nanocarriers for drug delivery*, Small. 9(20):3494-3505

[215] Ghosh, P., Han, G., De, M., Kim, C. K., Rotello, V. (2008) *Gold nanoparticles in delivery applications*, Adv. Drug Deliv. Rev. 60:1307-1315

[216] Sironi, L., Freddi, S.,Caccia, M., Pozzi, P., Rossetti, L., Pallavicini, P., Doná, A., Cabrini, E., Gualtieri, M., Rivolta, I., Panariti, A., D'Alfonso, L., Collini, M., Chirico, G. (2012) *Gold branched nanoparticles for cellular treatments*, J. Phys. Chem. C.116:18407-18418

[217] Hemmerich, P. H., von Mikecz, A. H. (2013) *Defining the subcellular interface of nanoparticles by live-cell imaging*, PLOS one. 8(4):e62018

[218] van den Broek, B., Ashcroft, B., Ooosterkamp, T. H., van Noort, J. (2013) *Parallel nanometric 3D tracking of intracellular gold nanorods using multifocal two-photon microscopy*, Nano Lett. 13:980-986

[219] Arcizet, D., Meier, B., Sackmann, E., Radler, J. O., Heinrich, D. (2008) *Temporal analysis of active and passive transport in living cells*, Phys. Rev. Lett. 101:248103

[220] Bruno, L., Levi, V., Brunstein, M., Despósito, M. A. (2009) *Transition to superdiffusive behavior in intracellular actin-based transport mediated by molecular motors*, Phys. Rev. E. 80:011912

[221] Weiss. M., Elsner, M., Kartberg, M. F., Nilsson, T. (2004) *Anomalous subdiffusion is a measure for cytoplasmic crowding in living cells*, Biophys. J. 87:3518-3524

[222] Guigas, G., Kalla, C., Weiss, M. (2007) *Probing the nanoscale viscoelasticity of intracellular fluids in living cells*, Biophys. J. 93(1):316-323

[223] Wu, J., Berland, K. M. (2008) *Propagators and time-dependent diffusion coefficients for anomalous diffusion*, Biophys. J. 95:2049-2052

[224] Mallik, R., Gross, S. P. (2004) *Molecular motors: strategies to get along*, Curr. Biol. 14:R971-R982

[225] Yeung, C., Shtrahman, M., Wu, X. (2007) *Stick-and-diffuse and caged diffusion: a comparison of two models of synaptic vesicle dynamics*, Biophys. J. 92:2271-2280

[226] Pallavicini, P., Chirico, G., Collini, M., Dacarro, G., Doná, A., D'Alfonso, L., Falqui, A., Diaz-Fernandez, Y., Freddi, S., Garofalo, B., Genovese, A., Sironi, L., Taglietti, A. (2011) *Synthesis of branched Au nanoparticles with tunable near-infrared LSPR using a zwitterionic surfactant*, Chem. Commun. 47:1315-1317

[227] Casu, A., Cabrini, E., Doná, A., Falqui, A., Diaz-Fernandez, Y., Milanese, C., Taglietti, A., Pallavicini, P. (2012) *Controlled synthesis of gold nanostars by using a zwitterionic surfactant*, Chem. Eur. J. 18(30):9381-9390

[228] Diaspro, A. (2002) *Confocal and two-photon microscopy: foundations, applications and advances*, John Wiley and Sons Inc., New York

[229] Denk, W., Strickler, J. H., Webb, W. W. (1990) *Two-photon laser scanning fluorescence microscopy*, Science 248:73-76

[230] Nakamura, O. (1993) *Fundamental of two-photon microscopy*, Micr. Res. Tec. 47(3):165-171

[231] Boustany, N. N., Boppart, S. A., Backman, V. (2010) *Microscopic imaging and spectroscopy with scattered light*, Annu. Rev. Biomed. Eng. 12:285-314

[232] Rodriguez-Lorenzo, L., Krpetic, Z., Barbosa, S., Alvarez-Puebla, R. A., Liz-Marzan, L. M., Prior, I. A., Brust, M. (2011) *Intracellular mapping with SERS-encoded gold nanostars*, Integr. Biol. 3:922-926

[233] Yuan, H., Khoury, C. G., Wilson, C. M., Grant, G. A., Bennett, A. J., Vo-Dinh, T. (2012) *In vivo particle tracking and photothermal ablation using plasmon-resonant gol nanostars*, Nanomedicine 8(8):1355-1363

[234] Goldburg, W. I. (1999) *Dynamic light scattering*, Am. J. Phys. 67(12):1152-1159

[235] Berne, B. J., Pecora, R. (1976) *Dynamic light scattering: with applications to chemistry, biology, and physics*, Dover Books on Physics Series, Courier Corporation

[236] Chu, B. (1991) *Laser light scattering: basic principles and practice*, Second Ed., Academic Press Inc.

[237] Bouzin, M., Sironi, L., Chirico, G., D'Alfonso, L., Inverso, D., Pallavicini, P., Collini, M. (2015) ***An intermittent-model Fourier-space analysis of the intracellular motion of gold nanostars by scattering image correlation*****, Biophys. J.** ***In press***

[238] Penjweini, R., Smisdom, N., Deville, S., Ameloot, M. (2014) *Transport and accumulation of PVP-Hypericin in cancer and normal cells characterized by image correlation spectroscopy techniques*, Biochim. Biophys. Acta. 1843:855-865

[239] Coppola, S., Estrada, L. C., Digman, M. A., Pozzi, D., Cardarelli, F., Gratton, E. (2012) *Intracellular trafficking of cationic liposome-DNA complexes in living cells*, Soft Matter. 8:7919-7927

[240] Kulkarni, R. P., Wu, D. D., Davis, M. E., Fraser, S. E. (2005) *Quantitating intracellular transport of poliplexes by spatio-temporal image correlation spectroscopy*, Proc. Natl. Acad. Sci. 102(21):7523-7528

[241] Coppola, S., Caracciolo, G., Schmidt, T. (2014) *Exact occupation probabilities for intermittent transport and application to image correlation spectroscopy*, New J. Phys. 16:113057

[242] Pandzic, E., Rossy, J., Gaus, K. (2015) *Tracking molecular dynamics without tracking: image correlation of photo-activation microscopy*, Methods Appl. Fluoresc. 3:014006

[243] Metzler, R., Klafter, J. (2004) *The restaurant at the end of the random walk: recent developments in the description of anomalous transport by fractional dynamics*, J. Phys. A: Math. Gen. 37:R161-R208

[244] Bressloff, P. C., Newby, J. M. (2013) *Stochastic models of intracellular transport*, Rev. Mod. Phys. 85:135

[245] Saxton, M. J., Jacobson, K. (1997) *Single-particle tracking: applications to membrane dynamics*, Annu. Rev. Biophys. Biomol. Struct. 26:373-399

[246] Metzler, R., Chechkin, A. V., Klafter, J. (2009) *Levy Statistics and Anomalous Transport: Levy Flights and Subdiffusion*, Encyclopedia of Complexity and Systems Science, pp-5218-5239, Springer-Verlag New York

[247] Saxton, M. J. (1993) *Lateral diffusion in an archipelago: single-particle diffusion*, Biophys. J. 64:1766-1780

[248] Das, R., Cairo, C. W., Coombs, D. (2009) *A hidden Markov model for single particle tracks quantifies dynamic interactions between LFA-1 and the actin cytoskeleton*, PLoS Comput. Biol. 5(11):e1000556

[249] Qian, H.m Sheetz, M. P., Elson, E. L. (1991) *Single particle tracking: analysis of diffusion and flow in two-dimensional systems*, Biophys. J. 60:910-921

[250] Levi, V., Gratton, E. (2007) *Exploring dynamics in living cells by tracking single particles*, Cell. Biochem. Biophys. 48:1-15

[251] Jin, S., Verkman, A. S. (2007) *Single particle tracking of complex diffusion in membranes: simulation and detection of barrier, raft, and interaction phenomena*, J. Phys. Chem. B. 111:3625-3632

[252] Gal, N., Lechtman-Goldstein, D., Weihs, D. (2013) *Particle tracking in living cells: a review of the mean square displacement method and beyond*, Rheol. Acta. 52:425-443

[253] Michalet, X. (2010) *Mean square displacement analysis of single-particle trajectories with localization error: Brownian motion in an isotropic medium*, Phys. rev. E. 82:041914

[254] Ruthardt, N., Lamb, D. C., Brauchle, C. (2011) *Single-particle tracking as a quantitative microscopy-based approach to unravel cell entry mechanisms of viruses and pharmaceutical nanoparticles*, Mol. Ther. 19(7):1199-1211

[255] Chechkin, A. V., Gonchar, V. Y., Klafter, J., Metzler, R. (2006) *Fundmentals of Lévy flights processes*, In Fractals, diffusion, and relaxation in disordered complex systems: advances in chemical physics, Part B, Vol.133

[256] Wong, I. Y., Gardel, M. L., reichman, D. R., Weeks, E. R., Valentine, M. T., Bausch, A. R., Weitz, D. A. (2004) *Anomalous diffusion probes microstructure dynamics of entangled F-actin networks*, Phys. Rev. Lett. 92(17):178101(4)

[257] Bouchaud, J., Georges, A. (1990) *Anomalous diffusion in disordered media: statistical mechanisms, models and physical applications*, Physics Reports 195:127-293

[258] Boon, J. P., Lutsko, J. F. (2015) *Nonlinear theory of anomalous diffusion and application to Fluorescence Correlation Spectroscopy*, J. Stat. Phys., Springer New York

[259] Klafter, J., Blumen, A., Zumofen, G., Shlesinger, M. F. (1990) *Lévy walk approach to anomalous diffusion*, Physica A 168:637-645

[260] Shlesinger, M. F., Zaslavsky, G. M., Klafter, J. (1993) *Strange kinetics*, Nature 363:31-37

[261] Barthelemy, P., Bertolotti, J., Wiersma, D. S. (2008) *A Lévy flight for light*, Nature 453:495-498

[262] Bartumeus, F., da Luz, M. G. E., Viswanathan, G. M., Catalan, J. (2005) *Animal search strategies: a quantitative random-walk analysis*, Ecology 86:3078-3087

[263] Ebeling, W., Romanovsky, M. Y., Sokolov, I. M. (2009) *Velocity distributions and kinetic equations for plasmas including levy type power law tails*, Contrib. Plasm. Phys. 49(10):704-712

[264] Corral, A. (2006) *Universal earthquake-occurrence jumps, correlations with time, and anomalous diffusion*, Phys. rev. Lett. 97:178501

[265] Brockmann, D., Hufnagel, L., Geisel, T. (2006) *The scaling laws of human travel*, Nature 439:462-465

[266] Mantegna, R., Stanley, H. (1995) *Scaling behaviour of an economic index*, Nature 376:46-49

[267] Shlesinger, M. F. (2006) *Random walks follow the money*, Nat. Phys. 2:69-70

[268] Castiglione, P., Mazzino, A., Muratore-Ginanneschi, P., Vulpiani, A. (1999) *On strong anomalous diffusion*, Physica D 134:75-93

[269] Klafter, J., Shlesinger, M. F., Zumofen, G. (1996) *Beyond Brownian motion*, Physics Today 33-39

[270] Mantegna, R. N., Stanley, H. E. (1994) *Stochastic process with ultraslow convergence to a Gaussian: the truncated Lévy flight*, Phys. Rev. Lett. 73(22):2946-2949

[271] Loverdo, C., Bénichou, O., Moreau, M., Voituriez, R. (2008) *Enhanced reaction kinetics in biological cells*, Nat. Phys. 4:134-137

[272] Huet, S., Karatekin, E., Tran, V. S., Cribier, S., Henry, J.P. (2006) *Analysis of transient behavior in complex trajectories: application to secretory vesicle dynamics*, Biophys. J. 91:3542-3559

[273] Caspi, A., Granek, R., Elbaum, M. (2002) *Diffusion and directed motion in cellular transport*, Phys. Rev. E 66:011916

[274] Bénichou, O., Loverdo, C., Moreau, M., Voituriez, R. (2006) *Two-dimensional intermittent search processes: an alternative to Lévy flight strategies*, Phys. Rev. E 74:020102(R)

[275] Bénichou, O., Loverdo, C., Moreau, M., Voituriez, R. (2007) *A minimal model of intermittent search in dimension two*, J. Phys. Condens. Matter 19:065141

[276] Brandao, H. B., Sangji, H., Pandzic, E., Bechstedt, S., Brouhard, G. J., Wiseman, P. W. (2013) *Measuring ligand-receptor binding kinetics and dynamics using k-space image correlation spectroscopy*, Methods 66:273-282

[277] Rice, S., Lin, A. W., Safer, D., Hart, C. L., Neber, N., Carragher, B. O., Cain, S. M., Pechatnikova, E., Wilson-Kubalek, E. M., Whittaker, M., Pate, E., Taylor, E. W., Milligan, R. A., Vale, R. D. (1999) *A structural change in the kinesin motor protein that drives motility*, Nature 16;402(6763):778-784

[278] Caspi, A., Granek, R., Elbaum, M. (2000) *Enhanced diffusion in active intracellular transport*, Phys. Rev. Lett. 85(26):5655-5659

[279] Kulkarni, R. P., Castelino, K., Majumdar, A., Fraser, S. E. (2006) *Intracellular transport dynamics of endosomes containing DNA polyplexes along the microtubule network*, Biophys. J. L42-L44

[280] Pallavicini, C., Desposito, M. A., Levi, V., Bruno, L. (2010) *Analysis of persistence during intracellular actin-based transport mediated by molecular motors*, XI Latin American Workshop on Nonlinear Phenomena, Journal of Physics:246:012038

[281] Roding, M., Guo, M., Weitz, D. A., Rudemo, M., Sarkka, A. (2014) *Identifying directional persistence in intracellular particle motion using Hidden Markov Models*, Math. Biosci. 248:140-145

[282] Gal, N., Weihs, D. (2010) *Experimental evidence of strong anomalous diffusion in living cells*, Phys. Rev. E 81:020903(R)

[283] Valentine, M. T., Kaplan, P. D., Thota, D., Crocker, J. C., Gisler, T., Prud'homme, R. K., Beck, M., Weitz, D. A. (2001) *Investigating the microenvironments of inhomogeneus soft materials with multiple particle tracking*, Phys. Rev. E 64:061506

[284] Monnier, N., Barry, Z., Park, H. Y., Su, K., Katz, Z., English, B. P., Dey, A., Pan, K., Cheeseman, I. M., Singer, R. H., Bathe, M. (2015) *Inferring transient particle transport dynamics in live cells*, Nat. Meth. 12:838-840

[285] Berezhkovskii, A. M., Bezrukov, S. M. (2011) *Effective drift and diffusion of a particle jumping between mobile and immobile states*, J. Electroanal. Chem. 660:352-355

[286] Martin, D., Forstner, M. B., Kas, J. A. (2002) *Apparent sub-diffusion inherent to single particle tracking*, Biophys. J. 83:2109-2117

[287] Suh, J., Wirtz, D., Hanes, J. (2004) *Real-time intracellular transport of gene nanocarriers studied by multiple particle tracking*, Biotechnol. Prog. 20: 598-602

[288] Baum, L. E., Petrie, T. (1966) *Statistical inference for probabilistic functions of finite state Markov chains*, Ann. Math. Stat. 37:1554-1563

[289] Ewens, W., Grant, G. (2005) *Statistical methods in bioinformatics*, Springer, 2nd Ed.

[290] Press, W. H., Teukolsky, S. A., Vetterling, W. T., Flannery, B. P. (2007) *Numerical recipes: the art of scientific computing*, Cambridge University Press, 3rd Ed.

[291] Grimmett, G., Strizaker, D. (2001) *Probability and random processes*, Oxford University Press, 3rd Ed.

[292] Kolin, D. L., Ronis, D., Wiseman, P. W. (2013) *k-Space Image correlation spectroscopy: a method for accurate transport measurements independent of fluorophore photophysics*, Biophys. J. 91:3061-3075

[293] Semrau, S., Schmidt, T. (2007) *Particle Image Correlation Spectroscopy (PICS): retrieving nanometer-scale correlations from high-density single molecule position data*, Biophys. J. 92:613-621